Coordination of Impedance Controllers and Flexible Power for Curative Congestion Management in Real-Time Applications

A thesis approved for the academic degree of

Doktor der Ingenieurwissenschaften (Dr.-Ing.)

at the

Faculty of Electrical Engineering and Information Technology

TU Dortmund University

by

Oliver Pohl, M.Sc.

Supervisor:	Univ.-Prof. Dr.-Ing. Christian Rehtanz, TU Dortmund University
Co-Advisor:	Univ.-Prof. Dr.-Ing. Dirk Westermann, TU Ilmenau

Day of Oral Examination: 17.04.2024

Abstract

As the share of feed-in from renewable energy sources rises in German electricity grids, established preventive congestion management processes are called into question. Curative congestion management may increase the utilization of already existing grid capacity without the large investments necessary for conventional grid expansion. The curative paradigm shift requires fast reacting remedial measures, such as innovative power flow controlling devices, as well as reliable algorithms to determine and activate them in due time. This work shows how an automated system can coordinate distributed FACTS devices, that influence a power line's series reactance, and active power from flexible units to solve line overloads in high voltage grids. First, linear sensitivities for gradual reactance changes are derived. Based on this, an optimization and a heuristic approach for automated curative coordination of both types of remedial measures is conceptualized as well as implemented and tested in simulations. Then, the heuristic approach is implemented within a distributed agent-based control algorithm, along with fallback strategies to be executed if agent communication fails. This system is then tested in a laboratory setup to evaluate its real-time applicability. The laboratory setup consists of multiple (Power) Hardware-in-the-Loop modules to create an experimental environment considering many real-world factors that are usually neglected in software simulations. This way, not just the agent algorithm itself, but also the influence of communication delays, reaction times of real power flow controlling devices as well as the integration into a control center environment are evaluated.

Kurzfassung

Aufgrund des steigenden Anteils der Einspeisung aus erneuerbaren Energien in die deutschen Stromnetze werden die etablierten Verfahren des präventiven Engpassmanagements in Frage gestellt. Kuratives Engpassmanagement könnte die Ausnutzung bereits existierender Netzkapazitäten erhöhen, ohne dass große Investitionen in konventionellen Netzausbau notwendig wären. Für diesen kurativen Paradigmenwechsel werden schnell reagierende Gegenmaßnahmen, wie beispielsweise innovative leistungsflussregelnde Betriebsmittel, ebenso wie verlässliche Algorithmen für die rechtzeitige Determinierung und Aktivierung selbiger benötigt. Diese Arbeit zeigt, wie ein automatisiertes System flexible Einheiten und verteilte FACTS-Geräte, die die Serienreaktanz einer Stromleitung beeinflussen, koordinieren kann, um Leitungsüberlastungen in Hochspannungsnetzen zu beheben. Zunächst werden lineare Sensitivitäten für schrittweise Reaktanzänderungen entwickelt. Darauf aufbauend werden ein Optimierungs- und ein heuristischer Ansatz zur automatisierten kurativen Koordination beider Maßnahmentypen konzipiert sowie implementiert und simulativ getestet. Anschließend wird der heuristische Ansatz in einem verteilten, agentenbasierten Algorithmus implementiert und um Fallback-Strategien ergänzt, die bei Ausfall der Agentenkommunikation ausgeführt werden. Dieses System wird dann in einem Laboraufbau getestet, um seine Echtzeitanwendbarkeit zu bewerten. Der Laboraufbau beinhaltet mehrere (Power) Hardware-in-the-Loop Module, um eine Testumgebung zu erschaffen, welche eine Vielzahl von Faktoren aus der realen Welt beinhaltet, welche in Software-Simulationen üblicherweise vernachlässigt werden. So werden nicht nur der Agentenalgorithmus selbst, sondern auch der Einfluss von Kommunikationsverzögerungen, Reaktionszeiten von realen Leistungsflusssteuerungsgeräten sowie die Integration in eine Leitstellenumgebung evaluiert.

Prelude

There are many people whom I need to thank with regards to the creation of this thesis. First and foremost, I would like to express my sincere gratitude to Univ.-Prof. Dr.-Ing. Christian Rehtanz for giving me the opportunity to go on this Ph.D. journey and support me over the entire course of it. Special acknowledgements go to Univ.-Prof. Dr.-Ing. Dirk Westermann for co-supervising this thesis.

Without the support and open discussion culture at TU Dortmund's ie^3, my Ph.D. experience would have been significantly less fruitful and enjoyable. I would like to thank my colleagues Dr.-Ing. Florian Rewald, Stefan Dalhues, and Oliver Kraft for providing helpful suggestions, discussions, and the team work in our research projects IDEAL and HONOR. For the fundamental contributions to the laboratory setup, I would like to thank Dr.-Ing. Alfio Spina. My gratitude also goes to all colleagues who gave valuable feedback to my writing, notably Dr.-Ing. Rajkumar Palaniappan, Charlotte Biele, Martin Lindner, and Sebastian Liemann. I would also like to express my thanks to my longtime student assistants Hadi Ibrahim, Omar al Samman, and Louay Hito for their contributions in the model and laboratory implementations.

Finally, I would like to give a massive thank you to my family for their support during this process and especially to my partner Anja for her support, understanding, and patience during the past years.

Dortmund, October 2023

Oliver Pohl

> *If you base medicine on science, you cure people. If you base the design of planes on science, they fly. If you base the design of rockets on science, they reach the moon. It works...*
>
> - Richard Dawkins

Contents

1 Introduction

As the share of feed-in from renewable energy sources in lower voltage levels rises as a result of Germany's energy transition, the occurrence of power flows directed from downstream to upstream grids becomes increasingly frequent. This puts the electrical grids under stress since they were not originally designed to handle these bidirectional power flows. Additionally, with the fluctuating generation from renewables alongside new load patterns stemming from sector coupling units, such as electric vehicles and heat pumps, power flows are becoming more difficult to predict for grid operators.

Conventional methods to relieve stress from the grids cannot quite keep up with the speed at which these problems are evolving; planning and building new or replacing old power lines and cables is a costly and time-intensive effort. This is why Germany's Transmission System Operators (TSOs) apply the NOVA[1] principle today, which favors optimizing the utilization of existing grid infrastructure before enhancing or extending it [1]. One area where such optimization could be applied effectively, is the adjustment of Congestion Management (CM) processes in place today. As Remedial Measures (RMs) for CM are determined and applied preventively in virtually all cases, in order to maintain (n-1)-secure grid operation at all times, the grid's transmission capacity is being limited below its physical capability. However, with the advent of fast acting Power Flow Control (PFC) devices such as Flexible AC Transmission Systems (FACTS), the need to prevent overloads and strictly maintain (n-1)-security has partially waned in theory [2]. Thus, a shift towards curatively applied measures can help freeing up blocked transmission capacity. By determining and activating these measures ad-hoc (i.e. post-fault) instead of day-ahead, the effectivity of RMs can also become more independent from the adequacy of forecasts. The relevancy of this approach is twofold: besides enabling higher utilization of existing infrastructure, it may also increase the power grid's resilience against high-impact low-probabilty events, causing unpredicted grid emergencies, which cannot realistically be accounted for by preventive CM processes but may be mitigated by curative ad-hoc measures.

Since both the ad-hoc determination of appropriate curative measures as well as their activation is highly time-critical, a reliable, robust, and fast automated CM system should be applied. Following the NOVA principle, such a system can make use of already existing Flexible Power Units (FPUs), i.e. generators and loads with flexibly controllable outputs,

[1] *NetzOptimierung vor NetzVerstärkung vor NetzAusbau* (English: *Network optimization before expansion before enhancement*)

to perform automated redispatch [1]. Fast acting PFC devices can be used to support these RMs. To keep grid enhancement efforts low, cost-efficient and easily installed Distributed Flexible AC Transmission Systems (D-FACTS) can be used. When implementing such a system in a real grid, it has to be integrated into existing processes for grid operation and operational planning as well as the associated software tools.

While such automated CM systems have been subject of research and sporadic field tests in the past, their actual application in real grids is yet to come. The aim of this thesis is to bridge the gap between previous software simulations of automated curative CM systems and their real-world application.

1.1 Objectives and research questions

This thesis makes a practice-oriented contribution to the more efficient utilization of existing grid infrastructure and higher resiliency against unforeseen congestions in the High Voltage (HV) level. To achieve this, an automated CM system is developed that determines and activates RMs involving D-FACTS and FPUs ad-hoc in the post-fault state. The system evaluation is done in the context of existing operational planning and live operation processes to determine its effectivity regarding overload relief, its efficiency in measure utilization, its reliability and robustness in case of communication issues, and its adequacy with regards to real-time application. A detailed derivation of these core properties and their relevancy is done in Chapter 2. Here, a more high-level approach is taken to derive the research questions this thesis strives to answer.

Until now, D-FACTS have been used for overload prevention of their carrier lines, i.e. the power lines they are installed on [3, 4, 5]. Such applications are effective since the devices have a large sensitivity towards their carrier line's power flow. However, their ability to affect all power flows in the grid by changing one line's reactance offers the possibility to solve congestions appearing on other lines as well. The influence of D-FACTS on power flows are limited since they can only partially shift power flows into alternative paths. By coordinating their utilization with redispatch of FPUs, potentially combined RMs can be determined that are more effective and efficient at solving congestions than the usage of either technology alone. For preventive CM this could be achieved through optimization approaches. However, for ad-hoc solutions that are determined post-fault, there is likely not enough time to run an optimization. Instead, new approaches have to be defined that can reliably determine effective RMs for CM in due time after a congestion occurred during live operation. Thus, the first research question here is:

i: **Coordinating distributed FACTS and flexible power:** *How can RMs for curative CM utilizing D-FACTS and FPUs be determined post-fault?*

Since reaction time to determine and activate RMs is limited in the post-fault state, these processes should be handled by an automated system. In the recent past, there have been a number of studies on the effectivity and efficiency of automated CM systems [6, 7, 8, 9, 10]. To decrease measure selection times and ensure reliability and robustness against communication failures, distributed control systems with no single point of failure have been shown to be adequate solutions for these applications. Since past studies were focused on simulative evaluations, the results neglect many real-world factors such as imperfect communication channels and reaction delays. Also, questions regarding the conceptualization and implementation of such a system on real off-the-shelf hardware have not been addressed. Thus, one of the main goals of this thesis is to determine how an automated curative CM system performs in a real-world environment in real-time. From this goal, the second research question can be formulated as:

ii: **Real-time reactions:** *What reaction times can distributed curative CM systems achieve in real-time applications?*

In a real grid, no system functions in an isolated manner; they have to be integrated with already existing processes and tools. This is especially true for automated systems that take over tasks previously handled manually by the System Operator (SO). Thus, the third research question is targeted at the integration of the developed system:

iii: **Control center integration:** *How can an automated curative CM system be integrated into existing Control Center (CC) processes and software?*

While previous works in this regard have implied perfect communication, when moving curative CM systems closer to real-world application, the issue of communication outages and how the system can react to them needs to be addressed. Thus the last research question is as follows:

iv: **Fallback strategy:** *How should an automated curative CM system react to communication failures?*

The thesis at hand was created alongside the research project IDEAL[2] [OP1]. To embed the aforementioned research questions within this context, the project's basic concept as well as the overlaps with and a delimitation from this thesis is briefly described as follows: The aim of IDEAL was to develop a distributed ad-hoc curative CM system using D-FACTS as well as FPUs and demonstrate this in a laboratory environment also consid-

[2]Impedanzregler und Dezentrales Engpassmanagement für Autonome Leistungsflusskoordinierung

ering CC requirements. Additionally, an algorithm to aggregate flexibility in the lower voltage levels to be made available to the upstream grid was to be developed and field-tested. While this thesis does not touch on the topic of flexibility aggregation (for this, see [11]), it goes beyond the project's scope through an in-depth look at the CM system's underlying sensitivities and alternative heuristics as well as possible fallback strategies and a more detailed evaluation of the resulting system reaction times.

1.2 Structure of this thesis

The thesis consists of eight chapters, including this introduction and a conclusion. Chapters 2–7 can be structured into three groups as shown in Fig. 1.1 and explained in the following:

Research Gap: In Chapter 2 the state of practice and research in preventive and curative CM is described to derive the research gap.

Coordination & Simulation: Following these basics, methods to coordinate D-FACTS and FPUs for CM are developed in Chapter 3. These consist of heuristic algorithms and an optimization approach used as a benchmark. To analyze the adequacy of the developed coordination methods for curative CM, they are implemented and tested in a simulation environment in Chapter 4. These chapters aim at answering research question i.

Multi-Agent System (MAS) & Laboratory: To make use of the developed coordination tools in a real-time environment, a MAS for curative CM is described in Chapter 5. Here, appropriate fallback solutions for communication outages are derived as well, addressing research question iv. The laboratory environment to test this system in is described in Chapter 6, including all four modules of the implemented multi-Hardware-in-the-Loop (HIL) setup as well as the implementation of the previously conceptualized MAS on distributed devices. The description of the CC module of the laboratory setup tackles research question iii. Test scenarios and laboratory results are described in Chapter 7 to answer research question ii. Finally, a conclusion and an outlook for future research is given in Chapter 8.

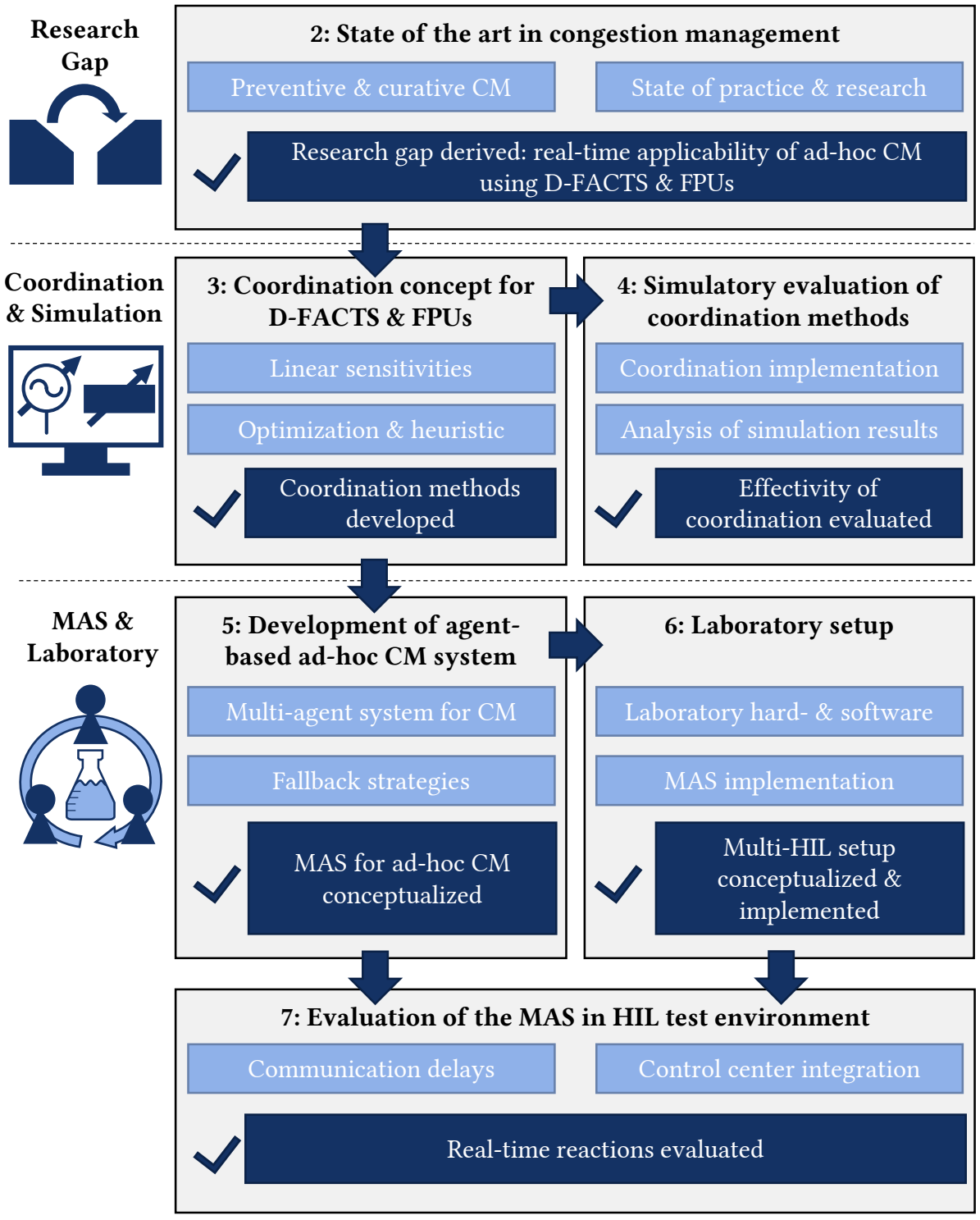

Figure 1.1: Thesis structure

2 State of the art in congestion management

In this chapter the concepts and processes to manage congestions in (sub-)transmission grids are explained as they are applied by SOs today, along with a review of recent research activities in this area. A brief categorical overview of CM is given first, with the remainder of the chapter focusing on CM in the operational planning and live operation phases. Relevant regulation and applied practices in operational CM are explained to describe today's state of practice. This is followed by a literature review on research in this field, supported by descriptions of relevant PFC devices and redispatch measures, including definitions for flexibility and Redispatch 2.0. A special focus is then put on research efforts regarding the automation of operational CM. Finally, conclusions are drawn regarding the requirements for CM systems that can keep the grids operational in the future.

2.1 Congestion management categorized

A physical congestion in an electrical grid is defined by [12] article 2 as:

> "any network situation where forecasted [within contingency analyses] or realised power flows violate the thermal limits of the elements of the grid and voltage stability or the angle stability limits of the power system"

Thermal limits are derived from the equipment's material properties and are often expressed as current or power flow limits such as Permanent Admissible Transmission Loading (PATL) [13]. Since current is the main driver of line temperature, current limits should be preferred over power limits when applicable as they are a more direct indicator of thermal behavior (i.e. 100 MW at 110 kV will cause different temperatures than 100 MW at 120 kV). CM includes all kinds of measures a grid operator can use to avoid or alleviate congestions in their grid [14]. With the liberalization of electricity markets in Europe in the late '90s, the importance of CM for grid operators has increased. In a competitive electricity market the grid within a bidding zone is assumed to be a figurative copper plate, i.e. the grid is free of congestion at all times. Tie lines connecting two bidding zones may experience congestion, which is why their capacity is allocated. This way, any demand can be met by any supplier within the same market zone without the need to account for the strain this might put on the grid. In reality, power flows through the grid resulting from market activity may well cause congestions if the grid does not possess the appropriate transmission capacity. Hence, SOs have been applying the (n-1) principle. This principle

states that a contingency, i.e. the outage of a grid device, must not lead to uncontrollable cascading outages propagating outside of the operator's responsibility area [15]. In practice, this means that the outage of one device may not lead to the overload of another device. The need for grid operators to ensure (n-1)-secure operation lowers the available transmission capacity because power lines cannot be operated at their actual physical limits. Additionally, the increase in installation of distributed energy resources over the last years is causing power flows to be more volatile and unpredictable. In Germany, the rising generation from wind power in the North and decommissioning of large power plants together with high energy demand in the South, along with slow conventional grid expansion is causing congestions in the transmission and also distribution grids to be more frequent. This is also apparent in the increasing CM costs reported by German TSOs over the last years [16]. Thus, the need for CM solutions has been subject of research and development activities for the past two decades.

As visualized in Fig. 2.1, CM measures can be categorized with regards to

- the incentive driving them (market- or grid-related measures)
- the domain they are applied in (structural, organizational, or operational), or synonymously their time frame (long- / mid- / short-term)
- the time of activation relative to a contingency (before or after)

When congestions appear frequently on the same power lines over several months or years, they are called structural congestions since they are caused by structural grid deficiencies. Any physical change of primary infrastructure in an electrical grid with the aim of alleviating overload situations in the long run, i.e. within years, fall under the category of *structural measures* for CM. An argument can be made that such grid expansion or enhancement measures are inevitable in the long run due to rising demand in electricity. However, structural CM measures involve large investments, long planning and installation times and the risk of sunk costs if generation and load patterns change faster than expected, which may render a previously installed expansive measure obsolete.

CM measures coming from the regulatory framework set up by policy-making institutions as well as grid operators themselves are counted as *organizational measures*. All of these are market-related since they aim at changing electricity market parameters and their effects on congestions emerge from market behavior. Various market designs and price incentives to counter congestions have been applied in different countries, such as nodal or zonal prices or market splitting mechanisms [17]. Another market-related organizational measure is the allocation of interconnector capacity and auction thereof, as

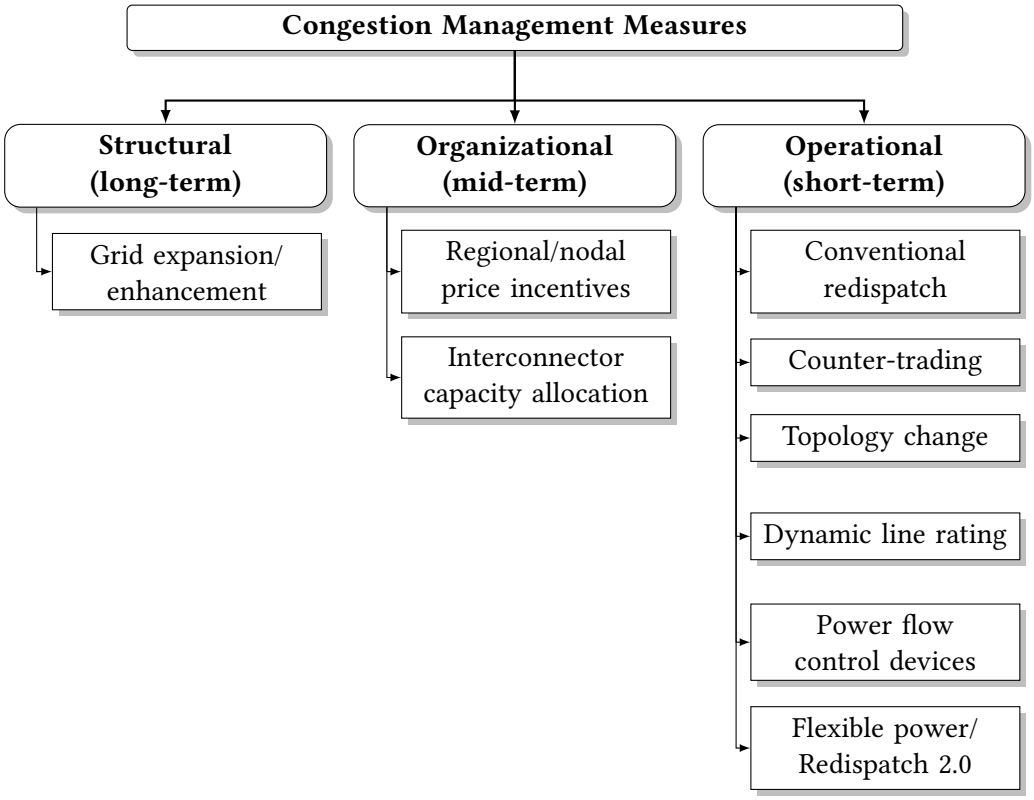

Figure 2.1: Congestion management measures categorized

regulated by [12]. This measure is aimed at controlling exchange of electricity between market zones in the medium (seasonal differences) and short run (day-ahead signals for the market).

With the power system undergoing faster and more unpredictable changes in recent years, while conventional grid expansion is being slowed down by regulatory and monetary issues, SOs have been required to shift their focus towards measures falling in line with the NOVA-principle, which states all grid optimization measures must be exhausted before considering grid enhancement or expansion [1]. Hence, the focus of research and industry is shifting towards *operational measures* for CM, also called *RMs* or *remedial actions*. Note that by definition, these terms include actions aimed at maintaining overall operational security, not just regarding congestions (e.g. also actions targeted at frequency stability). A comprehensive list of actions can be found in Article 22 of [18]. Within this thesis however, RMs mean those targeted at relieving congestion and thus include measures that involve setpoint changes of grid devices owned by the operator (at no cost) or generation and load units (including remuneration costs) during the operational planning and live operation phase. The remainder of this chapter explains the most relevant aspects of operational CM since this is the focus of this thesis.

2.2 State of practice in operational congestion management

While the regulatory framework for operational CM defines requirements and targets with sufficient clarity in [19] as well as [12] and [18], the actual processes for implementing these rules in Germany and throughout Europe are rather intransparent and dependent on the SO, as also noted in [20] – and even more so for sub-transmission SOs. The following explanations regarding CM processes in day-to-day operations of grids at nominal voltages equal to or higher than 110 kV are taken from [21] and personal correspondence with industry experts.

2.2.1 Operational planning and real-time operation

German TSOs are required by § 13 of [19] to eliminate any disturbances in the grid that interfere with safety of supply using operational CM measures. Operational planning performs rotating contingency analyses based on forecasts for a time frame of one hour up to seven days ahead. Due to changing grid situations, uncertainties in used (weather) forecasts, and possibly long ramp-up times of power plants, this process is split up into four consecutively executed processes shown in Fig. 2.2. First, redispatch potentials are secured in Week Ahead Planning Process (WAPP) and Preventive Redispatch (pRD1) to hold conventional power plants' output in reserve. Then, power plants' set points adjustment, coordination of PFC devices and topological switch measures are determined during Preventive Redispatch in Day-Ahead Congestion Forecast (pRD2/DACF) and Intraday Congestion Forecast (IDCF). All of these processes use optimization algorithms to determine RMs and are formulated by SOs as AC security-constrained optimal power flow problems.

Any necessary RMs that were calculated but not activated in the operational planning phase are activated by the SO during real-time operation. Additionally, contingency analyses and state estimations are used to evaluate already preventively applied RMs regarding their effectivity to adjust them if necessary.

The described operational measures can be separated into preventive and curative – also referred to as corrective – measures, depending on whether they are activated before or after a congestion has physically occurred during live operation, i.e. post-fault. Both types of measures and their application in grid operation today are explained in the following subsections.

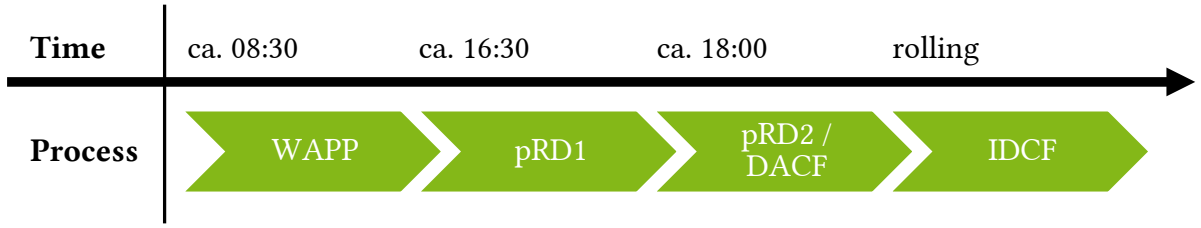

Figure 2.2: Operational planning processes in congestion management of German transmission SOs (based on [21])

2.2.2 Preventive operational congestion management measures

According to [22], preventive remedial actions are

> "[...] a remedial action that is the result of an operational planning process and needs to be activated prior to the investigated timeframe for compliance with the (N-1) criterion."

They are applied one week down to one hour in advance to a predicted contingency. Today, the vast majority of RMs is used preventively to secure (n-1)-safety at all times. This means, that if the contingency analysis detects a congestion in operational planning, the grid shifts from *normal operational state* to *alert operational state* and appropriate RMs have to be determined. These measures then need to be activated in due time before the contingency actually occurs to prevent going into *emergency operational state* if the respective device faults during real-time operation and the congestion actually occurs. [18]

Examples for such preventive operational measures are:

- *Topological changes*: by opening or closing busbar connectors, the distribution of power flows throughout the grid can be significantly changed.
- *Switching PFC devices*: increasing or decreasing the tap position of Phase-Shifting Transformers (PSTs) or set points of FACTS can partially push power flows out of heavily loaded lines onto parallel paths with lower loading.
- *Redispatch*: by decreasing feed-in or increasing load in front of a congestion while simultaneously increasing feed-in or decreasing load behind it, the congestion can be lowered without sacrificing frequency stability or fulfilment of the supply task. The SO has to remunerate the involved parties for changing their agreed-upon delivery schedules, resp. reduced power demand. [16]
- *Counter-trading*: two (or more) TSOs in different bidding zones trade electricity with

the goal of relieving congestion [23]. The principle is similar to redispatch but specifically for cross-border or cross-zonal congestions. The TSOs have no knowledge of the involved suppliers' locations within the bidding zone and the trades are executed on regular day-ahead and intraday markets.

- *Dynamic line rating (DLR)*: Instead of using fixed PATL limits, DLR allows to adjust maximum loading thresholds according to seasonally or even intra-daily changing values based on weather forecasts or temperature measurements [24]. While DLR does not relieve congestions per se, but rather dynamically redefines what a congestion is, it can still be counted as a preventive CM measure because it prevents congestions.

There is a regulatory incentive for SOs to consider grid-related measures before market-related measures since the former do not produce immediate costs for the operator except for possible maintenance costs caused by increased wearing of the respective grid devices.

Since the activation of RMs does not only affect the grid the measure is targeted at, but also adjacent grids, such measures must be coordinated among SOs. Since 01.10.2021 new regulations regarding CM, subsumed under the term *Redispatch 2.0*, have been applied in Germany through the amendment to the *Netzausbaubeschleungigungsgesetz (NABEG)*[1] [25] and the inclusion of feed-in management of renewable energy sources and combined heat and power plants into [19]. This allows SOs to utilize feeders with a nominal power of 100 kW or higher for redispatch. Units with lower nominal power can also be used if they are fully controllable by the Distribution System Operator (DSO). Loads are not considered within Redispatch 2.0; their usage for CM is covered by *Verordnung zu abschaltbaren Lasten (AbLaV)*[2]. The regulations on Redispatch 2.0 require SOs to coordinate RMs across voltage levels. In [26] these legal obligations are implemented within an operative framework to describe processes enabling such a coordination in day-to-day operations. The overall process can be split into three parts:

1. *Exchange of data for system operator coordination*: SOs exchange base data, planning data, non-claimabilities, and market-related adjustments of technical/controllable resources across voltage levels. These data cover a time horizon of the next 33.5 h in 15 min resolution. Updates are given at a 1 h rate, except for the time span of 2 h before fulfilment where the rate is 15 min.
2. *Coordinated dimensioning of redispatch measures*: based on the exchanged data, ev-

[1] Act for the Acceleration of Power Line Expansion
[2] Act on disconnectable loads

ery SO performs state estimations and contingency analyses for specific time intervals to identify congestions in their respective grid. Under the consideration of exchanged flexibility-related data, every operator then dimensions their needed flexibility usage and informs other operators about it. Sensitivities are used to allocate the correct amount and location of flexible power to solve a congestion. An actual activation of flexible power must be communicated separately as well.

3. *Activation of redispatch measures*: depending on the measures' required leading times, they are activated as late as possible and as early as needed to ensure the measure's adequacy to the current grid state. A flexible measure is activated by the SO with controlling authority over it, either because this operator needs the flexible measure to relieve congestion in their own grid, or because another operator demanded them to activate it.

By constantly updating and communicating planned redispatch measures, SOs can leverage synergies by utilizing flexibility already activated by another operator instead of activating additional power.

These preventive measures on the one hand ensure a secure transmission and supply of electrical energy, but on the other hand limit the degree of grid capacity usage. In the recent past, the supply task has been changing at a faster pace than long-term measures such as grid enhancement and expansion could compensate for. This is why many SOs are now starting to look for alternatives to preventive measures, which will be explained in the following subsection.

2.2.3 Curative operational congestion management measures

Curative remedial actions for CM are defined in [22] as

> "[...] a remedial action that is the result of an operational planning process and is activated straight subsequent to the occurrence of the respective contingency for compliance with the (N-1) criterion, taking into account transitory admissible overloads and their accepted duration"

Curative CM measures are defined during operational planning but are applied during live operation after a congestion has occurred but before grid devices are damaged. A qualitative depiction of the different effect of preventive and curative measures on line current is shown in Fig. 2.3. The main takeaway here is, that the preventive activation of RMs after a contingency has been detected during operational planning, will reduce line current – but will also do so even if the contingency does not actually occur. With

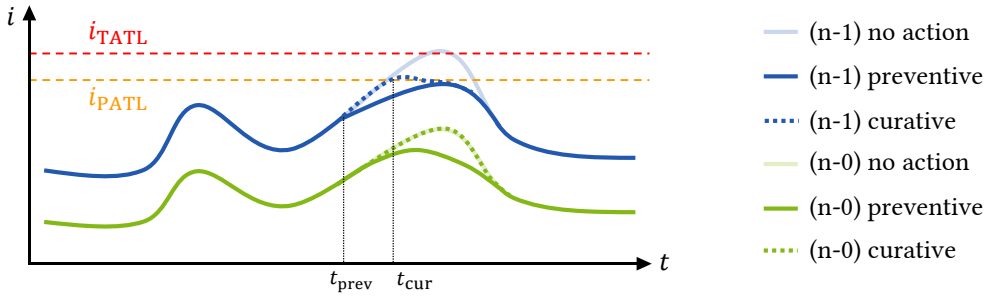

Figure 2.3: Exemplary line current under preventive/curative measures and inaction

curative activation, there is a short time where the line may exceed its PATL up to its Temporary Admissible Transmission Loading (TATL) if the contingency occurs, thus enabling higher admissible line currents in (n-0)-state. To retain (n-1)-security at all times, preventive measures are generally favored over their curative counterparts and SOs are advised to maintain a list of pre-defined curative measures for emergencies [15]. These measures are also communicated with other SOs within Redispatch 2.0 in the shape of flexibility restrictions [26]. Since relieving congestion post-fault is highly time-critical, only measures that can be activated quickly and have an immediate impact are viable options. Measures with long activation times, such as redispatch of large power plants or stepping slow power flow controlling devices, may be inadequate for curative CM. One of the main downsides of this procedure is that the effectivity of pre-defined curative measures depends on the quality of the forecasts they are based on. If the actual grid state post-fault diverts too far from the prognosis, the pre-defined curative measures may not be adequate anymore to completely and safely relieve a congestion [21].

An example of curative CM that has been applied for several decades [27] and is still used today are Special Protection Schemes (SPSs), also referred to as Remedial Action Scheme (RAS). These are systems that automatically detect abnormal power system conditions and activate pre-defined curative measures to mitigate harmful effects of said conditions. They are used to solve a variety of problems, such as angle, frequency, or voltage instability as well as cascading line trips. Measures taken can involve generation (rejection thereof or setpoint changes in fast feeders), load shedding, High Voltage Direct Current (HVDC) setpoint changes, topology changes - or even a combination of measures. SPSs can be activated event-based (e.g. when a certain outage occurs) or reaction-based (e.g. when a certain line overloads). Their fast reaction times of milliseconds to seconds often require extensive (enhancements to) communication infrastructure. Since the predefinition of adequate curative measures needs to take into account a large number of possible grid states, contingencies, and other external factors, SPSs are usually targeted at

a small part of a larger grid involving a manageable number of grid devices. [28] Similar to SPSs but with a larger geographical scope are Wide Area Control Systems (WACSs), which incorporate the basic functionality of SPSs by applying pre-defined curative measures automatically, but make use of Wide Area Monitoring Systems (WAMSs) to cover a much larger area and solve geographically distributed problems in the grid [29]. One notable implementation of such a system with regards to the topic of this dissertation is mentioned in [30], where a WACS with centralized PFC functions is tested on a laboratory scale.

2.3 State of research in operational congestion management

To ensure that grid operation processes can keep up with the challenges emerging from the combination of fast changing generation and demand patterns and slow grid expansion, governmental funding for research in this area has been abundant in the recent past. National calls, such as *OptiNet I* by Germany's Federal Ministry of Economic Affairs and Energy (BMWi), as well as international calls such as ERA-Net *RegSys* and *SG+* or HORIZON 2020's *CL5-2021-D3-02: Sustainable, secure and competitive energy supply* put a focus on improving grid operation processes. This is also apparent in the increase of funding spent by BMWi for safety of supply and grid operation projects [31]. Results and publications of operational CM research projects funded within these and other programmes are described in the follwoing subsections to give an overview of the state of research in this area.

2.3.1 Preventive grid operation

After Redispatch 2.0 enhanced conventional redispatch considerations by enabling participation of feeders down to nominal powers of 100 kW and implementing a consistent and continuous data exchange between SOs of different voltage levels, the underlying processes and infrastructures are now subject of research and innovation endeavors. In this regard, the research project *Redispatch 3.0* aims at improving Redispatch 2.0 concepts by integrating low voltage prosumers and expanding TSO / DSO communication. [32] The architecture for this has been published in [33] and the developed concepts are to be tested in a relevant laboratory environment including CC software. As of the writing of this thesis, one of the most recent (i.e. still ongoing) developments in this regard is that

the two European regional security coordinators Coreso and TSCNET have launched a joint programme called CorNet. Within this programme, existing tools to coordinate operational processes between TSOs will be enhanced and integrated into a joint platform, improving coordination processes for security analysis, capacity calculation, short term adequacy assessment and others. [34]

2.3.2 Curative grid operation

One of the earliest mentions in the literature of curative grid operation is mentioned in [35]. Although a lot of research followed this, its main principle and benefits are still the same: While preventive CM has been a tried and proven way to ensure safety of supply, the applied safety margins limit the grid's transmission capacity below its technical limitations. The extent to which the grid is limited by this is often described by the industry rule-of-thumb of limiting power line capacities at 70 % of their rating in (n-0)-state [36, 37, 38], which has also been confirmed analytically in [39]. Curative CM is one way to partially free up these 30 %. The curative approach provides that measures to relieve congestions are applied immediately after a congestion actually occurs in real-time operation, i.e. post-fault. This concept utilizes the thermal inertia of power lines which allows them to carry currents above their PATL limits for a short time without taking damage or risking unsafe degrees of sagging. Under this operating principle, emergency operational state is allowed for a short time, as long as measures to bring back the grid into alert operation state can be applied in due time before irreversible damage is caused or outages start cascading. [21] This short time frame is also one of the main reasons why preventive CM has prevailed for so long over curative operation: Determining optimal RMs requires long computation times, after which a grid operator has to activate these measures manually, and additionally, many types of measures, such as conventional redispatch or conventional PFC devices such as PSTs require long ramp-up, (resp. step-up) times, making them too slow to react in due time post-fault [2].

Since SPSs are already applied in several places in today's grid operation, as mentioned in Subsection 2.2.3, their improvement has been subject of investigation in several research projects. The comparison of conventional preventive grid operation with curative operation in form of five different types of SPS in [40] shows that the curative approach can deliver similar levels of supply safety as its preventive counter-part. The authors stress however, that possible communication failures may compromise the system. In accordance with this, cyber-security of SPSs has been subject of research in a multitude of projects, two of which shall be mentioned here. In [41], a cost-benefit analysis of SPSs

is executed that wages constraint costs against risks of demand curtailment if the SPS malfunctions. Since the necessary computations depend on a multitude of grid state variables, optimization methods are deemed inadequate and heuristic algorithms are chosen instead. The systems still manage to produce cost savings at low probabilities of load curtailments. Since SPSs strongly rely on a functioning communication infrastructure, [42] propose using agent-based communication to shield these critical systems from cyber attacks. The results show that applying agent-based control in these systems can increase their robustness.

As SPSs are usually only applied to a small grid area, they may not help in freeing up a lot of potentially available capacity with regards to an operator's entire grid. Hence, the idea of operating an entire grid under the curative approach, or at least decreasing the amount of preventive measures for a stronger reliance on curative measures, has been addressed by researchers in the recent past. The potential of curative measures to reduce the need for preventive measures is, for example, analyzed in [8, 9]. The simulation results of several different curative operation strategies show significantly reduced redispatch costs the more curative measures are favored over preventive ones. The authors do however point out that the application of the curative grid operation principle on a larger scale requires reliable controllability and response times and coordination of curative measures with protection systems as well as a high degree of automation within the related processes. In the project *InnoSys 2030*, a system has been developed to manage an adequate ratio of preventive and curative measures with a combined optimization thereof. Within this system, preventive and curative measures are pre-determined 1 h–48 h in advance to a possible contingency and selected based on a set of key performance indicators. The researchers also stress the importance of the integration of such systems within existing Supervisory, Control and Data Acquisition (SCADA) structures in the CC and provide a visualization concept. [10] The *grid booster* strategy further developed within this project that makes use of battery storages for curative CM is explained in more detail in [43] and [OP2]. The authors emphasize that other curative measures have to take over the initial battery storage activation before the storages are fully discharged, and that these additional measures also have to be pre-determined during the operational planning phase. In a similar approach, the authors of [44, 45, 46, 47, 48, 49] focus on using HVDC systems to solve congestions in the AC grid curatively. In [47], the authors describe their concept as a SPS because curative measures are pre-determined in operational planning and only activated post-fault during live operation, but since it takes into account a global grid view to solve all contingencies in a contingency list, the term Wide Area Control System (WACS) is likely more appropriate. The importance of integrating such novel systems

for curative CM within SCADA systems of a CC is stressed in [45, 46], where the authors demonstrate their tools in a HIL laboratory environment. Finally, detailed evaluations regarding the optimization algorithms to pre-determine curative measures are given in [47, 48, 49]. While the results achieved in these works are thorough and promising, the pre-determining approach comes with the caveat of being reliant on forecast quality and incapable of relieving contingencies that were unaccounted for during operational planning. Such downsides of pre-determining curative measures are explained and evaluated in [6]. When curative measures are determined based on forecasts, the adequacy of these measures upon their activation will be subject to uncertainty. According to the authors' simulation results, such a deterministic approach to curative CM presents a risk to grid security and comes with economic disadvantages, especially during unexpected events, such as outages of more than one grid device or large fluctuations in wind or solar power generation.

Another approach to curative grid operation is to not only activate but also determine RMs against overloads ad-hoc, so *after* a congestion occurs. When the calculation and coordination of RMs happens post-fault, they are based on the most recent measurements and momentary grid state, which can potentially make the measures better suited to relieve the congestion more adequately and more efficiently. In the case of high-impact low-probabilty events causing unforeseen overloads, this is not just a question of RM adequacy and efficiency, but actually a necessity in order to be able to handle such emergency states at all. However, this requires a fast, robust and reliable method to determine said measures. Thus, the calculation should not be triggered by a human operator post-fault, but executed automatically as soon as a contingency occurs during live operation. While many other parts of grid operation have already been automated, such as frequency control and transformer tapping, CM is still performed manually (with some automation in the decision support functions of the control center's SCADA systems). [7] To enable ad-hoc determination and activation of curative RMs for CM, a higher degree of automatization within the related systems and processes is necessary. Since the handling of congestions post-fault poses a paradigm change to today's preventive CM, the determination and activation of ad-hoc measures would have to be integrated within existing CM processes and the application of the (n-1)-principle in general.

2.3.3 Power flow control devices

Currents flow through an electrical grid according to Ohm's law. For an operator of a meshed grid, this means that they cannot choose which pathways power flows will take

through their system to get from source to sink. There are however several technical devices that allow an operator to influence electrical parameters in a grid to diverge power flows from heavily loaded lines into less loaded parallel paths. The most common types of such devices are explained as follows, with a short overview of more conventional instruments and a more detailed look into the devices used in Chapters 4 and 7.

2.3.3.1 Phase shifting transformers

According to [50], a PST is defined as:

> "A transformer that advances or retards the voltage phase-angle relationship of one circuit with respect to another."

The device consists of a transformer that is connected in series to a power line, with its secondary winding fed by a (tapped) shunt transformer. This way, it can inject a voltage in quadrature to the line voltage, creating a voltage phase angle difference proportional to the tap set point. The two main uses of PSTs are the control of loop flows through parallel paths and the control of power exchange between two large, independent transmission grids. Since they pose a mature and reliable PFC option and are widely used throughout European transmission grids [1, 51] research regarding these devices is mostly focused on their optimal and coordinated operation [52] and location planning [OP3]. The major downsides of this technology is the high cost and long planning times necessary before installation [1, 53], as well as their limited reaction time due to the fact that PSTs can only be tapped gradually and slowly to avoid wearing of the device [2].

2.3.3.2 Flexible AC transmission systems

In the late '80s FACTS were introduced [54]. They are defined by [55] as:

> "Alternating current transmission systems incorporating power electronic-based and other static controllers to enhance controllability and increase power transfer capability"

Today, various types of FACTS are in use with different areas of application, such as PFC or voltage stability control. The most relevant types of FACTS used for PFC are Thyristor Controlled Series Compensators (TCSCs), Static Synchronous Series Compensators (SSSCs), and Unified Power Flow Controllers (UPFCs).

A TCSC is an assembly of thyristor valves, thyristor reactor(s), and capacitors that can change the effective value of the line's series reactance. In a TCSC, the whole capacitor

bank or alternatively, a section of it, is provided with a parallel thyristor controlled inductor that adds current pulses in phase with the line current to increase the capacitive voltage. By keeping the additional voltage proportional to the line current, the TCSC increases the effective series reactance and with multiple modules, a TCSC bank can do so in a stepwise manner. [56]

An SSSC employs a voltage source converter connected in series to a transmission line through a transformer or multi-level inverters. It injects a voltage in series to the line, which leads or lags the line current by 90°, effectively emulating a controllable inductive or capacitive reactance. An SSSC performs similar to a TCSC but provides additional functions, most notably its ability to not only decrease but also increase power flow through its serially connected line by reducing the effective inductive reactance. [51]

A UPFC is considered the most flexible, powerful and comprehensive FACTS device, since it combines multiple functionalities, allowing an operator to operate it in different modes to pursue different goals. Its main components are a series converter, which can be used to control power flows through a line it is connected to, and a shunt converter, allowing for voltage and reactive power control. [57]

FACTS are powerful devices giving SOs additional degrees of freedom in PFC and other tasks. Due to their large size as well as high production and installation costs, they require thorough and thus time-consuming planning efforts, resulting in only a few installations in real grids worldwide; only three UPFCs were installed between 1995 and 2004. [55, 58]

2.3.3.3 Distributed flexible AC transmission systems

The disadvantages of FACTS mentioned in Subsection 2.3.3.2 caused researchers to look for alternative solutions that would provide similar functionalities but at lower costs and easier installation processes. In 2007 a dynamic power flow controller was introduced by ABB Ltd which provides bidirectional PFC functionality but at much faster reaction times than a PST and lower expected production costs than an SSSC [2]. It consists of several series-connected thyristor-switched capacitors and reactors for fast responses of small magnitudes and a PST for slower responses with a greater impact on power flows. Although its functionality was demonstrated in laboratory tests at TU Dortmund University [59, 60], the device never left the laboratory stage.

Around the same time, researchers at Georgia Institute of Technology proposed the concept of D-FACTS in [61, 62]. The basic principle of the technology is that D-FACTS pro-

vide the same functionality as FACTS but instead of one single large device, a D-FACTS installation consists of a fleet of many small devices. This way, mass production is possible instead of tailor-made solutions, providing much lower production costs through economies of scale. While market prices for D-FACTS are not publicly available, their original target price was placed at $100 per kVA, which would be below the costs of regular FACTS devices at $150–$300 per kVA [53]. Additionally, the modular character of the devices enables easier integration into (n-1) safety, since a malfunctioning device is automatically bypassed so the overall fleet does not have a single point of failure. The technology was further developed at Georgia Tech until first prototypes were tested and finally, the research endeavors resulted in founding the spin-off company *Smart Wires Inc.*. While the company developed and distributed different types of D-FACTS over the years, only the most relevant for this dissertation will be explained in detail here. An extensive review of literature on D-FACTS can be found in [58].

One of the first commercially available D-FACTS devices is the Distributed Series Reactor (DSR), three of which are shown in Fig. 2.4a. A schematic of a DSR is shown in Fig. 2.4b. DSRs are clamped directly onto overhead power lines and inject a small amount of reactance into the line when remotely activated. This is achieved through a single-turn transformer that uses the line conductor itself as the primary winding. This way, the module can draw the – comparatively negligible amount of – power to supply its communication module directly from the line. The transformer can be bypassed by opening the normally-closed electromechanical switch S_{M}, for example during fault conditions. With S_{M} open, the thyristor switch S_1 controls the injection of inductance into the line: if S_1 is closed, only an insignificant amount of inductance is injected due to the leakage inductance of the single-turn transformer, but if S_1 is opened, the transformer's magnetizing inductance is injected, resulting in an additional line series reactance of X_{M}. The magnitude of X_{M} depends on the turns-ratio of the transformer (usually rather large, e.g. $50 : 1$) and its air gap. Commercially available DSR models provide between 9.6 mΩ–40.7 mΩ of series reactance in the case of Smart Wire's devices called *PowerLine Guardian* [63]. A DSR has minimal insulation and voltage rating requirements since it is electrically floating on the power line, which is the reason for its low weight, allowing the on-line installation in the first place. While a single device can only inject a small amount of reactance, a fleet of devices can achieve a significant impact on a line's power flow, making it the distributed version of a TCSC. How large such a fleet can be, depends on which DSR type is chosen and how many devices are installed on a power line. To reduce line sagging due to the additional weight of the devices, it is recommended to install DSRs close to the towers carrying the line. With one DSR before and one behind the tower,

and a tower distance of 300 m–500 m, approx. 4 – 7 devices per phase per kilometer can be installed. For the common HV line type *Al/St 265/35* with 0.3875 Ω/km reactance and an appropriate DSR type *SD4-700* with 0.0178 Ω per device, this would mean a maximum line reactance change of 18 %–32 %. In addition to the lower production costs, installing DSRs on power lines is also much easier than installing FACTS devices. Installations have been done by only a few line men using cranes, helicopters, and – in the case of the laboratory installation described in Chapter 6 – fork lifts. Since deinstallation is just as easy, the devices can be used as interim solutions, for example to support reconstruction works on closely located lines [3], or re-deployed to other lines in case long-term power flow pattern changes necessitate this.

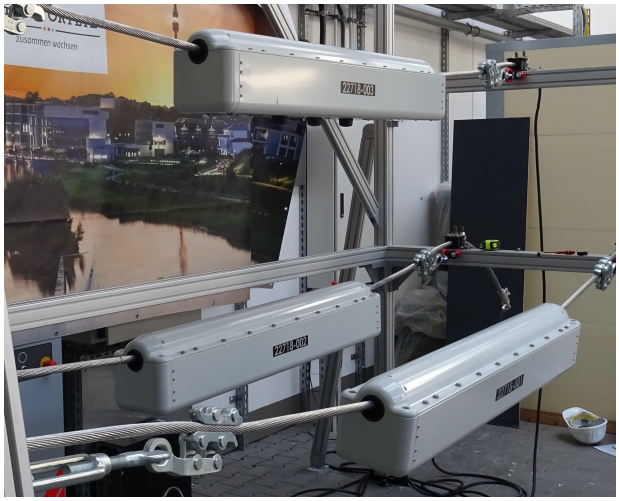

(a) Three PowerLine Guardians in a laboratory installation in TU Dortmund's Smart Grid Technology Lab

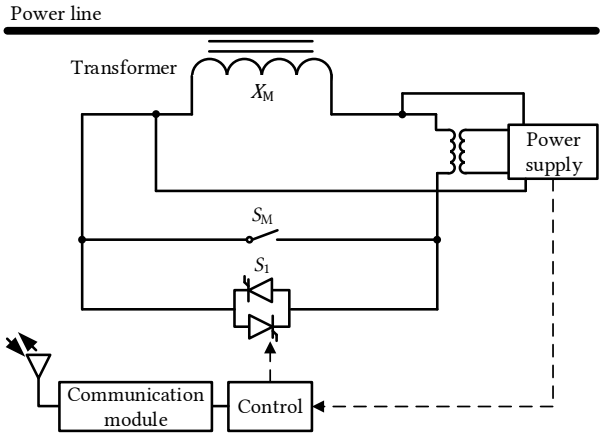

(b) Circuit schematic of a DSR (based on [61])

Figure 2.4: Distributed series reactors

The disadvantages of DSRs are the additional weight they put on the power lines, which in turn limits the amount of devices and thus the amount of additional reactance that can be injected, as well as the fact that DSRs can only provide inductive but not capacitive reactance. An alternative solution comes in the form of modular SSSCs, marketed by SmartWires as *SmartValves*. The concept of these devices is similar to that of DSRs except additional capacitive and inductive elements provide the functionality of injecting either inductive or capacitive reactance (or none at all). Since the devices are at several tons significantly heavier than DSRs, they cannot be mounted on a line directly. Alternatively,

Figure 2.5: Installation of SmartValves at a substation of Greek TSO IPTO ([65])

they can be installed on power line towers or on the ground (cp. Fig. 2.5), with the latter still taking up less space than a comparative SSSC installation. To make up for the higher weight, a single modular SSSC can inject up to 566 V–5660 V in quadrature to the line, which equals a significantly larger absolute additional reactance than a single DSR with only about 10 V–18 V, depending on the exact device model and current magnitude. [64] As of 2022, modular SSSCs have mostly replaced DSRs in the market (Smart Wires Inc. is not distributing or advertising them anymore online).

D-FACTS are used to control power flows in multiple installations in several countries all over the world [5]. So far, the algorithms used to control these devices in the field are limited to those that Smart Wires Inc. provides. These are current limiting concepts, that increase inductive reactance injection if the current of the line that the devices are installed on breaches a certain threshold to keep the current below this limit. For modular SSSCs there are also use cases to increase capacitive reactance of a line, if a parallel line breaches a current limit. Since these solutions are aimed at specific lines, they have the character of SPS. There are, however, no field applications of a broader usage of D-FACTS, where multiple fleets of devices are coordinated together to perform more efficient PFC tasks, enabled through more complex control algorithms under consideration of a larger section of the grid.

2.4 Conclusions and requirements for future congestion management systems

The changes in power flows caused by variations in generation and load patterns due to the energy transition call for innovative CM strategies. Structural and organizational measures can be an effective solution for this in the long run, but in the short and medium term they may be too slow to take effect in due time, which may lead to an increased risk of congestions and rising redispatch costs. The short-term solutions in place today, namely preventive operative CM, is a tried and proven way to operate the grid securely, but with low efficiency, since it limits transmission capacities significantly below technical thresholds. Curative CM appears as a viable alternative, as it frees up transmission capacities. By favoring curative over preventive measures, the risk of inadequacy of these measures to reduce overloads in due time post-fault rises. This is especially true if these curative measures are pre-defined based on forecasts. When curative measures are not pre-defined but determined ad-hoc after an overload has occurred, they are more likely to be adequate as they are based on momentary grid state. On the downside, the time to determine and activate measures ad-hoc before grid equipment is irreversibly damaged is short. Also, most curative approaches today, such as SPS, are only aimed at small grid areas with known weak spots, and thus do not offer solutions for the overall grid, and also do not make use of synergies between measures that could be leveraged through coordination thereof. As for the measures themselves, grid-related measures should be preferred over costly conventional market-related options. This is already done today, but mostly with devices that are either slow (PSTs) or expensive (FACTS).

This is why this thesis proposes an automated CM system that determines and applies curative RMs post-fault and ad-hoc, by utilizing D-FACTS and flexible power in a coordinated manner. The system needs to be

- *reliable*, with a very high availability and no single points of failure,
- *robust*, with ways to address unforeseen grid and control system states,
- *effective*, in terms of reducing overloads in due time without producing new ones,
- *efficient* in its use and coordination of available resources,
- *integratable* into existing control systems.

In the following chapters this system is conceptualized, implemented, verified and validated simulatively, and tested in a laboratory with a focus on real-time applicability.

3 Curative coordination of reactance changes and flexible power

With the requirements formulated in Chapter 2, concepts can be drawn for the simultaneous coordination of impedance controlling devices and flexible power to curatively solve overloads in an HV grid.

Since the concept is meant to be used in real-time applications and ad-hoc post-fault, it is vital to use calculation methods that find solutions fast and reliably. Hence, optimizations are inappropriate due to their long calculation times and the possibility that no optimal solution can be found. As an alternative, a heuristic approach seems fitting. A heuristic algorithm can be set up so that it does not need a lot of input to find a solution fast, which may not be optimal, but will be beneficial. In terms of coordinating PFC devices and flexible power this means that the measures at hand may not be used in the most efficient way, and in some cases, an overload may not be solved entirely, but it will be reduced and the overall grid situation will be improved. To make the algorithm fast, reliable and robust, i.e. to increase the chances of it finding a solution and do so even with limited input available, AC power flow calculations are not feasible. When operating in the AC-domain, iterative methods such as Gauss-Seidel or Newton-Raphson are applied to determine nodal voltages and currents and subsequently active and reactive power flows. While these methods yield precise results, they need a lot of input values, may take a long time iterating, and may not converge to a solution at all. So for the algorithm to be developed, DC power flow calculation is more appropriate. Even more so because the goal is to reduce current-driven congestions via impedance controlling devices – both of which mostly correlate with active power only.

The remainder of this chapter will introduce the necessary DC sensitivity calculations to determine appropriate set point changes of Impedance Controllers (ICs) and FPUs. This is followed by the description of an optimization approach in Subsection 3.2.1 to serve as a benchmark for the heuristic approach, explained in Section 3.2.2. Finally, quality indicators for such coordination algorithms are given in Section 3.3.

3.1 Linear Sensitivities

In the context of power systems, a sensitivity $\gamma_{d,m}$ describes the differential of a physical value α of the grid device d towards the physical value β of the RM, m. In other words, the sensitivity of α towards β describes by how much α will change due to an infinitesimal change of β. A general mathematical description can be given with eq. (3.1).

$$\gamma_{d,m} = \frac{\partial \alpha_d}{\partial \beta_m} \tag{3.1}$$

Sensitivities are used in a variety of applications, especially in those where multiple consecutive re-calculations of the grid state after introduced changes would be too computationally intensive. Instead, sensitivities for all relevant devices can be calculated once at the beginning and by multiplying them with the respective measures' changes, resulting effects can be determined without a re-calculation after every introduced change. This introduces an error due to the assumption of a linear relation between α and β, shown in eq. (3.2), which is untrue for most cases.

$$\hat{\alpha}_d = \alpha_d + \Delta\beta_m \cdot \gamma_{d,m} \tag{3.2}$$

Here, α describes the state before the introduction of a change, and $\hat{\alpha}$ is the state after the change $\Delta\beta$ has been introduced. Instead of determining a sensitivity as a true differential for an infinitesimal step, it is usually easier to calculate a sensitivity for a specific step size $\Delta\tau_{\text{step}}$ and then assume linear relation between α and β from there. The most precise way to do this is by performing two AC power flow calculations, one before and one after introducing a step sized change, and then subtracting the results, as shown in eq. (3.3).

$$\gamma_{d,m}^{\text{AC}}(\Delta\tau_{m,\text{step}}) = \alpha_d^{\text{AC}}(\Delta\beta_m = \Delta\tau_{m,\text{step}}) - \alpha_d^{\text{AC}}(\Delta\beta = 0) \tag{3.3}$$

This way, linearization happens around a specific operation point at an adequate interval for the specific application; the error in eq. (3.2) is small for $\Delta\beta_m \approx \Delta\tau_{m,\text{step}}$. For example, if a PST tap increment caused a phase angle shift of 0.1°, the linearization error would be larger for a sensitivity based on a shift of 0.001° than if it was based on 0.01°.

Often however, and also for the proposed heuristic, so-called linearized DC power flow equations are necessary, introducing additional linearization errors. The following derivation of DC power flow equations from AC power flow equations are based on [66], [67], and [68]. Eq. (3.4) and (3.5) show the AC power flow equations to calculate active (p) and

reactive (q) power flows from nodes i to j through nodal voltage magnitudes v and angles δ, resp. angle differences θ, via lines' susceptances b and conductances g.

$$p_{ij} = g_{ij}\left(v_i^2 - v_i v_j \cos(\theta_{ij})\right) - b_{ij} v_i v_j \sin(\theta_{ij}) \tag{3.4}$$

$$q_{ij} = b_{ij}\left(v_i^2 - v_i v_j \sin(\theta_{ij})\right) - g_{ij} v_i v_j \cos(\theta_{ij}) \tag{3.5}$$

This non-linear problem can be linearized by introducing several assumptions regarding the electrical properties at all N nodes and all L branches of a grid:

1. Voltage angle differences are small: $\sin(\theta_l) = \theta_l$, $\cos(\theta_l) = 1 \; \forall \; l \in [0; L]$
2. Voltages are at nominal level: $v_n = 1\,\text{pu} \; \forall \; n \in [0; N]$
3. Branch resistances are negligible (no losses): $r_l \ll x_l \; \therefore \; r_l = 0 \; \forall \; l \in [0; L]$
4. $-b_l \approx \frac{1}{x_l} \; \forall \; l \in [0; L]$

The result are the DC power flow equations shown in eq. (3.6) for nodal power injections, (3.7) for branch power flows, and eq. (3.9) as their combination.

$$\underset{[N\times 1]}{\boldsymbol{p}_\text{N}} = \underset{[N\times N]}{\boldsymbol{B}_\text{N}} \cdot \underset{[N\times 1]}{\boldsymbol{\delta}_\text{N}}, \quad \text{with } p_n = \sum_{k=0}^{N} b_{\text{N},nk}\delta_k \tag{3.6}$$

$$\underset{[L\times 1]}{\boldsymbol{p}_\text{L}} = -\underset{[L\times 1]}{\boldsymbol{b}_\text{L}} \odot \underset{[L\times 1]}{\boldsymbol{\theta}_\text{L}} = -\underset{[L\times L]}{\boldsymbol{B}_\text{D}} \cdot \underset{[L\times N]}{\boldsymbol{A}} \cdot \underset{[N\times 1]}{\boldsymbol{\delta}_\text{N}}, \quad \text{with } p_l = -b_l \cdot \theta_l = -b_l \cdot (\delta_i - \delta_j) \tag{3.7}$$

Here, $\boldsymbol{p}_\text{N}$ is the nodal power vector, $\boldsymbol{B}_\text{N}$ is the DC susceptance matrix of the grid and $\boldsymbol{\delta}_\text{N}$ is the nodal voltage angle vector. Likewise, $\boldsymbol{p}_\text{L}$ denotes the vector of power flows over all branches from their starting to their ending nodes, $\boldsymbol{b}$ designates the vector of all branch susceptances, and $\boldsymbol{\theta}_\text{L}$ comprises the voltage angle differences over all branches. $\boldsymbol{B}_\text{D}$ is the diagonal matrix of branch susceptances and the grid's incidence matrix $\boldsymbol{A}$ indicates a branch's starting node with 1, its ending node with -1, and is 0 otherwise. The non-bold, non-capitalized counterparts of these variables are their respective vector or matrix elements. Furthermore, the following conventions are applied throughout this chapter:

- n denotes any node in the grid
- n_P denotes a specific node whose active power is being manipulated
- l denotes any branch in the grid with starting and ending nodes i and j
- λ denotes a specific line whose reactance is being manipulated with starting and ending nodes v and w
- k is a counting variable

With these equations, calculating active power flows becomes relatively simple: When the susceptance matrix and nodal power values are known, eq. (3.6) can be solved for the voltage angles (cp. eq. (3.8)), which can in turn be put into eq. (3.7) to yield the active power flows for all branches (cp. eq. (3.9)).

$$\boldsymbol{\delta}_{\mathrm{N}} = \left(\boldsymbol{B}_{\mathrm{N}}\right)^{-1} \cdot \boldsymbol{p}_{\mathrm{N}}, \quad \text{with } \delta_n = \sum_{k=0}^{N} c_{nk} p_k,\ c_{ij} \in \left(\boldsymbol{B}_{\mathrm{N}}\right)^{-1} \tag{3.8}$$

$$\begin{aligned} \underset{[L\times 1]}{\boldsymbol{p}_{\mathrm{L}}} &= \underset{[L\times L]}{-\boldsymbol{B}_{\mathrm{D}}} \cdot \underset{[L\times N]}{\boldsymbol{A}} \cdot \underset{[N\times N]}{\left(\boldsymbol{B}_{\mathrm{N}}\right)^{+}} \cdot \underset{[N\times 1]}{\boldsymbol{p}_{\mathrm{N}}}, \quad \text{with } p_l = -b_l \cdot \sum_{k=1}^{N} \left(c_{ik} - c_{jk}\right) p_k \\ &= \boldsymbol{B}_{\mathrm{D}} \cdot \boldsymbol{A} \cdot \left(\boldsymbol{A}^{\mathrm{T}} \cdot \boldsymbol{B}_{\mathrm{D}} \cdot \boldsymbol{A}\right)^{+} \cdot \boldsymbol{p}_{\mathrm{N}} \end{aligned} \tag{3.9}$$

Note that in many cases $\boldsymbol{B}_{\mathrm{N}}$ is not invertible and thus the pseudo-inverse $\left(\boldsymbol{B}_{\mathrm{N}}\right)^{+}$ should be used instead. In comparison to AC power flow calculations, no iterations are necessary and convergence is guaranteed. On the downside, a linearization error is introduced regarding the results of $\boldsymbol{p}_{\mathrm{L}}$, and no statements can be made regarding reactive power.

A variety of linear sensitivities can be derived from the DC power flow concept, targeted at different events or devices. In the following subsections, the two sensitivities most relevant to this dissertation are explained in detail.

3.1.1 Power transfer distribution factors

One of the most widely used types of linear sensitivities is the Power Transfer Distribution Factor (PTDF), denoted here as $\gamma^{\Delta\mathrm{P}}$. The value of $\gamma^{\Delta\mathrm{P}}_{l n_{\mathrm{P}}}$ describes the sensitivity of a branch l towards a nodal power change of 1 pu at node n_{P} in pu. Accordingly, the PTDF-matrix $\boldsymbol{\Gamma}^{\Delta\mathrm{P}}$describes all branches' sensitivities towards all nodes, as shown in eq. (3.10).

$$\underset{[L\times N]}{\boldsymbol{\Gamma}^{\Delta\mathrm{P}}} = \begin{pmatrix} \gamma^{\Delta\mathrm{P}}_{1,1} & \gamma^{\Delta\mathrm{P}}_{1,2} & \cdots & \gamma^{\Delta\mathrm{P}}_{1,N} \\ \gamma^{\Delta\mathrm{P}}_{2,1} & \ddots & & \vdots \\ \vdots & & \ddots & \vdots \\ \gamma^{\Delta\mathrm{P}}_{L,1} & \cdots & \cdots & \gamma^{\Delta\mathrm{P}}_{L,N} \end{pmatrix}, \quad \text{with } \gamma^{\Delta\mathrm{P}}_{l,n} = \frac{\partial p_l}{\partial p_n} \tag{3.10}$$

To get the power flows after a nodal power change via the DC power flow equations, first the resulting voltage angles are calculated. This is shown in eq. (3.11) for a nodal power change Δp in a node n_{P} causing voltage angle changes $\Delta\boldsymbol{\delta}_{\mathrm{N}}$[1]. The added generation is

[1] While bold capital notation is used for matrices within this dissertation (see *List of Symbols*), note that Δ and also $\boldsymbol{\Delta}$ (bold print) indicate a change in a variable instead.

taken up by the slack node.

$$\boldsymbol{\delta}_{\mathrm{N}} + \Delta\boldsymbol{\delta}_{\mathrm{N}} = \left(\boldsymbol{B}_{\mathrm{N}}\right)^{+} \cdot \left(\boldsymbol{p}_{\mathrm{N}} + \Delta\boldsymbol{p}_{\mathrm{N},n_{\mathrm{P}}}\right), \quad \text{with } \Delta p_n = \begin{cases} \Delta p \;\forall\; n = n_{\mathrm{P}} \\ -\Delta p \;\forall\; n = n_{\mathrm{S}} \\ 0 \;\forall\; n \neq n_{\mathrm{P}}, n_{\mathrm{S}} \end{cases} \tag{3.11}$$

Since only the changes in power flows, and thus the changes in voltage angles, are of interest, $\boldsymbol{\delta}_{\mathrm{N}} = \left(\boldsymbol{B}_{\mathrm{N}}\right)^{+} \boldsymbol{p}_{\mathrm{N}}$ can be subtracted from eq. (3.11), yielding eq. (3.12).

$$\Delta\boldsymbol{\delta}_{\mathrm{N}} = \left(\boldsymbol{B}_{\mathrm{N}}\right)^{+} \cdot \Delta\boldsymbol{p}_{\mathrm{N},n_{\mathrm{P}}}, \quad \text{with } \Delta\delta_n = \sum_{k=0}^{N} c_{nk} \cdot \Delta p_k = \Delta p \left(c_{nn_{\mathrm{P}}} - c_{nn_{\mathrm{S}}}\right) \tag{3.12}$$

Overall power flows after an introduced nodal power change can be calculated with eq. (3.13).

$$\boldsymbol{p}_{\mathrm{L}} + \Delta\boldsymbol{p}_{\mathrm{L}} = -\boldsymbol{B}_{\mathrm{D}} \cdot \boldsymbol{A} \left(\boldsymbol{\delta}_{\mathrm{N}} + \Delta\boldsymbol{\delta}_{\mathrm{N}}\right) \tag{3.13}$$

Subtracting eq. (3.7) from (3.13) leaves only the resulting power flow changes in (3.14).

$$\Delta\boldsymbol{p}_{\mathrm{L}} = -\boldsymbol{B}_{\mathrm{D}} \cdot \boldsymbol{A} \cdot \Delta\boldsymbol{\delta}_{\mathrm{N}}, \quad \text{with } \Delta p_l = -b_l \cdot \left(\Delta\delta_i - \Delta\delta_j\right) \tag{3.14}$$

Finally, the resulting power flow changes can be calculated by putting eq. (3.12) into (3.14), as shown in eq. (3.15) for all lines and in eq. (3.16) for a single line from i to j.

$$\begin{aligned} \underset{[L\times 1]}{\Delta\boldsymbol{p}_{\mathrm{L}}} &= \left(-\boldsymbol{B}_{\mathrm{D}} \cdot \boldsymbol{A}\right) \cdot \left(\boldsymbol{B}_{\mathrm{N}}\right)^{+} \cdot \underset{[N\times 1]}{\Delta\boldsymbol{p}_{\mathrm{N},n_{\mathrm{P}}}} \\ &= \underbrace{\left(-\boldsymbol{B}_{\mathrm{D}} \cdot \boldsymbol{A}\right) \cdot \left(-\boldsymbol{A}^{\mathrm{T}} \cdot \boldsymbol{B}_{\mathrm{D}} \cdot \boldsymbol{A}\right)^{+}}_{\underset{[L\times N]}{\boldsymbol{\Gamma}^{\Delta\mathrm{P}}_{\mathrm{BASE}}}} \cdot \underset{[N\times 1]}{\Delta\boldsymbol{p}_{\mathrm{N},n_{\mathrm{P}}}} \end{aligned} \tag{3.15}$$

$$\Delta p_l = \underbrace{(-b_l)\left(\left(c_{in_{\mathrm{P}}} - c_{in_{\mathrm{S}}}\right) - \left(c_{jn_{\mathrm{P}}} - c_{jn_{\mathrm{S}}}\right)\right)}_{\gamma^{\Delta\mathrm{P}}_{ln_{\mathrm{P}}}} \cdot \Delta p \tag{3.16}$$

Note that $\Delta\boldsymbol{p}_{\mathrm{N},n_{\mathrm{P}}}$ only contains non-zero values in its elements n_{P} and n_{S} and thus with these equations only the sensitivities for one specific n_{P} can be calculated, but not the sensitivities for all lines towards all nodes as formulated in eq. (3.10). This is done in eq. (3.17) by multiplying $\boldsymbol{\Gamma}^{\Delta\mathrm{P}}_{\mathrm{BASE}}$ with a matrix that consists of N nodal power change vectors $\Delta\boldsymbol{p}_{\mathrm{N},n}$, each normalized to its power change (i.e. with 1 and -1 instead of $\Delta p_{n_{\mathrm{P}}}$ and

$-\Delta p_{n_\mathrm{P}}$). Column n_P of $\mathbf{\Gamma}^{\Delta\mathrm{P}}$contains the PTDFs of all lines towards a node n_P normalized to the respective power change Δp_{n_P}.

$$\mathbf{\Gamma}^{\Delta\mathrm{P}} = \mathbf{\Gamma}^{\Delta\mathrm{P}}_{\mathrm{BASE}} \cdot \underset{[N\times N]}{\mathbf{\Delta P}^{\mathrm{norm}}_{\mathrm{N}}}, \quad \text{with } \Delta p^{\mathrm{norm}}_{n_1 n_2} = \begin{cases} 1 \forall n_1 = n_2 \\ -1 \forall n_1 = n_\mathrm{S} \\ 0 \forall n_1 \neq n_2, n_1 \neq s \end{cases} \tag{3.17}$$

Within the DC power flow domain PTDFs are only dependent on the susceptances and linear towards nodal power changes, which allows multiplication and addition, making them a powerful tool to find redispatch solutions. When a SO wants to know how much they would have to increase active power generation at a node n_P to reduce the active power flow on a branch l by $\Delta p_{l,\mathrm{need}}$, they can use PTDFs as in eq. (3.18).

$$\Delta p_{n_\mathrm{P},\mathrm{need}} = \frac{\Delta p_{l,\mathrm{need}}}{\gamma^{\Delta\mathrm{P}}_{l n_\mathrm{P}}} \tag{3.18}$$

If they want to know by how much active power flow on l would change if active nodal power generation was increased, resp. decreased, by 3 pu at two nodes n_1 and n_2, this can be done as shown in equation eq. (3.19).

$$\Delta p_l \left(\Delta p_{n_1} = 3, \Delta p_{n_2} = -3\right) = 3 \cdot \gamma^{\Delta\mathrm{P}}_{l n_1} - 3 \cdot \gamma^{\Delta\mathrm{P}}_{l n_2} \tag{3.19}$$

The widespread usage of PTDFs is likely due to their simple definition, which only requires information about grid topology (static) but not about grid state (variable), and their linearity. There may be cases where the assumptions explained at the beginning of Section 3.1 are not valid anymore and the linearization error becomes too large to still rely on PTDFs, but for many applications in the domain of PFC, their usage is justified.

3.1.2 Reactance change distribution factors

A first concept to calculate power flow sensitivities for incremental reactance changes was presented in [OP4]. The necessary calculations were then simplified and the result is described in the following paragraphs. Although linear sensitivities exist for a variety of PFC devices, there is a research gap regarding DC sensitivities for devices that can control series impedances[2], such as TCSCs, SSSCs, or DSRs. The problem with impedance

[2]Note that these devices change the impedance by influencing the reactance but not the resistance.

changes is that they introduce a change into otherwise static variables, namely the nodal susceptance matrix $\boldsymbol{B}_{\mathrm{N}}$, making their case a bit more challenging than that of PTDFs. The basic idea of a DC-based sensitivity $\gamma^{\Delta \mathrm{X}}$ of a line l describing the power flow change ∂p caused by a gradual reactance change ∂x in a branch λ is described in eq. (3.20). Such sensitivities are furthermore called Reactance Change Distribution Factors (XCDFs).

$$\underset{[L \times L]}{\boldsymbol{\Gamma}^{\Delta \mathrm{X}}} = \begin{pmatrix} \gamma_{11}^{\Delta \mathrm{X}} & \gamma_{12}^{\Delta \mathrm{X}} & \cdots & \gamma_{1L}^{\Delta \mathrm{X}} \\ \gamma_{21}^{\Delta \mathrm{X}} & \ddots & & \vdots \\ \vdots & & \ddots & \vdots \\ \gamma_{L1}^{\Delta \mathrm{X}} & \cdots & \cdots & \gamma_{LL}^{\Delta \mathrm{X}} \end{pmatrix}, \quad \text{with } \gamma_{l\lambda}^{\Delta \mathrm{X}} = \frac{\partial p_l}{\partial x_\lambda} \tag{3.20}$$

It can be derived similarly as shown in eq. (3.11) but with a change Δx_λ in the reactance, resp. a change Δb_λ in the susceptance, of a line λ from node w to v instead of a nodal active power change Δp.

$$\boldsymbol{\delta}_{\mathrm{N}} + \Delta \boldsymbol{\delta}_{\mathrm{N}} = \left(\boldsymbol{B}_{\mathrm{N}} + \Delta \boldsymbol{B}_{\mathrm{N}} \right)^{+} \cdot \boldsymbol{p}_{\mathrm{N}}, \quad \text{with } \Delta b_{\mathrm{N},ij} = \begin{cases} -\Delta b_l \; \forall \; ij = vw, ij = wv \\ \Delta b_l \; \forall \; ij = ww, ij = vv \\ 0 \; \forall \; ij \neq vw, wv, ww, vv \end{cases} \tag{3.21}$$

Note that $b + \Delta b = -1 \,/\, (x + \Delta x)$ and thus $\Delta b = \Delta x \,/\, \left(x^2 + x \cdot \Delta x \right)$, and not $\Delta b = -1 \,/\, \Delta x$. In the same way eq. (3.12) was derived from eq. (3.11), $\boldsymbol{\delta}_{\mathrm{N}} = \left(\boldsymbol{B}_{\mathrm{N}} \right)^{+} \boldsymbol{p}_{\mathrm{N}}$ can be subtracted from eq. (3.21) to yield only the change of nodal voltage angles caused by the introduced reactance change, as shown in eq. (3.22).

$$\begin{aligned} \Delta \boldsymbol{\delta}_{\mathrm{N}} = \left(\left(\boldsymbol{B}_{\mathrm{N}} + \Delta \boldsymbol{B}_{\mathrm{N}} \right)^{+} - \left(\boldsymbol{B}_{\mathrm{N}} \right)^{+} \right) \cdot \boldsymbol{p}_{\mathrm{N}}, \quad \text{with } \Delta \delta_i &= \sum_{k=0}^{N} \left(c'_{ik} - c_{ik} \right) \cdot p_k \\ c_{ik} &\in \left(\boldsymbol{B}_{\mathrm{N}} \right)^{+} \\ c'_{ik} &\in \left(\boldsymbol{B}_{\mathrm{N}} + \Delta \boldsymbol{B}_{\mathrm{N}} \right)^{+} \end{aligned} \tag{3.22}$$

Then, the overall power flow changes after the introduced reactance change can be calculated analogue to eq. (3.14), as shown in eq. (3.23).

$$\boldsymbol{p}_{\mathrm{L}} + \Delta \boldsymbol{p}_{\mathrm{L}} = - \left(\boldsymbol{B}_{\mathrm{D}} + \Delta \boldsymbol{B}_{\mathrm{D}} \right) \boldsymbol{A} \left(\boldsymbol{\delta}_{\mathrm{N}} + \Delta \boldsymbol{\delta}_{\mathrm{N}} \right), \text{ with } \Delta b_{\mathrm{D},ij} = \begin{cases} -\Delta b_l \; \forall \; ij \in \{vw, wv\} \\ 0 \; \forall \; ij \notin \{vw, wv\} \end{cases} \tag{3.23}$$

Once again, subtracting $\boldsymbol{p}_\mathrm{L} = -\boldsymbol{B}_\mathrm{D}\boldsymbol{A}\boldsymbol{\delta}_\mathrm{N}$ (cp. eq. (3.7)) yields only the resulting power flow changes in eq. (3.24)

$$\Delta\boldsymbol{p}_\mathrm{L} = -\Delta\boldsymbol{B}_\mathrm{D} \cdot \boldsymbol{A} \cdot \boldsymbol{\delta}_\mathrm{N} - \left(\boldsymbol{B}_\mathrm{D} + \Delta\boldsymbol{B}_\mathrm{D}\right) \cdot \boldsymbol{A} \cdot \Delta\boldsymbol{\delta}_\mathrm{N} \tag{3.24}$$

Substituting the nodal voltage angle vectors $\boldsymbol{\delta}_\mathrm{N}$ and $\Delta\boldsymbol{\delta}_\mathrm{N}$ with eq. (3.8) and eq. (3.22) finally yields the XCDFs in eq. (3.25) and (3.26).

$$\begin{aligned}\Delta\boldsymbol{p}_\mathrm{L} &= \left(-\left(\boldsymbol{B}_\mathrm{D} + \Delta\boldsymbol{B}_\mathrm{D}\right)\boldsymbol{A}\left(\boldsymbol{B}_\mathrm{N} + \Delta\boldsymbol{B}_\mathrm{N}\right)^{+} + \boldsymbol{B}_\mathrm{D}\boldsymbol{A}\left(\boldsymbol{B}_\mathrm{N}\right)^{+}\right) \cdot \boldsymbol{p}_\mathrm{N} \\ &= \underbrace{\left(\left(\boldsymbol{B}_\mathrm{D} + \Delta\boldsymbol{B}_\mathrm{D}\right)\boldsymbol{A}\left(\boldsymbol{A}^\mathrm{T}\left(\boldsymbol{B}_\mathrm{D} + \Delta\boldsymbol{B}_\mathrm{D}\right)\boldsymbol{A}\right)^{+} - \boldsymbol{B}_\mathrm{D}\boldsymbol{A}\left(\boldsymbol{A}^\mathrm{T}\boldsymbol{B}_\mathrm{D}\boldsymbol{A}\right)^{+}\right)}_{\boldsymbol{\Gamma}^{\Delta\mathrm{X}}_{\mathrm{BASE}}} \cdot \boldsymbol{p}_\mathrm{N}\end{aligned} \tag{3.25}$$

$$\Delta p_l = \underbrace{\sum_{k=1}^{N}\left(-\left(b_l + \Delta b_l\right) \cdot \left(c'_{ik} - c'_{jk}\right) + b_{ij}\left(c_{ik} - c_{jk}\right)\right)}_{\gamma^{\Delta\mathrm{X}}_{l,\lambda} \cdot p_\lambda} \cdot p_k \tag{3.26}$$

For a given grid state with $\boldsymbol{p}_\mathrm{N}$ known, the power flow changes caused by the introduced reactance change can be calculated easily with these equations. Note however, that these sensitivities only apply for one specific grid state (described by $\boldsymbol{p}_\mathrm{N}$) and one specific reactance change (described by $\Delta\boldsymbol{B}_\mathrm{N}$), but not the sensitivities for all lines towards all lines as formulated in eq. (3.20). A similar problem for the case of PTDFs was solved by normalizing them to their respective nodal power change in eq. (3.17). This is only possible, because nodal power directly influences branch power flows, meaning the means of power flow manipulation coincides with the DC power flows' linear dependency on $\boldsymbol{p}_\mathrm{N}$. For the case of XCDFs this is not quite possible, because a reactance change only indirectly influences already existing branch power flows. These sensitivities are linearly dependent on $\boldsymbol{p}_\mathrm{N}$ but their means of power flow manipulation lies elsewhere, namely in the change of the susceptance matrix $\boldsymbol{B}_\mathrm{N}$. More precisely speaking: XCDFs are directly linearly dependent on the power flow through the branch whose reactance is being changed. This applies to other DC-based sensitivities as well, such as Line Outage Distribution Factors (LODFs), which are given as values relative to the power flow of the line to be outaged (cp. [67]). Thus, instead of normalizing the sensitivities to nodal powers, as was done with PTDFs, $\boldsymbol{\Gamma}^{\Delta\mathrm{X}}_{\mathrm{BASE}}$ can be normalized to each branch's power flow as follows.

Since eq. (3.25) does not include the power flows, i.e. $\boldsymbol{p}_\mathrm{L}$, directly, the normalization has

to be done via a modified $\boldsymbol{p}_{\mathrm{N}}$ that is furthermore called $\boldsymbol{p}''_{\mathrm{N},\lambda}$ as shown in eq. (3.27).

$$\Delta \boldsymbol{p}_{\mathrm{L}} = \boldsymbol{\Gamma}^{\Delta \mathrm{X}}_{\mathrm{BASE}} \cdot \boldsymbol{p}''_{\mathrm{N},\lambda} \cdot p_{\lambda} \tag{3.27}$$

This is the vector of nodal powers that is necessary to create a power flow of 1 pu on λ with all elements zero except for connecting nodes v and w of λ. Thus, $\boldsymbol{p}''_{\mathrm{N},\lambda}$ essentially represents the influence of the power flow of a single line λ on all other lines, isolated from all other power flow influences. Its derivation is described in the following paragraphs and shown graphically in Fig. 3.1. Kirchhoff's current law demands that the sum of all currents going into a node must equal the sum of all currents going out of the node. Thus, the power flows injected into all L_n lines connected to a node n must be equal to the node's nodal power p_n as shown in eq. (3.28) and Fig. 3.1 b).

$$\boldsymbol{p}_{\mathrm{N}} = \begin{pmatrix} \sum_{l}^{L_{n_1}} p_{n_1,l} \\ \vdots \\ \sum_{l}^{L_{n_N}} p_{n_N,l} \end{pmatrix} = \sum_{n=1}^{N} \boldsymbol{p}_{n,\mathrm{L}}, \quad \text{with } p_n = \sum_{l}^{L_n} p_l \tag{3.28}$$

While in this equation, the element n of $\boldsymbol{p}_{n,\mathrm{L}}$ is only the sum of the node's contribution to the lines that are connected to it, the node contributes to all lines in the grid. Thus, the nodal power of each node n can be formulated as a sum of this node's contribution to all lines. This results in a $[N \times 1]$ vector $\boldsymbol{p}_{n,\mathrm{L}}$ per node where each element is zero except for element n. By making use of the commutation law, this sum of N vectors $\boldsymbol{p}_{n,\mathrm{L}}$ each representing the contribution of one node to all lines can be split up into a sum of L vectors $\boldsymbol{p}_{l,\mathrm{N}}$ each representing the contribution of all nodes to one line. This results in one $[N \times 1]$ vector $\boldsymbol{p}_{l,\mathrm{N}}$ per line where each element is the corresponding node's contribution to that line. This is shown in eq. (3.29) and Fig. 3.1 c).

$$\underbrace{\begin{pmatrix} \sum_{l}^{L} p_{n_1,l} \\ \sum_{l}^{L} p_{n_2,l} \\ \vdots \\ \sum_{l}^{L} p_{n_N,l} \end{pmatrix}}_{\boldsymbol{p}_{\mathrm{N}}} = \underbrace{\underbrace{\begin{pmatrix} \sum_{l}^{L} p_{n_1,l} \\ 0 \\ \vdots \\ 0 \end{pmatrix}}_{\boldsymbol{p}_{n_1,\mathrm{L}}} + \cdots + \underbrace{\begin{pmatrix} 0 \\ \vdots \\ 0 \\ \sum_{l}^{L} p_{n_N,l} \end{pmatrix}}_{\boldsymbol{p}_{n_N,\mathrm{L}}}}_{\sum_{n}^{N} \boldsymbol{p}_{n,\mathrm{L}}} = \underbrace{\underbrace{\begin{pmatrix} p_{n_1,l_1} \\ p_{n_2,l_1} \\ \vdots \\ p_{n_N,l_1} \end{pmatrix}}_{\boldsymbol{p}_{l_1,\mathrm{N}}} + \cdots + \underbrace{\begin{pmatrix} p_{n_1,l_L} \\ p_{n_2,l_L} \\ \vdots \\ p_{n_N,l_L} \end{pmatrix}}_{\boldsymbol{p}_{l_L,\mathrm{N}}}}_{\sum_{l}^{L} \boldsymbol{p}_{l,\mathrm{N}}} \tag{3.29}$$

In the same way, the term $\sum_{l}^{L} \boldsymbol{p}_{l,\mathrm{N}}$ consisting of a sum of L vectors can be split up into a sum of $L \cdot N$ vectors, where each vector represents the contribution of one node to the

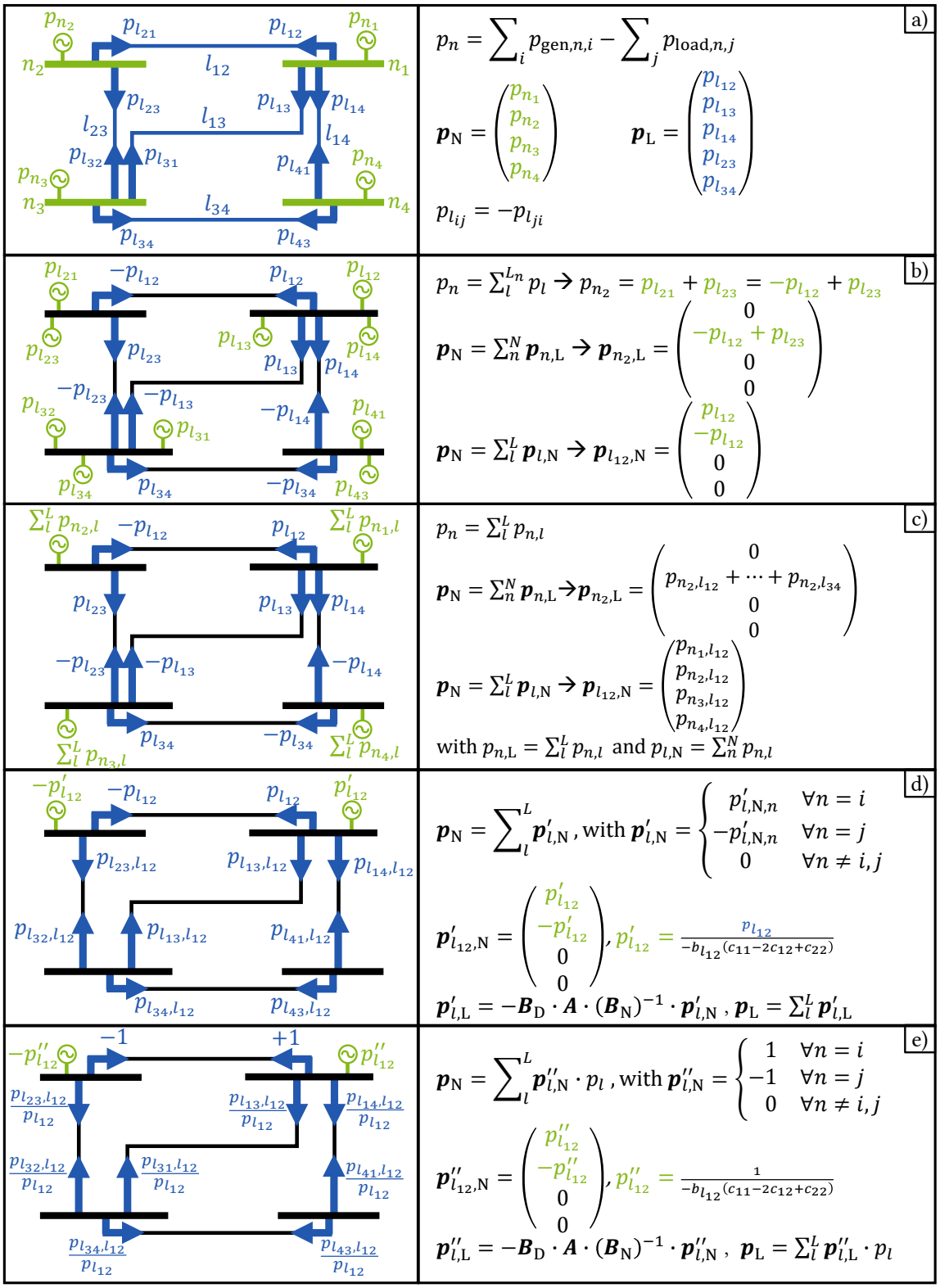

Figure 3.1: Derivation of nodal power vector creating $p_\lambda = 1\,\text{pu}$: Nodal power balances & nodal branch power flows (a) are described as sums of nodal branch power flows (b). From node-to-node contributions (c) branch-to-branch contributions are derived (d) and normalized for one branch's power flow (e).

power flow on one line. This is shown in eq. (3.30).

$$\sum_{l}^{L} \boldsymbol{p}_{l,\mathrm{N}} = \begin{pmatrix} p_{n_1,l_1} \\ 0 \\ \vdots \\ 0 \end{pmatrix} + \begin{pmatrix} 0 \\ p_{n_2,l_1} \\ \vdots \\ 0 \end{pmatrix} + \cdots + \begin{pmatrix} 0 \\ \vdots \\ 0 \\ p_{n_N,l_L} \end{pmatrix} \tag{3.30}$$

From these vectors, the two vectors representing the contribution of the lines' connecting nodes are combined, yielding the nodal power vector that represents each lines' influence on all power flows in the grid. By assuming equal absolute contribution from both connecting nodes, only with different signs, it is possible to define a nodal power vector $\boldsymbol{p}'_{\mathrm{N},l}$ that will create a power flow of p_l on l while the other resulting power flows can be interpreted as the contribution of p_l towards all other lines. This is shown in eq. (3.31) and in Fig. 3.1 d) for a line l_{12} connecting nodes n_1 and n_2.

$$\boldsymbol{p}'_{\mathrm{N},l_{12}} = \begin{pmatrix} p_{n_1,l_{12}} \\ 0 \\ \vdots \\ 0 \end{pmatrix} + \begin{pmatrix} 0 \\ p_{n_2,l_{12}} \\ \vdots \\ 0 \end{pmatrix} = \begin{pmatrix} p_{n_1,l_{12}} \\ p_{n_2,l_{12}} \\ \vdots \\ 0 \end{pmatrix} = \begin{pmatrix} p'_{l_{12}} \\ -p'_{l_{12}} \\ \vdots \\ 0 \end{pmatrix} \tag{3.31}$$

The value of p'_l can be calculated by using the PTDFs of l towards its connecting nodes i and j, to calculate by how much the nodal power of these nodes would have to change to cause a power flow of p_l, similar to eq. (3.19). This equation can then be solved for p'_l. These two steps are shown in eq. (3.32).

$$p_l = \gamma_{l,i}^{\Delta\mathrm{P}} \cdot p'_l + \gamma_{l,j}^{\Delta\mathrm{P}} \cdot \left(-p'_l\right) \;\Leftrightarrow\; p'_l = \frac{p_l}{\gamma_{l,i}^{\Delta\mathrm{P}} - \gamma_{l,j}^{\Delta\mathrm{P}}} = \frac{p_l}{-b_l \cdot \left(c_{ii} - 2c_{ij} + c_{jj}\right)} \tag{3.32}$$

To finally calculate the vector $\boldsymbol{p}''_{\mathrm{N},l}$, p'_l can be normalized to p_l by solving eq. (3.32) using a power flow of $p_l = 1\,\mathrm{pu}$, which is shown in eq. (3.33) and Fig. 3.1 e).

$$\boldsymbol{p}''_{\mathrm{N},l}, \quad \text{with } p_{l,n} = \begin{cases} p''_l \forall n = i \\ -p''_l \forall n = j \\ 0 \forall n \neq i, j \end{cases}, \text{and } p''_l = \frac{1}{-b_l \cdot \left(c_{ii} - 2c_{ij} + c_{jj}\right)} \tag{3.33}$$

With eq. (3.33) $\boldsymbol{p}''_{\mathrm{N},\lambda}$ is defined and can be put into eq. (3.27) to yield the XCDFs values normalized to the power flow of the line whose reactance is affected. Finally, eq. (3.34)

describes how the full XCDF-matrix $\mathbf{\Gamma}^{\Delta X}$, as shown in eq. (3.20), can be defined by horizontally concatenating the XCDF vectors consisting of the products of $\mathbf{\Gamma}^{\Delta X}_{\mathrm{BASE}}$ and $\boldsymbol{p}''_{\mathrm{N},\lambda}$ vectors for each of the L branches in the grid. Additionally, eq. (3.35) describes how the sensitivity of a line l from nodes i to j towards a line λ from nodes v to w can be derived from only the lines' susceptances b and elements of the inverted susceptance matrices before (c) and after (c') the introduced reactance change.

$$\underset{[L\times L]}{\mathbf{\Gamma}^{\Delta X}} = \begin{bmatrix} \underset{[L\times N]}{\mathbf{\Gamma}^{\Delta X}_{\mathrm{BASE},l_1}} \cdot \underset{[N\times 1]}{\boldsymbol{p}''_{\mathrm{N},l_1}} & \cdots & \underset{[L\times N]}{\mathbf{\Gamma}^{\Delta X}_{\mathrm{BASE},l_L}} \cdot \underset{[N\times 1]}{\boldsymbol{p}''_{\mathrm{N},l_L}} \end{bmatrix} \tag{3.34}$$

$$\gamma^{\Delta X}_{l,\lambda} = \frac{(b_l + \Delta b_l)\cdot(c'_{iv} - c'_{jv} - c'_{iw} + c'_{jw}) - b_l \cdot (c_{iv} - c_{jv} - c_{iw} + c_{jw})}{b_\lambda \cdot (c_{vv} - 2c_{vw} + c_{ww})} \tag{3.35}$$

One of the main characteristic differences between influencing power flows by changing nodal power and by changing series reactance, is that the former is only dependent on the size of the nodal power change, while the latter is dependent on the size of the series reactance change and the power flow on the branch where the reactance change is applied. The dependency of the power flows on the applied reactance change is assumed to be linear, but especially for large changes, it is not – not even within the DC-domain. This is clear because in eq. (3.25) and (3.26) the reactance change is applied within the (pseudo-)inverse operation, which is non-linear. More figuratively speaking: as soon as a reactance change is applied, all XCDFs have to be re-calculated because the reactance change changes the susceptance matrix and thus changes the XCDFs. So eq. (3.25), (3.26) and also (3.34) represent a linearization around a specific reactance change Δx_λ. If Δx_λ is chosen sufficiently small, and/or the point of linearization is not diverted from too much (i.e. only a few steps of reactance changes are activated), this linearization error may be negligible, depending on the application requirements. Thus, XCDFs may be applicable for reactance-changing PFC-devices that either introduce only one single large step of reactance (e.g. large switchable inductive coils) or devices such as DSRs that introduce very small steps of additional reactance. It may still be necessary to re-calculate the sensitivities if the number of steps to be applied is too large (cp. eq. (3.36)), or too many different devices are to be activated (cp. eq. (3.37)). When calculating the XCDFs, the size of Δx should thus be chosen according to the step size of the PFC device, and not as $\Delta x = 1\,\mathrm{pu}$. The degree to which the assumption of linear behavior of XCDFs is acceptable depends on the application and should be determined prior to deployment.

$$n_{\text{steps}} \cdot \gamma^{\Delta X}(\Delta x) \neq \gamma^{\Delta X}(n_{\text{steps}} \cdot \Delta x) \tag{3.36}$$

$$\gamma^{\Delta X}(\Delta x_{l_1}, \Delta x_{l_2}) \neq \gamma^{\Delta X}(\Delta x_{l_1}) + \gamma^{\Delta X}(\Delta x_{l_2}) \tag{3.37}$$

3.1.3 Combining sensitivities

Since PTDFs are linear with regards to nodal power changes, PTDFs of several nodes and/or several magnitudes of nodal power change can be combined, i.e. added up, for a given topology. As shown in eq. (3.36) and (3.37), this does not apply for XCDFs and hence it also does not apply for the combination of PTDFs and XCDFs.

PTDFs are non-linearly dependent on reactance changes, and power flow changes caused by reactance changes are linearly dependent on the power flow of the reactance-changed line. Thus, power flow changes caused by simultaneous nodal power and line reactance changes are not necessarily equal to the sum of the respective sensitivities – not even within the DC power flow domain. If the sensitivity $\gamma^{\Delta P}_{n_P,\lambda}$ of a node n_P towards a line λ is positive, increasing the nodal power of n_P will push power into λ and thus increase the absolute power flow changes caused by a change of x_λ. Likewise, these power flow changes are decreased by an increase of p_{n_P} if $\gamma^{\Delta P}_{n_P,\lambda}$ is negative. At the same time, changing x_λ can lower the PTDF of a line l towards n_P, if there are not enough electrically short parallel paths from n_P to l besides λ. Similarly, when the reactances of two lines λ_1 and λ_2 are supposed to be changed, their sensitivity $\gamma^{\Delta X}_{\lambda_1,\lambda_2}$ towards each other must be taken into account. A positive sensitivity towards each other will cause their reactance increases to amplify each other's effects on power flows because they push power into each other. When their sensitivity is negative, the opposite is true and they work against each other. When XCDFs are treated as if they were linearly addable, these effects are neglected and thus, the effects on other lines' power flows are underestimated for an amplifying effect between two measures and overestimated for measures that counter-affect each other.

When coordinating flexible power and reactance changes to manage congestions, this has to be taken into consideration. One way to ensure the precision of the used sensitivities, is to frequently update them throughout the process of determining appropriate RMs. In a PFC system that is supposed to find solutions in a fast and robust manner, frequent re-calculations may however increase calculation time and may also not be necessary to reach a sufficient solution.

3.2 Algorithms for the coordination of impedance controllers and flexible power

In this section, two approaches are described to relieve grid congestions by utilizing ICs and FPUs without creating new congestions. The overall problem these algorithms are aimed at solving can be described mathematically as a DC-based optimization problem with equations (3.38 – 3.40).

$$\min_{\Delta\tau_m} K = \sum_m |\Delta\tau_m| \cdot \kappa_m, \text{ with } m \in \{\mathcal{M}_{\mathrm{IC}} \cup \mathcal{M}_{\mathrm{FPU}}\} \tag{3.38}$$

Subject to:

$$|\boldsymbol{p}_{\mathrm{L}}| \leq \boldsymbol{p}^{\mathrm{lim}}, \text{ with } p_l^{\mathrm{lim}} \in \boldsymbol{p}^{\mathrm{lim}} = \begin{cases} p_l^{\mathrm{trg}} \; \forall \; l = l_{\mathrm{C}} \\ p_l^{\mathrm{crt}} \; \forall \; l \neq l_{\mathrm{C}} \end{cases} \tag{3.39}$$

$$\Delta\tau_m^{\mathrm{min}} \leq \Delta\tau_m \leq \Delta\tau_m^{\mathrm{max}} \; \forall m \in \mathcal{M} \tag{3.40}$$

$$\sum_m \Delta p_m = 0 \; \forall m \in \mathcal{M}_{\mathrm{FPU}} \tag{3.41}$$

The target function to be minimized in eq. (3.38) states that the cost K of setpoint changes is equal to the sum of setpoint changes $\Delta\tau$ multiplied by the variable costs κ of each IC- or FPU-measure m. Each measure's setpoint τ corresponds either to a variable reactance x in case of ICs, or to a variable active power output p in the case of FPUs, as stated in equations (3.42) and (3.43). If a measure is discretely stepped (e.g. DSRs), the resulting reactance change arises as the product of the number of steps $\Delta\tau_m$ and the stepsize $x_{m,\mathrm{step}}$. The power output changes in FPUs are calculated in the same way.

$$\Delta x_m = \Delta\tau_m \cdot x_{m,\mathrm{step}} \; \forall \; m \in \mathcal{M}_{\mathrm{IC}} \tag{3.42}$$

$$\Delta p_m = \Delta\tau_m \cdot p_{m,\mathrm{step}} \; \forall \; m \in \mathcal{M}_{\mathrm{FPU}} \tag{3.43}$$

The inequality constraint (3.39) ensures that the power flow over the congested line l_{C} is reduced to the line's target threshold and all other lines remain below their critical thresholds. Here, four relative line loading thresholds c are introduced: $c_{\mathrm{PATL}} = 1 \geq c_{\mathrm{crt}} > c_{\mathrm{trg}} > c_{\mathrm{rls}}$. The corresponding apparent power threshold limit values can be derived from the line's PATL[3] as shown in eq. (3.44).

[3] PATL limits are usually calculated using the line's nominal voltage. However, since the main factor driving the line's temperature is the current, the momentary voltage at the line's buses should be considered

$$s_l^{\text{lim}} = s_l^{\text{PATL}} \cdot c_l^{\text{lim}}, \quad \text{with } c_l^{\text{lim}} \in \left\{ c_l^{\text{crt}}, c_l^{\text{trg}}, c_l^{\text{rls}} \right\}, \; s_l^{\text{PATL}} = \sqrt{3} \cdot i_l^{\text{rated}} \cdot u_l \tag{3.44}$$

If a line is loaded above its critical threshold c_{crt}, it is considered overloaded and the RM selection algorithm is triggered. The algorithm will then try to find a solution that will lower the overloaded line's loading below its target threshold c_{trg} while all other lines must stay below their critical thresholds. Once the congested line's loading drops below its release threshold c_{rls}, previously activated measures are deactivated again as long as the loading of l_{C} does not go above c_{rls}. This bandwidth approach reduces the chances of swinging activation and deactivation of measures. Since a DC-based algorithm cannot account for reactive power changes, the needed change in apparent power to reach a certain limit is expected to come from active power only while reactive power is assumed to stay constant, as shown in eq. (3.45).

$$\Delta p_l^{\text{lim}} = \text{sgn}\left(p_l\right) \cdot \sqrt{\left(s_l^{\text{lim}}\right)^2 - {q_l}^2} - p_l, \quad \text{with } s_l^{\text{lim}} \in \left\{ s_l^{\text{crt}}, s_l^{\text{trg}}, s_l^{\text{rls}} \right\} \tag{3.45}$$

Additionally to the power flow limits, inequality constraint (3.40) ensures measure setpoint changes are kept within their technically possible value range. To ensure no frequency issues are introduced by activating FPUs, equality constraint (3.41) is applied, requiring balanced activation of positive and negative flexible power. In the following subsections an optimization and a heuristic approach to solve this problem are described.

3.2.1 Optimization approach: Applying setpoint changes within DC power flow equation as a non-linear constraint

Although optimization approaches are too time-consuming to be applied ad-hoc post-fault, they can be used as a benchmark to evaluate solutions found by heuristic approaches regarding their IC and FPU selection efficiency. In the literature, a variety of optimization algorithms is available for optimal usage of PFC devices and FPUs to manage congestions. Due to the mentioned time consumption, they are mostly applied in long-term structural CM measures and planning processes such as positioning of PFC devices (cp. [OP3]).

To implement this optimization problem, eq. (3.39) needs to be expressed as a function of the optimization variables $\Delta\tau_m$. For this, these power flow constraints can be integrated into the DC power flow equations (cp. eq. (3.15) and (3.25)) resulting in the non-linear

to determine its current maximum admissible power; at a higher voltage, the line might reach its current limit before reaching its power limit.

power flow constraint in eq. (3.46). The decision variables $\Delta\tau_m$ are integrated within $\Delta\boldsymbol{B}_{\mathrm{D}}$, which is a function of Δx_m, for ICs and $\Delta\boldsymbol{p}_{\mathrm{N}}$, which is a function of Δp_m for FPU.

$$\left(\boldsymbol{B}_{\mathrm{D}} + \Delta\boldsymbol{B}_{\mathrm{D}}\right) \cdot \boldsymbol{A} \cdot \left(\boldsymbol{A}^{\mathrm{T}} \cdot \left(\boldsymbol{B}_{\mathrm{D}} + \Delta\boldsymbol{B}_{\mathrm{D}}\right) \cdot \boldsymbol{A}\right)^{+} \cdot \left(\boldsymbol{p}_{\mathrm{N}} + \Delta\boldsymbol{p}_{\mathrm{N}}\right) \leq \boldsymbol{p}^{\mathrm{lim}} \tag{3.46}$$

One problem with using eq. (3.46) to calculate the power flows resulting from reactance and nodal power changes is that it is fully DC-based but the input used is AC-based. This means, that when a scenario is applied which is congested according to AC power flow equations, this congestion might not appear in a DC power flow calculation. At least the power flows calculated with eq (3.46) will look significantly different from AC power flow results. When only FPUs are used to solve a congestion, this may not be relevant since it suffices to calculate necessary *changes* in power flows but not the *actual* resulting power flows. But since power flow changes caused by reactance changes are dependent on the grid state, a different nodal power vector needs to be derived when ICs are used as well. To do this, the AC-calculated active power flows can be put into eq. (3.9) which is then solved for $\boldsymbol{p}_{\mathrm{N}}$, yielding a nodal power vector that would create these power flows also within the DC domain, as shown in eq. (3.47). Due to the pseudo-inverse of the sparsely filled incidence matrix $\boldsymbol{A}$, the result is not exactly equal – but it is still a better approximation than simply using the original $\boldsymbol{p}_{\mathrm{N}}$ within the DC domain.

$$\boldsymbol{p}_{\mathrm{N}} \approx \boldsymbol{A}^{\mathrm{T}} \cdot \boldsymbol{B}_{\mathrm{D}} \cdot \boldsymbol{A} \cdot \boldsymbol{A}^{+} \cdot {\boldsymbol{B}_{\mathrm{D}}}^{+} \cdot \boldsymbol{p}_{\mathrm{L}} \tag{3.47}$$

An AC-optimization would also include voltage and reactive power constraints. To enable comparability of optimization and heuristic results, a DC-optimization is used here.

3.2.2 Heuristic approach: Applying setpoint changes with DC-based linear sensitivities

To fulfill the requirements derived in Section 2.4, heuristic algorithms are more suitable than optimizations since they are faster, more reliable to find solutions, and more robust towards changing circumstances. On the downside, a heuristic may not find the global optimal solution to a problem, but it will at least find an improvement to the initial state. There have been a number of such algorithms developed at ie^3 and elsewhere that perform similar functions. The core concept of these algorithms is this: When a congestion appears, all measures to alleviate it are sorted by their sensitivity towards the congested line and then, starting with the most sensitive measure, their setpoints are changed step-

wise until the congestion is resolved or all maximum setpoints are reached. More detailed explanations, especially about the agent-based nature of these algorithms, which is not relevant for this chapter, are given in cp. Section 5.2. The algorithms presented here are based on these preceding achievements, but enhance them by including ICs and improving the measure utilization efficiency.

First, a general overview of the heuristic algorithm is presented in the form of an optimization problem. Since IC and FPU measures influence each other, their setpoint changes cannot be determined simultaneously in a linear way and non-linear equations could be too time-intensive for the heuristic approach. To keep costs minimal, grid-related measures should be exhausted before resorting to market-related measures that need to be remunerated by the SO. Hence, a congestion should be lowered as far as possible by using ICs first, and only the remaining overload should be solved with FPUs. Thus, the overall algorithm is split into two consecutive sub-algorithms for IC- and FPU-measures.

In the first execution eq. (3.38) is only applied for ICs ($m \in \mathcal{M}_{\mathrm{IC}}$) and in the second execution only for FPUs ($m \in \mathcal{M}_{\mathrm{FPU}}$). Eq. (3.39) is split into the XCDF-, resp. PTDF-based equations (3.48) and eq. (3.49). The power flow change $\Delta p_{l,m}$ on a line l caused by a measure m according to its setpoint change $\Delta\tau_m$ is determined using eq. (3.50). The overall algorithm is shown in Fig. 3.2 and explained in the remainder of this chapter.

$$-p_{l_{\mathrm{C}}}^{\mathrm{trg}} \leq p_{l_{\mathrm{C}}} + \sum_m \Delta p_{l_{\mathrm{C}},m} \leq p_{l_{\mathrm{C}}}^{\mathrm{trg}} \tag{3.48}$$

$$-p_l^{\mathrm{crt}} \leq p_l + \sum_m \Delta p_{l,m} \leq p_l^{\mathrm{crt}} \tag{3.49}$$

$$\Delta p_{l,m} = \begin{cases} \Delta\tau_m \cdot \gamma_{l,m} \cdot p_\lambda & = \Delta x_\lambda \cdot \gamma_{l,\lambda}^{\Delta \mathrm{X}} \cdot p_\lambda \quad \forall m \in \mathcal{M}_{\mathrm{IC}} \\ \Delta\tau_m \cdot \gamma_{l,m} & = \Delta p_{n_{\mathrm{P}}} \cdot \gamma_{l,n_{\mathrm{P}}}^{\Delta \mathrm{P}} \quad \forall m \in \mathcal{M}_{\mathrm{FPU}} \end{cases} \tag{3.50}$$

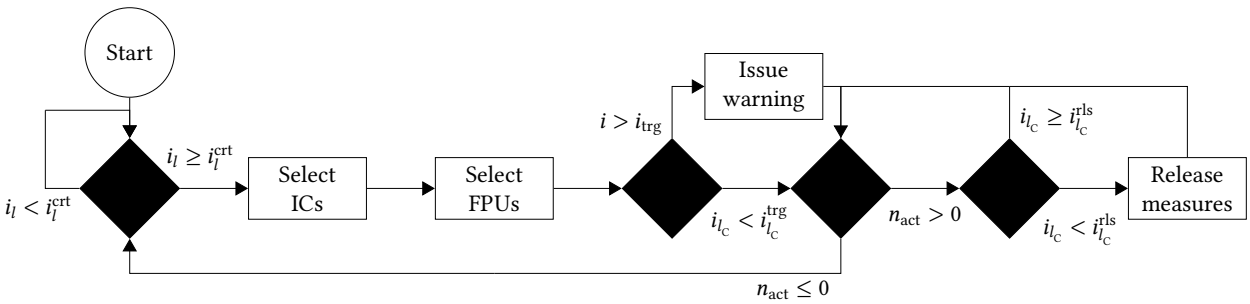

Figure 3.2: Simplified overview of the measure selection algorithm

3.2.2.1 Selection of impedance-changing power flow control devices

The selection of appropriate ICs is depicted in Fig. 3.3 and explained as follows. First, the XCDFs for all available ICs are calculated, either by calculating the full XCDF-matrix $\mathbf{\Gamma}^{\Delta X}$ or single XCDF-values $\gamma_{l,m}^{\Delta X}$ for the available ICs using equations (3.34) or (3.35). Then, if there are ICs available, the device that is best suited to alleviate the congestion is selected. In this context, best suited can either mean it has the highest sensitivity $\gamma_{l_C,l_m}^{\Delta X}$ towards the congestion, or it has the greatest leverage $\Delta p_{l_C,m} = \gamma_{l_C,l_m}^{\Delta X} \cdot p_{l_m} \cdot \Delta\tau_m^{\max} \cdot \Delta x_m^{\text{step}}$ on the congestion. By activating ICs with high leverage first, even for congestions they are not the most efficient option for (i.e. not the highest sensitivity), these ICs may be unavailable at a later time for congestions they may be better suited for. This is why the ICs should be sorted by their sensitivity rather than their actual leverage on the congestion at hand.

With an IC-measure m chosen, its setpoint change $\Delta\tau_{m,}$ is calculated. In previous implementations of similar algorithms, the setpoint change was determined in an iterative process, where the setpoint was incremented/decremented and effects on the line loadings were evaluated to see if the solution was reached or a constraint was violated. This process can be simplified by determining the final setpoint immediately instead of iteratively. For this, three setpoint change limits need to be considered:

1. $\Delta\tau_{m,l_C}^{\text{trg}}$: the *target* setpoint change theoretically needed to relieve the congestion
2. $\Delta\tau_m^{\text{tec}}$: the device's *technical* maximum or minimum setpoint change
3. $\Delta\tau_m^{\text{rst}}$: the maximum setpoint change that will not cause overloads in other lines and thus *restricts* the theoretically achievable setpoint change (note that both an increase and a decrease in setpoint may cause overloads)

To calculate $\Delta\tau_{m,l_C}^{\text{trg}}$ a more general equation is given in (3.51). This can be used to calculate the setpoint change needed to achieve a certain active power flow change, such as Δp_l^{trg} which will lower the line loading below its target threshold.

$$\Delta\tau_{m,l}^{\text{lim}} = \frac{\Delta p_l^{\text{lim}}}{\gamma_{l,l_m}^{\Delta X} \cdot p_\lambda} \rightarrow \Delta\tau_{m,l}^{\text{trg}} = \frac{\Delta p_l^{\text{trg}}}{\gamma_{l,l_m}^{\Delta X} \cdot p_\lambda} \tag{3.51}$$

Note that the limits are defined by the line current or the line apparent power flow but since the ICs mainly influence active power flows and DC power flow calculation does not consider reactive power, the entire change in apparent power is assumed to come from active power flow changes while reactive power flow stays constant. Of course, q_l will not stay constant when a line's reactance increases, but since the reactance changes

introduced by most FACTS and D-FACTS devices are small compared to the overall line reactance, this assumption is valid, and it is also at least more accurate than assuming zero reactive power flow. Eq. (3.52) shows how the sign of $\Delta\tau^{\mathrm{trg}}_{m,l_{\mathrm{C}}}$ indicates the direction d_m, i.e. whether $\Delta\tau_m$ has to be increased or decreased to lower the congestion, which is relevant for determining the other setpoint change limitations as described in the following.

$$d_m = \operatorname{sgn}\left(\Delta\tau^{\mathrm{trg}}_{m,l_{\mathrm{C}}}\right) \tag{3.52}$$

$\Delta\tau^{\mathrm{tec}}_m$ can simply be derived by subtracting the device's momentary setpoint from its maximum, resp. minimum, setpoint (e.g. number of DSR modules and 0 in the case of DSRs), as shown in eq. (3.53). The sign of $\Delta\tau^{\mathrm{trg}}_{m,l_{\mathrm{C}}}$ already indicates in which direction the setpoint of the chosen IC needs to be changed and thus, only the technical limit in the same direction has to be considered.

$$\Delta\tau^{\mathrm{tec}}_m = \begin{cases} \tau^{\max}_m - \tau_m, & \text{if } d_m = 1 \\ \tau^{\min}_m - \tau_m, & \text{if } d_m = -1 \end{cases} \tag{3.53}$$

The last setpoint change limit is determined by using eq. (3.51) on all lines in the grid to calculate the set $\Delta\mathcal{T}^{\mathrm{crt}}_m$ of setpoint changes of m that would cause each non-congested line to reach its respective critical limit. $\Delta\mathcal{T}^{\mathrm{rst}}_m$ is a subset of $\Delta\mathcal{T}^{\mathrm{crt}}_m$ which contains only those setpoint changes that would go in the same direction as the targeted setpoint change. Depending on whether τ_m has to be increased or decreased to lower the congestion on l_{C}, either the smallest positive or the absolute smallest negative $\Delta\tau^{\mathrm{crt}}_{m,l}$ restricts the setpoint change. This is shown in eq. (3.54).

$$\Delta\tau^{\mathrm{rst}}_m = \min\left(|\Delta\mathcal{T}^{\mathrm{rst}}_m|\right) \cdot d_m \tag{3.54}$$

Finally, depending on the direction of the necessary setpoint change, either the maximum or the minimum of the three setpoint change limitations is chosen as shown in eq. (3.55).

$$\Delta\tau_m = \begin{cases} \min\left(\Delta\tau^{\mathrm{trg}}_{m,l_{\mathrm{C}}}, \Delta\tau^{\mathrm{tec}}_m, \Delta\tau^{\mathrm{rst}}_m\right), & \text{if } d_m = 1 \\ \max\left(\Delta\tau^{\mathrm{trg}}_{m,l_{\mathrm{C}}}, \Delta\tau^{\mathrm{tec}}_m, \Delta\tau^{\mathrm{rst}}_m\right), & \text{if } d_m = -1 \end{cases} \tag{3.55}$$

Afterwards, power flows are calculated using eq. (3.56). Note that a circumflex indicates

a value updated with linearized sensitivities and is thus subject to linearization errors.

$$\hat{s}_l = \sqrt{\hat{p}_l^2 + q_l^2} = \sqrt{\left(p_l + \Delta\tau_m \cdot \gamma_{l,l_m}^{\Delta X} \cdot p_{l_C}\right)^2 + q_l^2} \tag{3.56}$$

Then, the estimated power flow on the congested line $\hat{s}_{l_C}$ is compared to its target threshold $s_{l_C}^{trg}$. If $|\hat{s}_{l_C}| \leq s_{l_C}^{trg}$ the congestion is considered relieved and selected ICs are activated. If l_C is still congested, the algorithm starts over with the next best IC. If the selection loop starts over, the linearization error introduced by now activated ICs must be considered. While re-calculating XCDFs with updated power flows and susceptances would reduce linearization errors, this requires additional time. Additionally, since changing an IC setpoint also changes the sensitivity of this IC, a decision has to be made whether this device should be reconsidered again after a sensitivity re-calculation. This may increase the accuracy of the solution but would also take more time. To prevent back-and-forth IC-switching, setpoint changes should only be allowed in one direction per device. To address these issues, four heuristic algorithms h1–h4 are considered as shown in Table 3.1.

Table 3.1: Heuristics

Heuristic	Sensitivity re-calculation	IC reconsideration	Stepwise IC-tapping
h1	No	No	No
h2	Yes (after IC maxed out)	No	No
h3	Yes (after IC maxed out)	Yes	No
h4	Yes (after each tap)	Yes	Yes

Heuristics h1-h3 only differ in their XCDF re-calculation and IC reconsideration. Heuristic h4 additionally requires considering d_m as a fourth limiting variable to $\Delta\tau_m$ in eq. (3.55), as shown in eq. (3.57), ensuring incremental setpoint changes: $\Delta\tau_m \in \{0; d_m\}$. The differences between these algorithms are evaluated in Chapter 4.

$$\Delta\tau_m = \begin{cases} \min\left(\Delta\tau_{m,l_C}^{trg}, \Delta\tau_m^{tec}, \Delta\tau_m^{rst}, d_m\right), & \text{if } d_m = 1 \\ \max\left(\Delta\tau_{m,l_C}^{trg}, \Delta\tau_m^{tec}, \Delta\tau_m^{rst}, d_m\right), & \text{if } d_m = -1 \end{cases} \tag{3.57}$$

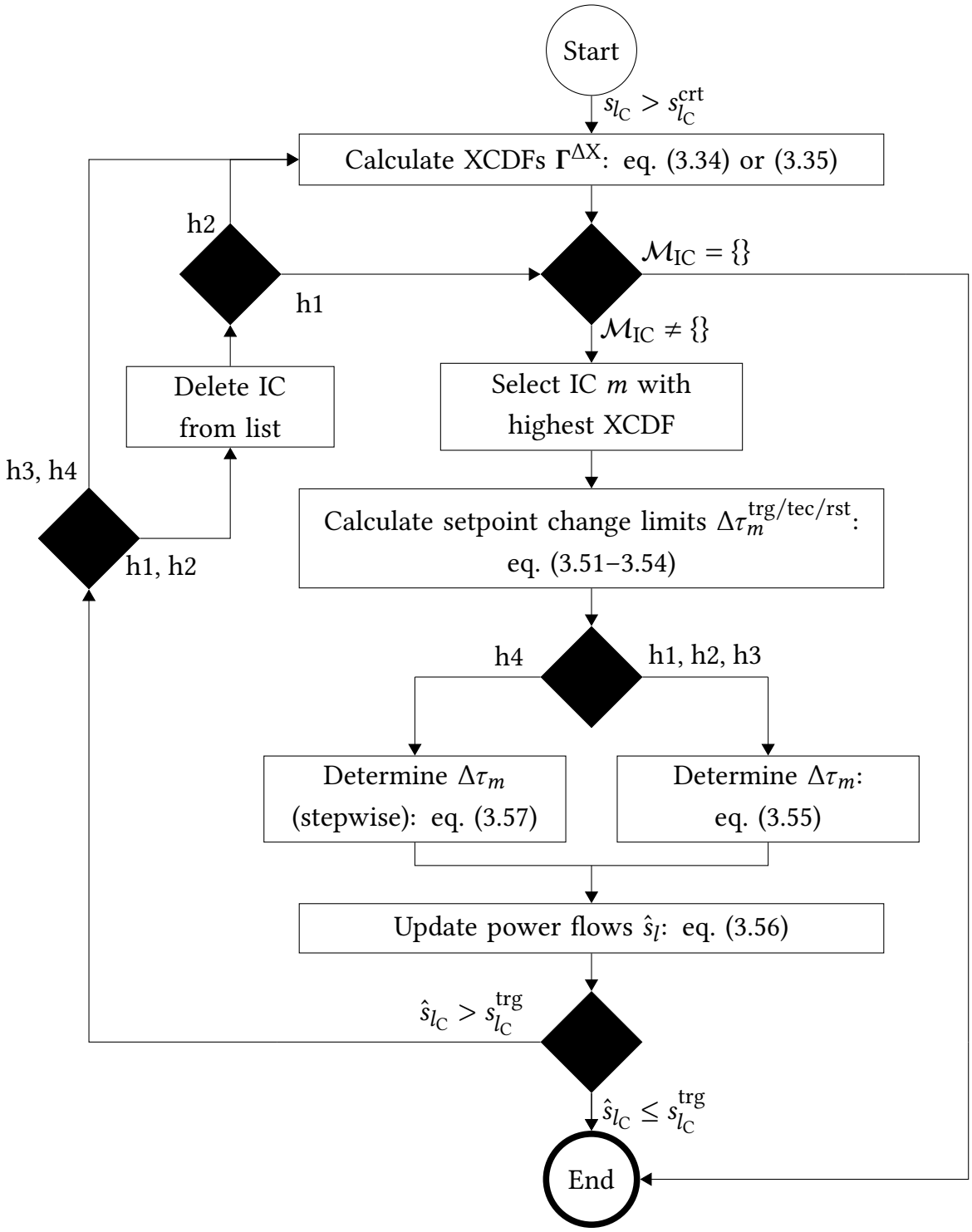

Figure 3.3: Four heuristic algorithms to select impedance controllers

3.2.2.2 Selection of flexible power units

The selection of FPUs has the same target as the selection of ICs, which is the alleviation of a congestion under the restriction that no other congestions are created. An additional restriction is the balancing of increased and decreased nodal power as to avoid frequency changes. The selection of appropriate FPUs is depicted in Fig. 3.4 and explained as follows.

A basic concept for such an algorithm has been shown in [69], which serves as a base for the algorithm used in this work and is explained as follows. The available FPUs are grouped into *UP*- and *DOWN* measures, depending on whether a unit needs to increase or decrease its active power output. Then, the most sensitive unit from each group is selected and their power outputs are adjusted equally in absolute value but in opposite directions either until the congestion is solved according to DC power flow calculation or until one of them reaches its maximum power output change. In the latter case, the next best FPU in that group is selected and the algorithm continues as before.

This version of the algorithm has two shortcomings. First of all, the separation of FPUs into *UP*- and *DOWN*-groups leads to an inefficient, and possibly even insufficient usage of flexible power. There may be situations in which there are still many *UP*-FPUs but no more *DOWN*-FPUs left (or vice-versa) but the congestion has not been relieved yet. By sticking to this fixed grouping, over-compensating effects of highly advantageous FPUs over only slightly disadvantageous FPUs are ignored. In more direct terms: activating 1 MW of an *UP*-FPU with a very high congestion-*decreasing* sensitivity together with the activation of −1 MW of another *UP*-FPU with a significantly lower congestion-*increasing* sensitivity will still result in an overall decrease of the congestion. This is why FPUs should not be grouped into *UP*- and *DOWN*-sets, but should just be sorted by their sensitivity towards the congestion. Then they can be selected consecutively pairwise from each end of this list, as long as their combined usage still contributes to relieving the congestion. This ensures the selection of the most effective units while also leveraging over-compensation of slightly disadvantageous units with highly advantageous units. An example for this is given in Table 3.2, where the grouping method results in a significantly lower power flow change in the overloaded line because it does not utilize flexible power available at nodes n_1 and n_2. In more general terms the process works as follows. First, the PTDFs for all lines towards the available FPUs need to be calculated – based on an updated susceptance matrix that includes any changes made to the topology by ICs – and FPUs need to be sorted according to these sensitivities. The targeted setpoint change now needs to encompass both measures: m_0 at the top of the sorted list, and m_M at the bottom. To ensure an

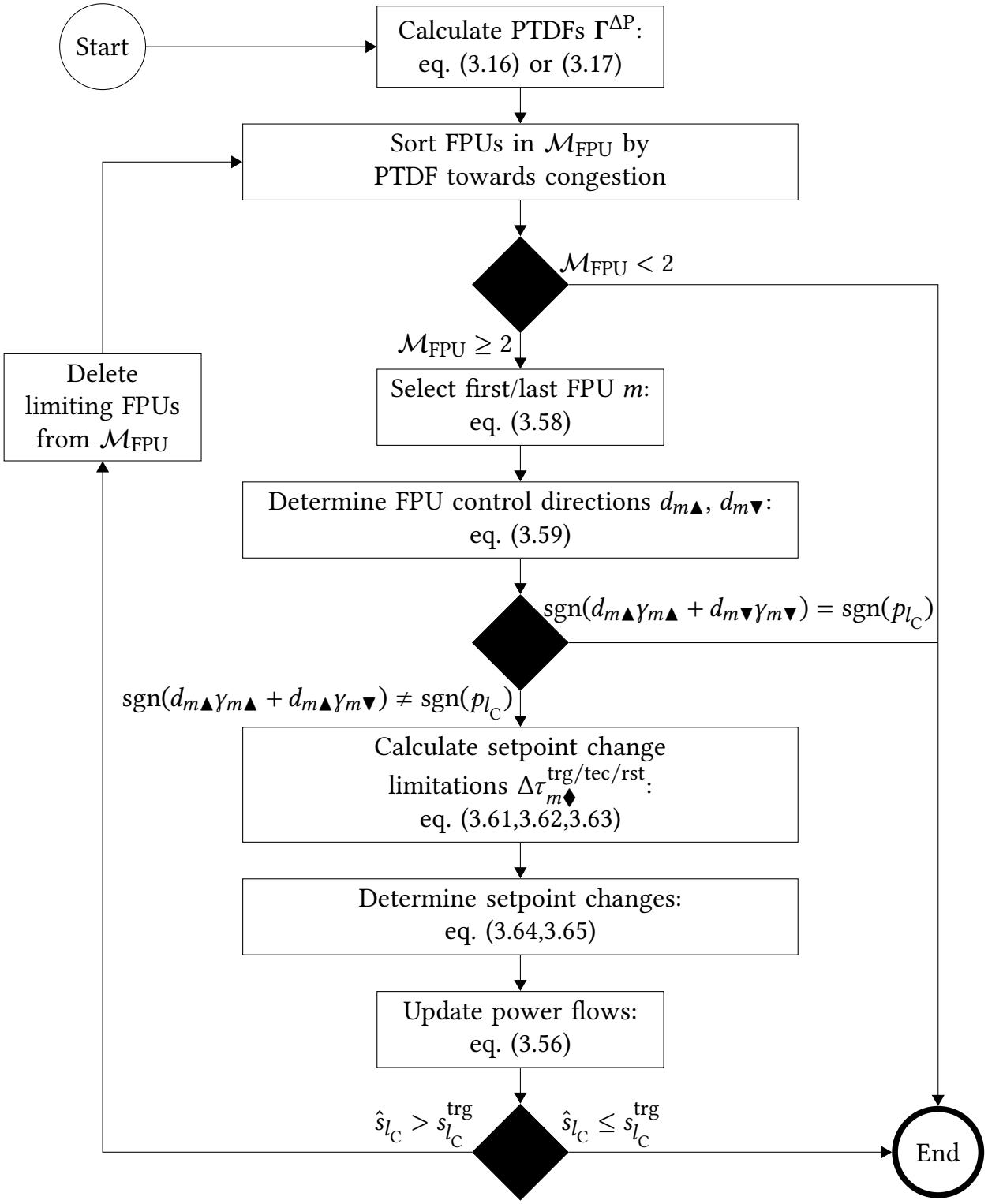

Figure 3.4: Heuristic algorithm to select flexible power units for curative congestion management

Table 3.2: Example for the improved FPU-selection

n	$\gamma_{lc,n}$	$\Delta p_{n,\max}$	UP	DOWN	Sorted
n_1	-0.1	± 2	$p_{n_3,\text{flx}} = +2$	$p_{n_5,\text{flx}} = -1$	$p_{n_3,\text{flx}} = +2$
n_2	-0.4	± 2	$p_{n_2,\text{flx}} = 0$	$p_{n_4,\text{flx}} = -1$	$p_{n_2,\text{flx}} = +2$
n_3	-0.5	± 2	$p_{n_1,\text{flx}} = 0$		$p_{n_1,\text{flx}} = -2$
n_4	+0.2	± 1			$p_{n_4,\text{flx}} = -1$
n_5	+0.4	± 1			$p_{n_5,\text{flx}} = -1$
			$\sum \Delta p_n = 4$		$\sum \Delta p_n = 8$
			$\Delta p_{l_C} = -1.6$		$\Delta p_{l_C} = -2.2$

overall benefit, the FPU $m\blacktriangle$ with the higher absolute sensitivity must be stepped into the direction $d_{m\blacktriangle}$ that will reduce the congestion and the FPU $m\blacktriangledown$ with the lower absolute sensitivity must then be stepped into the opposite direction $d_{m\blacktriangledown}$. This determination is shown in eq. (3.58) and (3.59).

$$\begin{aligned} m\blacktriangle &= m|\gamma^{\Delta\text{P}}_{l_C,m} = \max\left(|\gamma^{\Delta\text{P}}_{l_C,m_0}|, |\gamma^{\Delta\text{P}}_{l_C,m_M}|\right) \\ m\blacktriangledown &= m|\gamma^{\Delta\text{P}}_{l_C,m} = \min\left(|\gamma^{\Delta\text{P}}_{l_C,m_0}|, |\gamma^{\Delta\text{P}}_{l_C,m_M}|\right) \end{aligned} \tag{3.58}$$

$$d_{m\blacktriangle} = -d_{m\blacktriangledown} = -\text{sgn}\left(\gamma^{\Delta\text{P}}_{l_C,m\blacktriangle} \cdot p_{l_C}\right) \tag{3.59}$$

If the combined effect on the congestion is opposed to the direction of the congestion, $m\blacktriangle$ can be activated in balance with $m\blacktriangledown$ to reduce the congestion. Mathematically, this can be expressed by comparing the added sensitivities of both FPUs to the direction of power flow on the congested line, as in eq. (3.60).

$$\text{sgn}\left(d_{m\blacktriangle} \cdot \gamma_{l_C,m\blacktriangle} + d_{m\blacktriangledown} \cdot \gamma_{l_C,m\blacktriangledown}\right) \neq \text{sgn}\left(p_{l_C}\right) \tag{3.60}$$

If eq. (3.60) is fulfilled, the two measures can be used together to reduce the congestion, otherwise the algorithm ends since any combinations following this one will also not be beneficial due to the measure list being sorted.

The second shortcoming in [69] is that the FPU-setpoints are determined through an iterative process. This can be sped up by directly calculating necessary setpoint changes analytically similar to (3.55) but adjusted for the simultaneous changing of two FPUs. Hence, the calculations shown in Subsection 3.2.2.1 have to be adjusted, as follows. Considering eq. (3.38) with $m \in \mathcal{M}_{\text{FPU}}$ only, the minimization can be solved heuristically via pairwise increase and decrease of FPUs.

With the direction of both setpoint changes $\Delta\tau_{m\blacktriangle}$ and $\Delta\tau_{m\blacktriangledown}$ determined, only their absolute value $\Delta\tau_{m\blacklozenge}$ needs to be calculated. First, the theoretically needed output change needed from both FPUs to fully relieve the congestion without causing an imbalance in generation and load can be calculated with eq. (3.61)

$$\Delta\tau_{m\blacklozenge}^{\mathrm{trg}} = \left| \frac{\Delta p_l^{\mathrm{trg}}}{\gamma_{l,m\blacktriangle}^{\Delta\mathrm{P}} - \gamma_{l,m\blacktriangledown}^{\Delta\mathrm{P}}} \right| \tag{3.61}$$

Eq. (3.62) shows how the technical maximum possible setpoint change has to be chosen as the minimum of the individual absolute technical maxima which can be determined with eq. (3.53).

$$\Delta\tau_{m\blacklozenge}^{\mathrm{tec}} = \min\left(\left|\Delta\tau_{m\blacktriangle}^{\mathrm{tec}}\right|, \left|\Delta\tau_{m\blacktriangledown}^{\mathrm{tec}}\right|\right) \tag{3.62}$$

Lastly, the maximum / minimum setpoint change admissible with regards to the critical limits of all non-congested lines in the grid is determined with eq. (3.63).

$$\Delta\tau_{m\blacklozenge}^{\mathrm{rst}} = \min\left(\left|\Delta\mathcal{T}_{m\blacktriangle}^{\mathrm{rst}}\right| \cup \left|\Delta\mathcal{T}_{m\blacktriangledown}^{\mathrm{rst}}\right|\right) \tag{3.63}$$

Then, the setpoint change for both FPUs can be determined using eq. (3.64) and eq. (3.65).

$$\Delta\tau_{m\blacklozenge} = \min\left(\Delta\tau_{m\blacklozenge}^{\mathrm{trg}}, \Delta\tau_{m\blacklozenge}^{\mathrm{tec}}, \Delta\tau_{m\blacklozenge}^{\mathrm{rst}}\right) \tag{3.64}$$

$$\Delta\tau_m = d_m \cdot \Delta\tau_{m\blacklozenge}, \quad \text{with } m \in \{m\blacktriangle, m\blacktriangledown\} \tag{3.65}$$

The determined setpoint changes of $\tau_{m\blacktriangle}$ and $\tau_{m\blacktriangledown}$ are saved as part of the solution. Power flows are updated including the new setpoints of the two FPUs according to eq. (3.66). If a rest of the congestion remains, the FPU that limited the setpoint either by its technical maximum or by the restriction with regards to additional overloads, is deleted from the sorted list of FPUs and the algorithm starts over. Otherwise the algorithm successfully ends.

$$\hat{s}_l = \sqrt{\hat{p}_l^2 + q_l^2} = \sqrt{\left(p_l + \Delta\tau_{m\blacktriangle} \cdot \gamma_{l,m\blacktriangle}^{\Delta\mathrm{P}} + \Delta\tau_{m\blacktriangledown} \cdot \gamma_{l,m\blacktriangledown}^{\Delta\mathrm{P}}\right)^2 + q_l^2} \tag{3.66}$$

3.3 Quality indicators for power flow control systems

As explained in Chapter 1, automated CM systems need to be effective, efficient, reliable, and robust. Reliability and robustness are achieved by basing the algorithm on DC power flow equations. To quantify the effectivity and efficiency, several quality indicators are

derived in this section. To put the outcomes of these indicators for the heuristic algorithms into perspective, they should be compared to those of an optimization, serving as a benchmark.

First, to determine the effecitivity of the DC-based algorithm, the *accuracy* with which it reaches the targeted AC line loading can be used, as shown in eq. (3.67). An optimal solution will result in an accuracy of 1, while a value greater than 1 indicates an incomplete alleviation of the congestion and a value of less than 1 shows an inefficient overshoot of the target.

$$\psi = \frac{|i_{l_\mathrm{C}}^{\mathrm{post}}|}{i_{l_\mathrm{C},\mathrm{trg}}} \tag{3.67}$$

The accuracy alone does not paint a full picture of the algorithm's effectivity, since the state of the rest of the lines are not represented. For this, grid state severity indicators are introduced. The algorithm is supposed to improve the grid state in the sense that it solves a congestion without creating new ones. To indicate how the severity of the grid state changed through the activation of RMs, two *grid state severity change indices* $\Delta\chi_1$ and $\Delta\chi_2$ described in eq. (3.68) and (3.69) are derived from [70].

$$\Delta\chi_{\mathrm{rel},1} = \frac{\chi_1^{\mathrm{post}}}{\chi_1^{\mathrm{pre}}}, \quad \text{with } \chi_1^{\mathrm{post/pre}} = \frac{1}{L} \cdot \sum_{l=1}^{L} \left(\frac{|i_l^{\mathrm{post/pre}}|}{i_{l,\mathrm{r}}} \right)^2 \tag{3.68}$$

$$\Delta\chi_{\mathrm{rel},2} = \frac{\chi_2^{\mathrm{post}}}{\chi_2^{\mathrm{pre}}}, \quad \text{with } \chi_2^{\mathrm{post/pre}} = \frac{\sum_{l=1}^{L} \left(|i_l^{\mathrm{post/pre}}| - i_{l,\mathrm{r}} \right)^2}{\sum_{l=1}^{L} i_{l,\mathrm{r}}^2} \tag{3.69}$$

χ_1 is the quadratic sum of all line utilizations divided by the number of lines in the grid L. χ_2 is defined as the quadratic sum of all overloads and free capacities, divided by the sum of all line rated currents. While both indices range from 0 to 1 (unless lines are severely overloaded above their rated currents), χ_1 is an indicator for overall grid utilization, χ_2 indicates how much free capacity is still available in the grid. The quadratic character of these equations emphasize larger values, meaning single overloads, or respectively single highly unutilized lines, will have a larger effect on the overall value, making severe grid states detectable. The severity change indicators $\Delta\chi_{\mathrm{rel},1/2}$ describe the achieved relative change in overall line loading, resp. free capacity. When an algorithm finds a solution that solves a congestion ($\psi \leq 1$) without creating new congestions ($\chi_1^{\mathrm{post}} < 1$), its efficiency in doing so is indicated by values of $\Delta\chi_{\mathrm{rel},1/2}$ close to 1, marking a small change in overall grid state to achieve the targeted goal.

The last two indicators will indicate how *efficient* the usage of available measures by the algorithm is. In general, efficiency can be defined as the quotient of output and input. In the case of congestion, output is the achieved power flow change on the congested line $|\Delta p_{l_C}|$ and input is the sum of activated RMs. For FPUs the input can easily be defined as the absolute activated flexible power at each node $|\Delta p_n|$. For ICs the input could be defined as the amount of reactance activated – but this is not a value comparable to $|\Delta p_{l_C}|$ and $|\Delta p_n|$. This is why instead, the power flow change caused by an IC $|\Delta p_\lambda|$ is defined as the input of this type of device. To consider that Δp_l is influenced by other measures, Δp_l is calculated as the difference in power flows between a grid state in which only the FPU measures have been activated and the final grid state with also the IC measures active. The derived efficiency indicator η_1 is defined as the power flow change on the congested line divided by the sum of used flexible power that caused this change as described in eq. (3.70). The indicator ranges from 0 to 1, with 1 being the most efficient.

$$\begin{aligned}\eta_1 &= \frac{|\Delta p_{l_C}|}{\sum_n^{N_{\text{used}}} |\Delta p_n| + \sum_l^{L_{\text{used}}} |\Delta p_l|} \\ &= \frac{|\Delta p_{l_C}|}{\sum_n^{N_{\text{used}}} |\Delta p_n| + \sum_l^{L_{\text{used}}} |p_l^{\text{post}} - p_l^{\text{pre+FPU}}|}\end{aligned} \tag{3.70}$$

One problem that can occurr with this indicator, is that it may penalize the usage of ICs that amplify each other synergetically: A non-linear optimal coordination of ICs that takes into account how the devices influence each other, can achieve a higher change of power flow in IC-lines with less activated reactance than a linear heuristic that disregards inter-influence between ICs. This can make the obviously more efficient optimal solution have a lower value of η_1. So instead of the power flow actually made available by an IC, its input may rather be defined as the power flow change it would have caused on the congested line if it had been activated solely. This way, the synergetical usage of ICs is rewarded instead of penalized within the efficiency calculation, as shown in eq. (3.71). Theoretically, it can range from 0 to infinity but in scenarios with a realistic amount of synergy between ICs it will not go far above 1.

$$\eta_2 = \frac{|\Delta p_{l_C}|}{\sum_n^{N_{\text{used}}} |\Delta p_n| + \sum_l^{L_{\text{used}}} |\gamma_{l,l_C}^{\Delta X} \cdot \Delta p_l|} \tag{3.71}$$

3.4 Conclusions and neccessary evaluations of the derived sensitivities and algorithms

- One optimization and four heuristic algorithms for curative CM were conceptualized, using known PTDFs and a newly derived calculation method for sensitivities for gradual series reactance changes named XCDFs. Quality indicators were defined to evaluate these algorithms and compare them to each other.
- The sensitivities' linearization errors must be evaluated before they can be applied in CM algorithms.
- The different optimization and heuristic algorithms must be compared to each other to determine to what degree and under which circumstances they can be applied in CM systems.

4 Simulation and analysis of curative power flow control algorithms

In this chapter the sensitivities and heuristic CM algorithms defined in Chapter 3 are verified in software simulations. The goal is to test the accuracy of the sensitivities and to determine how well the algorithm can solve congestions with different parameterizations and for various Grid Use Cases (GUCs)[1]. The optimization described in Subsection 3.2.1 is used as a benchmark to evaluate the solution of the heuristic algorithm. Thus, this chapter highlights only the algorithm's CM functionality; real-time considerations are targeted in Chapter 7.

4.1 Simulation setup

The following verification of XCDFs as well as the validation of the CM heuristic are analyzed using Matlab MATPOWER [71] and the New England IEEE 39-Bus System [72] shown in Fig. 4.1. This grid model is chosen because it is a HV grid, meaning the usage of linearized DC power flow calculation is appropriate, and it is decently meshed, allowing for ICs to be able to shift power flows around.

4.2 Verification of sensitivities for reactance changes

While PTDFs behave linearly within the DC power flow domain, XCDFs do not. Changing a line reactance changes the grid's nodal susceptance matrix which is used to calculate XCDFs and thus, the resulting sensitivity is only precise within the DC power flow domain for the considered reactance change Δx. When XCDFs are used as linear factors to calculate power flow changes caused by a multiple of Δx or several reactance changes in different lines, an approximation error is introduced describing how far the expected power flow changes diverge from the actual results of the DC power flow equations (cp. eq. (3.36) and eq. (3.37)). This error is analyzed in this section to determine under which conditions it is still appropriate to assume XCDF linearity. To demonstrate the sensitivities' applicability in real world scenarios, the results are also compared to AC power flow calculations. Parts of the results presented in this section were first published in [OP4].

[1] In this work, a GUC describes a generation and load scenario combined with a specific grid topology.

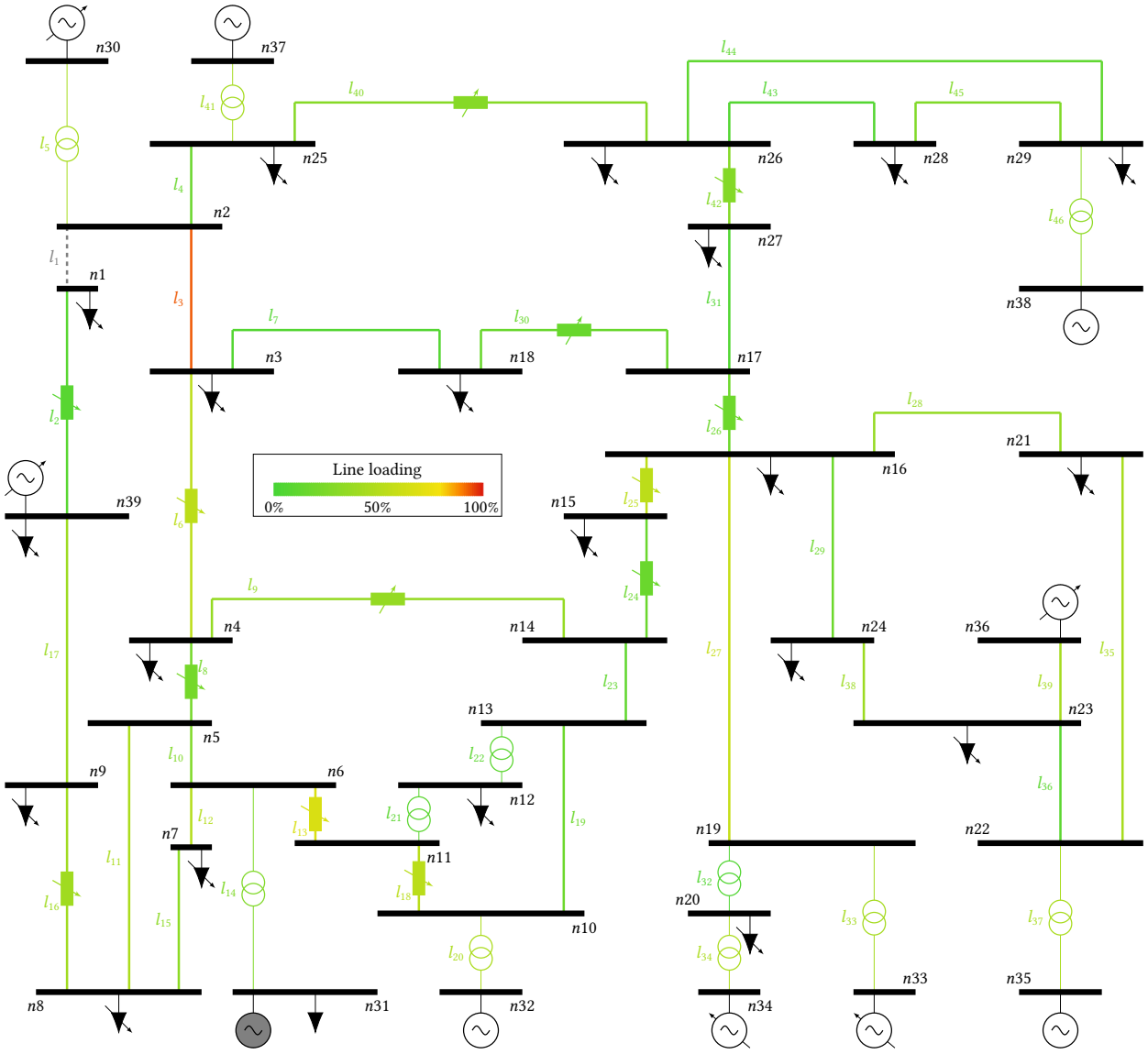

Figure 4.1: IEEE 39 bus test system with outage in line l_1 and congestion in line l_3. Impedance controllers and flexible power units are indicated with diagonal arrows, slack generator in grey.

First, XCDFs of all lines l towards a reactance change of $\Delta x_{\lambda,\text{step}} = 0.01 \cdot x_\lambda$ in each line λ are calculated. Then, a loop is carried out during which the reactance of each line (one at a time) is increased from 100 % to 200 % by adding $\Delta x_{\lambda,\text{step}}$ in each step[2]and XCDFs of all lines towards all lines are calculated in two ways: In the direct calculation, XCDFs are calculated with the full reactance change $\Delta x_\lambda = n_\text{step} \cdot \Delta x_{\lambda,\text{step}}$ applied to λ. In the indirect calculation, XCDFs are assumed to be linear towards Δx_λ, so the original XCDF-values for $1 \cdot \Delta x_{\lambda,\text{step}}$ are multiplied with n_step (cp. eq. (3.36)). The relative difference between these

[2]Whether x_λ is increased or decreased does not make a difference in the absolute linearization error.

two calculation methods describes the introduced linearization error ε shown in eq. (4.1). The results are shown in Fig. 4.2.

$$\varepsilon(n_{\text{step}}) = \frac{n_{\text{step}} \cdot \gamma_{l,\lambda}^{\Delta X}\left(\Delta x_{\lambda,\text{step}}\right) - \gamma_{l,\lambda}^{\Delta X}\left(n_{\text{step}} \cdot \Delta x_{\lambda,\text{step}}\right)}{\gamma_{l,\lambda}^{\Delta X}\left(n_{\text{step}} \cdot \Delta x_{\lambda,\text{step}}\right)} \tag{4.1}$$

Two aspects are interesting here: First of all, the relative differences are rather low, start-

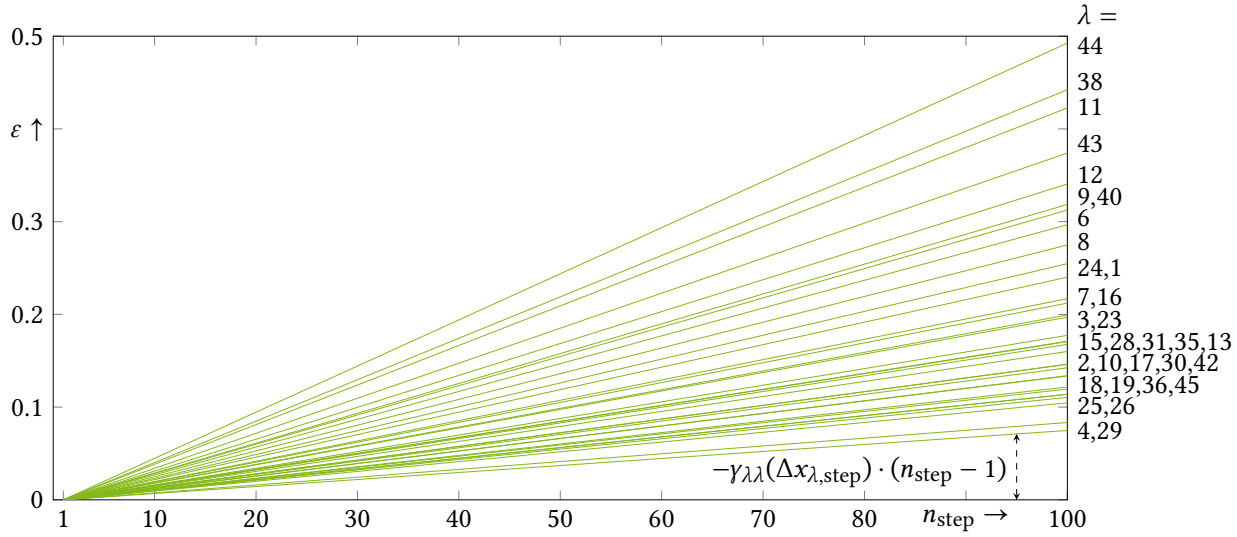

Figure 4.2: Linearization error introduced when XCDFs are assumed to be linear factors with $\Delta x_{\lambda,\text{step}} = 0.01 x_\lambda$

ing at 0 % for a reactance change of 1 %, and ending at a range of 7.5 %–49.3 %, depending on the selected line, for a very large reactance change of 100 %. Within a realistic range of $\Delta x_\lambda / x_\lambda < 0.3$, the linearization error remains below 7 % on average and never exceeds 15 % absolutely. Secondly, the slope of ε appears to increase in a strictly linear manner with n_{step}. In fact, the value of this slope is the same value for all lines, no matter which line is chosen as λ and it is equal to the negative sensitivity of λ to itself: $\gamma_{\lambda,\lambda}^{\Delta X}$. This observation, that was made in exemplary calculations but so far *has not been derived analytically*, is shown in eq. (4.2).

$$\frac{\partial \varepsilon}{\partial n_{\text{step}}} \approx \Delta\varepsilon = \varepsilon(n_{\text{step}} + 1) - \varepsilon(n_{\text{step}}) \approx -\gamma_{\lambda,\lambda}^{\Delta X} \tag{4.2}$$

This indicates that there may well be a way to utilize XCDFs as linear factors – just not as

simple as described in eq. (3.36). Assuming that the value found in exemplary calculations in eq. (4.2) is true, and accounting for the fact that $\varepsilon(1) = 0$, then a function to calculate the linearization error can be described with eq. (4.3).

$$\varepsilon(n_{\text{step}}) = \gamma_{\lambda,\lambda}^{\Delta X} \cdot \left(1 - n_{\text{step}}\right) \tag{4.3}$$

By setting eq. (4.1) equal to eq. (4.3), eq. (4.4) can be derived and solved for $\gamma_{l,\lambda}^{\Delta X}(n_{\text{step}} \cdot \Delta x_{\lambda,\text{step}})$ to show the linear characteristic of XCDFs.

$$\begin{aligned} \frac{n_{\text{step}} \cdot \gamma_{l,\lambda}^{\Delta X}(\Delta x_{\lambda,\text{step}})}{\gamma_{l,\lambda}^{\Delta X}(\Delta x_{\lambda,\text{step}} \cdot n_{\text{step}})} - 1 &= (1 - n_{\text{step}}) \cdot \gamma_{\lambda,\lambda}^{\Delta X}(\Delta x_{\lambda,\text{step}}) \\ \gamma_{l,\lambda}^{\Delta X}(\Delta x_{\lambda,\text{step}} \cdot n_{\text{step}}) &= \gamma_{l,\lambda}^{\Delta X}(\Delta x_{\lambda,\text{step}}) \cdot \frac{n_{\text{step}}}{(1 - n_{\text{step}}) \cdot \gamma_{\lambda,\lambda}^{\Delta X}(\Delta x_{\lambda,\text{step}}) + 1} \end{aligned} \tag{4.4}$$

In the described simulation setup the additional linearization error for XCDFs disappears when this correction is applied. Proving this analytically would require forming the partial derivative $\partial p_l / \partial b_\lambda$ with eq. (3.35), or putting eq. (3.35) into both sides of eq. (4.4). Unfortunately, eq. (3.35) contains elements of the numerically determined pseudo-inverted nodal susceptance matrix which cannot be partially differentiated to the knowledge of the author. And even if the regular inverted matrix $\left(\boldsymbol{B}_{\text{N}}\right)^{-1} = 1/|\boldsymbol{B}_{\text{N}}| \cdot \text{adj}\left(\boldsymbol{B}_{\text{N}}\right)$ was used, there is no analytic way to determine a single element in this recursively calculated matrix. However, within a range of some 10 %–30 % line reactance change, which is realistic for reactance controlling devices such as DSRs (cp. Subsection 2.3.3.3), the linearization error ε remains small enough for a safe utilization of the uncorrected linearity assumption expressed in eq. (3.36). To minimize the linearization error, re-iterating the XCDF-calculation, as described in h2–4 in Subsection 3.2.2.1, may be a valid method.

4.3 Verification and validation of heuristic coordination algorithms

To verify that the heuristic coordination described in Chapter 3 can curatively solve congestions and to validate their performance in comparison to preventive measures, these heuristics are implemented in Matlab MATPOWER and applied to a CM use case under varying conditions. Additionally, the optimization problem described in equations (3.38) – (3.41) is implemented in Matlab to serve as a preventive CM algorithm and as a benchmark to compare the heuristic algorithms to. Due to the large amount of control variables and

non-linear constraints within the optimization problem, genetic algorithm is chosen as a global solver. Note that impedance controlling devices are not explicitly modelled but realized by simply adding the respective reactance change to a power line's reactance. Parts of the results described in this section were first published in [BA1], resp. [OP5].

4.3.1 Grid use cases and parameter variations

ICs are positioned throughout the IEEE 39 bus test system according to [OP3]. The GUCs used in this chapter are taken from this paper as well, to show how the heuristics make use of the optimally positioned ICs. These GUCs were created by applying a daily load curve to all loads and determining fitting generation dispatch via optimal power flow.

First, a GUC is selected and the resulting congestion is solved with the heuristic algorithm under varying availability of ICs using different XCDF-recalculation approaches to analyze the benefit of a higher accuracy against an increased calculation time. Then, the performance of the heuristic approaches are compared to optimal solutions found through an optimization approach. Finally, limitations of the heuristic are shown in the form of edge cases that the algorithm cannot solve sufficiently.

Within the heuristic approach, ICs are always considered before FPUs because they are assumed to be free of cost to the operator. In an optimization, each control variable must be considered with a variable cost to ensure they are changed as little as possible – otherwise the optimization would always maximize the usage of ICs, even if the congestion has already been solved. Since the derivation of variable costs κ_{FPU} and κ_{IC} for FPUs and IC is out of scope for this thesis, the original idea of prioritizing ICs over FPUs is represented in the optimization by setting $\kappa_{\mathrm{IC}} = 1$ and $\kappa_{\mathrm{FPU}} = 10^9$.

4.3.2 Performance evaluation of the derived heuristics

To demonstrate how the (re-)calculation of XCDFs affects the outcome of the curative CM solution, the three versions of the heuristic algorithm are applied to a GUC under varying availability of ICs. In this GUC, the outage of line 1 causes line 3 to breach its critical threshold of $c_{\mathrm{crt}} = 0.9$. To better demonstrate the differences between the algorithms, and avoid all of them simply maxing out the IC on the overloaded line to reduce the congestion, this IC is deactivated, showcasing how adjacent ICs can help other lines as well.

Table 4.1: Calculation durations of heuristics and optimization

$\Delta x_l/x_l$	h1	h2	h4	opt
0 %	0.11 s	0.08 s	0.09 s	743.42 s
30 %	0.53 s	2.30 s	401.47 s	720.56 s
60 %	0.30 s	0.88 s	379.77 s	511.83 s

4.3.2.1 No impedance controllers available

To set a benchmark in form of the needed redispatch of distributed energy resources, the congestion is first solved with no ICs available and the setpoints of all FPUs can be changed by ±30 %. Fig. 4.3 shows the resulting line utilizations while the respectively activated FPUs as well as the quality indicators defined in Section 3.3 for the heuristic algorithm and the optimization can be seen in Fig. 4.4.

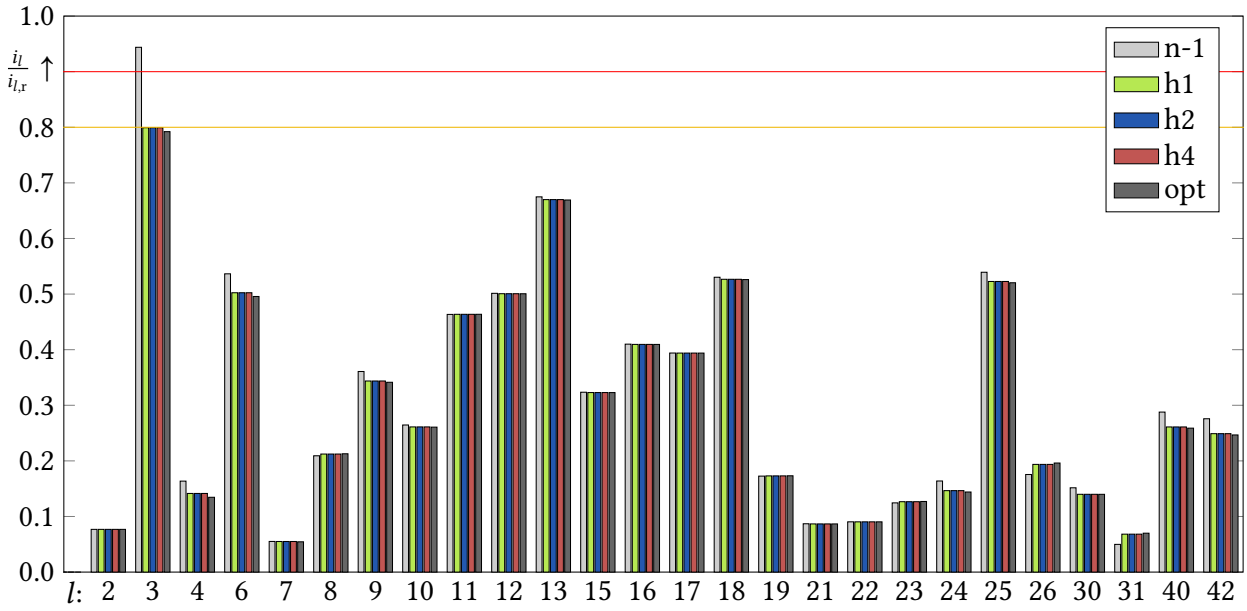

Figure 4.3: Line utilizations in scenario without impedance controllers

It is apparent that all three heuristics as well as the optimization activated FPUs in a manner that successfully relieves the congestion, with an accuracy ψ of almost 1. Hence, the severity indicators $\Delta\chi_1$ are slightly smaller than 1, indicating a state of decreased line loading severity, resp. a $\Delta\chi_1$ slightly above 1 shows slightly more available capacity in the grid than before the activation of RMs. All of the heuristics yield the same selection of

FPUs. This is not surprising, since no ICs were used, which is the only event in which the heuristics would treat re-calculation of sensitivities differently. Without this, the PTDFs remain the same throughout the algorithm execution, and their average manifests itself as the efficiency indicators η_1 and η_2. The two indicators are the same here, since no inter-influencing between measures occurs when only FPUs are activated. The optimization approach produced a very similar result, except it activated slightly more flexible power in nodes n_4 and n_{25}. This is due to the non-linearity of the power flow constraints used in the optimization which are not considered in the heuristics. This causes the heuristics to seem slightly more accurate and efficient than the optimization in this case.

Regarding the calculation times needed to find the solutions, Table 4.1 shows that all heuristics needed less than 100 ms whereas the optimization required over 10 min. This vast difference in calculation time showcases the strongest advantage of the heuristic approach. Several different optimization approaches were tried as well, but while local solvers (e.g. fmincon) did converge within seconds to a few minutes, they often only found local optimal solutions at the expense of measure efficiency, i.e. more activated flexible power. It should be noted however, that the time-consuming consideration of non-linear power flow constraints are only necessary due to reactance changes introduced by ICs, so an optimization of FPUs alone would not actually need to consider them.

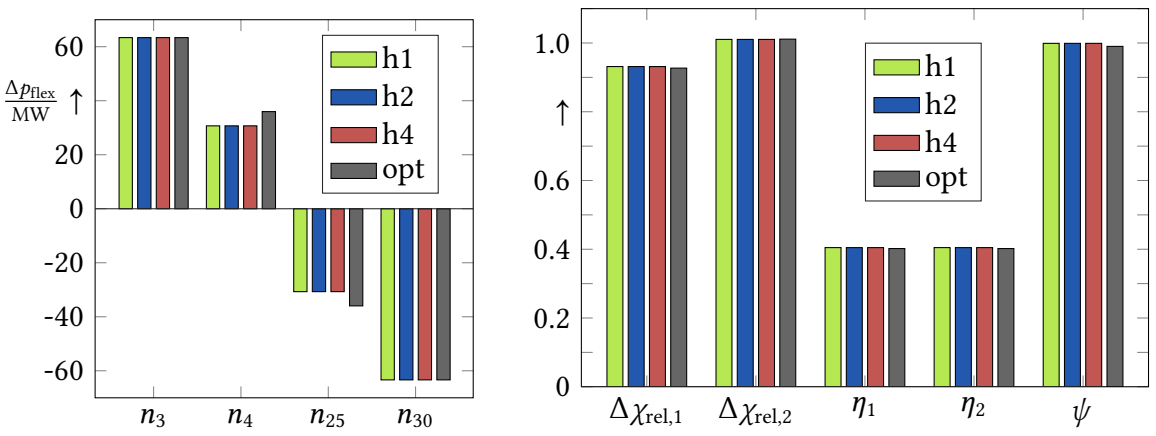

(a) Activated flexible power (b) Quality indicators severity χ, efficiency η, accuracy ψ

Figure 4.4: Results of test case without impedance controllers

4.3.2.2 Combined coordination of flexible power and impedance controllers

To analyze the trade-off between ICs and FPUs, the same congestion is now solved in a scenario where all FPU setpoints are changeable by ±30 % and the ICs can change their equipped lines' reactances by ±30 %, resulting in the line loadings shown in Fig. 4.5.

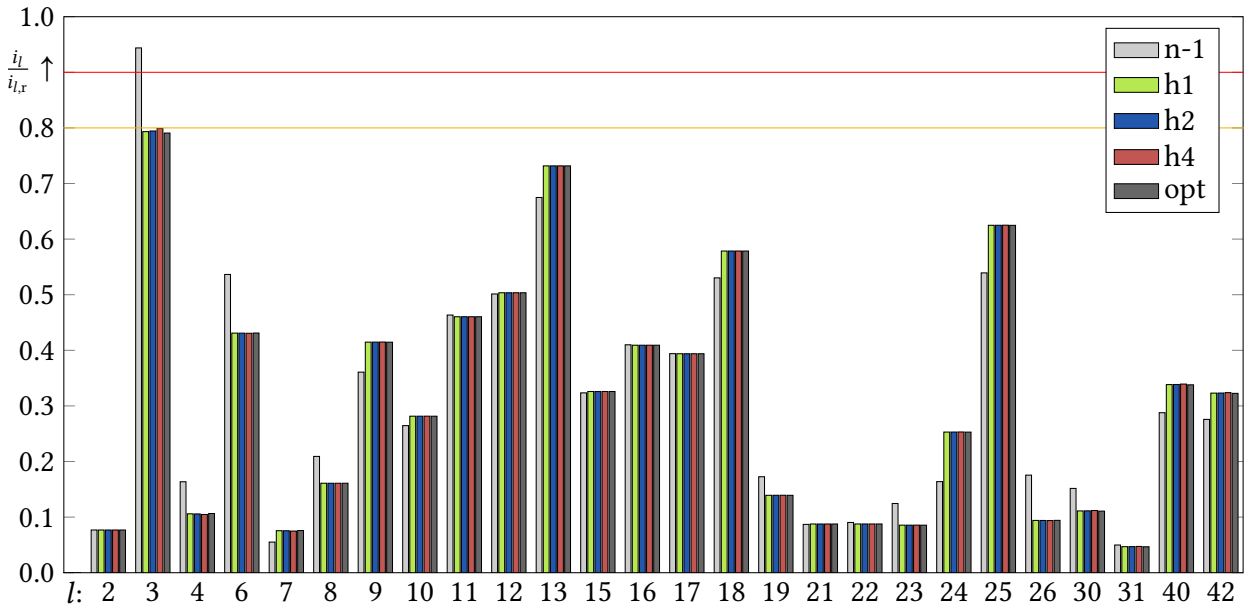

Figure 4.5: Line utilizations in scenario with low impedance controller availability

Again, heuristic and optimization results only vary slightly; the congestion is solved with an accuracy $\psi \approxeq 1$ and all algorithms selected the same eleven ICs and two FPUs (cp. Fig. 4.6). However, this scenario shows lower severity change indicators due to slightly higher overall line loading because of ICs shifting power flows into adjacent lines. Yet, the lower activated flexible power yields a more economical solution.

Since eight of the ICs have positive XCDFs towards the congested l_3, they are tapped in negative direction, pulling power flows into the grid's righthand side. Only the ICs on l_6 and l_8 increase their reactances, since they have negative XCDFs towards the congestion. Independent of tapping direction, ICs closer to the congestion are used more extensively since their absolute XCDFs are higher. Although the heuristics exhaust all ICs before considering FPUs the ICs on l_2 and l_{16} are not used because the outage in l_1 cuts them out of the mesh, zeroing all of their XCDFs. The used ICs approximately halve the redispatch demand, so only FPUs at two nodes are needed instead of four.

Heuristic h4 activates slightly less flexible power than the others although it selected the same constellation of ICs, so the grid topology considered when starting the FPU selection is the same in all the heuristics. However, since h4 calculates the effects of the last selected IC more precisely through the many XCDF re-calculations, the level of congestion after the activation of the selected ICs is determined more precisely than by h1 and h2.

The combined use of ICs and FPUs also showcases the difference between η_1 and η_2: when looking at η_1, the set of selected RMs appears to be less than half as efficient when compared to the solution only involving FPUs. However, η_1 does not consider leveraged synergies between measures. This is considered by η_2, which is 50 % higher than in the FPU-only case because the ICs amplify each other and the selected FPUs.

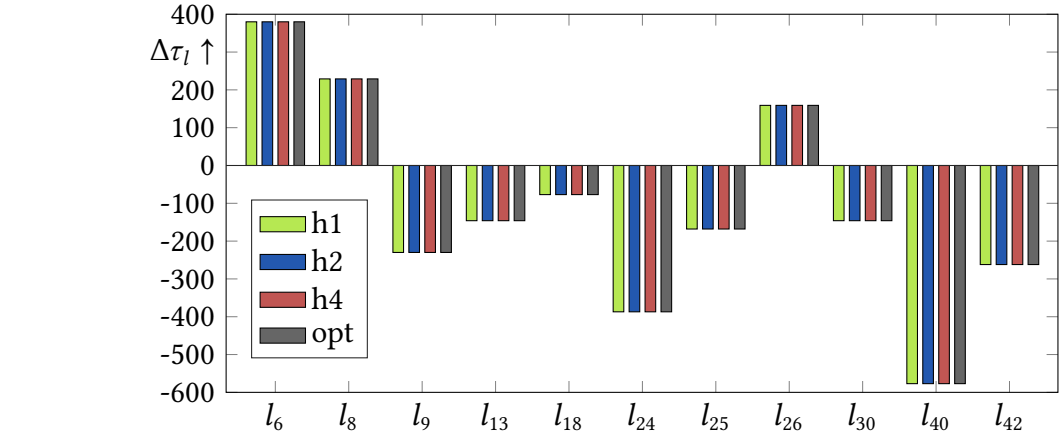

(a) Activated impedance controllers

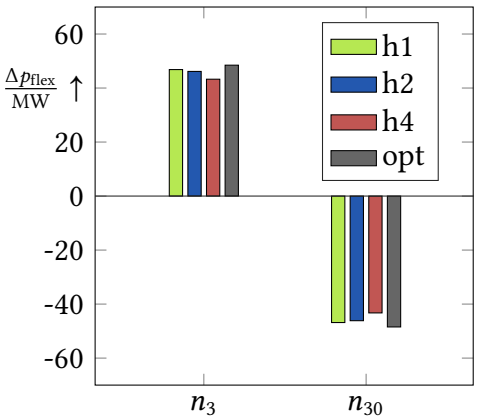

(b) Activated flexible power

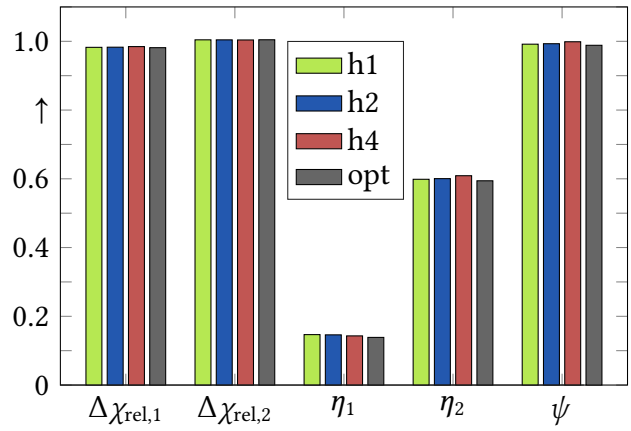

(c) Quality indicators severity χ, efficiency η, accuracy ψ

Figure 4.6: Results of test case with low impedance controller availability

4.3.2.3 High availability of Impedance controllers

In Section 4.3.2.2 the heuristics max out available IC steps no matter the type of XCDF-recalculation strategy. To showcase the effect of different XCDF-recalculation strategies, the same congestion is now solved in a scenario where ICs can change their equipped lines' reactances by ±60 %, which is overall more than necessary to solve the congestion. Resulting utilizations are shown in Fig. 4.7.

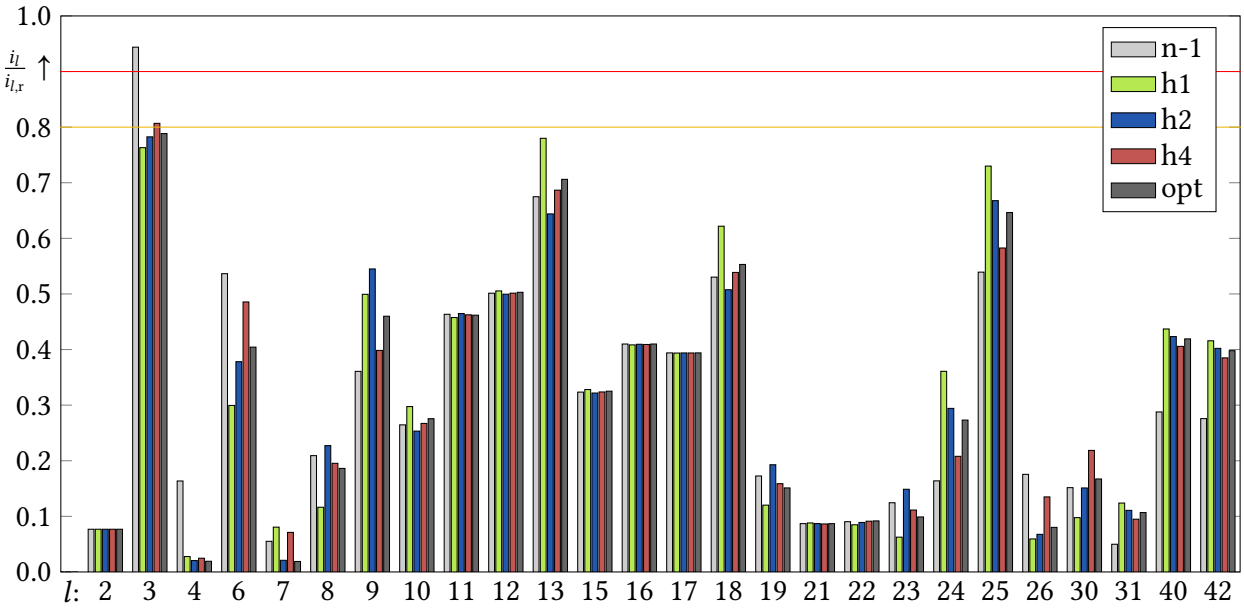

Figure 4.7: Line utilizations in scenario with high impedance controller availability

This time, the results vary more significantly between the different algorithms, mainly due to the larger size of the reactance changes (cp. Fig. 4.8). While the optimization and h2 managed to solve the congestion with high accuracies of 0.97, resp. 0.98, h1 overcompensated the congestion more than necessary at an accuracy of 0.95, and h4 even did not quite solve the congestion, but only reached a utilization of 80 % in l_3. Two linearization errors are responsible for these phenomena. The linearization error introduced through the XCDF calculation apparently leads to an *underestimation* of the overall effect of the activated ICs, leading to the overcompensation in h1. This underestimation actually leads to h1 being the only algorithm activating a few Megawatts of flexible power in addition to the ICs. This error is minimized through sensitivity re-calculations in h4, leaving it virtually with only the linearization error between AC and DC power flow equations. This leads to an *overestimation* of the IC effect, resulting in a loading of l_3 higher than

expected and above the target value of 80 %. According to $\Delta\chi_1$, h1 actually worsened the grid state, while h4 slightly improved it, and the other two algorithms kept it roughly at the same level. A look at $\Delta\chi_2$ shows that regardless of the chosen algorithm, the overall amount of free capacity was not significantly changed despite the differences in line loadings. Regarding the efficiency η of the activated RMs two things can be said: First, the large reactance changes of several hundreds of IC-steps on single lines introduce a high amount of synergy between them ($\eta_2 > 1$). Secondly, the seemingly high value of η_1 for h4 has to be put into context of h4 not fully solving the congestion. This showcases why it is necessary to consider multiple indicators to assess the quality of the algorithms.

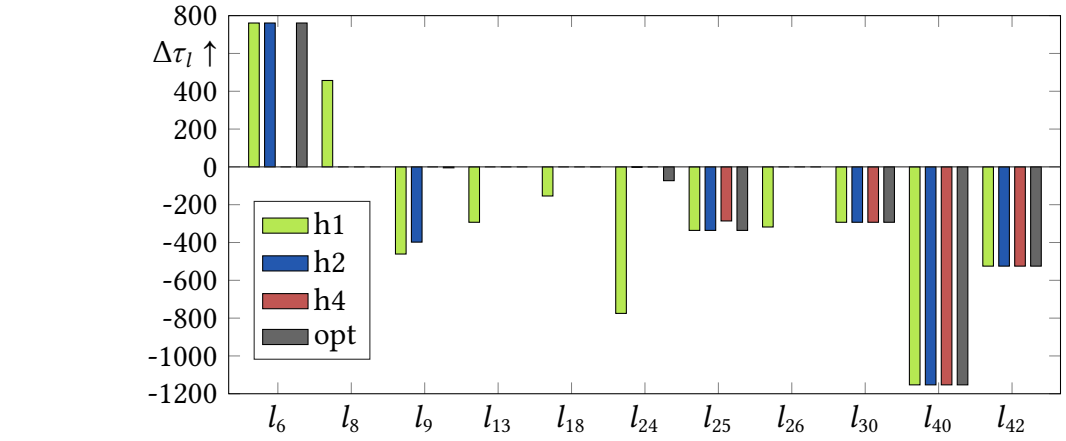

(a) Activated impedance controllers

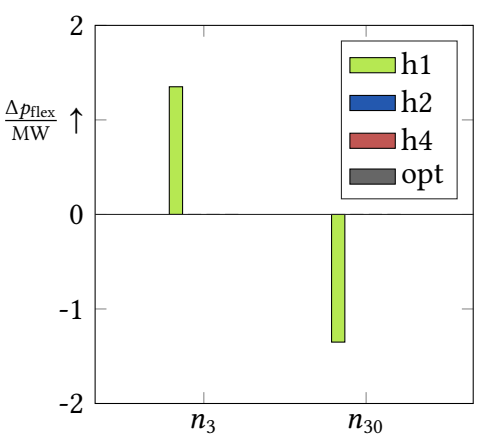

(b) Activated flexible power

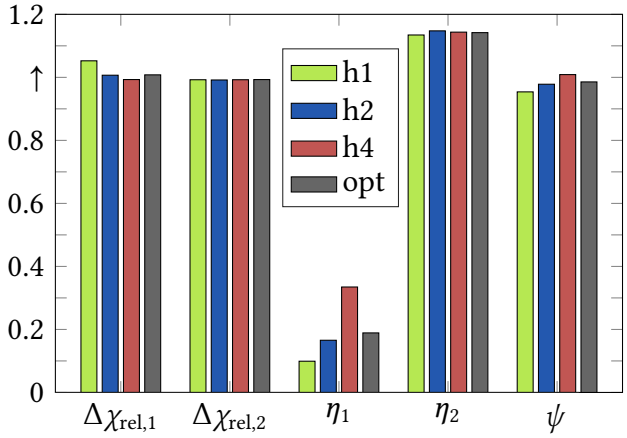

(c) Quality indicators severity χ, efficiency η, accuracy ψ

Figure 4.8: Results of test case with high impedance controller availability

4.4 Quality assessment of the developed algorithms and implications for real-time applications

- The derived sensitivities and CM algorithms were tested in Matlab MATPOWER simulations, applying appropriate overload use cases in the IEEE 39 bus test system.
- The sensitivities' linearization errors are below 10 % within line reactance changes up to 30 % – which is a typical amount of reaction for a fleet of DSRs.
- The optimization as well as heuristic 4 only provided marginally more accurate and efficient results than the heuristics 1–3 but required significantly more calculation time (several minutes) compared to heuristics 1–3 (< 3 s).
- Heuristics 2 and 3 outperformed heuristic 1 regarding all quality indicators and only converged insignificantly slower.

5 Multi-agent system for automated curative ad-hoc congestion management

In this chapter, the concept for an agent-based ad-hoc curative CM system is explained and an implementation thereof is described. This system incorporates the coordination algorithms for the activation of ICs and FPUs in a distributed manner, with a focus on real-time application. To improve the system's resilience against communication outages, considerations for fallback strategies are given as well. The heuristic algorithms for curative CM described in Chapter 3 can be implemented in a variety of ways. While centralized implementations, for example within the SCADA tools of a CC, are a tried and proven method, one major disadvantage of such systems is their single-point-of-failure. Especially for a system that is supposed to react ad-hoc in a post-fault state, this poses a significant risk for safe grid operation. Decentralized or distributed control systems do not carry this vulnerability and can offer additional advantages as well. Since the meaning of the terms *centralized*, *decentralized*, and *distributed* vary by topic, context, and author, in this work their meaning is taken as defined in [73] and depicted in Fig. 5.1. In a centralized control system, all involved subsystems are controlled by a single controller (e.g. SCADA tools in CCs). Decentralized control is established by having a local controller for each subsystem operating without exchanging information with other controllers (e.g. tap regulators in on-load tap-changing transformers). When every subsystem is controlled by a local controller but these devices communicate with each other, this is considered distributed control (e.g. MAS). Since an automated CM system operates in overall high line loading situations, distributed control is preferable over decentralized control, as the communication between controllers enables avoiding accidental creation of additional overloads in lines not directly monitored by the executing controller.

A MAS as a specific form of a distributed control system can also improve system efficiency due to its ability to perform parallel computations and operate asynchronously. Another advantage is that agent-based systems scale well, for example if the grid topology changes, parts of the grid experiences a blackout, or simply if the control system is to be applied in different grids. [74] Additionally, MAS provide benefits as solutions for grid operation due to their inherent *flexibility* in selecting actions from a pool of possibilities, *robustness* by redundancy achieved through multiple agents, and *extensibility* due to the possibility of adding or subtracting agents from the system, even during live operation. [75] Finally, [76] showed that MAS outperform centralized approaches for problems that

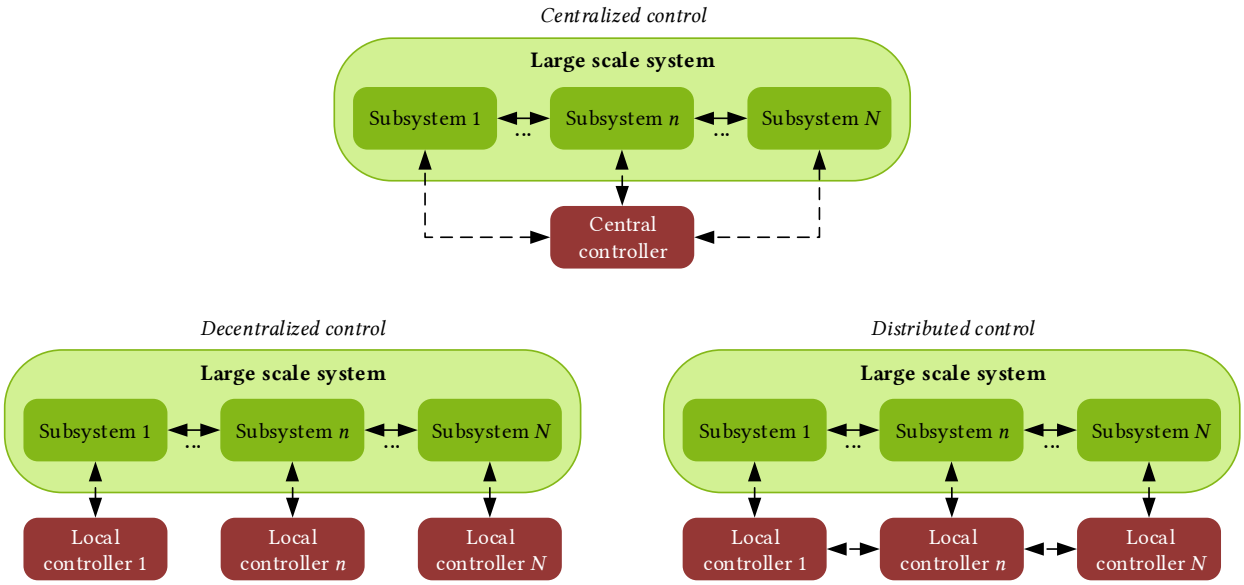

Figure 5.1: Different control system topologies (based on [73])

are of high urgency (e.g. imminent overloads) and of medium to large scale (e.g. transmission or sub-transmission grids). Hence, the implementation of the automated CM algorithms as a MAS is sensible.

5.1 Fundamentals of multi-agent systems

Although details in definitions differ, consensus in the literature appears to be that an agent is a software instance that can sense and interact with its environment autonomously in pursuit of a certain goal. A MAS is a system consisting of two or more agents that may communicate and cooperate with each other while following their respective individual goals. From this interaction an overall MAS behavior emerges, whose overall goal is not explicitly defined but stems from the individual goals of all agents. Furthermore, *intelligent* agents display reactivity towards external events, pro-activeness in changing their behavior to reach their goals, and the ability to socially interact with other agents to negotiate actions and cooperate. These definitions and design recommendations for agent modelling in power systems can be found in [75]. More general definitions and agent frameworks can be found in the Foundation for Intelligent Physical Agents (FIPA) standards.

To clarify the scope of the system developed in the following chapters, a distinction needs to be made between agent-based simulations and agent-based control systems (which are in the focus of this dissertation). While the former strive to replicate real-life phenom-

ena as MAS, such as human group behavior (cp. [OP6]), the latter are targeted at implementing distributed control over certain parts of a real world environment. Besides this applicational difference between the two, a more practical, significant distinction is that agent-based simulations usually adhere to a centralized clock, ensuring all agents perform their individual tasks within one simulation time step, resulting in synchronized behavior. Agent-based control systems on the other hand may have their agents follow individual clocks and execute their tasks asynchronously, making a central coordinating instance obsolete, thus fully decentralizing the MAS.

In power systems, an agent of an agent-based control system usually is – or is installed on – some kind of controller, the environment can be (parts of) an energy grid and possibly a communication grid that can be sensed by the agent via measurement devices and sensors, and the agent can interact with this environment through actuators or switches.

5.2 Preceding works on agent-based grid operation

The MAS developed in this work is based on multiple preceding research projects carried out at ie^3. The following sections give a brief overview over these works and a description of the remaining research gap.

5.2.1 Preceding works

Based on [77] the first concepts for a PFC MAS were presented in [78], followed by [79] and [80], showing first simulation results. The MAS shown in these publications consists of monitoring agents installed at each passive grid device (i.e. one agent per bus, line and transformer) and controlling agents installed at each PFC device. A distributed algorithm is introduced to share information about the grid state between agents and to activate a variety of PFC devices to lower congestions. Each controlling agent determines the most critical power line and appropriate PFC devices with a weighting function taking into account line loading and the respective device sensitivity. This way, a distributed control loop is created allowing agents to share measurements, determine imminent overloads, and increment or decrement PFC device taps. The system was enhanced in [81] to adapt step sizes according to the severity of an overload and utilize HVDC links besides PFC devices to alleviate overloads. Incrementing or decrementing set points in a stepwise manner can be a significant disadvantage if measurements are only available at a low rate or if the agent calculations and PFC activation take longer than expected – both of

which can be real-life phenomena. However, it may not be necessary to perform stepwise changes if the final set point needed to alleviate the overload could be calculated from the start. This was not possible in the previously mentioned works, since the sensitivity calculation only indicated the direction – but not the magnitude – of power flow changes caused by a PFC device's tap change. An example for a case in which the final set point is determined iteratively although it could be calculated directly, is given in [69]. There, the system was enhanced to add the usage of redispatch as a last resort if PFC actions could not completely alleviate an overload. The sensitivities needed for redispatch considerations, i.e. for nodal power changes, are PTDFs, which are explained in Subsection 3.1.1. Thus, the stepwise process of sensitivity calculation and incremental set point change can be exchanged for an immediate calculation of the final necessary set point and its immediate activation. Instead of a completely decentralized activation of measures, for the redispatch measure a *Contract Net Protocol* (cp. [82]) is implemented: One agent acts as the initiator, sending a Call For Proposals (CFP) to all other agents, who in turn answer with proposals for generation redispatch before the initiator selects the most appropriate proposals and orders their activation.

Lastly, there have been some additional research endeavors with the MAS that are branching off into different directions but that shall still be mentioned here. The basic agent algorithm was extended in [83] to perform voltage stability control. Alongside these developments, agent communication traffic management has been improved in [84] and [85] through software-defined networking.

The works cited in this subsection so far all stemmed from ie^3 and thus directly or indirectly preceded or influenced the MAS developed in this dissertation. Naturally, ie^3 is not the only research institute concerned with agent-based PFC. While agent-based control is a common topic in micro-grid research papers (cp. [86]), such distributed control algorithms in HV grids and especially for CM are less common. In [87], an approach similar to the undertakings at ie^3 was taken, with an agent-based control system implemented in Java Agent DEvelopment Framework (JADE) offering system services such as voltage control, CM and grid restoration. The concept of distributed intelligent substations developed in this work was also taken into laboratory tests in [46]. Another grid operation MAS that was tested in a laboratory environment is explained in [88]. Here, the agents prevent cascading failures in HV grids by controlling generator dispatch. While parts of the grid are implemented on laboratory-scale hardware, the agents themselves are not implemented on dedicated computing units but on a central simulation instance. Lastly, the [89] describes a MAS performing corrective security constrained optimal power flow

to determine optimal generator dispatch and curative CM utilizing D-FACTS. While the general idea is similar to that of the dissertation at hand, [89] does not put a focus on real-time applicability or robustness as the tests are carried out in pure software simulations and the algorithms rely on optimizations whose convergence depends on the given input data.

5.2.2 Research gap

While these publications have demonstrated the system's functionality and improved and adapted the MAS for various scenarios, there are several research gaps regarding its application in real-time and subsequently in a real grid.

Firstly, the installation of one agent per every single grid device is unpractical and may introduce unnecessary costs, especially if every agent is supposed to run on dedicated hardware. Instead, one agent per substation suffices, since every grid device is connected to at least one substation, and measurements as well as control communication paths to PFC devices are available there anyways.

Secondly, the PFC devices the MAS has been tested with so far, were either experimental (e.g. distributed power flow controller), slow in their tap changes (e.g. PST), or too costly and therefore not widely available in real grids (e.g. FACTS and HVDC terminals). To add to this, the MAS can either make use of PFC devices that are already installed in the grid or new devices would have to be installed along with the agents. The positioning of existing devices was done under the premise of preventive CM considerations and thus an optimal leveraging of their capabilities by the agents cannot be guaranteed, and installing new devices for the curative premise may be costly. With the advent of D-FACTS there are new PFC devices available today, whose modularity, affordability, ease of (re-)installation and activation speed could potentially synergize well with the agent algorithm. In the project IDEAL the type of device used is the DSR. The communication infrastructure of these devices does not allow for reception of fast subsequent control messages; after a control command has been received, there is a 10 s deadband during which any newly arriving control messages are discarded. Thus, DSRs cannot be integrated into the existing agent algorithm based on stepwise changes of PFC device set points.

Another aspect that has been disregarded so far, is the question of how such a MAS can be integrated into a CC environment. During operational planning and live operation, a CC operator needs tools that allow them to predict the behavior of the MAS in specific situations (e.g. contingencies accounted for in (n-1) calculations). This is especially prob-

lematic for the stepwise distributed activation algorithms since they are path-dependent: the decision on a PFC device set point change depends on all set point changes undertaken before and the grid state change since the last change. Thus, the outcome of the stepwise reaction of the MAS to a specific overload cannot be precisely predicted.

Furthermore regarding CC integration, all of the cited developments build on the premise that each control loop can be carried out within at least 30 ms, so PFC device set points can be changed stepwise and effects on line utilizations can be observed before deciding the next set point change. If the MAS is used to mitigate the effects of high-impact low-probabilty events, such a fast reaction time is useful and wanted. If it is used however to increase grid utilization within normal grid operation, the integration into the CC has to be considered. The CC operator will usually receive an updated grid state estimation only once per minute [90]. If the agents start changing set points in the meantime, this makes agent behavior even more unpredictable for the CC and can lead to disadvantageous interferences between agent and operator interventions. There are many other examples for automated control systems operating faster than CC grid state updates, and in the far future, an automated curative CM system may also operate in this way. However, the aim of this dissertation is to bridge the gap between ideal functionality and real world application with CC integration, so some trade-offs between functionality and applicability have to be considered in favor of the latter.

Finally, so far the MAS was only tested in a simulation based on discrete time steps, meaning agents share measurements, analyze the grid state and change set points before the next simulation time step is executed. Since in real-time applications, the grid does not wait for the agents to finish their calculations, additional discrepancies between agent and grid behavior may occur. Hence, the MAS should be tested within a real-time environment.

To sum up the research gap, a look at the Technology Readiness Level (TRL) of the MAS developed at ie^3 is insightful. While the MAS has been applied to a variety of use cases in different scenarios, it has never left the simulation stage. With this, proof of concept has been delivered for several applications, but a laboratory or field test validation has not been done yet. According to the most common definitions of TRLs (cp, [91, 92, 93]), this places the MAS at a TRL of only 3. Since these definitions were originally aimed at more hardware-related technologies rather than software – which the MAS arguably is closer to – it could be more appropriate to apply a more software-related definition of TRLs, such as defined in [94]. Based on this scale, the TRL of the MAS can be placed at 3 or 4. Thus, the current research gap consists of integrating reliable software components implemented

on systems close to actual operational environment in a high-fidelity laboratory setup to increase the TRL to 5, including integration with actual external entities to reach TRL 6.

5.3 Algorithm overview

The MAS described in this chapter was developed alongside the IDEAL project and a first concept has been presented in [OP1]. An overview is given in Fig. 5.2. The image is structured into two columns, depicting the hard- and the software perspective, and three rows which show the implementations within (sub-)transmission and distribution grids as well as the CC. Sub-transmission grids are explicitly mentioned since the IDEAL project revolved around German 110 kV grids. The core of the MAS is implemented within the HV grid level, where every substation is equipped with one agent that can be installed on a Remote Terminal Unit (RTU).

Additional RTUs may be installed in the lower voltage levels to take care of flexibility aggregation and serve as an interface between agents and FPU-control. This way, there remains a clear separation between TSO and DSO operations. The bottom right-hand side shows how the lower level RTUs analyze the aggregated flexible power that can be exchanged with the upstream grid considering all FPUs in the monitored distribution grid. This flexibility potential can be depicted in a PQ-diagram as an area of possibly achievable setpoints. An aggregation method for this is described in [OP7] and [11]. Since the MAS only considers active power, the lower level RTUs transmit to them only the maximum and minimum P-values achievable without changing the current Q-setpoint. When an agent orders the changing of active power exchange with a distribution grid through the activation of aggregated flexible power, the lower level RTU takes care of the exact unit dispatch necessary to achieve this setpoint. Supervision and control software is installed at the TSO CC level to monitor the MAS and intervene in emergency situations.

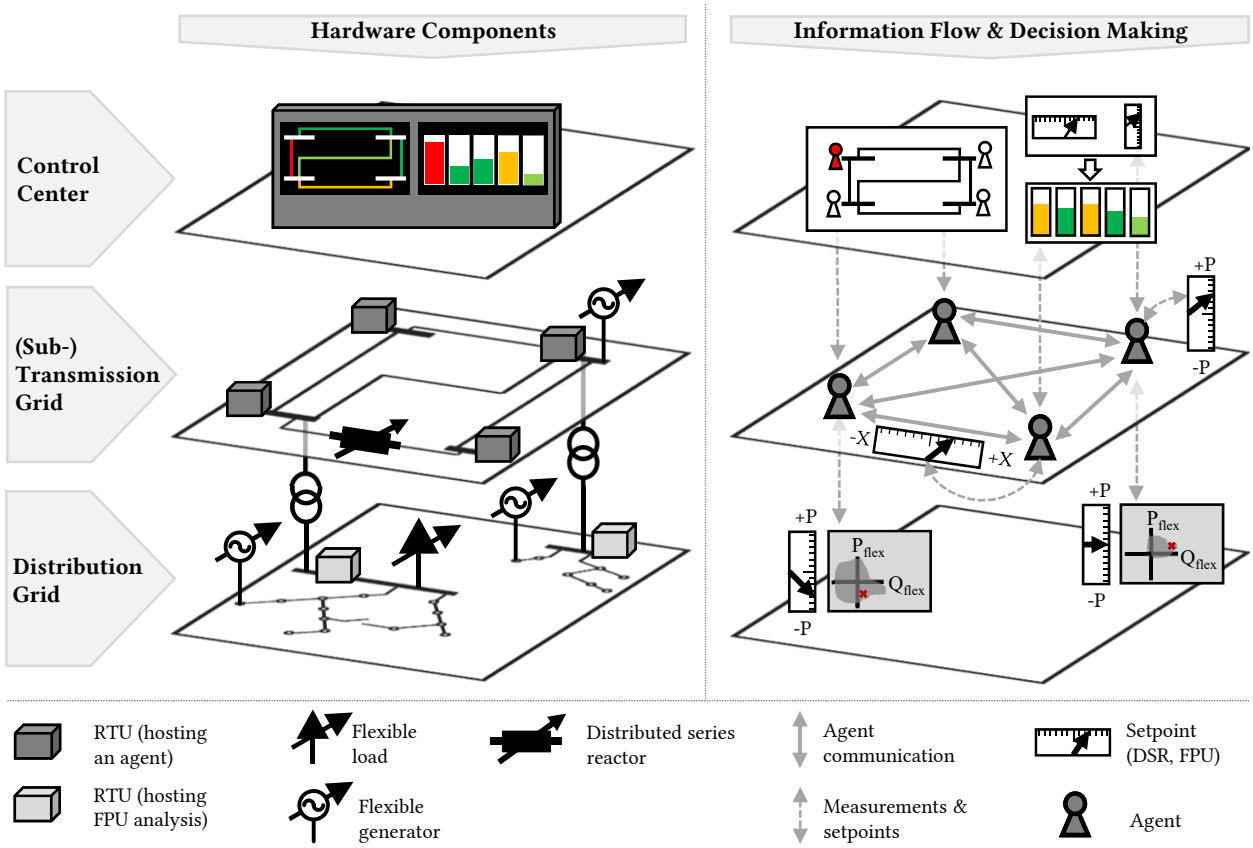

Figure 5.2: Overview of the MAS in a (sub-)transmission grid with CC-supervision and supporting systems for flexibility analysis and control in lower voltage levels

With the requirements explained in Section 5.1 the agent-based algorithm is defined as a Finite State Machine (FSM) as shown in Fig. 5.3. Note that this is not the algorithm for the overall MAS but for a single agent. Each agent goes through the described states and executes the respective functions. The interaction and communication between the agents, and thus the overall MAS behavior then arises as the sum of all single agent behaviors. Note also that a real-time implementation of a MAS works asynchronous as there is no central instance coordinating agent calculations and state changes; agents may switch states at different rates than others.

In any of the four FSM-states an agent loops through five main functions, as shown in Fig. 5.4. It reads new messages, retrieves local measurements from its substation, updates its internal grid state with received foreign and retrieved local measurements, broadcasts a State Inform Message (SIM) to all other agents, and then finally goes into the state-specific functions. The two gray boxes *Read messages* and *Execute FSM state* contain somewhat more complex sub-functions which are explained in the flow charts in Fig. 5.5–5.9.

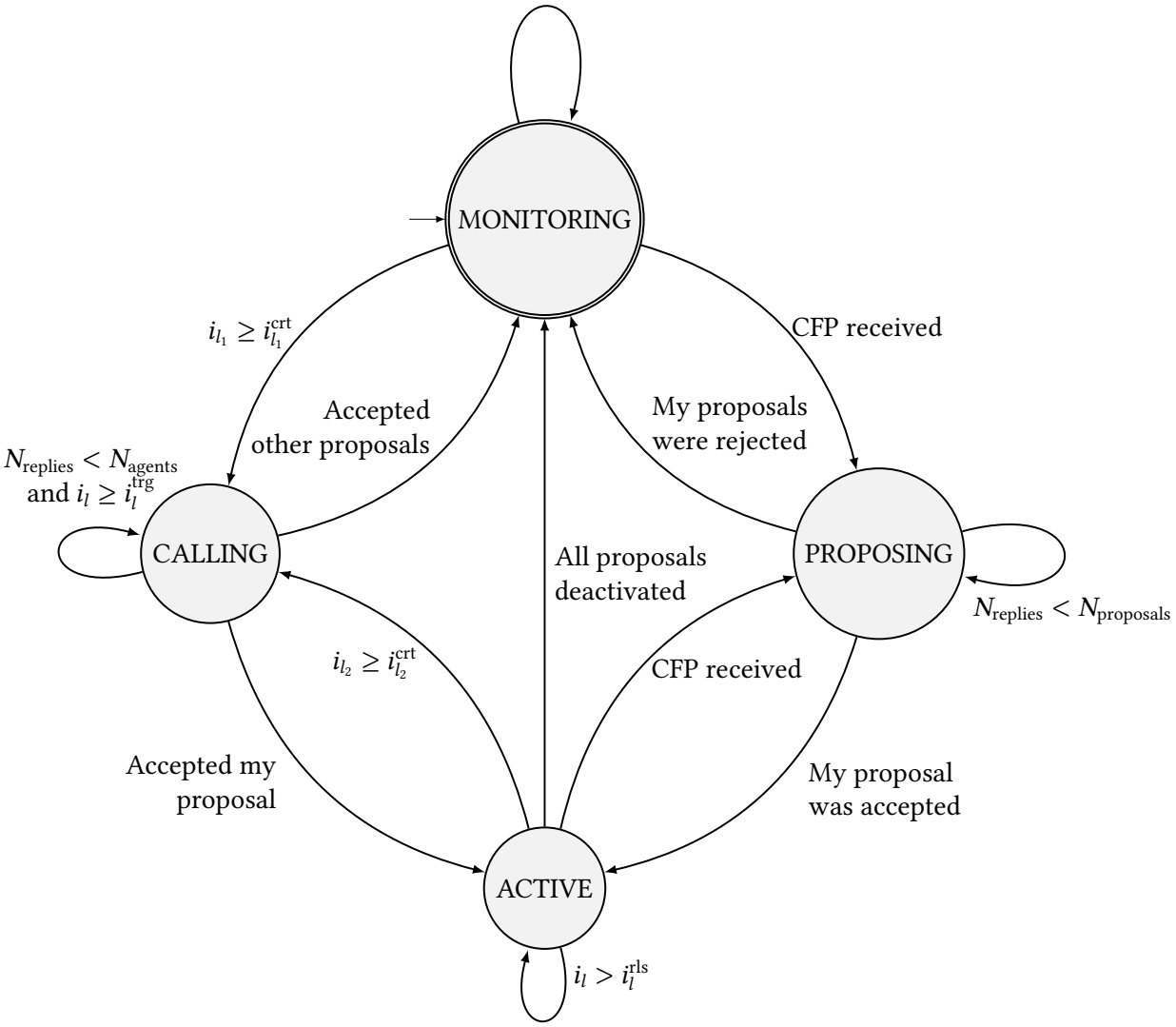

Figure 5.3: Overview of the agent-based control algorithm (of one single agent)

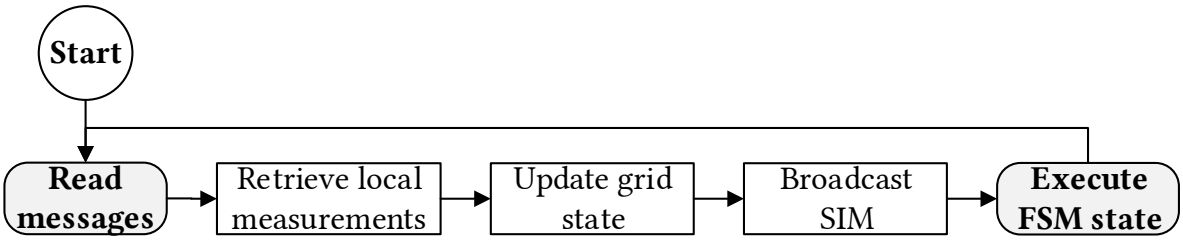

Figure 5.4: An agent's basic loop in every FSM-state

5.3.1 Agent communication

To establish communication within the proposed MAS, seven different types of messages are needed, which are based on the Agent Communication Language specifications defined by FIPA [95]. These messages contain different information and are handled differently, depending on their type, or performative, as shown in Table 5.1. While SIMs are sent every loop, the other message types are only sent if a specific trigger event occurs. In turn, SIMs are the only messages handled immediately upon reading. This ensures FSM-states are changed based on a pre-defined importance logic and not first-come-first-serve. The receiver stores incoming CFPs or proposals to be handled once it enters the respective state. The status of a proposal is updated when a proposal reply (Accept, Reject, Done, Refuse) is received, but proposal handling is done within the respective FSM-state.

Table 5.1: Message types used by the agents

Type	Content	Sending trigger	Receiver action
SIM	Collected measurements	Every loop	Update grid state
CFP	ID and loading value of congested line	Sender detected local congestion	Store CFP to be handled in PROPOSING state
Propose	For each proposed measure: ID, sensitivities, technically possible setpoint range	Sender received a CFP	Store proposal information to be handled once receiver enters CALLING state
Accept	ID and requested setpoint change of accepted measure	Sender selected receiver's proposal	Mark receiver's proposal as accepted by sender
Reject	ID of rejected measure	Sender rejected receiver's proposal	Mark receiver's proposal as rejected
Refuse	ID of failed measure	Sender failed to activate a proposal accepted by receiver	Mark sender's proposal as failed to exclude it from further selections
Done	ID of executed measure	Sender successfully activated accepted proposal	Mark sender's proposal as activated

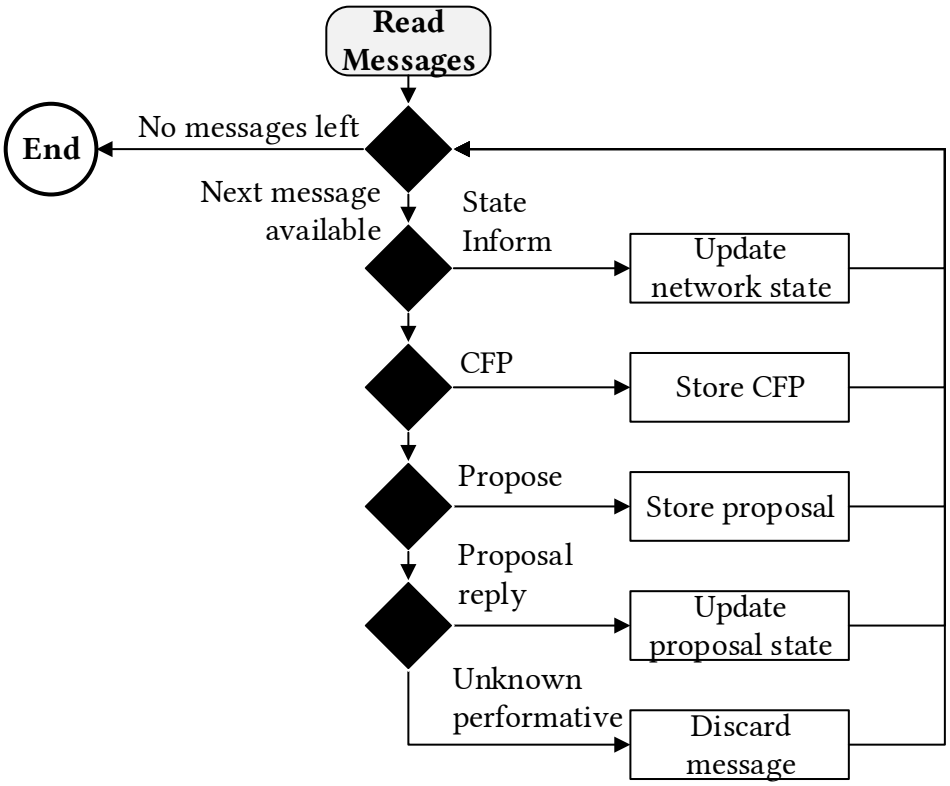

Figure 5.5: An agent's sub-algorithm to read messages

To execute the necessary calculations, each agent needs information about the electrical grid and its fellow agents, some static and some variable over time. For each grid device every agent needs to know the device's internal ID, the device type, and which agent is responsible for this device. Additionally, there is device type-specific topological and electrical information that every agent must know. First of all, the nominal bus voltages must be known. For lines and transformers, the rated currents must be known, as well as the IDs of their start and end buses. Then, the maximum and minimum active power of each FPU must be known, as well as their connecting buses. Finally, the maximum and minimum reactance changes as well as the respective step size and location (i.e. connected line) of the DSRs must be known. This information must be equal for all agents and cannot change during live operation unless there are communication outages and the MAS executes fallback strategies (see Section 5.4).

Furthermore, the agents need several RMS measurements of the different device types which are included in the SIMs. To determine whether a line (or transformer) is overloaded, agents need to know the current going into the line. Since the agents' calculations are power-flow-based, the agents need to know momentary bus voltages to determine the

momentary rated power of each line corresponding to its rated current. More precisely, the agents only perform DC power flow calculations. Thus, to respect that their actions will only influence branch utilizations through active power changes, measured active and reactive power flows through all lines and transformers are required. As for the controllable devices, agents need to know how far the devices' respective set points can be changed. Accordingly, the DSRs must communicate their momentary injected reactance and active and reactive power of flexible loads and generators need to be available. All of this is stored in the agent database, shown in Table 8.7 in the appendix.

5.3.2 Monitoring state

The MONITORING state is an agent's initial and idle state. Here, the agent only checks for newly found congestions, as shown in Fig. 5.6. If the agent received a CFP during the last message reading, it switches into PROPOSING state to offer RMs to the calling agent. If no CFPs have been received, the agent checks for congestions in lines monitored by itself. If it finds a local congestion, it broadcasts a CFP to all other agents and switches into CALLING state. Note that the answering of received CFPs is handled at a higher priority than starting new CFPs for local congestions. This is done deliberately, to ensure already started CFPs are taken care of first, before new ones are initiated. If no congestions were detected by any agents, the agent remains in MONITORING state.

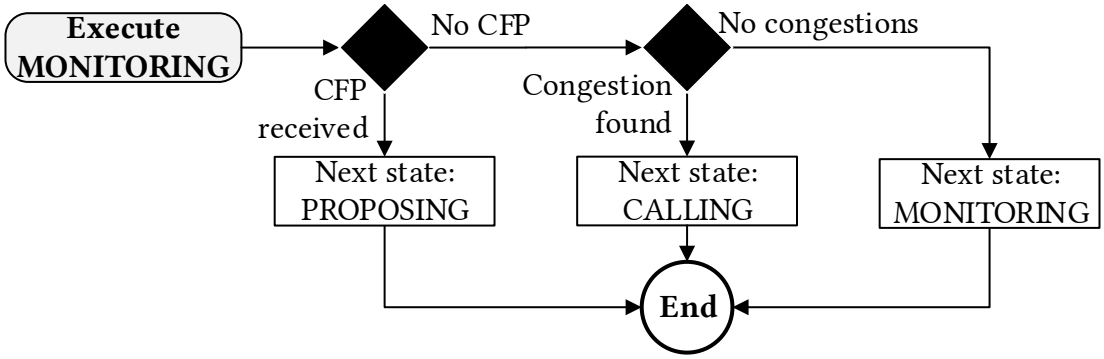

Figure 5.6: MONITORING state

5.3.3 Calling state

If an agent detects a local congestion during MONITORING state, it switches into CALLING state to initialize and handle the coordination of RMs, as depictured in Fig. 5.7.

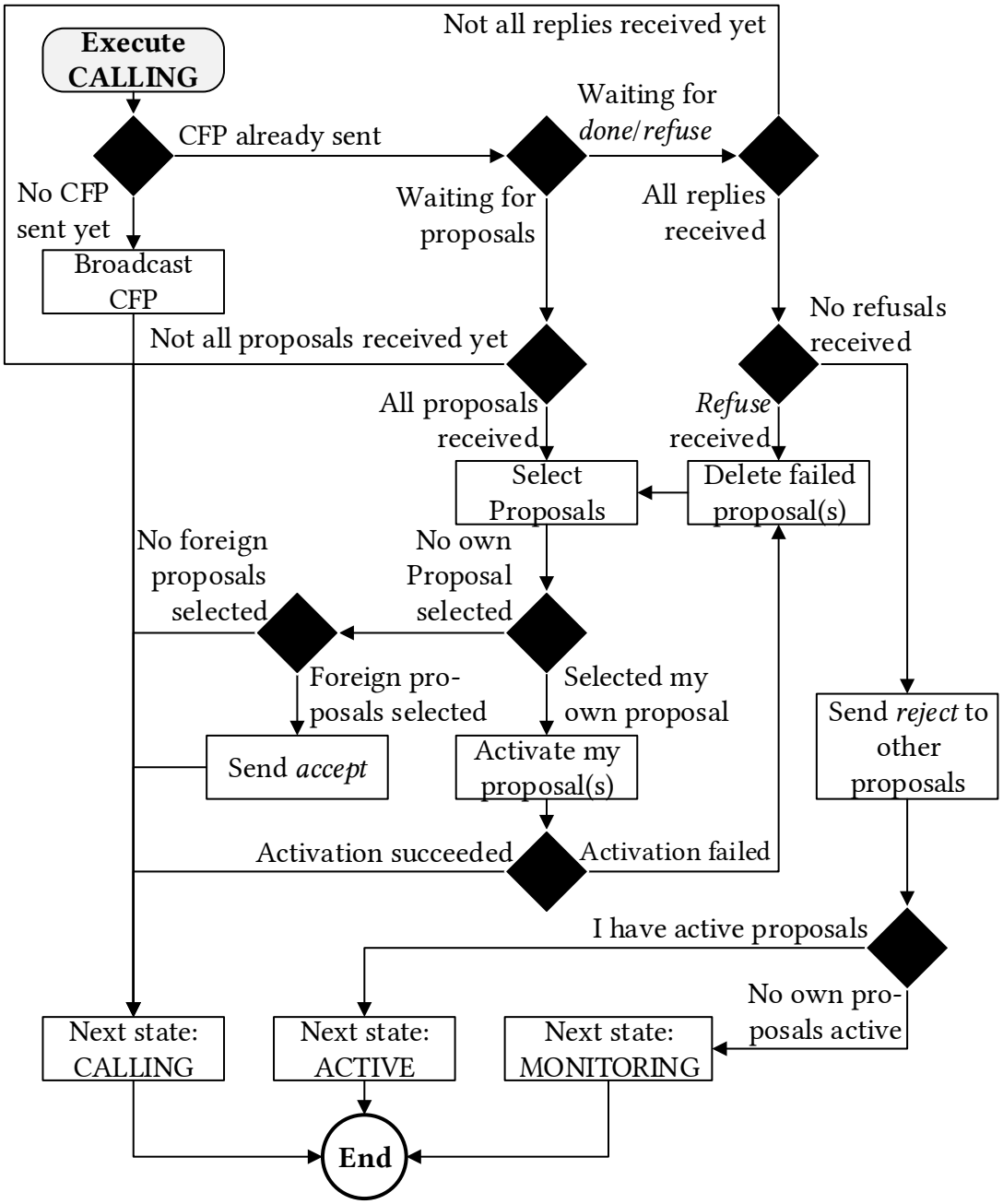

Figure 5.7: CFP state

Upon first entering the state after a congestion was detected, the agent broadcasts a CFP and then stays in CALLING state to wait for proposals. Once the agent has received proposals from all agents, it selects the most appropriate combination thereof to reduce the congestion. To avoid getting stuck in a loop if an agent fails to reply, an additional timer can be set after which the selection starts. The selection is done as described in Section 3.2.2, except the sensitivities are not calculated by the calling agent, but by each proposing agent for their respective proposals. This parallelizes the necessary computational effort, especially regarding DSR-measures, since one matrix-pseudo-inversion has to be done for each DSR. The selected proposals are either activated by the calling agent or ordered to be activated by other agents through *accept* messages. If the agent failed to activate its own proposal, it deletes this measure from the list and starts over with the selection. Otherwise it waits for replies regarding the accepted foreign proposals. Once all needed replies have been received, the calling agent checks for refusals (i.e. failed measure activation attempts). If any refusals were received, the calling agents deletes the respective proposals from its list and starts over with the selection. Otherwise it concludes that the congestion has been handled and sends *reject* messages to all remaining agents still waiting for proposal replies. The agent finally exits the CALLING state either into ACTIVE state if it has activated proposals of its own, or into MONITORING state if it does not.

5.3.4 Proposing state

If a monitoring agent receives a CFP, it switches into PROPOSING state shown in Fig. 5.8. First, the agent calculates all lines' sensitivities towards each of its RMs and determines their technically feasible setpoint ranges. After proposing this information to the calling agent, the agent remains in PROPOSING state to wait for decisions. An *accept* triggers the agent to activate the demanded setpoint change and reply with *done* if activation was successful or *refuse* if not. A *reject* causes the agent to delete this proposal. The agent remains in PROPOSING state until it has received a decision on all of its proposals. Afterwards it leaves either for ACTIVE state if it has activated RMs to manage, or MONITORING if not.

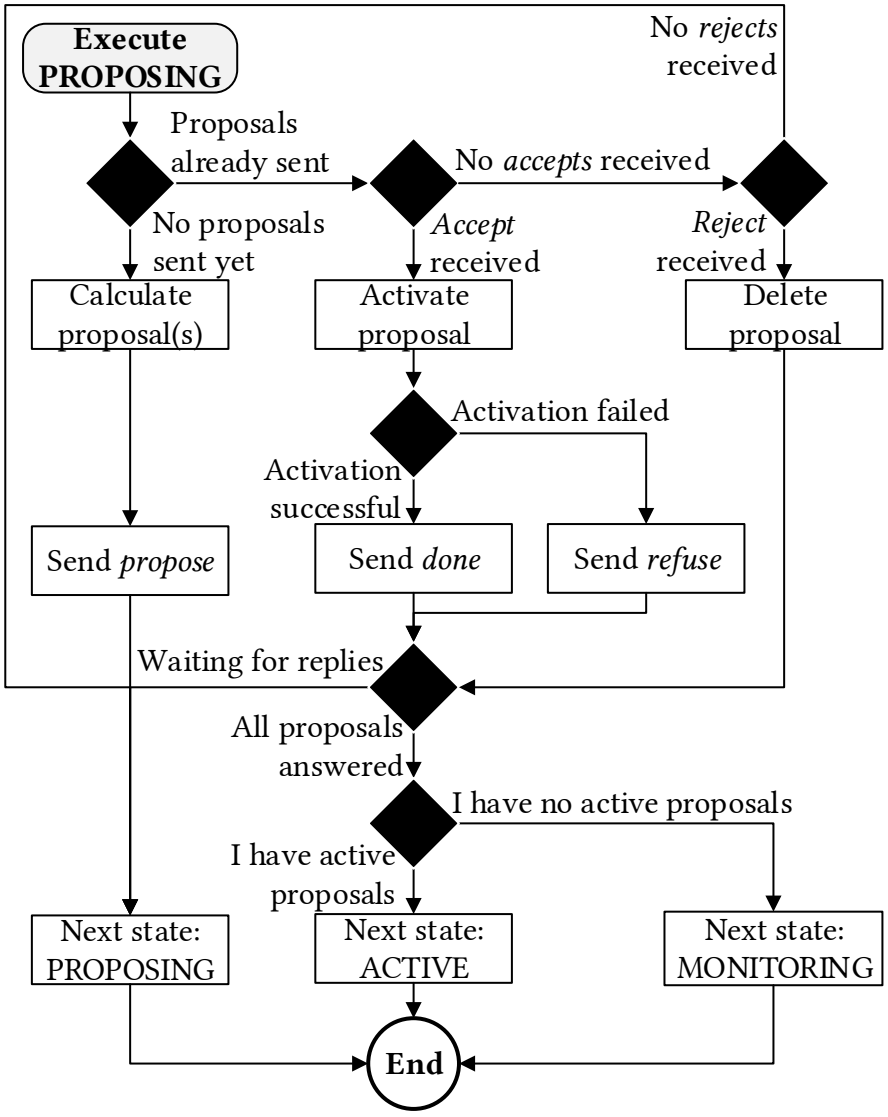

Figure 5.8: PROPOSING state

5.3.5 Active state

An agent goes into ACTIVE state (cp. Fig. 5.9) when it activated RMs, either for a CFP initiated by itself or called for by another agent. The main function during this state is for the agent to determine whether the congestion has been lowered so far that previously activated measures can be taken out again. It is also important to keep the basic functionality of the MONITORING state within this state, so the agent can switch into CALLING or PROPOSING state in case new congestions occur. If there are no additional congestions, the agent checks whether the current of any of the lines it has activated measures for has decreased below its release threshold i^{rls}. If so, the agent calculates how far it can

deactivate its activated proposals without causing the current of the previously congested line to breach the release threshold or causing new congestions. For this, the agent uses the algorithms described in Section 3.2.2 – but starting with the measures with the lowest sensitivity, opposite tapping directions, and with the goal of fully deactivating all measures. As long as the agent cannot deactivate all of its previously activated measures, it cannot go back into MONITORING state.

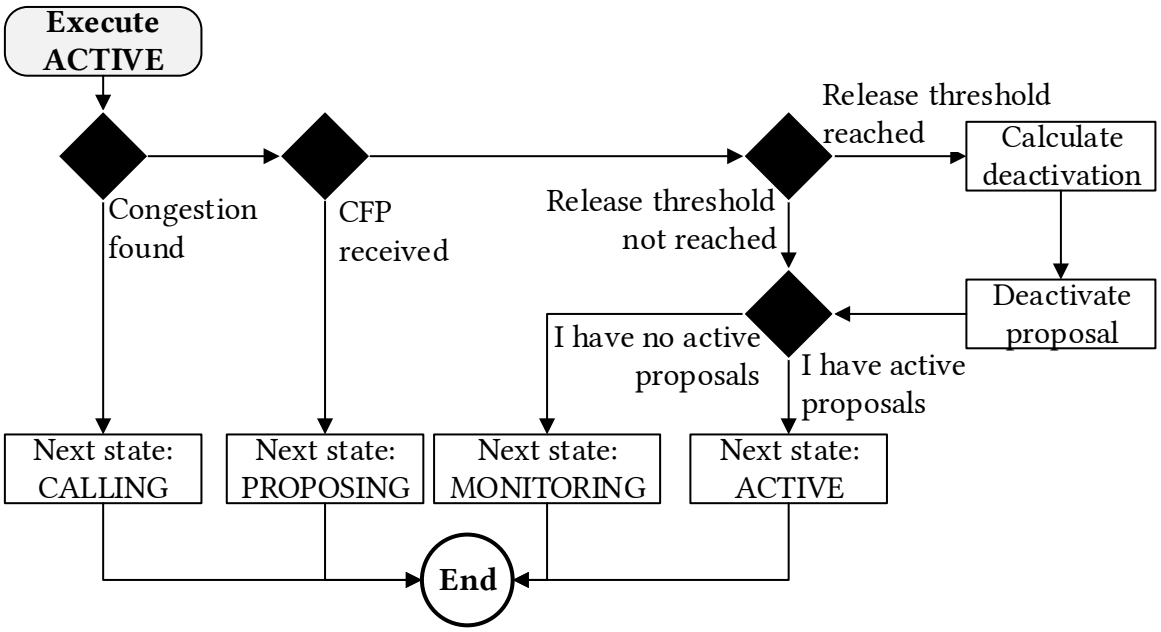

Figure 5.9: ACTIVE state

5.4 Fallback strategies

The individual autonomy of each agent makes the MAS robust against failures of single devices; the agents *can* work together, but they do not *have to*. With the algorithm described in Section 5.3, the MAS already covers outages of proposing agents, as long as the other agents can still offer sufficient proposals to alleviate the congestion. Additionally, since every series element can be monitored by two agents, the system is potentially inherently redundant against single outages. To leverage this, a simple rule can be implemented that shifts responsibility for monitoring a specific line from its start-node agent to its end-node agent, if the first one fails.

However, several questions remain regarding the robustness in case of larger scale communication outages:

1. How should an agent behave when it notices that it has lost communication to the rest of the MAS?
2. How can the MAS ensure safe automated grid operation when no measurements for one or more lines are available anymore due to outage of multiple agents?

To answer these questions, emergency *fallback strategies* can be implemented, that are activated once a communication failure of one or more agents has been detected. In order to react quickly to communication outages of one or more agents, heuristic algorithms can be implemented that mitigate negative effects on system functionality. In a worst case scenario, two or more agents in geographic vicinity of each other fail simultaneously, causing one or multiple lines to be unobservable to the MAS. To maintain overall functionality, two strategies have to be implemented. First, the agents whose communication links are still up and running have to determine which devices have become unobservable and assign them to the responsibility of an agent that is still functioning. This agent must then approximate developments of power flows within the unobservable island and take over initialization of CFPs for potentially congested lines within the island. Secondly, agents whose communication has failed must keep all measure setpoints unchanged and cease to call for or send out proposals. This ensures power flow developments stay as predictable as possible for the rest of the MAS.

5.4.1 Detection of communication outages

Since the agents act and communicate asynchronously, determining whether an agent is only performing calculations for a longer period than usual or is actually not responding anymore due to communication failure, is not a trivial task. A simple solution for this is to use the frequently sent SIMs as *keepalive*-messages, confirming that the sender is still alive. If an agent has not received a SIM from one agent for a pre-defined amount of time, the receiver has to assume that either the sender or itself is irresponsive. To determine in a simple manner which one is true, the agent can check whether it has received SIMs from other agents, in which case it assumes the agent with the missing SIM is the one that has gone offline. If the agent notices it has not received SIMs from any other agents for a significant amount of time, it has to assume that it itself has lost communication connection to the rest of the collective. The time frame during which a SIM is expected to arrive can be set to a small multiple of the expected maximum state execution time, to

account for ongoing agent calculations as well as a small amount of failed communication attempts. Other methods to determine which agents have gone offline, that may be more complex but possibly more robust and reliable, could be implemented as well, but are out of scope for this work.

5.4.2 Determining unobservable islands and responsibility transfer

Once an agent has detected to be offline, the agents that are still alive need to determine which parts of the grid have become unobservable to them and which agents need to take over responsibility for the respectively unobservable devices. For this, unobservable islands made up of offline agents have to be evaluated: if there is an electrical connection between two offline agents with no substations with an online agent in between them, they belong to the same unobservable island. The online agents located at substations that have a direct connection to an offline agent's substation with no other online agents in between are considered border-agents. If a border agent detects that it is bordering on an unobservable island, it takes over responsibility for the series elements within the island and announces this to the rest of the MAS. The border agent then includes approximations of unobservable line power flows in its SIMs and the other agents treat them as if they were regular measurement values. An example for a grid with two unobservable islands and their respective border agents is given in Fig. 5.10, with approximated power flows indicated by a chevron. The unobservable island on the right hand side of this figure also aptly depicts the system's resilience by redundancy against single agent failures, since all lines affected by the outage of the agent at bus 7 are still observable without any approximations necessary.

To ensure exactly one agent is responsible for every device in the grid, every agent maintains a list of agent-device responsibilities. When an agent receives a SIM, it notes the timestamp of the message and updates the responsibility-list: if the responsibility-timestamp for one device is more recent than the last one noted in the list, the responsibility changes to the more recent one. This way, if multiple border agents could take over for an unobservable island, there is consensus among them over which one of them shall be responsible. This functionality can be easily included in the agent's basic algorithm between *Update grid state* and *Broadcast SIM* (cp. Fig. 5.4).

An agent that notices it has lost communication connection to the rest of the MAS assumes that other agents are still online and will take over its monitoring responsibilities. The

offline agent will only retrieve local measurements, update its internal grid state and try to broadcast SIMs. This can be modeled as an additional FSM state *OFFLINE* that can be entered from any other state when a disconnection from the collective is noticed, and is only exited to the MONITORING state once a reconnection has been observed. The only state-specific function executed in this state is checking the connection to the rest of the MAS, indicated by received SIMs.

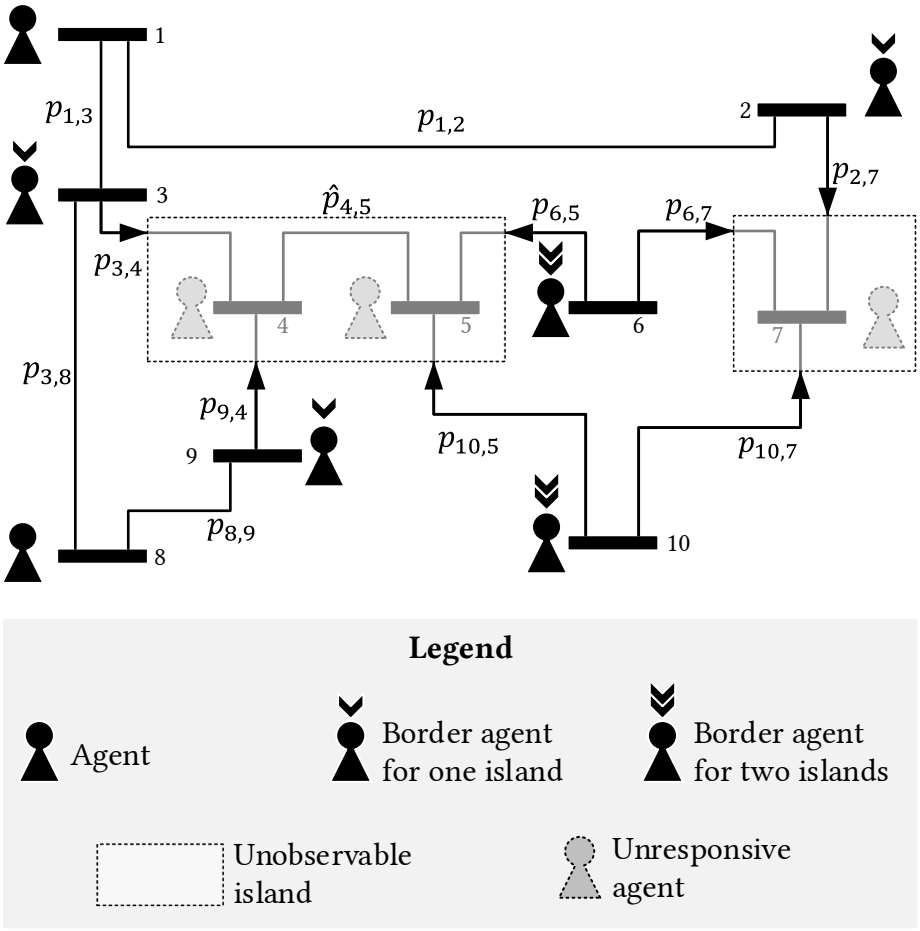

Figure 5.10: Example for two unobservable islands within a grid

5.4.3 Approximating measurements in unobservable islands

There are numerous ways to approximate measurements within an unobservable part of a grid, such as state estimation or methods relying on forecasts. Here, a simple method

is used. The border agent responsible for the unobservable island saves the last measurements it received for the unobservable grid devices, such as active power flow $p_{l^*}^{\text{init}}$ of an unobservable line l^*. Then, it determines the susceptance matrix for only the islanded part of the grid to calculate the PTDFs $\gamma_{l,n}^{\Delta\text{P,island}}$ for this isolated grid. Assuming none of the loads and generators within the unobservable grid have changed their output, the border agent treats the differences of power flows going into the unobservable grid as nodal power changes at the unobservable border nodes. Then this agent can use the PTDFs of the unobservable nodes $n_{l,\text{unobsv}}$ of the border lines $\mathcal{L}_{\text{border}}$ to calculate how these external influxes change the power flows within the unobservable grid to yield the approximated power flow $\hat{p}_{l^*}$ as shown in eq. (5.1).

$$\hat{p}_{l^*} = p_{l^*}^{\text{init}} + \sum_{l}^{L_n^{\text{border}}} \gamma_{l^*,n_{l,\text{unobsv}}}^{\Delta\text{P,island}} \cdot \left(p_l - p_l^{\text{init}}\right), \quad \text{with } l \in \mathcal{L}_{\text{border}} \tag{5.1}$$

Keeping this approximation as adequate as possible is the main reason why unobservable agents should not change any setpoints of their controllable FPUs or DSRs.

5.4.4 Simulative validation of fallback strategies

To demonstrate the functionality of the derived fallback strategies, the MAS is implemented and tested in communication outage simulation scenarios. Exemplary results are shown in this section.

5.4.4.1 Implementation in Java / JADE

The MAS mentioned in Section 5.2 have all been implemented in Java within the JADE framework [96]. This framework allows for the centralized implementation of MAS based on FIPA-standards. In this context, *centralized* means that all agents are implemented and executed on the same computer, and there is a coordinating agent ensuring synchronized behavior across all agents in deterministic time steps. The agent simulation is coupled via an OPC server to a quasi-dynamic PowerFactory grid simulation that runs synchronously to the agent simulation. This means, that within one time step, PowerFactory performs a power flow calculation, sends the resulting measurements to the OPC server, from which the agents read measurements, execute a single loop through their FSM behavior, and enter any grid operational commands into the OPC server, which are then read by PowerFactory before executing the next time step. Throughout this, the coordinating agent

manages agent communication and ensures the next time step does not start before all agents have finished their FSM behavior.

This implementation comes with the advantage of supporting grids with a large number of buses and agents, enabling scaling tests and evaluation of algorithm functionality under ideal communication conditions. The disadvantage therein is the disregard of real communication paths and the requirement of a coordinating agent, which would, in a real world implementation, give the MAS a possible single point of failure and prevent asynchronous behavior execution.

Thus, a JADE implementation of a MAS is not the appropriate platform to test real-time behavior of agents implemented on several different machines under realistic communication conditions. It is however adequate for testing the fallback solutions described in Section 5.4 because these only make sense within a system supporting a significant amount of agents distributed throughout a large grid – which is difficult to provide in a real-time environment due to the large calculation effort for such grids. The JADE-based MAS used in this work extends the preceding agent algorithm implementations by a fallback solution. Since only the fallback is tested, the usage of DSRs is not included, and the agents use PSTs instead since these were already installed in the grid model used. The line loading thresholds at which the agents start activating RMs are selected as follows for the fallback tests: $c_{\mathrm{crt}} = 1.0$, $c_{\mathrm{trg}} = 1.0$, and $c_{\mathrm{rls}} = 0.9$.

5.4.4.2 Simulation test cases and results

The overall MAS functionality can be disturbed to different extents by agent communication outages, depending on the involvement of the failing agents in an upcoming congestion scenario. The outage of agents that only provide tangential information to the overall grid state but do not monitor or control significant grid equipment may have less of an effect than the outage of an agent that monitors a congested line and is in charge of controlling significant RMs. To cover a significant span of agent outage severity showcasing the fallback, three Test Cases (TCs) are drawn up for the following simulations:

- TC1: Communication outage of agents only passively involved in congestion scenario (agents 5, 7, 11, and 12)
- TC2: Communication outage of agents monitoring a highly loaded line equipped with a PST (agents 17 and 18)
- TC3: Communication outage of agents monitoring a congested line equipped with a PST (agents 4 and 14)

To test the fallback strategies within a grid with a sufficient but not unmanageable size, the IEEE 39 bus New England test system was chosen, as shown in Fig. 5.11. The grid's substations are equipped with agents, four of which can control the PSTs installed in the grid between buses 16-17, 2-3, 4-14, and 17-18 (PSTs are controlled by agents at underlined buses). Buses 1–29 and 39 are equipped with agents, while buses 30–38 are (uncontrollable) generator buses without agents. In the selected scenario, the power line connecting nodes 4 and 5 trips after 0.5 s of simulation time, causing line 4-14 to overload at 108 % and line 17-18 to be heavily loaded at 93 %.

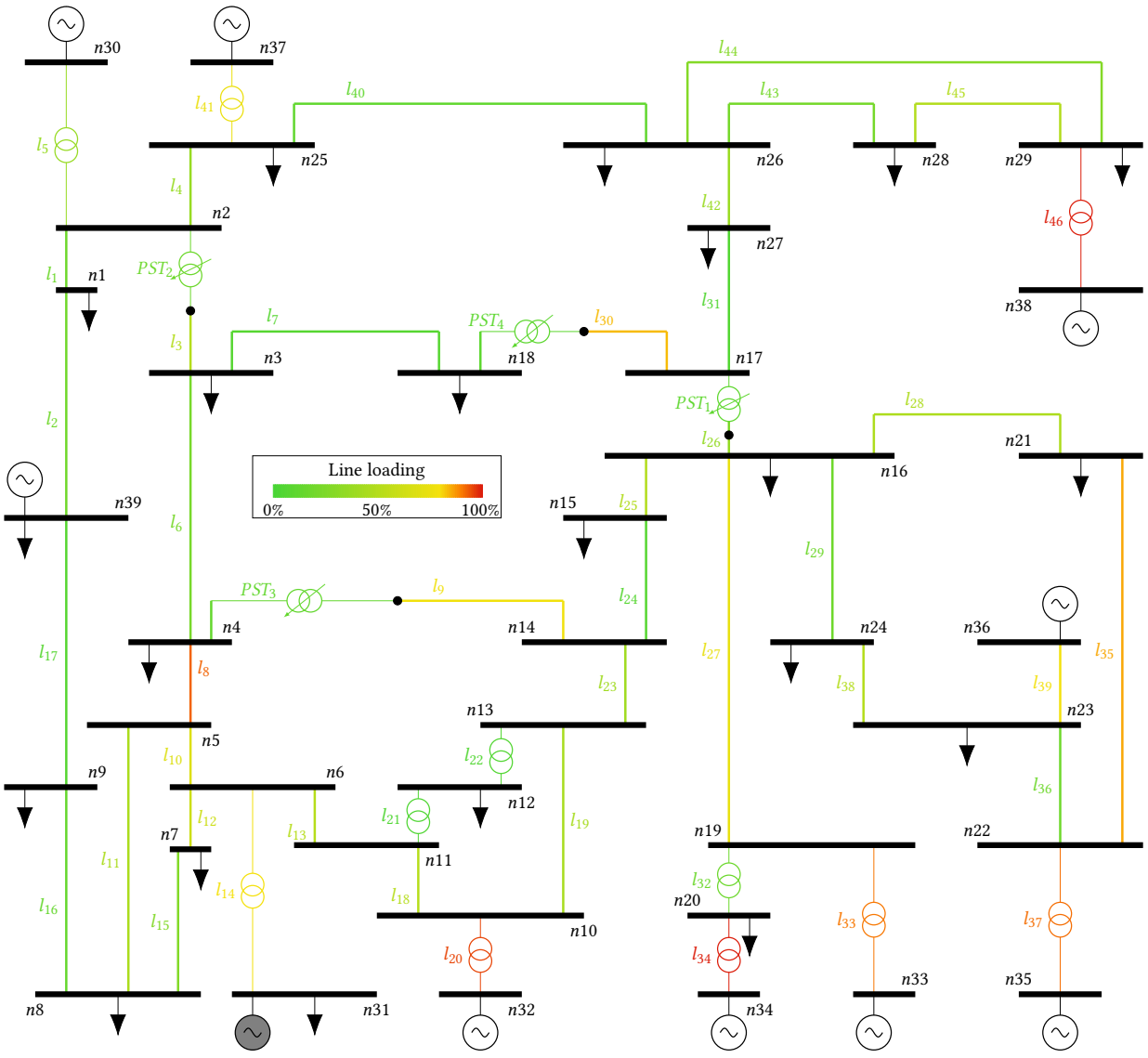

Figure 5.11: 39 bus test system in pre-fault condition of the fallback test

In TC1, the unavailable agents only control RMs with a low sensitivity towards the congestion. Their contribution to the CM process is merely passive as they provide their local measurements and offer inferior RMs. Hence, the outage of these agents does not significantly influence the MAS; the tap changes chosen to alleviate the overload come out virtually identical to the base case scenario with all agents active, setting PST3 to 30 in the base case and 31 during fallback. Simulation results for this are shown in Fig. 5.12.

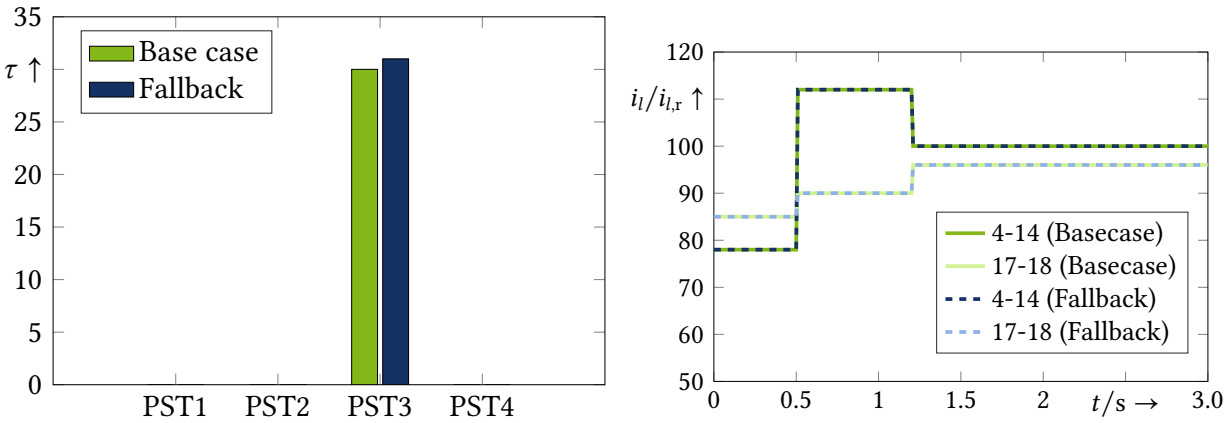

(a) PST taps in test case 1

(b) Line loadings in test case 1

Figure 5.12: Results of fallback simulation in test case 1 (agents inactive: 6, 7, 11, 12)

In the second TC, the agents monitoring heavily loaded line 17-18 are communicationally unavailable. This makes the agents' CM process more difficult, since the activation of RMs has to consider the loading of line 17-18 which can only be approximated now that the line's start and end node's agents are offline. The simulation results indicate that this approximation works well, since there is no difference in the RMs chosen in the base case and TC2. Agent 3 acts as the border agent and approximates the power flows on line 17-18 with adequate accuracy. This accuracy may vary however, if the loads at buses 17 or 18 changed their setpoints, or if line 17-18 was far off its natural operation point since this would increase the influence of reactive power on line loading, which is not considered in the PTDF-based approximation method. Simulation results for this are shown in Fig. 5.13.

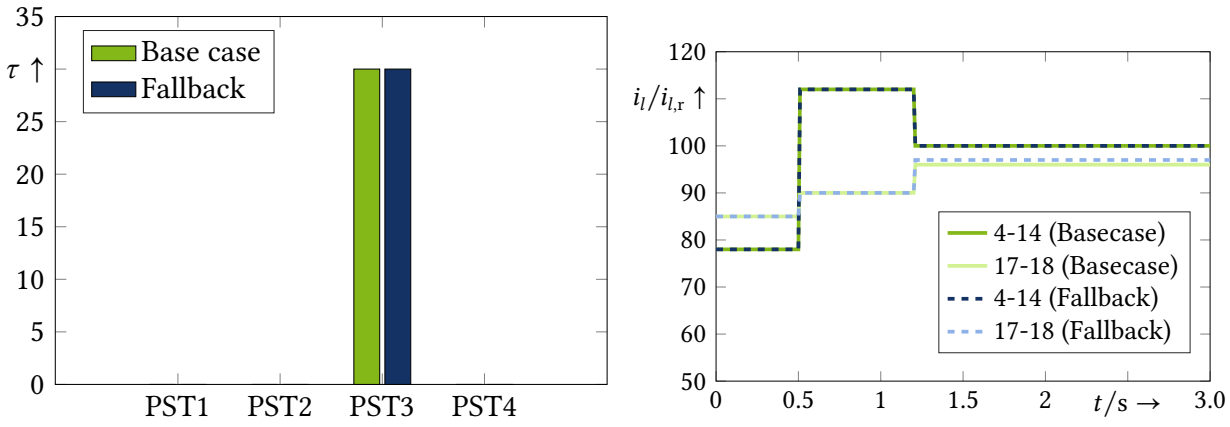

(a) PST taps in test case 2

(b) Line loadings in test case 2

Figure 5.13: Results of fallback simulation in test case 2

Finally, in TC3, the agents located at the start and end buses of the congested line 4-14 are outaged. This causes two problems: first, one of the border agents 3, 16, or 27 has to detect the congestion using the approximation method for line 4-14, and secondly, the RM with the highest sensitivity, PST3, is uncontrollable in this scenario. Thus, the resulting taps differ from the base case, with PST1 at −72 and PST4 at 15 instead of PST3 at 30. The resulting line loadings after the activation of the PSTs show a slightly worse outcome than in the basecase: the congestion on line 4-14 can not be entirely cleared at 101 %, as a further increase of the PST taps would overload line 17-18. Thus, the fallback improved the grid situation but if not enough alternative RMs are available, the agents may not be able to fully alleviate a congestion. Simulation results are shown in Fig. 5.14.

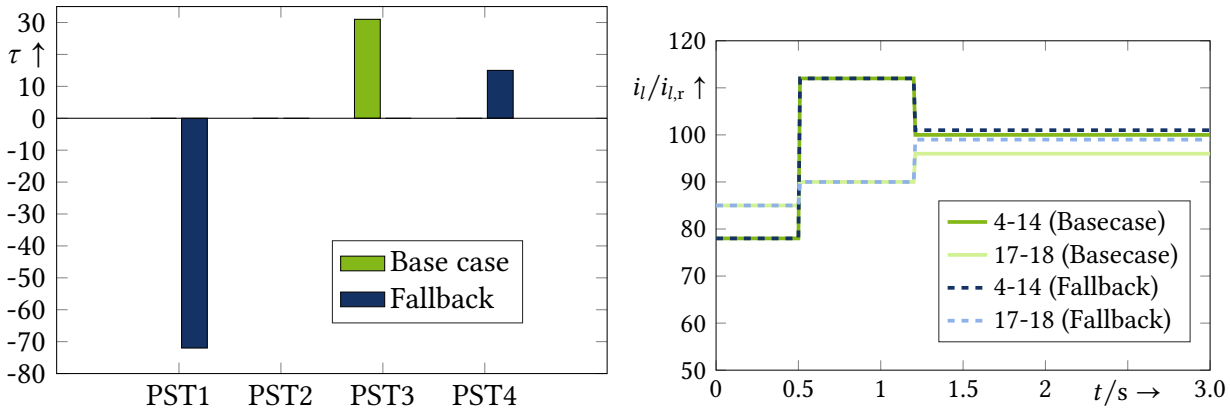

(a) PST taps in test case 3

(b) Line loadings in test case 3

Figure 5.14: Results of fallback simulation in test case 3

The simulations with these three TCs show that a rather simple fallback strategy can increase the resiliency of the MAS towards communication outages. However, if there is not a large RM redundancy available in the grid, SOs may want to simulate agent outage scenarios preventively to determine whether the MAS still has enough measures at hand to solve congestions even during communication failures. Also, the implemented fallback strategy can only be recommended for short agent outages due to the assumption that generators and loads in unobservable islands will maintain their power levels.

5.5 Conclusions and necessary evaluations of the designed multi-agent system

- A MAS was designed built upon previous works at ie^3 which it improves upon (direct instead of stepwise calculations), and extends (integration of DSRs and fallback strategy).
- The usage of DSRs necessitates a distributed instead of decentralized control due to the devices influencing each other.
- It can potentially be used to ensure safe grid operation with less preventive CM through ad-hoc curative measures or as a means to prevent cascading outages in emergency states caused by high-impact low-probabilty events.
- Its real-time applicability must be evaluated in an authentic environment to pave the path for the MAS towards real-world applications.
- During partial communication outages isolated agents should halt all actions while the remaining agents take over for them to ensure uninterrupted safe system operation.

6 A modular HIL test environment for automated power flow control systems

To test the developed algorithms in an environment that is closer to reality than pure software simulations, a laboratory test environment was developed and implemented at TU Dortmund's Smart Grid Technology Lab (SGTL)[1]. The different modules of this test environment and their interactions with each other are explained in this chapter. The chapter is divided into sections for each module and contains subsections for used hardware devices and software implementations. An overview of the laboratory installation is depicted in Fig. 6.1.

On the top left the **Real-Time Simulation (RTS) module** is shown, in which an HV grid is simulated on a real-time simulator. The transparent agents and DSR represent the location where the respective physical devices are interfaced with the RTS; they are not actually modelled software-side. Simulated measurements are sent to the **MAS module**, consisting of five PSI Smart Telecontrol Units (STUs), on which the MAS is implemented. This is depicted on the bottom right. The STUs analyze these measurements, detect congestions and communicate with each other to alleviate overloads by activating simulated FPUs and the physical DSRs. The **DSR module**, shown on the top right, is looped into the overall setup in two ways: First, simulated current measurements from the RTS are sent to Power Amplifiers (PAs), creating a current through the DSRs. The voltage drop caused by the DSRs is looped back into the RTS, completing this Power Hardware-in-the-Loop (PHIL) setup. Secondly, a communication between the DSRs and the MAS is established, to enable distributed control of the DSRs in a Controller Hardware-in-the-Loop (CHIL) setup. The STUs also forward all measurements they receive to the **CC module** depicted on the bottom left for monitoring and supervisory functions. Parts of this laboratory setup, especially the PHIL-coupling of the RTS- and the DSR-module, have also been described in [98].

[1] For further information about the SGTL see [97].

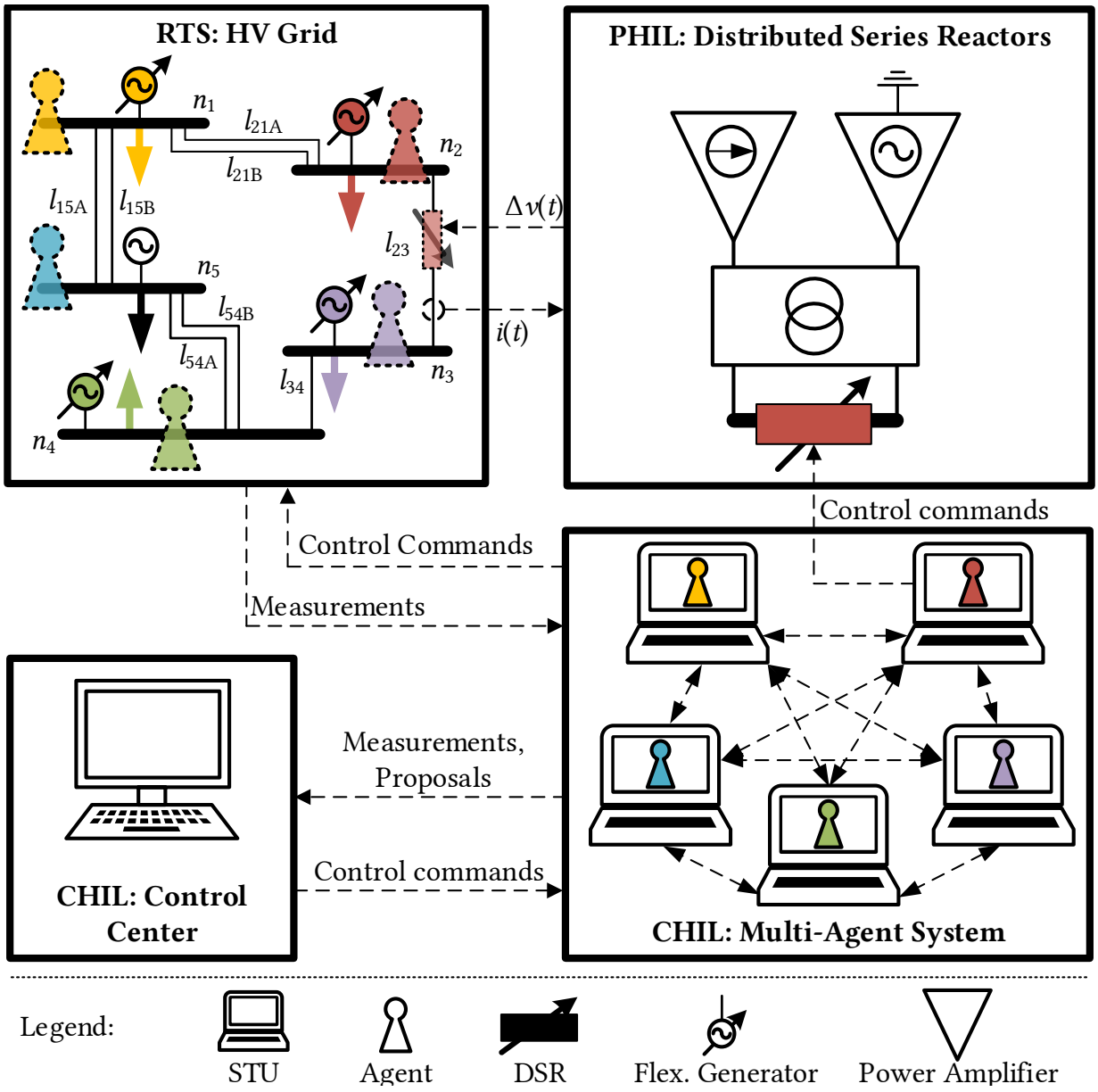

Figure 6.1: Overview of the laboratory modules

6.1 Real-time simulation module

The RTS is the core of the overall laboratory setup. A RTS of a 110 kV grid is executed on an OPAL-RT OP5600 real-time simulator, using the Matlab Simulink based OPAL-RT software RT Lab. The interface towards the MAS module is established via Ethernet and IEC 60870-5-104 Transmission Protocols (short: IEC 104) [99]. The exchange of simulated and physical current and voltage measurements with the DSR module is established via

fiber optical cables. More detailed descriptions of this module is given in the remainder of this section.

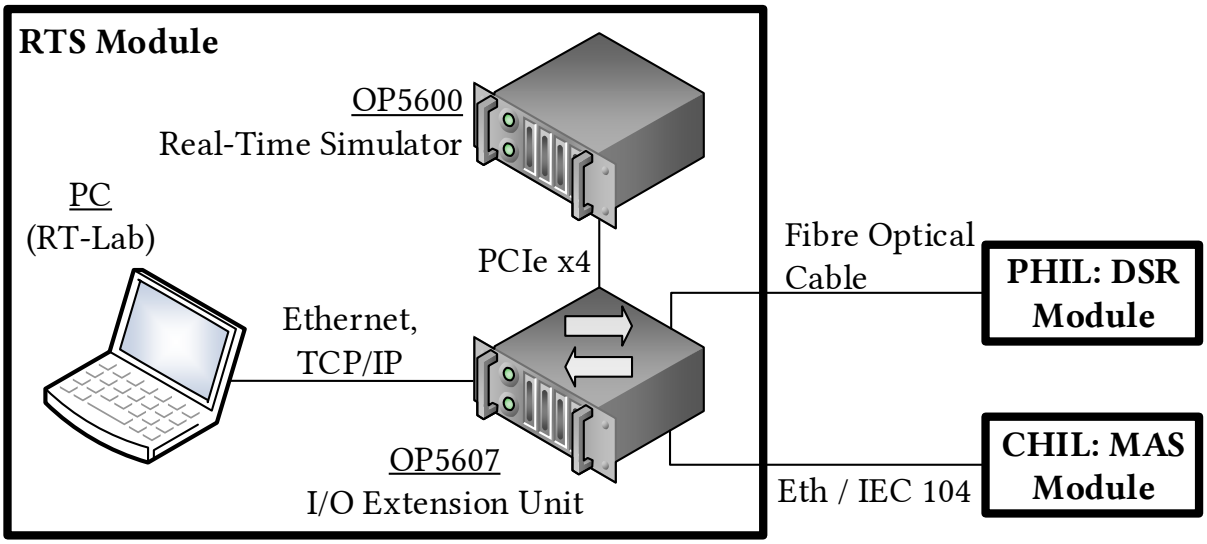

Figure 6.2: Hardware setup of the real-time simulation module

6.1.1 OPAL-RT real-time simulator

The RTS hardware setup consists of two devices: an OP5600 real-time simulator and an OP5607 I/O expansion unit. The grid model is uploaded to the OP5600 real-time simulator which performs all simulative calculations. It is equipped with eight 3.2 GHz cores and 8 GB of memory - but since the grid model is rather small, only a single core is needed to perform the RTS. The I/O expansion unit serves as the interface to the MAS and the PHIL modules. The device's multiple digital and analogue inputs and outputs allow the exchange of data with external devices during an ongoing RTS. Any kind of simulated measurement can be sent to the MAS via Ethernet and IEC 104 and the agents can send command messages into the simulation in the same manner. Simulated currents or voltages can be sent as analogue sinusoidal signals via fiber optical cables to PAs as setpoints to reproduce physical currents or voltages. The DSR module is connected to the RTS module in this way. The overall hardware setup with its connections to other modules is depicted in Fig. 6.2.

6.1.2 RT Lab and grid model

The grid model used in this experimental setup is a three-phase 5-bus 110 kV test grid. These buses are connected to each other via eight power lines and additionally two 10.5 kV and four 30 kV buses are connected to the HV grid via transformers. Node 5 is the slack bus and all other buses are PQ-buses. While a simplified visualization of the grid model is shown in Fig. 6.1, an image of its Simulink implementation along with all relevant grid device data can be found in the Appendix in Section 8.2. Since testing the control functionality of the MAS algorithm is secondary in the laboratory tests, the size of the grid is kept low on purpose. This facilitates adjusting GUCs and analysis of test results, and also reduces calculation times for the real-time simulator.

IEC 104 is used to exchange simulated measurements and control commands between the RTS and the MAS. IEC 104 is a communication protocol for telecontrol equipment and systems with coded bit-serial data transmission for monitoring and controlling geographically distributed processes. It is a companion standard for telecontrol systems that enables data exchange between compatible telecontrol equipment. [99] Its widespread application as well as its lower overhead and implementation effort compared to other standards such as IEC 61850 make it a suitable candidate for this laboratory setup. The implementation of the IEC 104 addresses was greatly facilitated by troubleshooting with the open source software QTester104, which was enhanced and in turn published as open source in the course of this work [100].

6.2 Multi-agent system module

The MAS module is realized in form of five STUs. It serves two purposes: Firstly, it contains the curative CM control functions. Secondly, it acts as an interface to exchange data between the RTS module and the CC module. An overview of the hardware connections of this module is visualized in Fig. 6.3 and more detailed description of its functions follows in the remainder of this section.

6.2.1 Smart telecontrol units

STUs are devices developed by PSI GridConnect GmbH for substation monitoring, control and automation. They act as RTUs with multiple sensors and communication interfaces, the most important for this work being the two Ethernet interfaces with IEC 104 capabil-

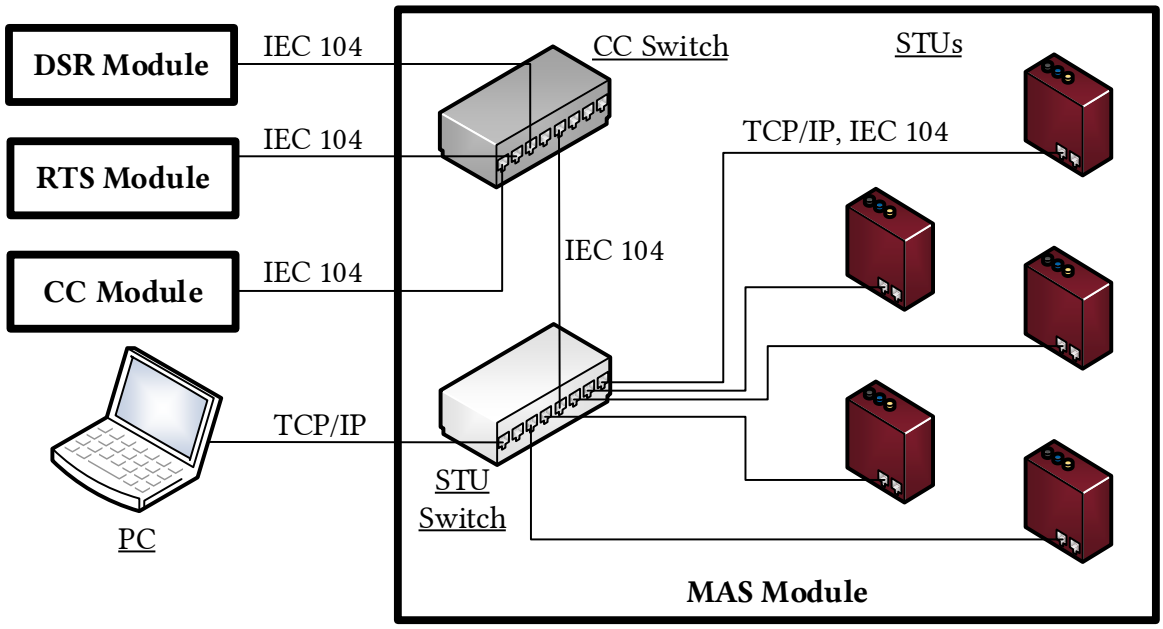

Figure 6.3: Hardware setup of the multi-agent system module

ity. Thus, an STU can receive field data such as measurements and alerts from connected grid equipment, perform analyses and send control commands to certain devices. They also serve as an interface between grid devices and the CC and allow for proprietary applications to be installed on them for a variety of purposes. [101]

In this laboratory installation, five STUs are installed in a server rack with Ethernet connections to each other as well as connections to

- the RTS module to receive simulated measurements and send control commands,
- the DSR module to receive physical measurements and send control commands,
- the CC module to forward received measurements as well as control decision information.

The connections are realized via Ethernet and TCP/IP. The STUs, or rather the agents installed on them, exchange information using FIPA Agent Communication Language. Data exchange between the STUs and the other three laboratory modules is established with IEC 104. A computer can be connected to the STUs' network to transfer applications such as the MAS algorithm. The STUs are implemented as PSI IEC 104 Security Proxies. This means, that an STU acts as an IEC 104 master towards measurement points (i.e. the OPAL-RT simulator), and as IEC 104 slaves towards the CC. This communication channel separation enables secure connection of the CC and end user devices. [102]

6.2.2 Agent-based control algorithm

The distributed control concepts explained in Chapter 5 were implemented on five STUs in C++. The focus of this thesis is not on the general functionality of the MAS but on its applicability in real environments. This is why only the FIPA core concepts, such as Agent Communication Language [95] and contract net interaction protocol [82], are thoroughly applied. Other FIPA concepts, such as agent management [103], are only implemented in a very lean manner. Since the MAS implemented in this thesis is entirely distributed, central instances such as a directory facilitator or an agent creator, are not needed. The implementation lays more focus on applicability and proper interfacing with external devices. The basic communication interfaces between the STUs were implemented in [PG1], which was then used as a module within the rest of the agent algorithm implementation done in this thesis.

Received measurements and control commands are stored within the STU's database. The agent algorithm is interfaced with this database to retrieve data and trigger the sending of IEC 104 telegrams.

In a pure software simulation the agents' and the grid simulator's calculations are synchronized. For each simulation step the agents would poll all measurements, analyze them and negotiate solutions when necessary, before the next solution step is calculated by the grid simulator. This enables an analysis focused on the implemented algorithm's theoretical functionality. However, in a real grid there are no deterministic time steps - and even in a RTS the simulator's calculation time steps at 50 µs are much faster than any of the agents' calculations. Additionally, common measurement devices in real grids send measurements with a frequency of a few seconds to a few minutes, depending on the application requirements. Deterministic synchronicity between RTS and MAS can thus not be ensured for every calculation step. Instead, agents poll measurements from their STU's database whenever they go through the respective behavior. The measurement values stored in this database may be outdated, depending on how often the measurement device sends data.

It is also not recommendable for the agents to wait for each single agent to finish a certain task before moving on with negotiations or other operations. Some agents may take longer than others to determine their proposals, depending on the complexity of their calculations. In case of communication failures or single agent program crashes, waiting for all agents may even result in a failure of the entire MAS. Stepwise synchronicity among the agents can thus not be ensured either. Instead, appropriate time windows are

put in place when a CFP agent is waiting for proposals. This can potentially slow down the decision making process but if adequate durations are chosen, solutions can still be found within a reasonable time.

6.3 Distributed series reactors module

Besides simulated flexibilities, the MAS is also supposed to use impedance controlling devices for curative CM. In this laboratory setup, three physical DSRs are installed and coupled into a RTS through a PHIL using PAs and transformers. The DSRs can be controlled manually or by the described MAS through CHIL. This section will explain this implementation, which has also been presented in [OP8].

6.3.1 Scaffold

One of the main advantages of DSRs over conventional PFC devices is their ability to be clamped directly onto existing power lines. The devices are powered by the current of the line they are installed on and operate under the (floating) electrical potential of the line, while being isolated from ground by air. This makes the installation process significantly easier and also reduces costs since they do not take up space within a substation. However, in a laboratory environment with no existing power lines, this necessitates the installation of a structure to hold power lines under current equipped with DSRs. The requirements for this structure are explained in this subsection.

To enable a decent amount of versatility in the usage of the three available DSRs, the structure should be able to hold three short power line stubs, each equipped with one DSR. These stubs can then be electrically connected in series with or in parallel to each other, to realize different configurations of the DSRs. Since the IDEAL project is concerned with CM in 110 kV grids, a common line type with a high current rating was chosen: 264-AL 1/34-ST1A (formerly known as Al/St 265/35) [104, 105]. The DSR type chosen for this type of line is PowerLine Guardian 700-SD4 since its conductor diameter of 28.1 mm and current rating of 700 A fit well with (i.e. are slightly higher than) that of the line type (22.4 mm, 680 A). The length of each line stub at 4 m was chosen to be long enough to allow easy accessibility while taking up as little laboratory space as possible. There are five inter-dependent requirements a structure to hold the DSRs must meet:

1. Hold the **weight** of the DSRs and power lines (approximately 300 kg in total)

2. Keep the DSRs and power lines **insulated** from ground and from each other (amplifiers' maximum phase-to-ground voltage is 250 $V_{AC,RMS}$ [106])
3. Hold the power lines under varying **temperatures** (up to 80 °C)
4. Ensure **electromagnetic fields** do not violate work safety regulations
5. Stay within the project's **budget**

To ensure electrical insulation, and also to not risk damaging the DSRs' antennae located on their bottom side, a scaffold structure was chosen. This way, power lines and DSRs can be hung mid-air, allowing ground insulation through air. Since the DSRs weigh 300 kg and the power lines need to be installed under tension, the scaffold needs to be made of metal. To reduce costs and possible complications with magnetic effects like induction, aluminum was chosen as a suitable scaffold material. To allow for an easy installation of the DSRs within the scaffold, it was chosen to be 4 m in length, 1.5 m in width, and 3 m in height. The power lines are installed in the scaffold using two types of clamps: First, common power line clamps in combination with shackles and turnbuckles are used to install the lines and manually apply tension. To insulate this metal clamping equipment from the scaffold, supporting insulators with a rating of 1 kV are used as anchor points. Secondly, plastic pipe clamps are installed as well, in case the metal clamps fail and also to easily keep the lines in place. A conceptual draft of this scaffold by the company Item Industrietechnik GmbH can be found in the appendix in Fig. 8.2. To lower the risk of humans coming in contact with any parts of the laboratory test setup that may be under voltage, an additional horizontal aluminum beam was added in the front, as well as plexiglass protection to both sides. As a final safety measure, the scaffold is always surrounded by a fence when tests are carried out.

Electromagnetic fields need to be within work safety regulation limits. In [107] three areas are designated with maximum allowed exposition values each. These areas describe at what rate the strength of electrical and magnetic fields needs to decrease with increasing distance from the fields' source, i.e. the laboratory installation. In the case of the described laboratory setup, the *area of higher exposition* is inside of the scaffold, *exposition 1* is inside the fence around the scaffold and *exposition 2* is the rest of the laboratory. A graphical representation of these areas can be seen in the appendix in Fig. 8.3.

According to [107] for *exposition 2* the maximum allowed strength of an electrical field at a frequency of $f = 50\,\text{Hz}$ can be calculated to be $E_{\text{max},2} = \frac{333.3}{f} = 6.666\,\text{kV/m}$. Since the line voltage will never exceed 0.25 kV due to the amplifiers' limitations, the electrical field is of no concern to work safety regulations here. In *exposition 2* the maximum allowed

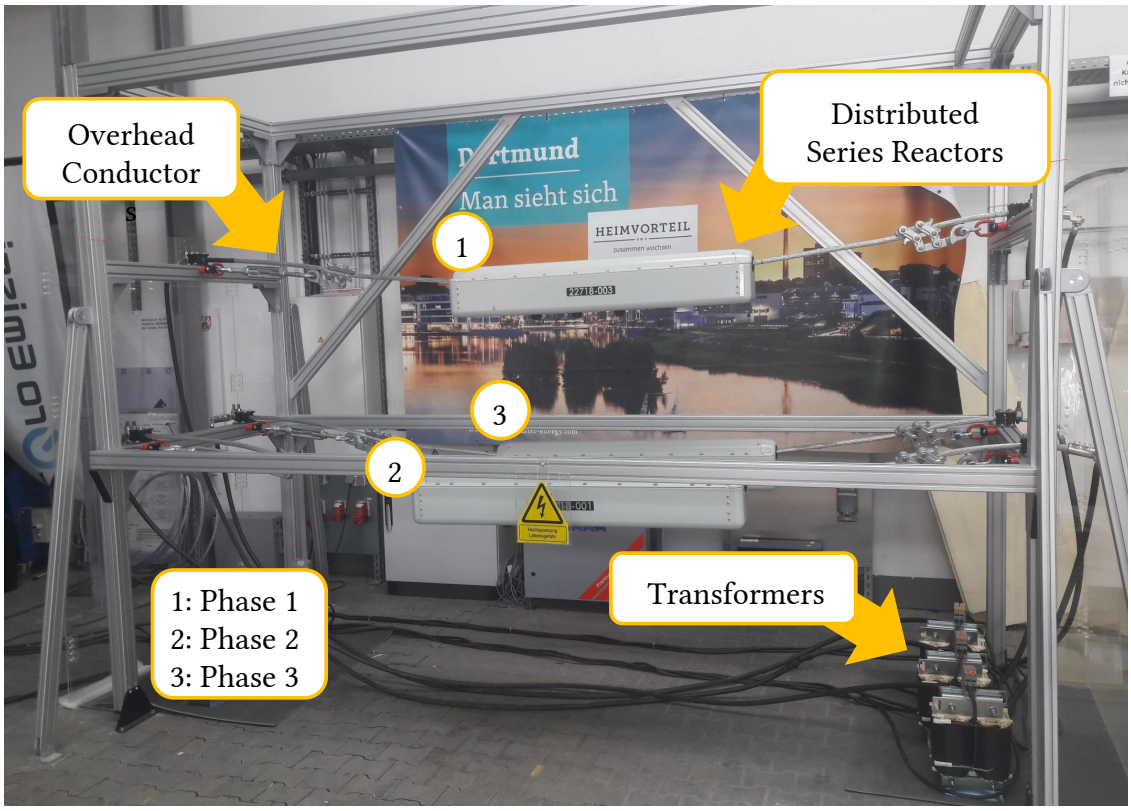

Figure 6.4: Installed scaffold with DSRs and transformers

magnetic flux density $B_{\text{max},2}$ at a frequency of 50 Hz is $B_{\text{max},2} = \frac{21.22}{f/\text{Hz}}\text{mT} = 0.424\,\text{mT}$. The magnetic flux density B can be calculated as the product of the magnetic constant $\mu_0 H$ and the magnetic field strength H as shown in eq. (6.1).

$$B = \mu_0 H = \mu_0 \frac{i}{2\pi r} \tag{6.1}$$

To find out within which radial distance r around the power lines this limit would be breached, eq. (6.1) can be solved for r. With $i_{\text{max}} \leq i_{\text{l,r}} = 680\,\text{A}$ and $B_{\text{max},2}$ the radius can be calculated as $r_{\text{min},2} = 0.32\,\text{m}$. Thus, *exposition 2* could theoretically start outside of a radius of 32 cm around the power lines. Likewise, *exposition 1* and the *area of higher exposition* can be calculated analogously to be within radii of 10 cm–32 cm and 5 cm–10 cm respectively around the power lines. To be able to mechanically install the DSRs within the scaffold, it needs to be 100 cm–200 cm wide. This shows that the mechanical requirements have a significantly higher influence on the dimensions of the scaffold and thus magnetic fields are well within their limits regarding work safety regulations. The scaffold in its final form can be seen in Fig. 6.4.

After the scaffold and lines were installed, the DSRs were mounted onto the conductors us-

Figure 6.5: Installation of DSRs in the scaffold

ing a special mounting device hung from a forklift as shown in Fig. 6.5. Since the mounting device weighs an additional 100 kg, each line stub needs to be able to safely hold the combined weight of DSR and mounting device 200 kg. The installation process itself is easy enough for untrained personell (e.g. the author of this thesis, as can be seen in Fig. 6.5), but giving the task to professional staff is strongly recommended in field installations.

6.3.2 Power hardware-in-the-loop setup

The purpose of the PHIL setup is to create a physical electrical current on the power lines that is equal to a simulated current in the RTS and loop back the DSRs' influence into the simulation. This can be achieved via a power interface which creates physical current or voltage from simulated measurements. The design, validation and first test runs of this module have also been published in [OP8]. In this case, the power interface consists of two identical groups of 4-module PAs with a rated power of 100 kVA per group [106]. Each PA group can be operated either in current or in voltage source mode, depending which of the two variables are to be controlled. This way, a three phase system including neutral conductor can be fed by four modules. The PAs communicate with the OP5607 through a dedicated interface based on optical fiber. This communication link allows for

the exchange of setpoints and measurements between the RTS and the PA system with a minimal data transfer delay. The PA are connected via cables to the power lines and thus to the hardware under test: the DSRs. The DSRs reach nominal operation mode between 300 A–700 A of line current. Since this exceeds the maximum current of the PAs at 125 A, transformers have to be connected in between the PAs and power lines to reach line currents typical for 110 kV grids. While these transformers increase the current, they also decrease the voltage on their secondary side, where the power lines are connected. As the DSRs' functionality is not influenced by the voltage, because they are on the same electrical potential as the power lines, this is not detrimental to the PHIL setup. On the contrary: The low voltage on the secondary side facilitates insulation of the power lines against each other and towards the scaffold they are installed in (see Subsection 6.3.1). This already hints at one of the major advantages of this setup and a scientific contribution of this work: *The described PHIL setup can be used to safely test off-the-shelf PFC devices meant for HV systems within a low voltage laboratory.*

To create the required physical current on the power lines and to be able to run the PHIL simulation in a stable and accurate manner, a suitable interface algorithm between RTS and hardware under test must be chosen. The interface algorithm defines not only the equivalent model of the hardware within the simulation but also the configuration of the PAs and the transformers. In the course of this work, two interface algorithms have been considered: voltage and current type ideal transformer method. They are explained in the remainder of this subsection, based on [OP8].

6.3.2.1 Interface algorithm: Voltage type ideal transformer method

Fig. 6.6 depicts the implementation of the voltage type ideal transformer method for one phase of a three phase power line equipped with a DSR. With this interface algorithm the DSR is modeled in the RTS as a current source in series to the line the DSR is installed on. Measurements of the simulated voltages before and after the current source are sent as set points to the PAs. Due to the PAs' voltage output limitations the RTS measurements need to be normalized from the grid model's nominal voltage $u_{\mathrm{RTS,n}} = 110\,\mathrm{kV}$ to the PAs' nominal voltage $u_{\mathrm{PA,n}} = 0.25\,\mathrm{kV}$ with the factor $k_{\mathrm{PA}} = \frac{u_{\mathrm{PA,n}}}{u_{\mathrm{RTS,n}}}$. To account for the fact that the amplitude of the simulated current will only be reached after the transformers, the simulated voltage measurements also need to be adjusted for the transformer's turns ratio n_{T}. This is achieved through the scaling factors for voltage and current with $k_{\mathrm{V}} = k_{\mathrm{I}}^{-1} = n_{\mathrm{T}} = \frac{u_{\mathrm{T,sec,n}}}{u_{\mathrm{T,prim,n}}}$ (note that the transformers' primary voltage is higher than their secondary voltage). The PAs create these voltages at their outputs, which are connected to

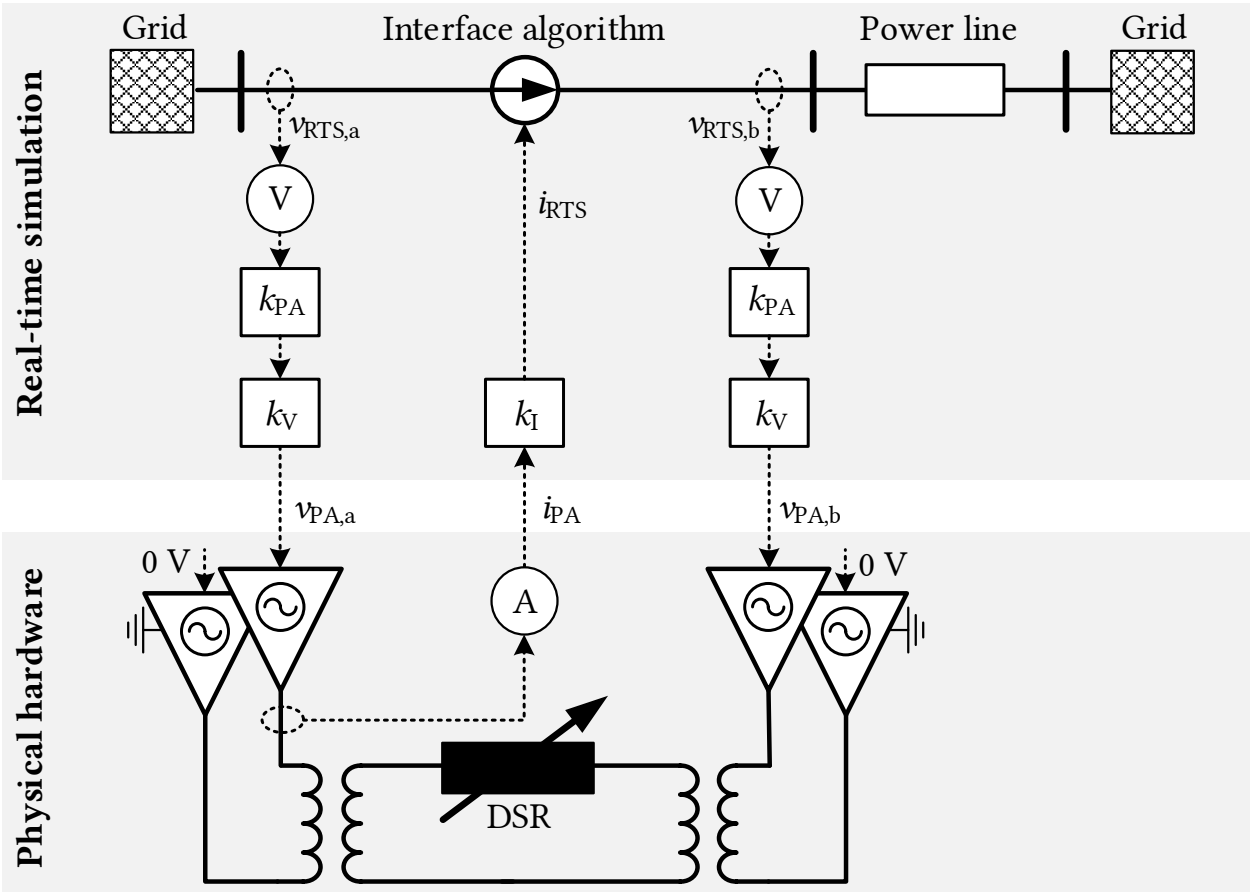

Figure 6.6: PHIL configuration for the voltage type ideal transformer method for one distributed series reactor

the transformers' primary sides. Note that to create a voltage, two PA modules are needed, where one of them has to provide a ground reference potential. With appropriate initialization values chosen for the current source representing the DSR, the voltage difference at both ends of the DSR will create a current over the power line on the transformers' secondary side. This is shown in eq. (6.2), neglecting cable and line impedances.

$$i_{\mathrm{DSR}}(t) = k_{\mathrm{PA}} k_{\mathrm{V}} \frac{\hat{u}_{\mathrm{RTS,a}} \sin(\omega t + \delta_a) - \hat{u}_{\mathrm{RTS,b}} \sin(\omega t + \delta_b)}{2 \cdot z_{\mathrm{T}} + n_T^2 \cdot z_{\mathrm{DSR}}} \tag{6.2}$$

This current is equal to the simulated current and should be sent back into the simulation to close the PHIL setup's control loop. However, measuring at the secondary side using third-party equipment (i.e. not specifically designed for this interface) will most likely introduce delays so large that PHIL RTS stability cannot be guaranteed. This is why the current measurement taken at the primary side, which is directly measured by the PA at their outputs, is looped back into the simulation instead. Obviously, this measurement

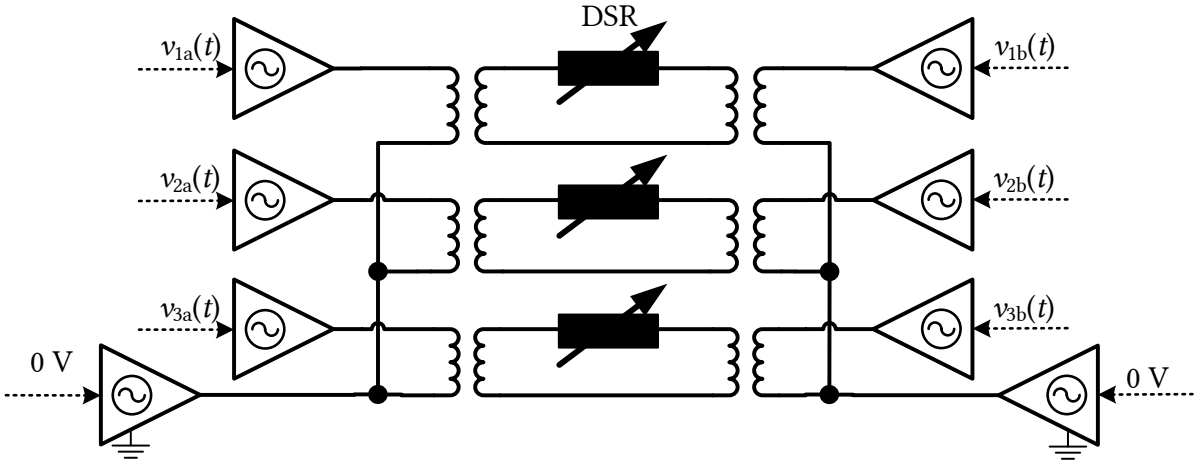

Figure 6.7: Connections of power amplifiers and transformers in the voltage type ideal transformer method

has to be scaled up again, using the factor k_I. When the DSR starts injecting reactance, the line current decreases since the PAs keep the voltage at the same level as before. Thus, the physical DSR and the simulated grid can interact with each other and the PHIL setup is complete.

This kind of interface algorithm appears plausible and intuitive, since the voltage difference on both sides of the power line is what causes the the desired current flow - which is exactly what happens in real grids with real power lines. However, it has been proven to be disadvantageous for several reasons. First of all, for each of the three DSRs to be tested, four PA modules (two of each group) are necessary. Since only two groups of four modules each are available in the laboratory, this necessitates the usage of one module per group as a ground potential reference for that group. Fig. 6.7 depicts this constellation for all three DSRs. With such a setup, three single-phase transformers are essentially connected as a single three-phase transformer. This means that the three phases cannot be operated independently of each other, which limits the possible testing variations of the setup. Also, if voltage imbalances occur, for example because the DSRs do not start injecting reactance simultaneously, the phase currents will overlap in the neutral conductor. This way, the current on the neutral conductor can increase to values as high as $i_\mathrm{max} = 3 i_\mathrm{PA,max} = 375\,\mathrm{A}$ - and even much higher on the secondary side, where the current is scaled up by the transformer turns ratio. Secondly, the two PA groups, acting as separate voltage sources, are connected to each other via a relatively small impedance of only two transformers and some conductors. This causes the voltage control algorithms of both groups to interfere with each other, rendering a stable PHIL simulation challeng-

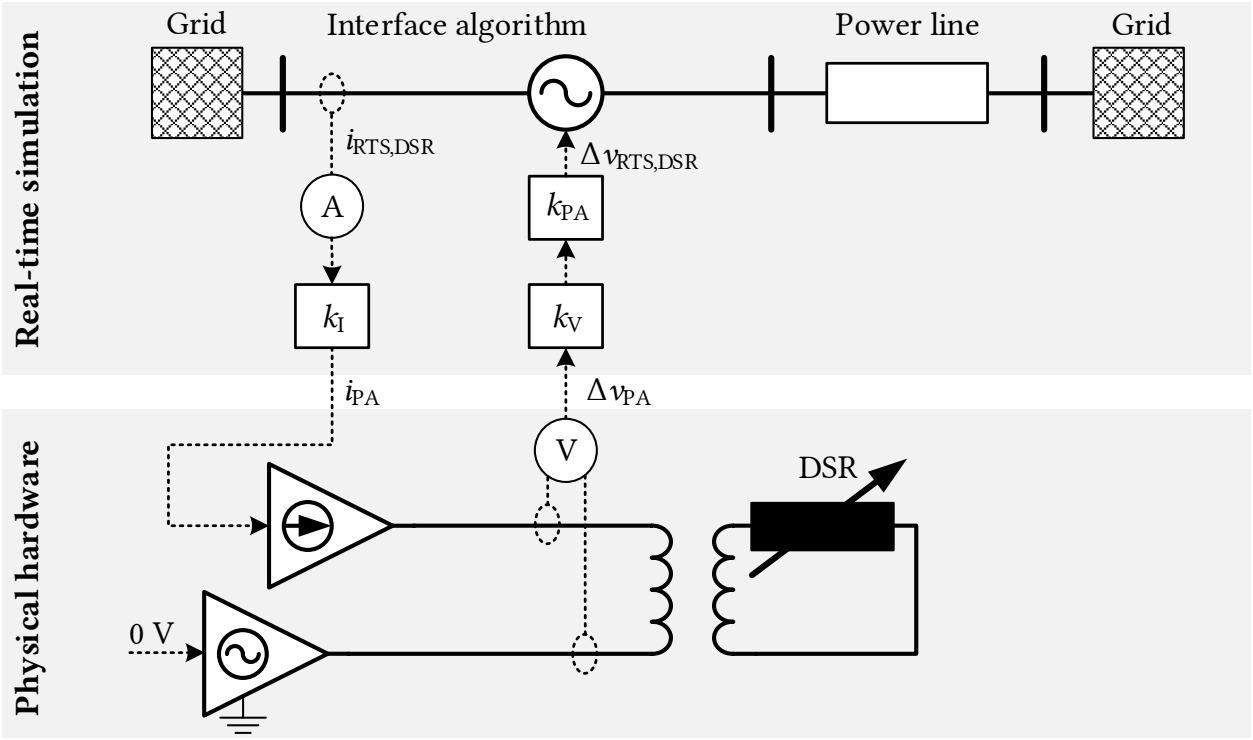

Figure 6.8: PHIL configuration for the current type ideal transformer method for one distributed series reactor

ing. Lastly, when reconsidering eq. (6.2), the scaling of the measurements is not trivial. Scaling down the voltage measurements to the nominal voltage of the PAs, while keeping the phase angle difference between the two measurements unchanged, also decreases the voltage drop over the DSR - and thus decreases the corresponding current. Theoretically, the voltage phase angles could be scaled as well with a specific factor to create a physical current of the same magnitude on the transformer secondary side. The current measured at the PAs output would then need to be phase-shifted accordingly before it is looped back into the simulation. However, the necessary control loop would be complex and leave only small margins of error to ensure a stable operation of the setup. Since these disadvantages pose a serious threat to equipment safety and stable test operation, this interface algorithm is not recommended for this setup.

6.3.2.2 Interface algorithm: Current type ideal transformer method

An alternative interface algorithm is the current type ideal transformer method. Its implementation for this setup is shown in Fig. 6.8. In the RTS a DSR is modeled as a voltage source in series with the line it is installed on. The simulated current going into this voltage source is measured and sent as a set point to a PA module operating in current source

mode. Due to the PAs' current limitations the simulated current amplitude can only be reached on the transformer's secondary side. Thus, the current measurement is scaled down for the PA according to the transformer's turns ratio using k_I. The PA module is connected to the primary side of a transformer. Another PA module of the same group is connected at the other pole of the transformer's primary side. This module however, acts as a voltage source providing ground reference potential. Thus, a current of $i_\mathrm{PA} = k_\mathrm{I} i_\mathrm{RTS}$ flows from the current source module through the transformer primary to the voltage source module. On the secondary side, this current is scaled up by the transformer turns ratio to be equal to the simulated current. When the DSR starts injecting reactance, the voltage drop between the two PA modules increases. This voltage drop is measured and sent back into the simulation to close the PHIL control loop. Once again, measuring on the secondary side would be the more direct way to retrieve the correct values, but due to the critical time delay the voltage drop is measured on the primary side by the PAs where it can be looped back through the optical fiber interface. Unfortunately, this way the voltage drop not only over the DSR is measured, but also over the impedances of the transformers z_T, the cables (primary and secondary side) z_C and the power line z_l, causing a small voltage injection into the RTS even when the DSRs are not injecting reactance. So the overall impedance of all hardware parts connected to the PAs can be calculated as in eq. (6.3):

$$z_\mathrm{HW} = z_\mathrm{Setup} + n^2 z_\mathrm{DSR} = z_\mathrm{C1} + n^2(z_\mathrm{T} + z_\mathrm{C2} + z_\mathrm{l} + z_\mathrm{DSR}) \tag{6.3}$$

To compensate this inaccuracy and ensure the effect of the DSRs can be examined isolated from the rest of the setup, the voltage drop caused by the setup's impedances can be subtracted from the control loop. This is visualized in Fig. 6.9 which depicts the block diagram in the Laplace domain of the overall PHIL setup. The diagram also includes the delay due to the discrete simulation with time step T_s, along with the transfer function of the PA and the transfer function of the measurement system, $G_\mathrm{PA}(s)$ and $G_\mathrm{Meas}(s)$ respectively. On the upper part of the diagram the setup impedance compensation algorithm is depicted. In practice, this algorithm can be applied as follows. The algorithm takes as inputs both the current and the voltage measurements from the PAs to estimate the setup impedance z_Setup as the equivalent impedance $z_\mathrm{Est}(s)$. Upon starting a PHIL simulation, all DSRs should be in monitoring mode, i.e. not injecting reactance: ($z_\mathrm{DSR} \approx x_\mathrm{DSR} = 0\,\Omega$). The voltage drop measured at the PAs output now corresponds only to the setup impedance z_Setup (s), i.e. $\Delta v_\mathrm{HW}(s) = \Delta v_\mathrm{Setup}(s)$. Thus, the estimated setup impedance derived from voltage and current measurements can be obtained as $z_\mathrm{Est}(s) = \frac{v_\mathrm{PA}(s)}{i_\mathrm{PA}(s)}$. This impedance can then be multiplied with the measured simulated line current to yield the necessary

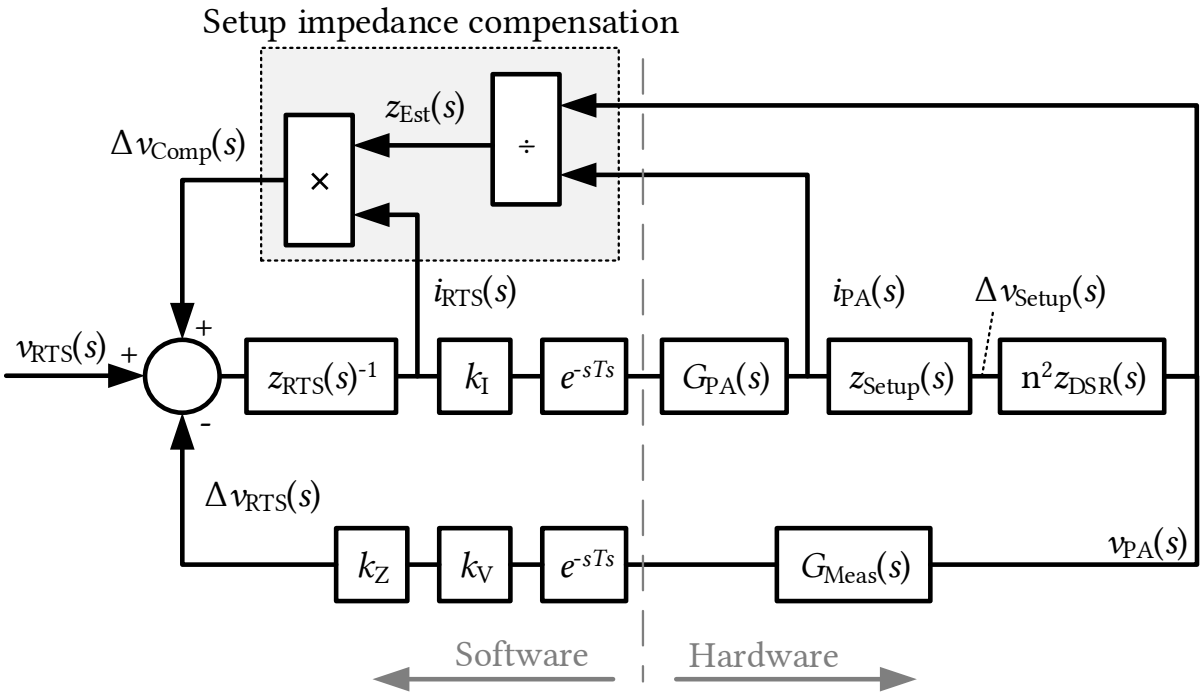

Figure 6.9: Block diagram of the PHIL setup in Laplace domain

compensation voltage as in $\Delta v_{Comp}(s) = z_{Est}(s) \cdot i_{RTS}(s)$. By adding Δv_{Comp} in the loop the aforementioned voltage injection caused by z_{Setup} is effectively compensated. The estimation of z_{Setup} is also a suitable method to properly quantify the impedance of the looped components in case of lack of data. Furthermore, by comparing z_{Est} with z_{RTS} it is possible to evaluate the system stability online.

The stability of the ideal transformer method strongly depends on the ratio between equivalent impedance of the simulated grid (z_{RTS}) and the equivalent impedance of the hardware parts (z_{HW}) [108]. As explained in the previous paragraph, the latter includes not only the impedance of the DSR but also the inevitable contribution of the hardware parts involved within the setup. While the setup impedances are not of research interest for the tests, they have to be considered in the PHIL stability evaluation. In case of an ideal interface ($G_{PA}(s) = 1$ and $G_{Meas}(s) = 1$) the stability condition for the open loop transfer function is expressed as shown in eq. (6.4):

$$G_{OL}(s)^* = k_Z k_I k_V \frac{z_{HW}(s)}{z_{RTS}(s)} e^{-s2T_s} = \frac{z_{HW}(s)}{z_{RTS}(s)} e^{-s2T_s} \tag{6.4}$$

According to the Nyquist criterion, the resulting stability condition is given by:

$$\frac{z_{HW}(s)}{z_{RTS}(s)} < 1 \tag{6.5}$$

The current factor k_I and the voltage factor k_V are set according to the transformer ratio n_T with the relation $k_V = k_I^{-1} = n$. In this condition these scaling factors do not affect the system stability and the current flowing through the DSRs corresponds to the current of the simulated power line. The impedance scaling factor k_Z can be arbitrarily set to manipulate the DSR impedance within the simulated grid. If $k_Z = 1$, the equivalent hardware impedance seen within the simulation ($z_{HW,eq}$) is equal to $n^2 z_{DSR}$ because of the transformer connection. The simulated grid gets the contribution of n^2 series connected DSRs instead of a single one. Setting $k_Z = n^{-2}$ the contribution of the transformer to the total impedance is neglected. However, k_Z impacts the system stability so it must be limited according to eq. (6.5). The PHIL accuracy can be estimated by evaluating the transfer function of the system response with respect to interface disturbances [108]. The system response to a disturbance $\Delta i(s)$ on the PA is obtained as follows:

$$i_{HW}(s) = \frac{G_{OL}(s)^* e^{s2T_s}}{1 - G_{OL}(s)^*} \Delta i(s) \tag{6.6}$$

According to eq. (6.6), a small amplitude of $G_{OL}(s)^*$ contributes on improving system resilience to disturbances thereby improving the PHIL accuracy. According to eq. (6.4) and (6.6), the impedance factor k_Z must also be limited to not exceed a predefined accuracy threshold. In the event that eq. (6.5) is widely satisfied, the contribution of $G_{PA}(s)$ and $G_{Meas}(s)$ is not compromising the stability and accuracy evaluated considering $G_{OL}(s)^*$. However, if operating close to the stability limit or if additional elements such as filters are needed to improve feedback signal quality, a more detailed stability and accuracy analysis is required. Furthermore, k_Z must also be limited with regards to the PA limits. When k_Z is decreased, a larger current will flow through the same physical impedance, requiring a larger voltage output by the PAs. If k_Z is set too low, the required voltage may exceed the PAs' maximum voltage, possibly causing stability issues as the voltage amplitude is capped, forming a non-sinusoidal output. The minimum scaling factor can be determined with eq. (6.7).

$$k_{Z,min} \geq \frac{z_{HW} \cdot i_{PA}}{v_{PA,max}} \tag{6.7}$$

Since each power line can be operated independently with the current type ideal transformer method three different constellations of DSRs can be realized in the PHIL setup, as can be seen in Table 6.1. To realize these constellations, only some simple physical re-wiring has to be done and the RTS model has to be adjusted slightly. The three constellations are visualized in Fig. 6.10 and explained in Table 6.1.

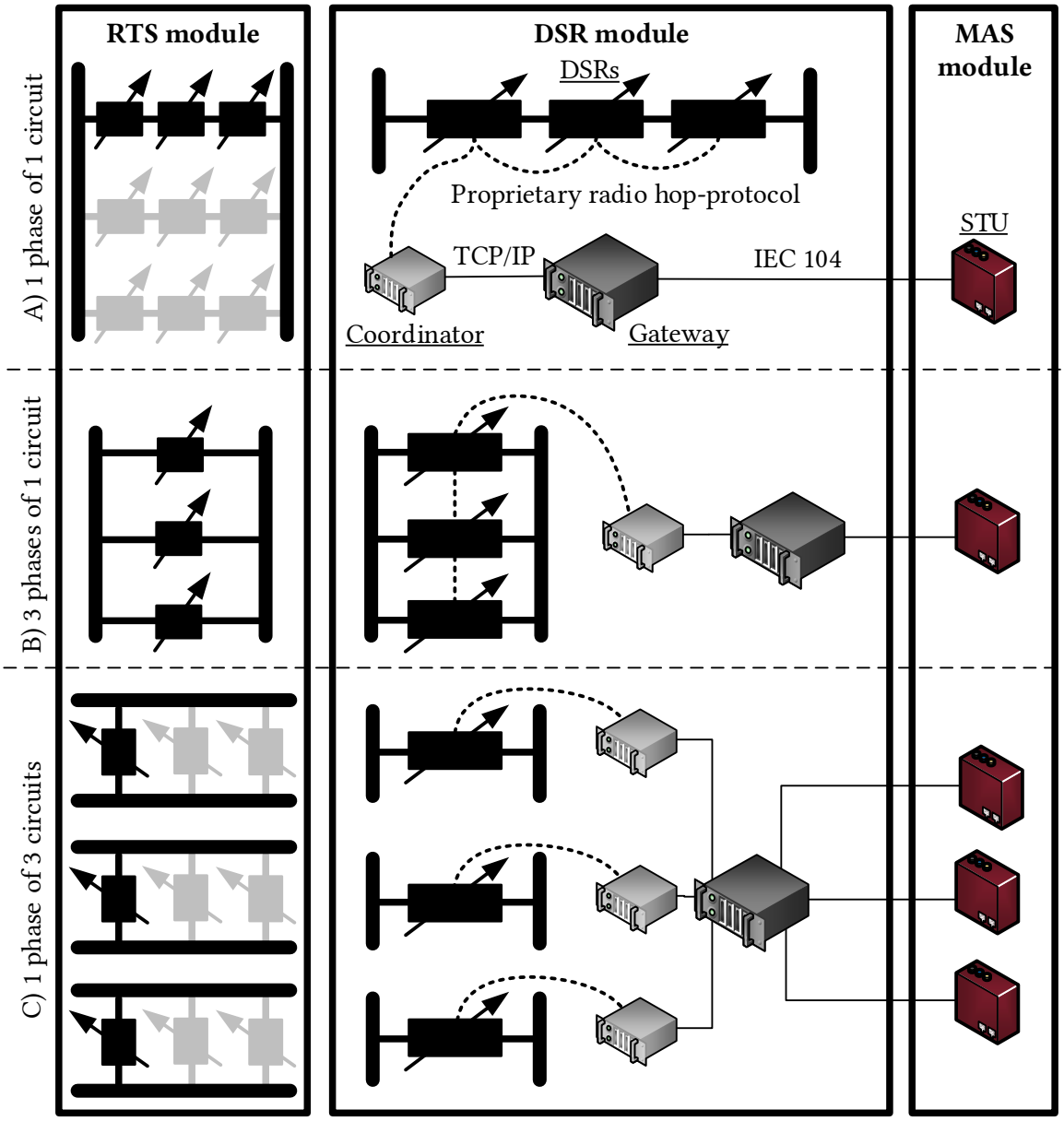

Figure 6.10: Three possible constellations of the laboratory setup

Table 6.1: Possible DSR constellations

	A	B	C
Line connections:	Three lines connected in series	Each line operated as one phase of same three-phase circuit	Each line operated as one phase of three different three-phase circuits
DSR constellation:	Three DSRs in series on same phase	One DSR per phase of same three-phase circuit	Each DSR independent on one phase of three different three-phase circuits
RTS adjustments:	Copy physical measurements into other two phases with $\pm 120^\circ$	-	Copy physical measurements into other two phases of each circuit with $\pm 120^\circ$
Resulting behavior:	Three-phase circuit with three DSRs per phase	Three-phase circuit with one DSR per phase	Three different three-phase circuits, each with one DSR per phase

6.3.2.3 PHIL hardware components and communication connections

One of the most important hardware considerations for this setup is the type of transformer used. It has to fit well with the requirements and parameters of the overall setup described in this section. To choose an appropriate transformer the transformer's primary and secondary nominal voltage and current, as well as the corresponding turns ratio and its series reactance need to be determined. According to the purpose of the PHIL setup, the transformers must fulfill the following requirements:

1. Secondary nominal current must be within the nominal operational range of the DSRs but lower than the line current rating:
   $i_{\mathrm{DSR,n,min}} = 300\,\mathrm{A} \leq i_{\mathrm{T},2} \leq 680\,\mathrm{A} = i_{\mathrm{l,r}}$
2. Nominal primary current must be below the maximum current of the PAs:
   $i_{\mathrm{T},1,\mathrm{n}} \leq 125\,\mathrm{A} = i_{\mathrm{PA,max}}$
3. Nominal primary voltage must be below the maximum voltage of the PAs:
   $v_{\mathrm{T},1,\mathrm{n}} \leq 250\,\mathrm{V} = v_{\mathrm{PA,max}}$

The output voltage of the PAs is not directly controllable but created as a result of the PA output current and the connected impedances. With sudden impedance increases, e.g.

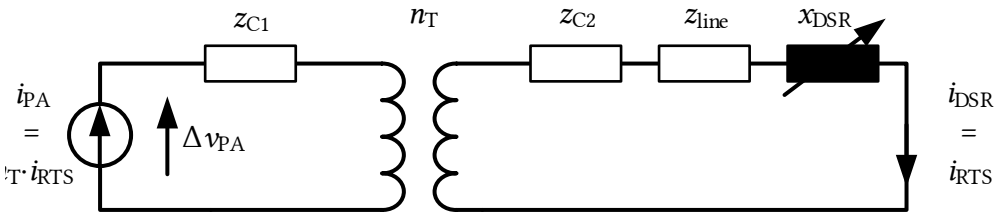

Figure 6.11: Equivalent circuit of one phase of the power hardware-in-the-loop setup

DSR injection, the voltage may unexpectedly jump to the PA maximum voltage. To ensure a safe operation, the transformer primary voltage is chosen at $v_{T,1,n} = v_{PA,r} = 250\,V$. The transformer primary nominal current could be chosen to be equal to the PA maximum current with $i_{T,1,n} = i_{PA,r} = 125\,A$. With a turns ratio of $n_T = \frac{i_{l,max}}{i_{T,1,n}} = \frac{680\,A}{125\,A} = 5.44$ the secondary current would reach the maximum allowed line current when the primary current reaches the maximum allowed current for the power interface. This would however put the transformer's apparent power at $s_{T,r} = v_{T,1,n} \cdot i_{T,1,n} = 250\,V \cdot 125\,A = 31.25\,kV\,A$. Three transformers of this size would be outside of the project's budget. Since i_{PA} can be safely controlled and it is not necessary to actually approach $i_{l,r}$, $s_{T,r}$ can be reduced in favor of increasing n_T. To determine a suitable turns ratio, a solution space of all applicable turns ratios can be calculated, as follows. Considering the equivalent circuit of the PHIL setup, as shown in Fig. 6.11, the following electrical relations can be derived. The cable and power line impedances can be roughly estimated considering their lengths and types. By varying the primary and secondary current within their allowed ranges, the necessary turns ratio can be calculated which would be needed to enable this transformation. This is shown in eq. (6.8).

$$n_T = \frac{i_{T,2}}{i_{T,1}} \tag{6.8}$$

The secondary current creates a voltage drop over the connected impedances, as shown in eq. (6.9).

$$v_{T,2} = i_{T,2} \cdot (z_{C2} + z_l + z_{DSR}) \tag{6.9}$$

In eq. (6.10) this voltage drop is scaled up by the turns ratio on the transformer primary side.

$$v_{T,1} = v_{T,2} \cdot n_T \tag{6.10}$$

Considering the voltage drop over the cables between PAs and transformers, the necessary PA output voltage can be obtained via eq. (6.11). If this output voltage is within the PA

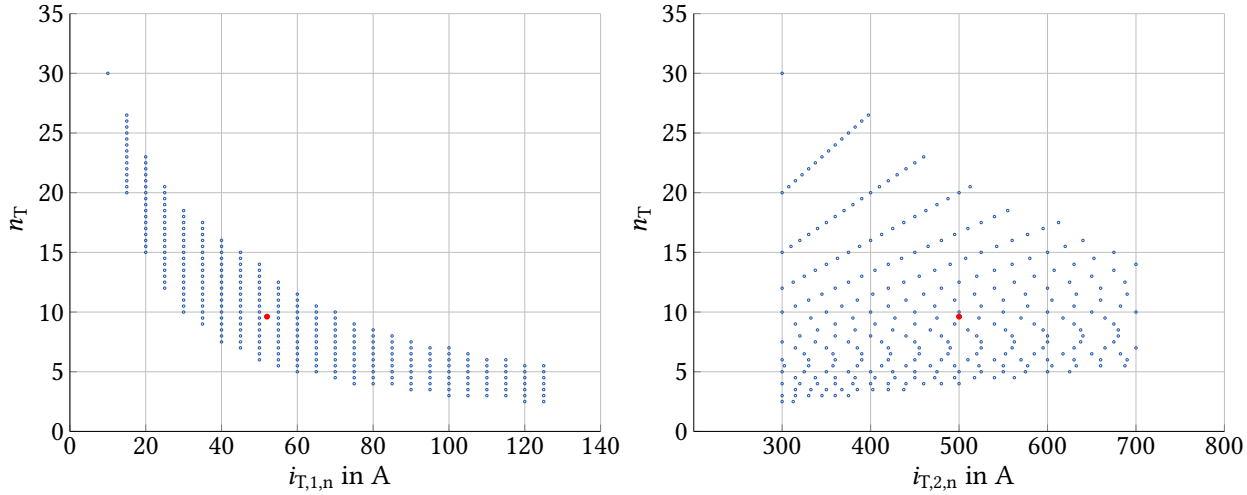

(a) Primary current and turns ratio

(b) Secondary current and turns ratio

Figure 6.12: Results of transformer dimensioning

Table 6.2: Transformer type installed in laboratory setup

$s_{T,n}$	$v_{T,1,n}$	$v_{T,2,n}$	$i_{T,1,n}$	$i_{T,2,n}$	n_T	x_T
13 kVA	250 V	26 V	52 A	500 A	9.62	0.095 Ω

limits of 250 V, a transformer with such a turns ratio could be used for the PHIL setup.

$$v_{PA} = v_{T,1} + i_{PA} \cdot z_{C1} \leq 250\,\text{V} \tag{6.11}$$

The results of these calculations for the primary and secondary current ranges are shown in Fig. 6.12. Unsurprisingly, transformers with a low primary current would need a higher turns ratio to create the appropriate secondary current. The relation between these two variables however is not linear. With a turns ratio between 5 and 15, the entire operational range of the secondary current can be achieved. Values above this would need too high a voltage from the PAs, whereas values below this would require too high a current from the PAs. To account for possible inaccuracies in this rather simplified dimensioning, a value in the center of the calculated solution space was chosen and indicated in red in the figure. The entire chosen transformer dimensions are thus shown in Table 6.2.

The DSRs can be controlled remotely. For this purpose a *Smart Wire Gateway* and three *PowerLine Coordinators* are installed in a server rack near the scaffold in the laboratory. The DSRs send measurement values to the coordinator via a hop radio protocol proprietary to Smart Wires Inc. Depending on their constellation, the DSRs communicate with different coordinators: In constellations A and B, one DSR becomes a *super-DSR* and acts

as an interface between a coordinator and the rest of the DSRs. Thus, only one coordinator is needed. In constellation C, each DSR communicates with its own dedicated coordinator. The coordinators are connected to the gateway via an ethernet switch and forward any messages received from the DSRs to the gateway via TCP. The STUs are also connected to said switch. All IEC 104 addresses concerning the DSRs are configured on the gateway. Thus, the gateway forwards all messages coming from the DSRs to the respective STU set to monitor and control them. The STUs can in turn control the DSRs by sending IEC 104 command telegrams to the gateway, which forwards these to the coordinators and thus to the DSRs. To adjust the communication paths to the DSR constellation, a configuration change has to be executed on the gateway which forwards this information to the coordinators and the DSRs. A computer with Smart Wires Inc. software can also be used to monitor and control the DSRs via the gateway and coordinators.

6.4 Control center module

To bring automated PFC systems from pure software simulations towards real grid implementation, their integration into existing CC structures has to be considered. An operator has to be able to monitor, predict and, in emergency situations, control the proposed MAS behavior. Therefore, a laboratory-scale CC was implemented in the laboratory, providing basic SCADA functions as well as necessary adjustments and enhancements for the MAS. The remainder of this section provides explanations for these components and functions, which have also been presented in [OP9].

6.4.1 Control center hardware

Regarding hardware, the CC implemented in the laboratory consists of an operator computer, three monitors, a server hosting multiple virtual machines and a firewall. The virtual machines hosted are a database computer, an interface computer and a coupling computer. The database computer processes and archives data, whereas the coupling computer connects the CC and the MAS. The interface computer provides interfaces between the operator computer and the other two virtual machines, and thus between the operator and the MAS. The operator computer is connected to three monitors and offers CC functionalities, such as technological operations, dialogues and human-machine-interfaces [109]. All communication connections between the CC computers and to the rest of the laboratory setup are shown in Fig. 6.13.

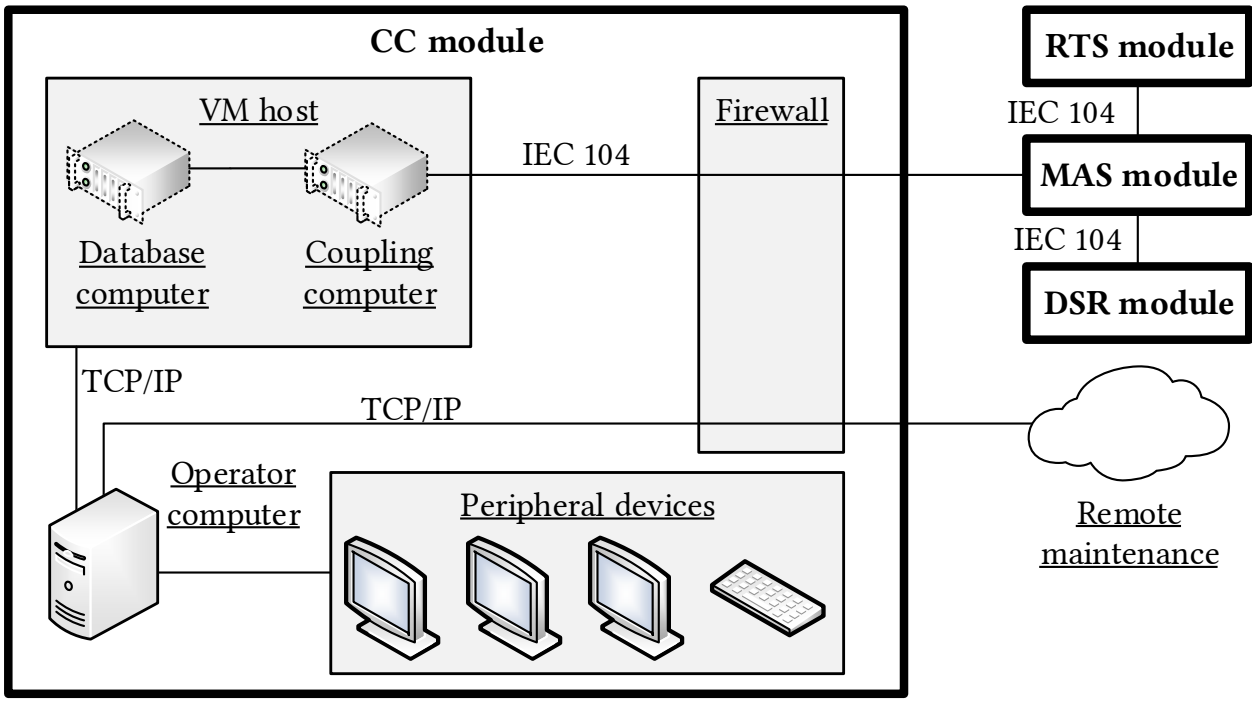

Figure 6.13: Hardware setup of the control center module

6.4.2 Control center software

To monitor and control the grid model simulated in real-time, the CC setup provides regular SCADA functions as well as grid calculation and analysis functions such as state estimation, power flow analysis, sensitivity analysis, short-circuit analysis, optimal power flow and contingency analysis. A model of the same grid running in the RTS module is implemented within the CC. Since asymmetrical operation is not of interest for the MAS integration, a single-phase representation of the RTS grid model is implemented within the CC. To integrate the MAS into existing CC systems, PSI was assisted in developing and implementing additional CC tools. The operator needs to know the current state of every agent, as well as how the agents would react to changes in the grid's operational state or topology. For this, several graphical interfaces were added or enhanced in the CC software. An overview dashboard for every agent, (cp. Fig. 8.4 in the appendix), allows the operator to see the current active and reactive power load and feed-in as measured by the agent, along with current flexibility activation proposals for these units. The loading of the lines monitored by the agent can be observed here as well.

The application of automated curative CM renders the prevention of overloads in case of outages obsolete - but only when it is clear that curative actions will be able to alleviate overloads post-contingency. In the status quo, when the operator performs a congestion

Name	(n-0)	(n-1) before MAS	(n-1) after MAS
Current limit violations:	I/I_r [%]	I/I_r [%]	I/I_r [%]
Line 21B			
Line 21A	64.00	96.51	85.81
Line 54A			
Line 54B	75.21	101.13	95.36

Figure 6.14: Example congestion analysis results including curative measures

Figure 6.15: Laboratory control center

analysis, its results show line loadings in (n-0) and (n-1) state, and congestions are additionally indicated by color coding. If a congestion in case of a certain outage is detected, the operator applies preventive measures. To let the operator know whether a congestion can be alleviated by an automated curative CM system, the congestion analysis output needs to be enhanced. For this purpose, a centralized version of the heuristic algorithm is implemented within CC software. This version encompasses the power flow and sensitivity calculations as well as the heuristic flexibility decision process. However, instead of distributing these tasks and communicating their results among several processing units, the algorithm is centrally executed on one machine. When the operator executes a congestion analysis, the results additionally show the line loadings in (n-1) state *after* the application of the forecasted curative measures. An example for this can be seen in Fig. 6.14. All tools and enhancements explained in this chapter can be controlled via the operator computer in the CC laboratory installation shown in Fig. 6.15.

6.5 Summary: Laboratory test environment

- A laboratory test environment was designed and installed in Smart Grid Technology Lab (SGTL) to examine how a distributed automated system for curative CM performs in real-time and how it can be integrated into CC software.
- This test environment consists of four modules: a real-time simulator, a CHIL setup of a MAS implemented on dedicated distributed RTUs, a CHIL setup of a small CC, and a PHIL setup of three DSRs.
- Since the DSR, MAS, and CC modules are implemented on industry-standard hard- and software instead of laboratory-scale in-house developments, the overall system emulates an authentic environment, including a variety of real-world factors neglected in most software simulations.
- The DSR module is highly versatile in its PHIL capabilities but limited by maximum allowed currents – which must be closely monitored during testing.

7 Demonstration of agent-based power flow control in a HIL test environment

To validate the real-world applicability of the MAS, multiple experiments are carried out with the laboratory installation described in Chapter 6. The primary goal is to answer research question ii, i.e. determine reaction times the MAS can achieve in a real-time application and identify temporal bottlenecks. A secondary goal is to demonstrate how the MAS can be applied in a close to real-world environment and integrated into existing CC systems. From this, design and implementation suggestions are derived to be considered in future applications, thus answering research question iii. For the tests described in this chapter, h1 is implemented in the agent algorithm, so no re-calculation of sensitivities is performed to ensure high calculation speeds at the expense of accuracy (cp. Chapter 4).

First, the GUCs for the tests are shortly described in Section 7.1. For one GUC, the general functionality of the MAS and its adequacy for solving congestions ad-hoc, as well as the behavior of the PHIL-interface is shown in Sections 7.2 and resp. 7.3. This is followed by an evaluation of the MAS real-time communication for both of these scenarios in Section 7.4. The chapter closes with the demonstration of how the MAS can be integrated into CC systems under GUC2 in Section 7.5.

7.1 Grid use cases

In addition to the applicational requirements, practical restrictions from the laboratory setup must also be considered. This means, the grid must be in alert operational state in (n-0) conditions due to a specific outage but the congestion in (n-1) condition may not cause a current on the DSR-equipped line that is too high to handle for the PHIL-setup. Also, the Nyquist equilibrium of the PHIL interface must be satisfied (cp. eq. (6.5)). With the described laboratory setup and grid model, a line outage can easily violate this equilibrium, which is why for the laboratory tests with the DSR-module, a load outage was chosen over a line outage since this does not influence the overall equivalent grid impedance. With these restrictions in mind, two GUCs, i.e. combinations of generation, load, and outage, were defined to showcase the MAS behavior. The static grid states in (n-1) state of these GUCs can be seen in Fig. 7.1. The availability of RMs varies between the three different TCs, as will be explained in the following subsections.

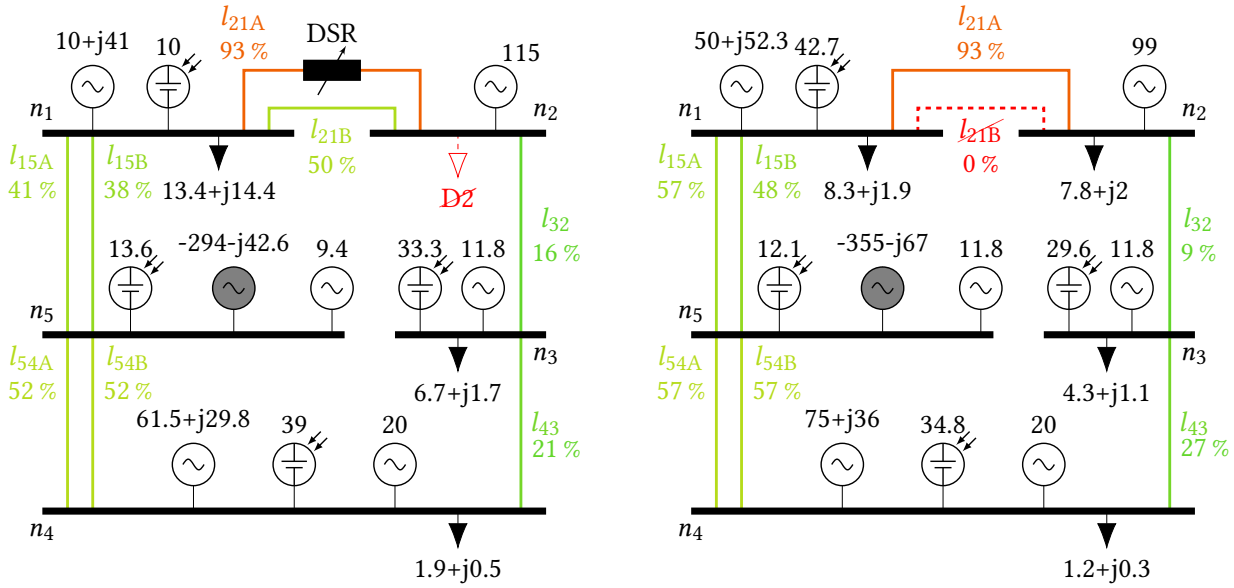

(a) (n-1) state in GUC1 (load outage)

(b) (n-1) state in GUC2 (line outage)

Figure 7.1: Static grid states of both grid use cases (power in MW, resp. Mvar)

7.2 TC 1: Utilization of distributed series reactors

TC 1 depicts a scenario with a large fleet of DSRs on line 21A, meaning all three DSRs are available for the agents and $k_Z = 1$, yielding a maximum additional reactance of $\Delta x = 3 \cdot 0.02\,\Omega \cdot \left(\frac{250\,\mathrm{V}}{26\,\mathrm{V}}\right)^2 = 5.55\,\Omega$ (cp. Section 6.3). For this experiment, the DSR-module is in constellation A (cp. Table 6.1). The additional amount of reactance is so large that FPUs are not needed for CM. Here, GUC1 is applied and RTS measurements are made available to the agents at a rate of 1 Hz. Initially the grid is in (n-0)-state and all line utilizations are well below their thresholds. After a few seconds, the load at node n_2 disconnects and due to the large fleet of generating units in the grid, line 21A is heavily loaded at $\frac{i_{21A}}{i_{r,21A}} = 93\,\%$, triggering a reaction from the MAS to solve the congestion. After some time the outage is resolved and the MAS deactivates previously activated RMs again.

7.2.1 Congestion management feasibility

The MAS can resolve the congestion as required. The line utilizations over the entire test duration as well as RM de-/activation are shown in Fig. 7.2. Additionally, static grid state snapshots of the most important time steps can be found in the appendix in Fig. 8.5.

Line 21A experiences a current above its critical threshold when D2 disconnects at $t = 6$ s. This is noticed by agent 2, causing it to switch from monitoring to CFP-state. Agent 2 calculates the required power flow change to be $\Delta p_{l_{21\mathrm{A}}} = -11.68$ MW which would reduce the power flow on l_{21A} from 79.55 MW to 67.88 MW to bring the line below its target threshold of 80 %. The CFP sent out by agent 2 is answered with FPU-proposals by the other agents, and agent 2 adds its own DSR-proposal to the list of available RMs. Within the laboratory setting, the DSR sensitivity is quite large at $\gamma^{\Delta X}_{l_{21\mathrm{A}},\mathrm{DSR}} = -4.83\,\mathrm{MW}/\Delta\tau_{\mathrm{step}}$ due to the transformers that increase the effective reactance of one DSR as seen from the transformer primary to $x_{\mathrm{DSR,prim}} = x_{\mathrm{DSR,sec}} \cdot n_{\mathrm{T}}^2 = 1.85\,\Omega$. Thus, agent 2 concludes it must activate all three DSRs to relieve the overload but no FPUs. The congestion is solved with the DSR-activation at $t = 33.6$ s, approx. 27.6 s after the overload appeared.

The activation of the DSRs reduces the loading of $l_{21\mathrm{A}}$ to 74.81 % while all other line loadings remain well below their critical thresholds. The somewhat large overshoot of $74.81\,\% - 80\,\% = -5.19\,\%$ is caused by two phenomena: the large step size of the DSRs, which makes reaching specific operation points difficult, and the DC power flow linearization error. Based on their calculations, the agents expected to reduce the line loading to 76.69 % with all three DSRs activated. Thus, it can be concluded that out of the −5.19 % overshoot, the PHIL-setup is responsible for $76.69\,\% - 80\,\% = -3.31\,\%$ and the linearization error contributes $74.81\,\% - 76.69\,\% = -1.88\,\%$. The latter would have been even lower if the DSRs had a lower step size and thus less additional reactance would have been activated, keeping the grid state closer to its operation point around which the linearization for the sensitivity calculation was done. It is also beneficial to the accuracy of the DC calculations that $l_{21\mathrm{A}}$ is operated at a very low level of reactive power demand. While this is coincidental in this GUC, it is not unusual for highly loaded lines. Lowering the loading on the congested line further than necessary is generally unproblematic but if this extended to a higher than expected increase of loading on other lines, additional overloads could be created. In reality however, a DSR deployment comes with a significantly smaller step size, decreasing the overshoot caused by adding more reactance than necessary, and in turn also decreasing the linearization error.

After D2 is reconnected at $t = 64$ s, $i_{l_{21\mathrm{A}}}$ drops below its release threshold. Agent 2 concludes that it can safely deactivate all three DSRs without causing any threshold violations, causing the line utilization to rise back up to its initial level of 68 % at $t = 66.4$ s. Now all agents are back in monitoring state and the grid is under normal operation again.

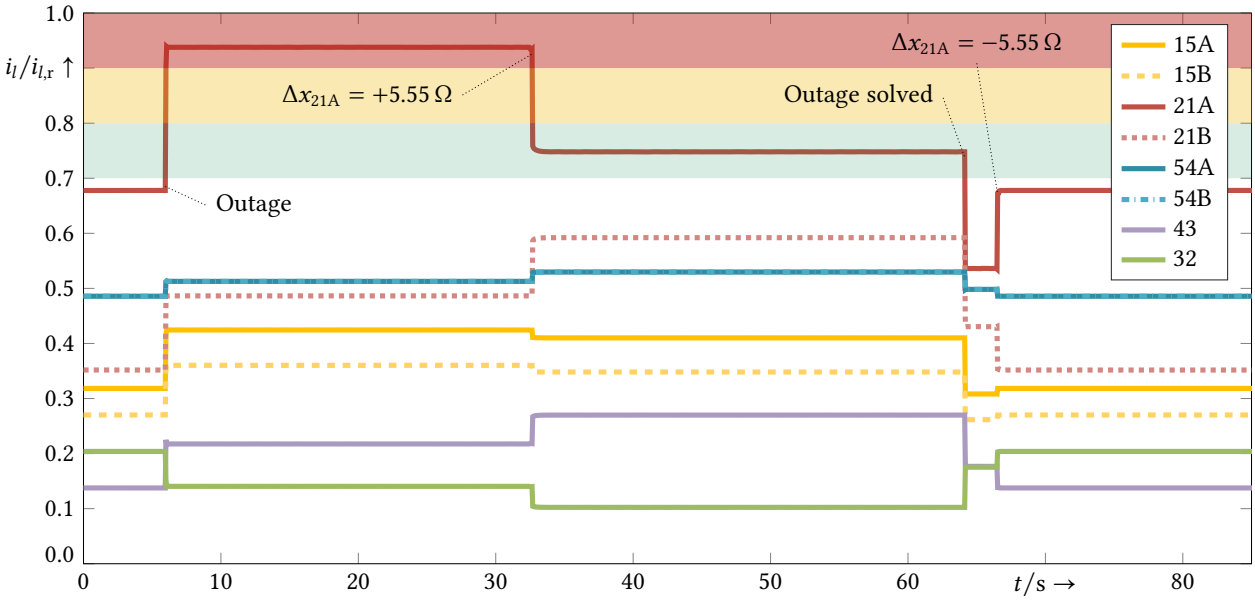

Figure 7.2: Line utilizations during TC1 (GUC1, $\Delta x_max = 5.55\,\Omega$)

7.2.2 PHIL functionality

In this subsection, the functionality of the DSRs and of the PHIL-interface in TC1 is analyzed. The current at the output of the PA in current-mode as well as the voltage drop between the two PAs are shown in Fig. 7.3 for the four most important time steps as sinusoidal signals, and in Fig. 7.4 as RMS values over the entire experiment duration.

(n-0) state: After the initialization of the PHIL-interface with the RTS and the compensation of the setup impedance (cp. Subsection 6.3.2.2), the grid is in (n-0) state and the DSRs are in monitoring state without injecting reactance.

(n-0) → (n-1): In Fig. 7.3a at $t = 5.93$ s the disconnection of load D2 increases the current on l_{21A} from 285 A_{rms} to 394 A_{rms} in the simulation. Accordingly, the PA current setpoint is increased from 30 A_{rms} to 41 A_{rms}. To achieve this, the PA increases its output voltage amplitude from 67 V to 93 V, keeping the sinusoidal form after initial transients over two periods. Since output current and voltage are below the PA limitations of 125 A_{rms} and 250 V_{rms}, the PHIL interface operates in stable and smoothly sinusoidal condition.

DSR-activation: The DSRs are activated at $t = 32.61$ s, as can be seen in Fig. 7.3b. The higher impedance seen by the PA causes it to increase its output voltage to still reach the current setpoint. Due to the closed-loop control of the PHIL-interface, the increased impedance also partially shifts the current on line 21A into parallel lines, lowering the

current setpoint sent by the RTS to the PA. Thus, the current amplitude is decreased from 57.8 A to 47.3 A, while the voltage amplitude is increased from 98.1 V to 378.1 V. Note that the voltage loses its smooth sinusoidal shape as it breaches the maximum voltage amplitude achievable by the PA. That is because the impedance increase exceeds the current decrease in such a way that the resulting necessary output voltage is narrowly above the PA limit, causing its amplitude to be capped, flattening the sinus curve at the very top. The sine cutoff is stronger immediately after the DSR activation but diminishes after a few seconds, as can be seen at the start of Fig. 7.3d where the tops of the sine curves are not as flat anymore. Since this effect is small, the PAs still reach the required current setpoint, keeping the simulation stable and the output current smoothly sinusoidal.

(n-1) → (n-0): Fig. 7.3c shows the effect of the reconnection of the outaged load at $t = 64.08$ s. Within the RTS, power flows are once again more evenly distributed throughout the grid, lowering the current on line 21A to 230.3 A_{rms}, resulting in a current amplitude of 41.7 A at the PA-output. The current is now lower than it was at the start of the experiment but since the impedance is still increased by the DSRs, the PA still has to keep the voltage amplitude at a higher level of 73.6 V.

DSR-deactivation: After the outage resolve, the DSRs are deactivated, dropping current and voltage to their initial states after a few transient periods, shown in Fig. 7.3d.

Overall, the PHIL-interface remained stable across the duration of the simulation and reflected the operation of a fleet of DSRs into the RTS. However, the breaching of PA limits upon DSR-activation was unexpected since previous software simulations showed current and voltage to remain below these thresholds. A possible explanation for this is the imperfect compensation of the setup impedance, which is only done manually in the beginning of the simulation. The transformer ratio amplifies any remaining impedance that is not fully compensated by a factor of $\left(\frac{250}{26}\right)^2 = 92.46$, so even a slipping impedance of only 0.01 Ω will be seen by the PAs as 0.92 Ω, requiring additional voltage to reach a given current setpoint. The compensation method should thus be improved, for example by an automated control loop. Additionally, to ensure the DSRs experience exactly the simulated current, the current on the power line stubs should be measured and fed back into the PHIL-interface instead of the PA output current since there might be losses in between PAs and DSRs that are unaccounted for in the described setup. This was not possible with the given laboratory environment since a PHIL-interface requires extremely fast and accurate measurements, that could only be provided by the optical-fiber-connected measuring of the PA output. Currents on the power lines were frequently measured manually using current clamps, assuring the currents were in fact equal to the simulated current.

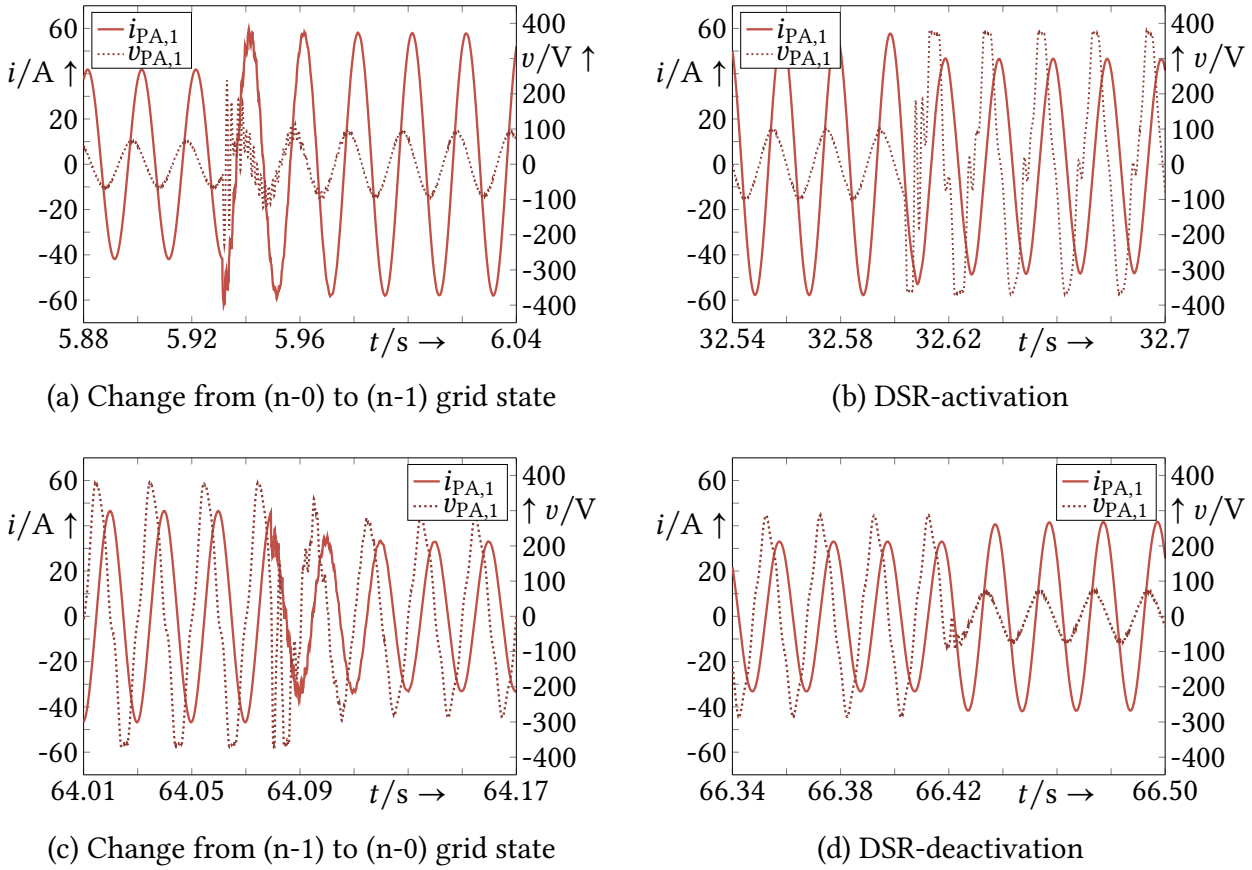

(a) Change from (n-0) to (n-1) grid state

(b) DSR-activation

(c) Change from (n-1) to (n-0) grid state

(d) DSR-deactivation

Figure 7.3: Performance of the PHIL-interface during TC1 (DSRs only)

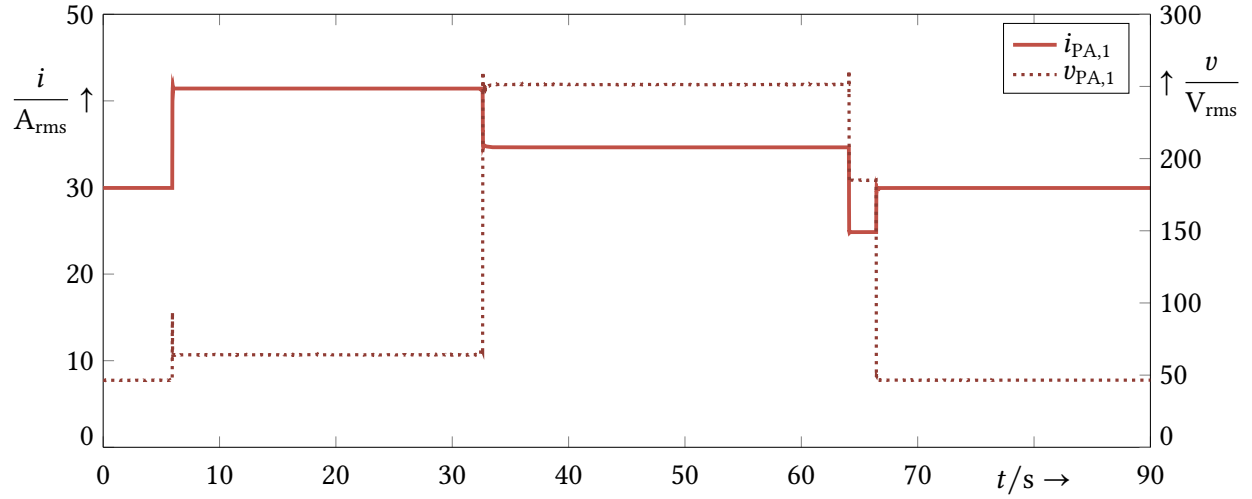

Figure 7.4: Power amplifier output during the entire TC1 (DSRs only)

7.3 TC 2: Coordination of distributed series reactors and flexible power units

In TC 2, GUC1 is applied and DSRs on line 21A are supposed to be coordinated with FPUs to solve the congestion. This is why all generators and loads, except those connected to the slack bus, are assumed to be ±90 % flexible in their power output. To achieve this, the influence of the DSRs is artificially decreased to 2.77 Ω using k_Z so that the overall amount of available additional reactance will not suffice to solve the congestion alone and FPUs will be needed, too. For this, k_Z would have to be decreased to around 0.5. Unfortunately, the minimum k_Z for this setup is 0.92 according to eq. (6.7). So instead, only one DSR is connected and k_Z is set to 1.5 – yielding the same effect as three DSRs with $k_\mathrm{Z} = 0.5$ but without the PA limitation breach. To ensure the MAS coordinates RMs offered by several agents, the generator's flexible power at n_2 is set to 0, forcing agent 2 to call for help from other agents if its DSRs do not suffice. The course of events is the same as in the previous TC, described in Section 7.2, except this time a different set of RMs needs to be activated. Also, the overall time for which D2 remains disconnected is longer for reasons that are unimportant for this section but will be explained in Subsection 7.4.3. The RTS measurements rate is again set to 1 Hz.

7.3.1 Congestion management and coordination feasibility

Once again, the MAS can resolve the congestion as required. Respective line utilizations over time as well as RM activations are shown in Fig. 7.5. Additionally, static grid states of the most important time steps and nodal power balances of nodes 1–5 can be found in the appendix in Fig. 8.6 and Fig. 8.7.

Upon detecting the congestion, agent 2 sends out a CFP to the other agents with the same content as in the previous TC and calculates the proposal for the DSR. With the changed PHIL-setup, the DSR now has an increased sensitivity of $\gamma^{\Delta\mathrm{X}}_{l_{21\mathrm{A}},\mathrm{DSR}} = -8.74\,\mathrm{MW}/\Delta\tau_\mathrm{step}$ – but only one step available. Thus, agent 2 concludes that after the DSR-activation a remaining $\Delta p_{l_{21\mathrm{A}}} = -11.68\,\mathrm{MW} + 8.74\,\mathrm{MW} = -2.93\,\mathrm{MW}$ will need to be solved by coordinated FPU-activation. Sorting and selecting FPUs according to the descriptions in Subsection 3.2.2.2, agent 2 orders agent 3, which offers FPUs with a PTDF of 0.32, to increase the load at node 3 by 6 MW while decreasing one of its generators by 3 MW. This combined generation decrease of −9 MW must be met by an equal generation increase. For this, only agent 1 is available as it is the only agent offering FPUs with a negative

sensitivity of −0.02 MW/MW. This small sensitivity does not contribute much to solving the congestion but it prevents frequency deviations by the generation decrease at n_3.

This time, the loading of line 21A is first lowered by DSR-activation at $t = 17.6$ s, followed by FPU-activations at nodes 1 and 3 until the congested line drops slightly below its target utilization of 70 % at $t = 21.3$ s, putting the duration for which the line utilization was above its target threshold at 15.3 s. The reasons for the faster reaction of the MAS in this case are explained in Section 7.4. Notably, the MAS does not overshoot the target threshold as much as in the first TC. This is because the FPUs have a lower sensitivity per step than the DSRs, which allows the agents to meet the target setpoint more precisely. Considering the FPUs' combined sensitivity of $0.32 + 0.02 = 0.34$, favoring DSR over FPU activation prevented the activation of approximately $2 \cdot |\pm 22\,\text{MW}| = 44\,\text{MW}$ of flexible power. Deactivation of previously activated RMs happens after the disconnected load is reconnected at $t = 104.3$ s over 11.1 s when all lines drop below their release thresholds.

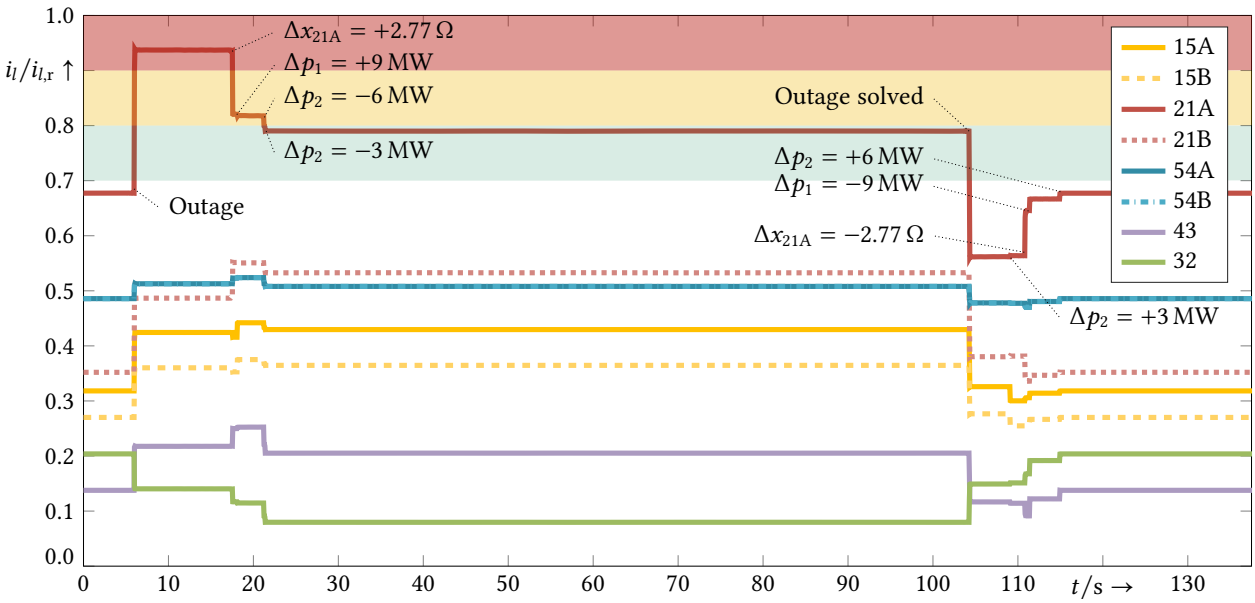

Figure 7.5: Line utilizations during TC2 (GUC1, $\Delta x_max = 2.77\,\Omega$)

7.3.2 PHIL functionality

To demonstrate the effects of the lower DSR reactance on the PHIL interface, the PA output during TC2 is shown in Figs. 7.6 and 7.7 and evaluated as follows. Up to the outage, results

are the same as before since no DSRs are active. When the DSR is activated, the voltage is only increased by 66.9 V_{rms} – which is unsurprisingly roughly a third of the previous voltage drop since only a third of the additional reactance is activated. The current drop however is not a third of the results seen in the previous test but almost half of it. This discrepancy is caused by k_Z and demonstrates well the advantages of the setup: within the simulation, the overall DSR reactance in TC2 is 2/3 of that in TC1, even though the physical reactance is only 1/3 of that in the first experiment. Since k_Z only affects the simulation but not the physical reactance, the effect of larger reactances on the grid can be evaluated without the need to have them physically in the laboratory or maxing out the PAs. This way, the voltage signal also stays much closer to a smooth sinusoidal curve in this experiment. The activation of flexible power at 21.4 s only changes the PA current setpoint but not the DSR reactance; current and voltage changes are thus proportional to each other. The reconnection of D2 and subsequent deactivation of RMs follows a similar pattern as before, albeit at lower absolute values.

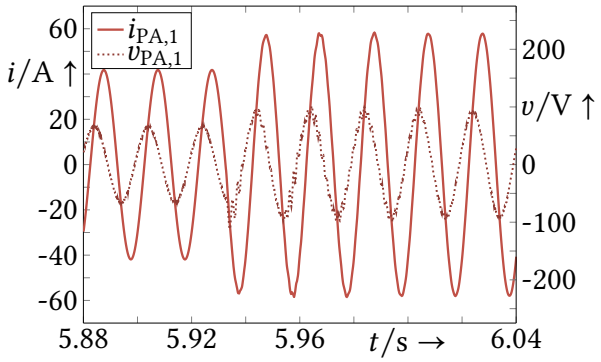

(a) Change from (n-0) to (n-1) grid state

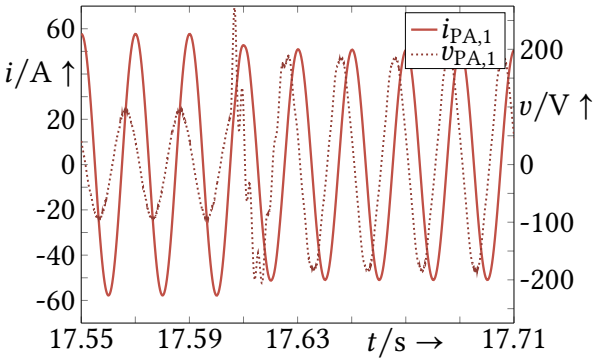

(b) DSR-activation

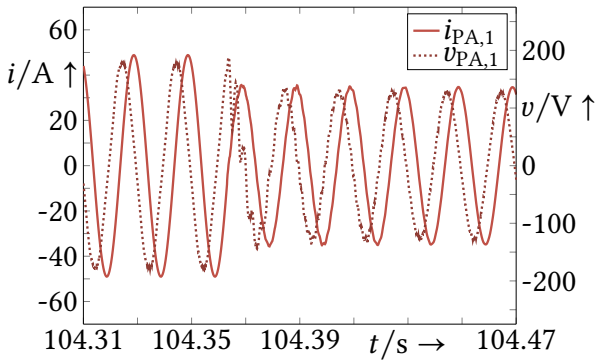

(c) Change from (n-1) to (n-0) grid state

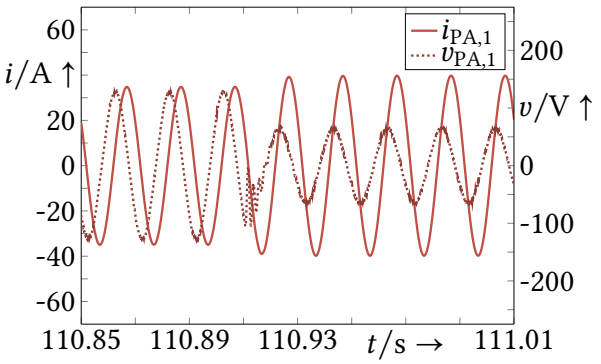

(d) DSR-deactivation

Figure 7.6: Performance of the PHIL-interface during TC2 (DSRs + FPUs)

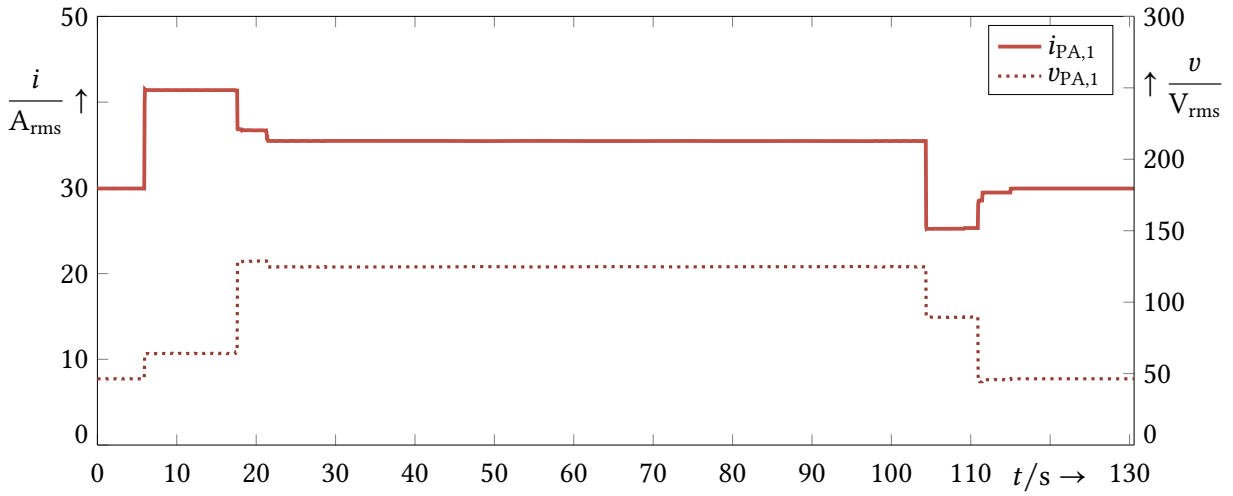

Figure 7.7: Power amplifier output during the entire TC2 (DSRs + FPUs)

7.4 Analysis of MAS reaction times

To answer research question ii, the examplary MAS reaction times measured in the laboratory are summarized in Table 7.1 and evaluated in this section. The agents' FSM state processes are put into sequence diagrams to identify time consuming tasks, quantify them with laboratory results, and estimate achievable reaction times via worst case analysis.

Table 7.1: Durations of processes executed by the MAS

Process	Variable	Duration TC1	Duration TC2
Detecting congestion			
Measuring	Δt_{meas}	50 µs	50 µs
IEC 104 sending rate	$\Delta t_{\mathrm{IEC104}}$	1 s	1 s
Monitoring function	Δt_{mon}	3 s	3 s
$\sum$	$\Delta t_{\mathrm{detect}}$	4 s	4 s
Solving congestion			
Initialize CFP	$\Delta t_{\mathrm{CFP,init}}$	10 s	7 s
Select & activate DSRs	$\Delta t_{\mathrm{CFP,DSR}}$	4 s	1 s
Select & activate FPUs	$\Delta t_{\mathrm{CFP,FPU}}$	-	4 s
$\sum$	Δt_{CFP}	17 s	15 s

7.4.1 Time needed to detect a congestion

The time an agent needs to detect a new grid state can be placed at 7.4 s, calculated with eq. (7.1) and explained as follows.

$$\Delta t_{\text{detect}} = \Delta t_{\text{meas}} + \Delta t_{\text{IEC104}} + 2 \cdot \Delta t_{\text{mon}} = 50\,\mu\text{s} + 1\,\text{s} + 2 \cdot 3.2\,\text{s} = 7.4\,\text{s} \tag{7.1}$$

At the beginning of a MAS reaction, all agents usually start in monitoring state. Within this state, the processes shown in Fig. 7.8 are looped. Here, the thread of one specific agent a in monitoring state is depicted on the left and the rest of the agents are aggregated in one thread on the righthand side. At t_0 a new grid state appears. First, the measurement devices detect this within their device-dependent measuring rate Δt_{meas} and then make these measurements available to the agents within their predefined IEC 104 sending rate Δt_{IEC104}. This rate is set for each device by the SO depending on their requirements and can range from milliseconds to minutes. Since agents execute their behaviors asynchronically to grid operations (and to each other), new measurements and SIMs may, in a worst case scenario, arrive at the agent right after it has started a new monitoring loop, in which case the agent will miss the new measurements. Thus, between the arrival of new measurements at t_2 and the analysis thereof by the agent at t_3, a full monitoring cycle with the duration Δt_{mon} may pass. During execution of the monitoring function, the agent reads newly arrived messages and updates its internal grid model with any information received from other agents and new local measurements, before communicating the updated grid state with the rest of the MAS via SIM-broadcast. The time needed for this process depends on the number of agents in the MAS that a exchanges messages with, as well as the number of grid devices in the agent's internal grid model. Since measurement devices were modeled without delay, measurements were taken at every step of the RTS, setting the measuring rate at the simulation step rate of the OPAL-RT simulator of $\Delta t_{\text{meas}} = \Delta t_{\text{RTS}} = 50\,\mu\text{s}$, effectively achieving instantaneous measuring. This value can be higher for real measurement devices, such as phasor measurement units, which can range from 0.005 s–1 s.

The IEC 104 cyclic sending interval Δt_{IEC104} can be set by the SO. For the MAS to react as quickly as possible, this sending rate should be set as fast as possible. However, as explained in Section 7.5, if the MAS is not only used as an emergency solution for unexpected contingencies to increase grid resilience, but as a means to increase grid utilization through automated CM, a fast sending rate could make the agents' behavior unpredictable for the operator if they get information faster than the CC. In the laboratory tests the

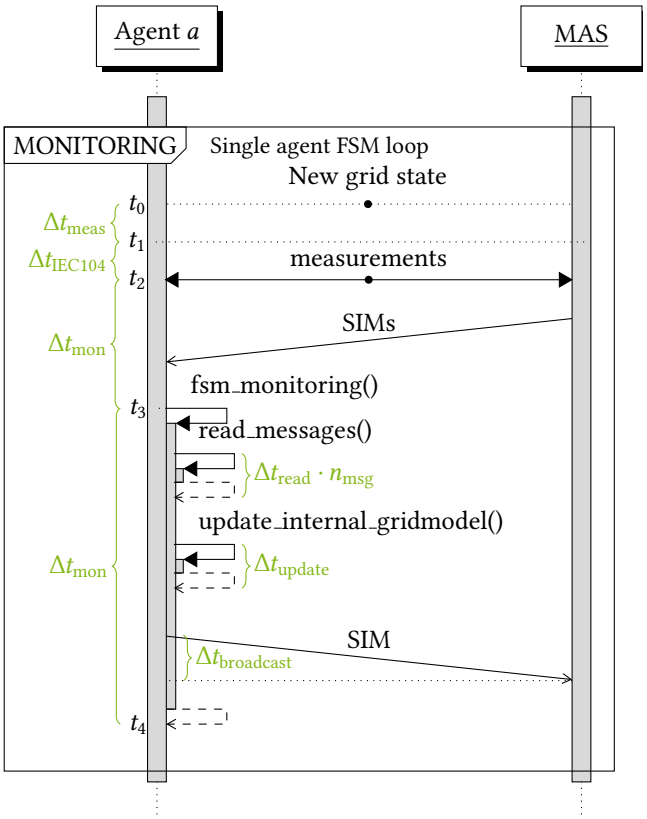

Figure 7.8: UML sequence diagram of one agent in MONITOR FSM-state

sending rate was set to $\Delta t_{IEC104} = 1$ s, which is slightly faster than the time a single agent needs to execute its monitoring behavior Δt_{mon}, making new measurements available to the agents virtually immediately.

The time needed for one agent to execute its monitoring function ranged from 3.0 s–3.2 s in the laboratory tests, depending on the amount of messages the agent received and the number of devices the agent needs to monitor. This duration comes with the caveat, that waiting times had to be implemented to give each agent time to receive new messages within the asynchronous communication scheme. These sleep times consisted of a 0.5 s after each message sent and a 0.8 s after each cycle. This overall waiting time of 2.8 s can likely be reduced significantly with a more sophisticated implementation of the basic MAS communication scheme and reducing the amount of exchanged data since this was not a main focus of this work and its influence on communication times was underestimated at the time of implementation. It should be noted that in implementations of previous works, the synchronous interaction between agents and grid simulation allowed the agents to thoroughly update their entire internal grid model in each cycle, including more time-consuming calculations such as updating the pseudo-inverted susceptance matrix. In a real-time application with asynchronous agent behavior execution, this is not

advisable since the agents will have to perform these calculations again upon entering CFP or proposing state anyways.

7.4.2 Time needed to solve a congestion

After the time needed to detect a congestion, the second part of the overall MAS reaction time is the time needed to solve this congestion. This is visualized in Fig. 7.9.

At t_0 a congestion occurs in the grid, which is detected by the CFP-initiating agent a after Δt_{detect} has passed at t_4 (the numbering is kept consistent here with Fig. 7.8). Agent a switches to CFP-state, broadcasts a CFP-message to all other agents, and immediately starts calculating proposals for countering the congestion using its own RMs. In the meantime, the other agents react to the CFP by switching to PROPOSE-state, calculating their proposals and then sending them to a. After all proposals have arrived at agent a, it will have to go through one additional monitoring loop to handle the most recent proposal messages before starting the DSR-selection at t_5. Agent a executes the selection process described in Subsection 3.2.2.1 and orders the respective agents to activate their proposed DSRs while potentially also activating its own. Afterwards, a checks for replies indicating whether the proposals have been successfully activated (DONE message) or not (REFUSE message). Only if all previously accepted proposals were answered with DONE messages, does a proceed to the FPU-selection process at t_6. Otherwise, a deletes failed measure activations from its proposal list and repeats the selection process without them.

The overall time needed for the activation of DSRs within the CFP-process is described with $\Delta t_{\text{CFP,DSR}}$ and is dependent on the amount of proposals received, the time needed to communicate with the respective measures (e.g. agents sending set points to DSRs), and how often measures fail to properly activate for any kind of reason. The FPU-activation takes the same course as the DSR-activation, except for the details described in Subsection 3.2.2.2. After the time $\Delta t_{\text{CFP,FPU}}$ has passed, meaning all accepted proposals have been successfully activated, or none are left, a switches either back into monitoring state or proceeds into active state if it activated any of its own measures.

Within the laboratory tests, the main process durations during the CFP state were determined as follows. Detecting the congestion took $\Delta t_{\text{detect}} = 3\,\text{s}$, followed by $\Delta t_{\text{CFP,init}} = 10\,\text{s}$ for initializing the CFP. Here, the agent-based advantage of parallel proposal calculation comes into effect, since the initialization process is only dependent on the maximum time one agent needed to calculate its proposals, instead of the sum of all proposal calculations,

as shown in eq. (7.2).

$$\Delta t_{\mathrm{CFP,init}} = \Delta t_{\mathrm{broadcast}} + \max\left(\Delta t_{\mathrm{pro},a}, \Delta t_{\mathrm{mon}} + \max\left(\Delta t_{\mathrm{pro,MAS}}\right)\right) + \Delta t_{\mathrm{mon}} \tag{7.2}$$

During this time, all agents had their proposals sent to agent 2 after $\Delta t_{\mathrm{broadcast}} + \Delta t_{\mathrm{mon}} + \Delta t_{\mathrm{pro,MAS,max}} = 7\,\mathrm{s}$, followed by 3 s needed for agent 2 to read the last messages. The DSRs were activated after another $\Delta t_{\mathrm{CFP,DSR}} = 13\,\mathrm{s}$. This duration is made up of the times needed for the selection process by a, activating selected DSRs, and communication between agents, as shown in eq. (7.3).

$$\Delta t_{\mathrm{CFP,DSR}} = \left(\Delta t_{\mathrm{sel,DSR}} + \max\left(\Delta t_{\mathrm{act,DSR,MAS}}\right) + \Delta t_{\mathrm{mon}}\right) \cdot n_{\mathrm{DSR,try}} \tag{7.3}$$

Note that no reiterations of the DSR-selection were necessary as the DSRs were activated by agent 2 on first try, but the setpoint was only changed $\Delta t_{\mathrm{act,DSR}} = 4\,\mathrm{s}$ after the agent sent the respective signal to the DSRs. In all the laboratory tests done in the course of this work, this DSR reaction delay ranged from 1 s–5 s and is apparently caused by the DSRs internal communication, i.e. the communication between Smart Wire Gateway, PowerLine Coordinator, and DSRs. There is also no process implemented in the agent code to verify the activation of measures; the agents only check whether there is an active communication connection available and assume setpoint changes sent to the devices will be activated without fail. The time needed to then select and activate FPUs is made up similarly, as eq. (7.4) shows.

$$\Delta t_{\mathrm{CFP,FPU}} = \left(\Delta t_{\mathrm{sel,FPU}} + \max\left(\Delta t_{\mathrm{act,FPU,MAS}}\right) + \Delta t_{\mathrm{mon}}\right) \cdot n_{\mathrm{FPU,try}} \tag{7.4}$$

Since the FPUs are modeled as simple power sources and sinks within the RTS, the real communication necessary to activate them stops at the OPAL-RT simulator and thus their selection and activation only required a total of $\Delta t_{\mathrm{CFP,FPU}} = 4\,\mathrm{s}$. This includes time needed for sending and reading activation messages between agents, which was not needed for activating the DSRs since they are controlled by the CFP-initiating agent.

7.4.3 Discussion of durations observed in laboratory tests

The absolute duration values presented in this chapter have to be understood as exemplary and not generally applicable. Not even with this exact laboratory setup did the experiments always take the exact same time. Several uncertainty factors influence the overall time that is necessary for the MAS to perform different tasks. This can be seen

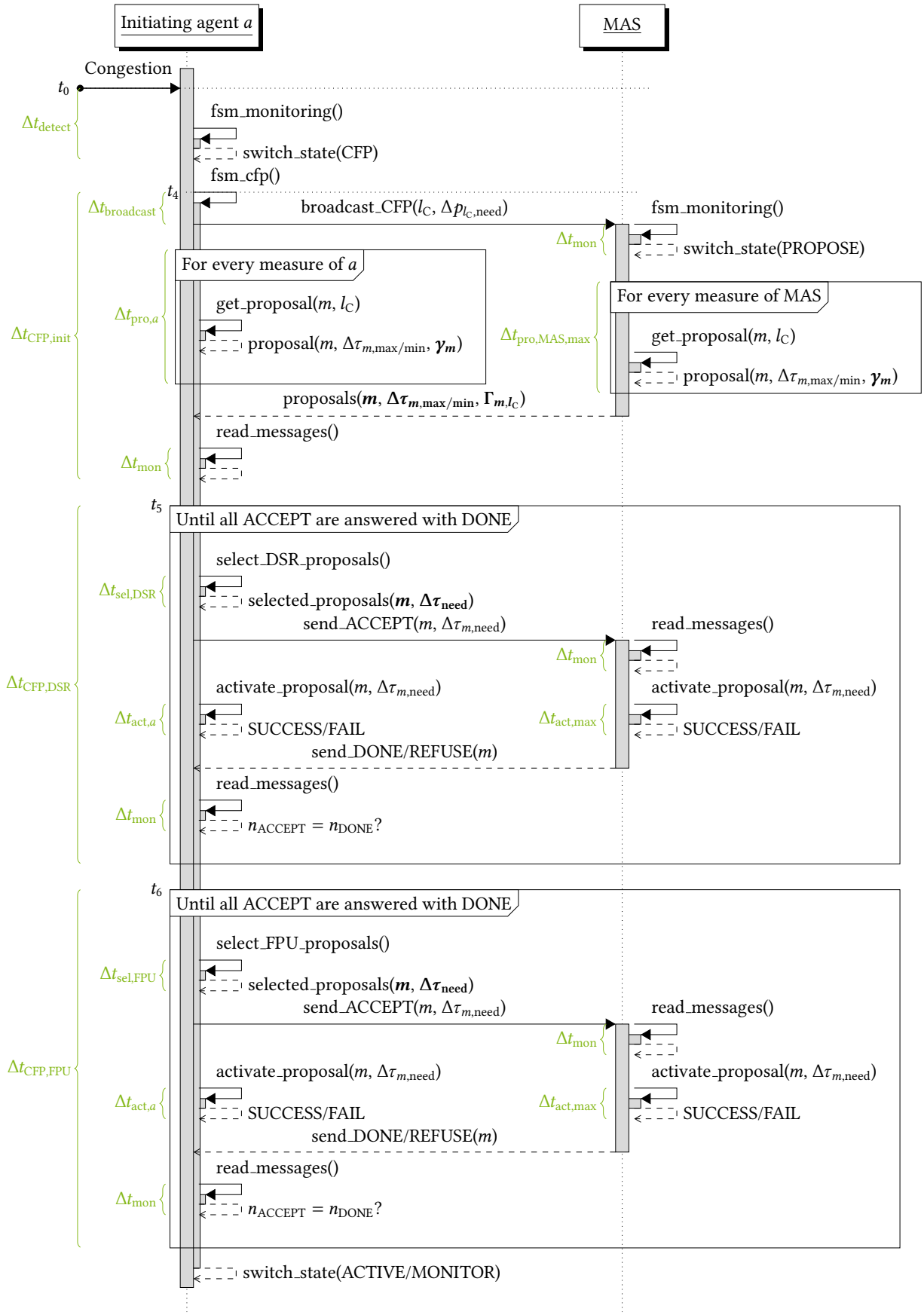

Figure 7.9: UML sequence diagram of one agent in CFP FSM-state

for example in the counter-intuitive phenomenon that solving the congestion took longer when only one RM had to be activated instead of multiple. The asynchronous agent execution can lead to such slight time deviations when the beginning and end of a task do not align perfectly with the arrival of new measurements or messages. Nonetheless, the durations seen in these tests are an indicator of what is possible with such a system.

The strong effect $\Delta t_{\mathrm{IEC104}}$ has on the MAS reaction times is depicted in Fig. 7.10. Here, the PHIL-simulation described in Section 7.3 is repeated three times with different sending rates. The loading of the congested line follows the same pattern as before but with a time offset for the two slower measurement update rates. The markers on the lines indicate when measurements were made available for the agents. Since $\Delta t_{\mathrm{mon}} > 1\,\mathrm{s}$, the case of $\Delta t_{\mathrm{IEC104}} = 1\,\mathrm{s}$ can be seen as a base case, showing only the reaction times of the MAS, since new measurements are virtually available at all times. Here, the minimum reaction time of the MAS is $\Delta t_{\mathrm{react}} = 11.3\,\mathrm{s}$. When $\Delta t_{\mathrm{IEC104}}$ is increased to 15 s, the MAS needs $\Delta t_{\mathrm{react}} = 23\,\mathrm{s}$ to react because the congestion is only detected 12 s after it occurred. With a measurement update rate of 30 s, this reaction time is increased to 46 s in this scenario. In the slowest scenario, DSRs were activated after FPUs due to the DSR reaction delays.

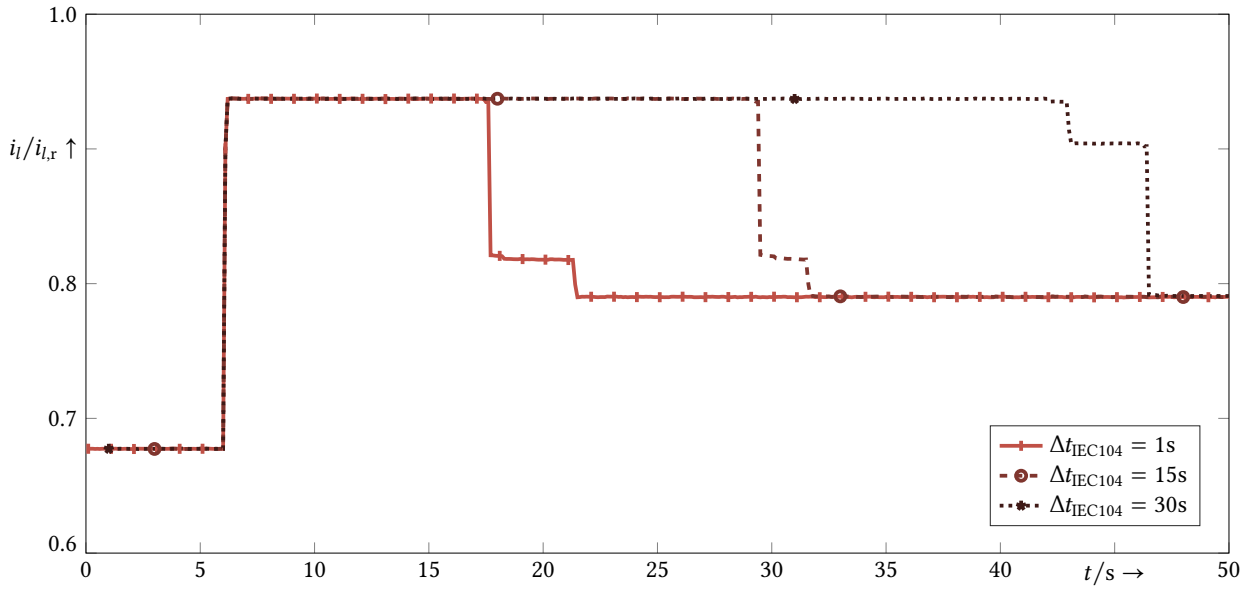

Figure 7.10: Congested line loading with different IEC 104 sending rates

In a worst case scenario the maximum reaction time of the described MAS – and to some extent of any similar automated ad-hoc CM system – can be summed up with eq. (7.5).

This equation is based on several assumptions:

- one of the proposing agents has the most measures at hand (and not the CFP-initiating agent): $\Delta t_{\text{pro},a} < \Delta t_{\text{mon}} + \Delta t_{\text{pro,MAS,max}}$
- rate of measurements is negligible: $\Delta t_{\text{meas}} = 0\,\text{s}$
- the agent with the most DSRs at its disposal controls at least one FPU, so it will have to calculate PTDFs and XCDFs: $\Delta t_{\text{pro,max}} = \Delta t_{\text{XCDF}} \cdot n_{\text{DSR,max}} + \Delta t_{\text{PTDF}}$

Eq. (7.5) shows how the overall MAS reaction time is made up of the times needed for detecting an overload, initializing a CFP, and selecting and activating RMs. Disecting these durations into the times needed for communication and calculations shows that only some parts of the overall time – namely the times needed for sending and reading messages and for calculating sensitivities – are dependent on the number of grid nodes. This allows the conclusion that the MAS is likely to scale well with grid size.

$$
\begin{aligned}
\Delta t_{\text{react}} &= t_{\text{trg}} - t_{\text{crt}} \\
&= \underbrace{\Delta t_{\text{meas}} + \Delta t_{\text{IEC104}} + 2\Delta t_{\text{mon}}}_{\Delta t_{\text{detect}}} + \underbrace{\Delta t_{\text{send}} \cdot n_{\text{N}} + 2\Delta t_{\text{mon}} + \Delta t_{\text{pro,max}}}_{\Delta t_{\text{CFP,init}}} \\
&\quad + \underbrace{\Delta t_{\text{sel,DSR}} + 2\Delta t_{\text{mon}} + \Delta t_{\text{DSR,act,max}}}_{\Delta t_{\text{CFP,DSR}}} + \underbrace{\Delta t_{\text{sel,FPU}} + 2\Delta t_{\text{mon}} + \Delta t_{\text{FPU,act,max}}}_{\Delta t_{\text{CFP,FPU}}} \\
&= \Delta t_{\text{IEC104}} + 8\Delta t_{\text{mon}} + \Delta t_{\text{send}} n_{\text{N}} + \Delta t_{\text{pro,max}} + \Delta t_{\text{sel,DSR}} + \Delta t_{\text{sel,FPU}} \\
&\quad + \Delta t_{\text{act,DSR,max}} + \Delta t_{\text{act,FPU,max}} \\
&= \underbrace{\Delta t_{\text{IEC104}} + n_{\text{N}}(9\Delta t_{\text{send}} + 8\Delta t_{\text{read}}) + \Delta t_{\text{act,DSR,max}} + \Delta t_{\text{act,FPU,max}}}_{\text{Communications}} \\
&\quad + \underbrace{\Delta t_{\text{XCDF}}(n_{\text{N}}) \cdot n_{\text{DSR,max}} + \Delta t_{\text{PTDF}}(n_{\text{N}}) + \Delta t_{\text{sel,DSR}} + \Delta t_{\text{sel,FPU}}}_{\text{Calculations}}
\end{aligned}
\tag{7.5}
$$

In the end, the MAS reactions in the laboratory tests were significantly slower than assumed in previous pure software simulations (cp. Section 5.2), i.e. within seconds rather than milliseconds. The centralized RM selection operated on a similar time scale in Chapter 4 but for a much larger grid. Therefore, a significant time advantage of an agent-based approach due to its distribution of calculation efforts in comparison to a centralized implementation could not be proven in this work. However, the reaction times are still easily fast enough to relieve congestions early enough to prevent damage of equipment: in [9],

the curative timeframes are, for example, set to 2 min and 15 min, depending on the type of measure. Additionally, there are also obvious improvements that can be made to decrease the reaction times even further. First of all, the agent implementation in C++ can certainly be improved upon to increase execution performance. After all laboratory tests had already been performed, some improvements were implemented within the code's communication module, mostly to reduce listening times to receive messages, resulting in a reduction of Δt_{mon} from 3 s to 0.5 s. With the resulting decreased monitoring time Δt_{mon}, the sending rate Δt_{IEC104} can also be reduced – if this is in line with CC requirements. Another factor that was not directly addressed in the laboratory tests is the large amount of agents a CFP-initiating agent would have to correspond with in a real grid – even though most of them will have no beneficial measures available due to the large electrical distance between them and the congestion. Work in this regard has been done in the past (cp. [85]) but needs to be re-evaluated within laboratory or field tests.

7.5 TC 3: MAS control center integration

For the MAS, or any other type of automated PFC tool, to be safely applied in a real grid, the SO needs appropriate tools to monitor this new system and interact with it. The monitoring functions needed consist not only of live agent status surveillance but also tools to predict agent behavior to planned and unplanned events such as busbar couplings or outages. To create such an agent behavior prediction tool the processes described in Chapter 3 were implemented by PSI in the SCADA systems in the laboratory in the course of the IDEAL project. As interaction functions, the operator needs a way to pause the execution of agent behavior in emergencies, and switch the system from autonomous to semi-autonomous mode, in which agents only calculate RMs but only present them to the operator instead of activating them themselves. This way, an operator can ensure the MAS does not interfere with their day-to-day operations and also integrate and utilize the MAS within operational processes.

This section shows exemplary results of the CC demonstrator described in Chapter 6 to answer research question iii. Parts of these results were presented first in [OP9].

In this TC, applying GUC2, no DSRs are available and all generators and loads are ±30 % flexible in their power output. Since the DSR module is not used here, a regular line outage of line 21B is applied, overloading line 21A. Note that the thresholds in this test were chosen with smaller bandwidths of $c_{\text{crt}} = 0.9$, $c_{\text{trg}} = 0.85$, and $c_{\text{rls}} = 0.8$.

For demonstration purposes the storyline here goes as follows: During the operational

planning phase, the SO in the CC performs a contingency analysis for the next day. The SCADA tools show that there is a contingency the next day at a specific time (the visualization of this in PSIcontrol can be found in the appendix in Fig. 8.8): If line 21B trips, 21A will be loaded above its critical threshold at 96.51 %. However, with the extensions implemented to forecast the MAS reaction, the operator can see that the agents will be able to reduce this overload to 85.81 % by decreasing the generation at node 2 by 12 MW, while increasing the load at this node by 2 MW and simultaneously increasing the generation at node 1 by 12 MW while decreasing the load by 2 MW. As the prognosis shows only a small target threshold breach, the operator decides not to apply preventive RMs.

The next day, line 21B actually does trip, causing line 21A to breach its critical threshold. Agent 2 detects this and broadcasts a CFP, causing the other agents to calculate and send in their RM proposals. After all proposals have been received, agent 2 heuristically selects the best options to create a power flow reduction of $\Delta p_{l_{21A},\text{need}} = -8.3\,\text{MW}$. It determines its own proposals to be the most effective with a sensitivity of $\gamma^{\Delta P}_{21A,n_2} = 0.77$, meaning agent 2 will have to decrease generation at its own bus. To match this with an appropriate generation increase, agent 2 needs to select a proposal with a lower sensitivity. The best option is agent 1 with a sensitivity of $\gamma^{\Delta P}_{21A,n_1} = -0.02$. Thus, agent 2 lowers the output of its generator by 11 MW and orders agent 1 to increase generation by 11 MW, creating an overall power flow change of $\Delta p_{l_{21A}} = -8.7\,\text{MW}$. All of this is visualized in Fig. 7.11.

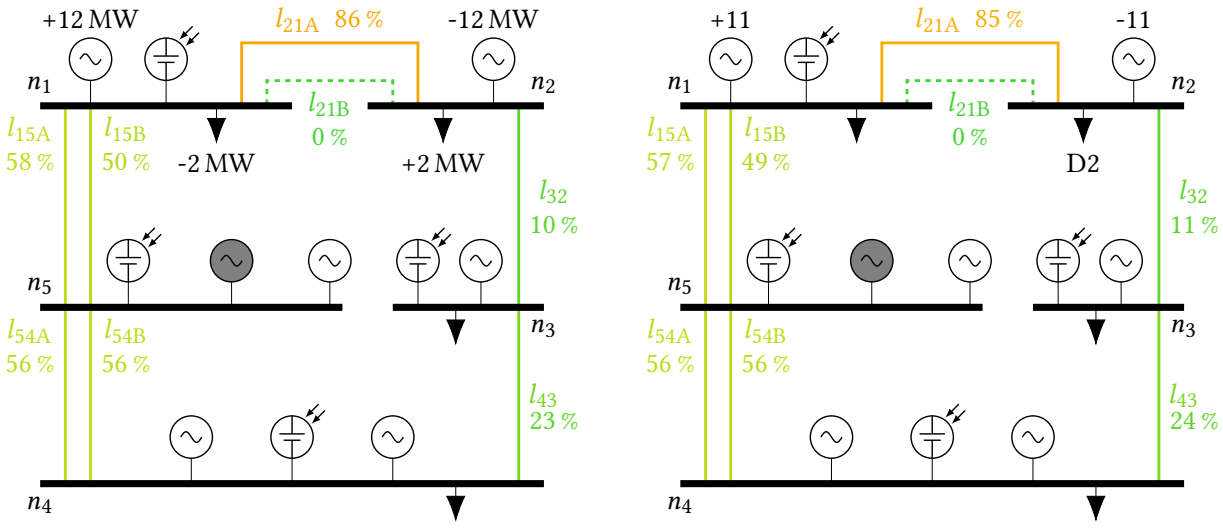

(a) Prognosis of grid state after RM-activation

(b) Actual grid state after activation of RMs

Figure 7.11: Static grid states as expected by thecontrol center and after MAS reaction

The contingency analysis slightly over-estimates the flexible power needed to reduce the overload. This is likely due to the over-estimation of line loading caused by the outage at 97 % instead of 93 %. A reason for this may be small discrepancies in grid modeling and the different power flow calculation cores used in the CC and the RTS. However, the prognosis is accurate regarding sensitivities and location of flexible units activated – and both prognosis and measured results show that the congestion is solved by the MAS. The operator's SCADA tools can easily integrate the agents' actions with only a single additional column in the contingency analysis to distinguish visually between *n-1 before remedial actions* and *n-1 after remedial actions*. If additional information about the remedial actions is needed, the operator can refer to the agent dashboard visualizations available at every agent-equipped node in the grid. Additionally, the operator can switch the MAS into semi-autonomous mode during which the operator will only receive a notification of where the agents propose to change a DSR or FPU setpoint – but without activating this change autonomously. If the operator fears for any reason that the MAS may not be able to activate the proposed measures in time post-fault, the prognosis tool can also be used manually to quickly determine RMs to be activated preventively.

7.6 Conclusions regarding the agent-based system's real world applicability

- The developed distributed CM system was tested in the described laboratory setup.
- The PHIL interface operated close to its maximum current, indicating the need for test use cases with larger buffers regarding maximum currents unless laboratory infrastructure with higher current ratings are available.
- The ad-hoc curative CM functionality of the MAS in real-time applications was confirmed by the tests.
- Real-time reaction was at 11 s–46 s higher than assumed in previous works (milliseconds), but still far below critical times regarding TATL currents (2 min–15 min).
- The MAS can be neatly integrated into CC environments but this requires both systems to use the exact same grid model and calculation approaches.

8 Summary, conclusion and outlook

In this chapter, the results of this thesis are summarized under the consideration of the research questions *i*–*iv* derived in Chapter 1. Furthermore, an outlook towards future research is given to conclude this dissertation.

8.1 Conclusion

The overall goal of this dissertation is to analyze under a practice-oriented approach how novel impedance-controlling devices can be coordinated with flexible power in an automated curative CM system to improve utilization of existing grid infrastructure and secure power supply under unforeseen outages. While ICs have been used for CM in the past, their coordination with FPUs in an ad-hoc curative CM system is a novel approach in this work. Likewise, agent-based control systems for curative CM have been analyzed in the past but the concept for their utilization in a real-time application within a laboratory environment including CC integration is unique to this dissertation.

Research question *i* covers the topic of *how ICs and FPUs can be coordinated post-fault to ensure fast and reliable CM.* For this, first DC power flow based sensitivities called XCDFs are defined to determine the effect of gradual impedance changes on power flows in the grid. Then, a heuristic CM algorithm is developed and four variants of it are presented and tested in software simulations. The variants differ within the way how they assume linear additivity of the XCDFs. Here, a trade-off is highlighted between the accuracy of the calculated RM combination and the time needed to determine this combination. The linearization error made is small enough to justify the usage of the derived sensitivities for realistic ranges of impedance changes between 0 %–30 %. To improve accuracy without investing significantly more time, sensitivity re-calculation can be done after an IC's capacity is used up within the algorithm, but a reconsideration of an already maxed-out device at a later point does not improve the result and is therefore not recommended. A sensitivity re-calculation after each IC-step is also not encouraged, as the significantly larger calculation times outweigh the small improvements regarding outcome accuracy. The same is true for applying an optimization approach instead of a heuristic.

The actual *real-time speed of an automated system utilizing such a heuristic CM approach* is concerned in research question *ii*. For this, an elaborate laboratory environment was installed, consisting of an HV grid RTS with a PHIL-interface to three DSRs and a CHIL-

interface to an agent-based curative CM system. While the reaction times achieved within this setup are not directly transferable to real grid applications without the consideration of additional real world factors such as grid size and number of available controllable devices, they give an indication to what is at least possible. The CM system reaction times monitored in the laboratory ranged between 11 s–46 s. The largest influence on this time is the measurement device update rate. If the system is used for wide are monitoring and control to protect the grid against inadmissibly long overcurrents after unforeseen outages, measurement devices should obviously send updated values as fast as possible, preferably faster than one agent's update cycle (which means 1 s in the laboratory). If the system is supposed to increase grid utilization under the assumption of a loosened-up (n-1) criterion, the measurement update rate has to be aligned with the needs of the CC operator to ensure the agents do not react unpredictably. In both cases, the reaction times are fast enough to prevent irreparable damage from current-driven equipment overheating.

A laboratory-sized CC enabled the demonstration of *how such an automated CM system can be integrated into a state-of-the-art CC environment*, as was asked in research question *iii*. Besides easy-to-use and -understand graphical interfaces, an operator needs to be able to predict MAS behavior. For this, a centralized version of the heuristic used by the agents can be implemented and coupled to the SCADA tools, for example as an enhancement to the (n-1) calculation. The laboratory tests showed that such a centralized implementation can determine the outcome of the agents' decision making process, but the congruency of grid models used by the centralized and decentralized systems is vital for the prediction's accuracy.

Lastly, research question *iv* asked *how the agents should react in case of partial communication outages among them.* This is answered by implementing robust MAS fallback strategies and testing them in software simulations. Within this approach, agents cut off from the rest of the system do not change their controllable RMs' setpoints anymore to not disturb the control actions of the rest of the system, which might still be operational. The rest of the agents try to extrapolate line currents in unobservable areas from other measurements that are still available, allocate still functional agents to monitor these estimated line data, and include these lines in their overall CM processes. The outage of single agents can be covered by this simple yet robust approach without significant differences in MAS behavior. This underlines the advantage of the redundancy within the distributed agent approach and also offers a possibility to determine the minimum amount of agents needed to cover a grid.

8.2 Outlook

The results of this thesis point towards further research demand in the following areas.

Several approaches of how to deal with the XCDF linearization error are given in the heuristics described in Chapter 3. However, a direct eradication of this error ex-ante could only be hinted at in Section 4.2. An analytical investigation in this regard could potentially improve the XCDF accuracy and facilitate their utilization and combination together with common DC power flow based sensitivities such as PTDFs.

The heuristic algorithm could be improved by considering more detailed FPU flexibility models, i.e. not just a unit's maximum and minimum active and reactive power setpoints, but more detailed operational diagrams as described in [11]. Additionally, by including the indicators derived in Section 3.3 as constraints or additional objectives within the problem description, the heuristics could be tuned towards them. The next step in CM research in general would be to properly flesh out the necessary SO-interfaces of the system described in this thesis, including not just flexibility de-/aggregation methods but also communication and data exchange between the involved SOs to integrate this system into the recently implemented processes of redispatch 2.0.

The MAS has come a long way since its inception, as described in Section 5.2 but can yet be improved upon. It could be enhanced by artificial intelligence approaches to identify or predict outages and congestions as well as agent behavior during communication outages to improve the described fallback strategies. Also, the inclusion of thermal line models to determine the time left before TATL is reached could improve the MAS efficiency. A simplification made in this work is the assumption that the SO can freely control the FPUs and remuneration is out of scope. In reality, different operators would have to interact to enable agent-control over these units, and business models for the remuneration of flexibility activation would have to be derived and integrated into the coordination. Furthermore, while the laboratory tests did consider real communication between state-of-the-art hardware devices, cyber security concerns have been neglected. Before such a distributed system can be applied in the field, extensive research in regards of its security vulnerabilities must be executed.

The laboratory setup described here is quite extensive, covering one versatile power- and multiple controller-HIL interfaces, but can yet be improved. The FPUs were modeled only as controlled power sinks or sources; new setpoints were realized immediately. A more realistic approach would cover more detailed load and generator models, including ramp-functions and possibly discrete stepping of certain devices. This could have significant

influence on the reaction times and the RM accuracy towards solving congestions.

Finally, from a TRL perspective, the next step for testing of the described system, would be its application in the field. However, more extensive HIL simulations with the additions suggested above are recommended first.

References

[1] German Transmission System Operators. *Netzentwicklungsplan Strom 2035, second draft* (cit. on pp. 1–2, 9, 19).

[2] C. Rehtanz. "Dynamic Power Flow Controllers for transmission corridors". In: *2007 iREP Symposium - Bulk Power System Dynamics and Control - VII. Revitalizing Operational Reliability*. 2007, pp. 1–9. DOI: 10.1109/IREP.2007.4410515 (cit. on pp. 1, 16, 19–20).

[3] C. Thomas and J. Ham. "A Case Study on the Use of D-FACTS Devices to Support Construction of New Transmission Facilities". In: *Cigre US National Committee 2015 Grid of the Future Symposium*. 2015 (cit. on pp. 2, 22).

[4] K. Krommydas, A. Stratigakos, C. Dikaiakos, G. Papaioannou, M. Jones, and G. McLoughlin. "A Novel Modular Mobile Power Flow Controller for Real-Time Congestion Management Tested on a 150kV Transmission System". In: *IEEE Access* 10 (Sept. 2022), pp. 96414–96426. DOI: 10.1109/ACCESS.2022.3205589 (cit. on p. 2).

[5] Smart Wires Inc. *Installations*. URL: https://www.smartwires.com/case-studies/ (visited on 05/31/2024) (cit. on pp. 2, 23).

[6] R. Moreno, D. Pudjianto, and G. Strbac. "Transmission Network Investment With Probabilistic Security and Corrective Control". In: *IEEE Transactions on Power Systems* 28.4 (2013), pp. 3935–3944. DOI: 10.1109/TPWRS.2013.2257885 (cit. on pp. 3, 18).

[7] M. Braun, H. Hoppe-Oehl, J. König, A. Kubis, M. Lindner, I. Löser, C. Rehtanz, R. Schwerdfeger, and W. Wellßow. *Systematisierung der Autonomiestufen in der Netzbetriebsführung*. VDE Impuls. 2020 (cit. on pp. 3, 18).

[8] A. Hoffrichter, K. Kollenda, M. Schneider, and R. Puffer. "Simulation of Curative Congestion Management in Large-Scale Transmission Grids". In: *2019 54th International Universities Power Engineering Conference (UPEC)*. 2019, pp. 1–6. DOI: 10.1109/UPEC.2019.8893627 (cit. on pp. 3, 17).

[9] K. Kollenda, A. Schrief, C. Biele, M. Lindner, N. Sundorf, A. Hoffrichter, A. Roehder, A. Moser, and C. Rehtanz. "Curative measures identification in congestion management exploiting temporary admissible thermal loading of overhead

lines". In: *IET Generation, Transmission & Distribution* 16.16 (2022), pp. 3171–3183. DOI: 10.1049/gtd2.12512 (cit. on pp. 3, 17, 133).

[10] J. Hachenberger, R. Kuesters, A. Kubis, T. Rzymek, M. Abel, C. Greiten, A. Gumbel, R. Schwerdfeger, A. Wasserrab, and P. Hoffmann. "Development of a Preventive and Curative Congestion Management Module for Close to Real-Time Transmission System Operations". In: *ETG Congress 2021*. 2021, pp. 1–6 (cit. on pp. 3, 17).

[11] F. Rewald. "Engpassmanagement mit Flexibilitäten in Mittel- und Niederspannungsnetzen bei unsicheren Netzzuständen". German. PhD thesis. Technische Universität Dortmund, 2021. 151 pp. ISBN: 978-3-8440-8256-2 (cit. on pp. 4, 71, 139).

[12] European Commission. "Commission Regulation (EU) 2015/1222 of 24 July 2015 establishing a guideline on capacity allocation and congestion management". In: *OJ* L 197 (2015), pp. 24–72 (cit. on pp. 7, 9–10).

[13] European Union Agency for the Cooperation of Energy Regulators (ACER). *Methodology for coordinated redispatching and countertrading for the Core CCR*. ACER Decision on Core RDCT Methodology. 2020 (cit. on p. 7).

[14] Bundesnetzagentur für Elektrizität, Gas, Telekommunikation, Post und Eisenbahnen (BNetzA). *Engpassmanagement*. URL: https://www.bundesnetzagentur.de/DE/Fachthemen/ElektrizitaetundGas/Versorgungssicherheit/Netzengpassmanagement/Engpassmanagement/start.html (visited on 05/31/2024) (cit. on p. 7).

[15] Union for the Co-ordination of Transmission of Electricity (UCTE). *UCTE Operational Handbook - Policy 3: Operational Security*. 2009 (cit. on pp. 8, 14).

[16] P. Fekete. *Fakten - Redispatch in Deutschland*. Ed. by BDEW Bundesverband der Energie- und Wasserwirtschaft e.V. URL: https://www.bdew.de/media/documents/2021_Q2_Bericht_Redispatch.pdf (visited on 05/31/2024) (cit. on pp. 8, 11).

[17] European Commission, Joint Research Centre, G. Antonopoulos, S. Vitiello, G. Fulli, and M. Masera. *Nodal pricing in the European internal electricity market*. Publications Office of the European Union, 2020. DOI: 10.2760/41018 (cit. on p. 8).

[18] European Commission. "Commission Regulation (EU) 2017/1485 of 2 August 2017 establishing a guideline on electricity transmission system operation". In: *OJ* L 220 (2017), pp. 1–169 (cit. on pp. 9–11).

[19] *Energiewirtschaftsgesetz of 07.07.2005 (BGBl. I S. 1970, 3621)*. last changed by Article 1 of the law of 8. July 2022 (BGBl. I S. 1054) (cit. on pp. 10, 12).

[20] H. Schermeyer. "Netzengpassmanagement in regenerativ geprägten Energiesystemen". German. PhD thesis. Karlsruher Institut für Technologie (KIT), 2018. 170 pp. DOI: 10.5445/IR/1000086513 (cit. on p. 10).

[21] T. van Leeuwen, A.-K. Meinerzhagen, S. Raths, and A. Roehder. "Integration kurativer Maßnahmen in das Engpassmanagement im deutschen Übertragungsnetz". In: *Symposium Energieinnovation*. Vol. 16. Graz, Österreich: Graz University of Technology, Feb. 2020, pp. 1–11 (cit. on pp. 10–11, 14, 16).

[22] Agency for the Cooperation of Energy Regulators (ACER). *Methodology for coordinating operational security analysis*. 2019 (cit. on pp. 11, 13).

[23] European Commission. "Commission Regulation (EU) No 543/2013 of 14 June 2013 on submission and publication of data in electricity markets". In: *OJ* L 163 (2013), pp. 1–12 (cit. on p. 12).

[24] European Network of Transmission System Operators for Electricity (ENTSO-E). *Dynamic Line Rating for overhead lines – V6: CE TSOs current practice*. Mar. 2015 (cit. on p. 12).

[25] *Netzausbaubeschleunigungsgesetz Übertragungsnetz of 28. July 2011 (BGBl. I S. 1690)*. last changed by Article 6 of the law of 20. July 2022 (BGBl. I S. 1325) (cit. on p. 12).

[26] BDEW Bundesverband der Energie- und Wasserwirtschaft e.V. *Anwendungshilfe - Netzbetreiberkoordinationskonzept für Redispatch 2.0* (cit. on pp. 12, 14).

[27] P. M. Anderson and B. K. LeReverend. "Industry experience with special protection schemes". In: *IEEE Transactions on Power Systems* 11.3 (1996), pp. 1166–1179. DOI: 10.1109/59.535588 (cit. on p. 14).

[28] Cigre Task Force 38.02.19. "System Protection Schemes in Power Networks". In: *International Conference on Large High Voltage Electric Systems*. Ed. by Cigre. 2001 (cit. on p. 15).

[29] J. Mccalley, O. Olatujoye, V. Krishnan, R. Dai, C. Singh, and K. Jiang. *System Protection Schemes: Limitations, Risks, and Management*. Dec. 2010. DOI: 10.13140/RG.2.1.1946.3842 (cit. on p. 15).

[30] D. Westermann and H. Sauvain. “Power system operation with wide area control including real time atc calculation and power flow control”. In: *2009 IEEE Bucharest PowerTech*. 2009, pp. 1–5. DOI: 10.1109/PTC.2009.5281847 (cit. on p. 15).

[31] Bundesministerium für Wirtschaft und Energie (BMWi). *Bundesbericht Energieforschung 2020*. Berlin (cit. on p. 15).

[32] J. Kamsamrong. *RD3.0 - Redispatch 3.0*. 2021. URL: www.offis.de/offis/projekt/rd30.html (visited on 05/31/2024) (cit. on p. 15).

[33] C. Krueger, M. Otte, S. Holly, S. Rathjen, A. Wellssow, and S. Lehnhoff. “Redispatch 3.0 - Congestion Management for German Power Grids - Considering Controllable Resources in Low-Voltage Grids”. In: *ETG Congress 2023*. 2023, pp. 1–7. ISBN: 978-3-8007-6108-1 (cit. on p. 15).

[34] CORESO SA. *Yearly Activity Report 2022* (cit. on p. 16).

[35] A. Monticelli, M. V. F. Pereira, and S. Granville. “Security-Constrained Optimal Power Flow with Post-Contingency Corrective Rescheduling”. In: *IEEE Transactions on Power Systems* 2.1 (1987), pp. 175–180. DOI: 10.1109/TPWRS.1987.4335095 (cit. on p. 16).

[36] S. Kohler, A.-C. Agricola, and H. Seidl. *dena-Netzstudie II. Integration erneuerbarer Energien in die deutsche Stromversorgung im Zeitraum 2015 - 2020 mit Ausblick 2025*. Ed. by Deutsche Energie-Agentur GmbH. Berlin (cit. on p. 16).

[37] T. Brown, P.-P. Schierhorn, E. Tröster, and T. Ackermann. “Optimising the European transmission system for 77 percent renewable electricity by 2030”. In: *IET Renewable Power Generation* 10.1 (2016), pp. 3–9. DOI: 10.1049/iet-rpg.2015.0135 (cit. on p. 16).

[38] M. Gathmann. *The world’s first dynamic control center*. URL: https://www.siemens.com/global/en/company/stories/infrastructure/2019/dynamic-power-grid.html (visited on 05/31/2024) (cit. on p. 16).

[39] A. Shokri Gazafroudi, F. Neumann, and T. Brown. “Topology-based approximations for N-1 contingency constraints in power transmission networks”. In: *International Journal of Electrical Power & Energy Systems* 137 (2022). ISSN: 0142-0615. DOI: 10.1016/j.ijepes.2021.107702 (cit. on p. 16).

[40] K. Kamps, F. Möhrke, K. F. Schäfer, M. Zdrallek, A. Wasserrab, R. Schwerdfeger, and M. Thiele. "Modelling and Risk Assessment of Special Protection Schemes in Transmission Systems". In: *2020 International Conference on Probabilistic Methods Applied to Power Systems (PMAPS)*. 2020, pp. 1–6. DOI: 10.1109/PMAPS47429.2020.9183639 (cit. on p. 16).

[41] J. L. Calvo, S. H. Tindemans, and G. Strbac. "Incorporating failures of System Protection Schemes into power system operation". In: *Sustainable Energy, Grids and Networks* 8 (2016), pp. 98–110. ISSN: 2352-4677. DOI: 10.1016/j.segan.2016.10.002 (cit. on p. 16).

[42] K. J. Ross, K. M. Hopkinson, and M. Pachter. "Using a Distributed Agent-Based Communication Enabled Special Protection System to Enhance Smart Grid Security". In: *IEEE Transactions on Smart Grid* 4.2 (2013), pp. 1216–1224. DOI: 10.1109/TSG.2013.2238261 (cit. on p. 17).

[43] M. Lindner, D. Mende, A. Wasserrab, I. Sacar, M. Ariatabar, C. Lakenbrink, T. van Leeuwen, M. Lassig, and U. Hager. "Corrective Congestion Management in Transmission Grids Using Fast-Responding Generation, Load and Storage". In: *2021 IEEE Electrical Power and Energy Conference (EPEC)*. IEEE, 2021, pp. 1–6. ISBN: 978-1-6654-2928-3. DOI: 10.1109/EPEC52095.2021.9621491 (cit. on p. 17).

[44] F. Sass, A. Rothstein, V. Staudt, and D. Westermann. "Critical contingency management based on characteristic fault pattern for AC-HVDC-systems". In: *13th IET International Conference on AC and DC Power Transmission (ACDC 2017)*. 2017, pp. 1–6. DOI: 10.1049/cp.2017.0042 (cit. on p. 17).

[45] F. Sass, T. Sennewald, C. Brosinsky, D. Westermann, M. Mangold, C. Heyde, S. Becher, and R. Krebs. "Control Center Implementation of Advanced Optimization and Decision Support Applications". In: *2018 International Conference on Smart Energy Systems and Technologies (SEST)*. 2018, pp. 1–6. DOI: 10.1109/SEST.2018.8495658 (cit. on pp. 17–18).

[46] E. Glende, P. Trojan, I. Hauer, A. Naumann, C. Brosinsky, M. Wolter, and D. Westermann. "Communication Infrastructure for Dynamic Grid Control Center with a Hardware-in-the-Loop Model". In: *2018 IEEE PES Innovative Smart Grid Technologies Conference Europe (ISGT-Europe)*. 2018, pp. 1–6. DOI: 10.1109/ISGTEurope.2018.8571464 (cit. on pp. 17–18, 68).

[47] F. Sass, T. Sennewald, and D. Westermann. “Automated Corrective Actions by VSC-HVDC-Systems: A Novel Remedial Action Scheme”. In: *IEEE Transactions on Power Systems* 35.1 (2020), pp. 385–394. DOI: 10.1109/TPWRS.2019.2928887 (cit. on pp. 17–18).

[48] J. Kayser, S. Schlegel, and D. Westermann. “Activation of Curative Actions as Contribution to System Security in DC-Interconnected Distribution Systems”. In: *2020 IEEE Power Energy Society General Meeting (PESGM)*. 2020, pp. 1–5. DOI: 10.1109/PESGM41954.2020.9281632 (cit. on pp. 17–18).

[49] T. Sennewald, F. Linke, and D. Westermann. “Preventive and Curative Actions by Meshed Bipolar HVDC-Overlay-Systems”. In: *IEEE Transactions on Power Delivery* 35.6 (2020), pp. 2928–2936. DOI: 10.1109/TPWRD.2020.3011733 (cit. on pp. 17–18).

[50] International Electrotechnical Commission (IEC). *IEC 62032:2012(E) (IEEE Std C57.135-2011) Guide for the Application, Specification, and Testing of Phase-Shifting Transformers*. Tech. rep. International Electrotechnical Commission (IEC), 2012, pp. 1–44. DOI: 10.1109/IEEESTD.2012.6238289 (cit. on p. 19).

[51] European Network of Transmission System Operators for Electricity (ENTSO-E). *Technology Factsheets*. URL: https://eepublicdownloads.entsoe.eu/clean-documents/RDC%20documents/2021_Technology%20Factsheet.pdf (visited on 05/31/2024) (cit. on pp. 19–20).

[52] J. Verboomen, D. Van Hertem, P. H. Schavemaker, W. L. Kling, and R. Belmans. “Analytical Approach to Grid Operation With Phase Shifting Transformers”. In: *IEEE Transactions on Power Systems* 23.1 (2008), pp. 41–46. DOI: 10.1109/TPWRS.2007.913197 (cit. on p. 19).

[53] F. Kreikebaum, D. Das, Y. Yang, F. Lambert, and D. Divan. “Smart Wires - A distributed, low-cost solution for controlling power flows and monitoring transmission lines”. In: *2010 IEEE PES Innovative Smart Grid Technologies Conference Europe (ISGT Europe)*. 2010, pp. 1–8. DOI: 10.1109/ISGTEUROPE.2010.5638853 (cit. on pp. 19, 21).

[54] N. G. Hingorani. “High Power Electronics and flexible AC Transmission System”. In: *IEEE Power Engineering Review* 8.7 (1988), pp. 3–4. ISSN: 0272-1724. DOI: 10.1109/MPER.1988.590799 (cit. on p. 19).

[55] IEEE. "IEEE Guide for Technology of Unified Power Flow Controller Using Modular Multilevel Converter-Part 2: Terminology". In: *IEEE Std 2745.2-2021* (2021), pp. 1–25. DOI: 10.1109/IEEESTD.2021.9525319 (cit. on pp. 19–20).

[56] ABB AB FACTS Sweden. *TCSC Thyristor Controlled Series Compensation - Keeping grids together*. URL: library.e.abb.com/public/fdf0b019e1fe08a48325771f002dbfc5/A02-0158.pdf (visited on 05/31/2024) (cit. on p. 20).

[57] IEEE. "IEEE Guide for Technology of Unified Power Flow Controller Using Modular Multilevel Converter - Part 1: Functions". In: *IEEE Std 2745.1-2019* (2019), pp. 1–87. DOI: 10.1109/IEEESTD.2019.8913755 (cit. on p. 20).

[58] P. K. Bhatt. "Smart Wires and Modular FACTS Controllers for Smart Grid Applications: A Review". In: *Journal of Electrical Engineering and Automation* 3.4 (2021), pp. 286–304. DOI: 10.36548/jeea.2021.4.004 (cit. on pp. 20–21).

[59] U. Häger, K. Görner, and C. Rehtanz. "Hardware model of a Dynamic Power Flow Controller". In: *2011 IEEE Trondheim PowerTech*. 2011, pp. 1–6. DOI: 10.1109/PTC.2011.6019397 (cit. on p. 20).

[60] A. Spina, R. Palaniappan, D. Hilbrich, U. Häger, and C. Rehtanz. "Comparison between CHIL simulation and hardware test of a Dynamic Power Flow Controller". In: *2017 IEEE Manchester PowerTech*. 2017, pp. 1–6. DOI: 10.1109/PTC.2017.7980968 (cit. on p. 20).

[61] D. Divan and H. Johal. "Distributed FACTS - A New Concept for Realizing Grid Power Flow Control". In: *IEEE Transactions on Power Electronics* 22.6 (2007), pp. 2253–2260. DOI: 10.1109/TPEL.2007.909252 (cit. on pp. 20, 22).

[62] D. M. Divan, W. E. Brumsickle, R. S. Schneider, B. Kranz, R. W. Gascoigne, D. T. Bradshaw, M. R. Ingram, and I. S. Grant. "A Distributed Static Series Compensator System for Realizing Active Power Flow Control on Existing Power Lines". In: *IEEE Transactions on Power Delivery* 22.1 (2007), pp. 642–649. DOI: 10.1109/TPWRD.2006.887103 (cit. on p. 20).

[63] Smart Wires Inc. *PowerLine Guardian SD4 MD4 LD4 Spec Sheet - Version 170619*. Union City, CA, 2019 (cit. on p. 21).

[64] Smart Wires Inc. *SmartValve 10-1800 v1.04 (Technical Specifications)*. 2021 (cit. on p. 23).

[65] Smart Wires Inc., ed. *FARCROSS IPTO Smart Valve Installation Sept 2021 3*. 2021. URL: https://www.smartwires.com/wp-content/uploads/2021/10/FARCROSS-IPTO-Smart-Valve-Installation-Sept-2021-3-scaled.jpg (visited on 05/31/2024) (cit. on p. 23).

[66] D. Van Hertem, J. Verboomen, K. Purchala, R. Belmans, and W. Kling. "Usefulness of DC power flow for active power flow analysis with flow controlling devices". In: *Studies in Surface Science and Catalysis - STUD SURF SCI CATAL*. Apr. 2006, pp. 58–62. ISBN: 0-86341-613-6 (cit. on p. 26).

[67] B. Stott, J. Jardim, and O. Alsac. "DC Power Flow Revisited". In: *IEEE Transactions on Power Systems* 24.3 (2009), pp. 1290–1300. ISSN: 0885-8950. DOI: 10.1109/TPWRS.2009.2021235 (cit. on pp. 26, 32).

[68] K. Van den Bergh, E. Delarue, and W. D'haeseleer. *DC power flow in unit commitment models*. TME Working Paper - Energy and Environment, Last update: May 2014. KU Leuven Energy Institute, 2014 (cit. on p. 26).

[69] L. Robitzky, S. C. Müller, S. Dalhues, U. Häger, and C. Rehtanz. "Agent-based redispatch for real-time overload relief in electrical transmission systems". In: *2015 IEEE Power Energy Society General Meeting*. 2015, pp. 1–5. DOI: 10.1109/PESGM.2015.7285886 (cit. on pp. 46, 48, 68).

[70] G. C. Ejebe and B. F. Wollenberg. "Automatic Contingency Selection". In: *IEEE Transactions on Power Apparatus and Systems* PAS-98.1 (1979), pp. 97–109. DOI: 10.1109/TPAS.1979.319518 (cit. on p. 50).

[71] R. D. Zimmerman, C. E. Murillo-Sánchez, and R. J. Thomas. "MATPOWER: Steady-State Operations, Planning, and Analysis Tools for Power Systems Research and Education". In: *IEEE Transactions on Power Systems* 26.1 (2011), pp. 12–19. DOI: 10.1109/TPWRS.2010.2051168 (cit. on p. 53).

[72] T. Athay, R. Podmore, and S. Virmani. "A Practical Method for the Direct Analysis of Transient Stability". In: *IEEE Transactions on Power Apparatus and Systems* PAS-98.2 (1979), pp. 573–584. DOI: 10.1109/TPAS.1979.319407 (cit. on p. 53).

[73] Y. Sabri, N. El Kamoun, and F. Lakrami. "A Survey: Centralized, Decentralized, and Distributed Control Scheme in Smart Grid Systems". In: *2019 7th Mediterranean Congress of Telecommunications (CMT)*. 2019, pp. 1–11. DOI: 10.1109/CMT.2019.8931370 (cit. on pp. 65–66).

[74] H. Li, H. Sun, J. Wen, S. Cheng, and H. He. "A Fully Decentralized Multi-Agent System for Intelligent Restoration of Power Distribution Network Incorporating Distributed Generations [Application Notes]". In: *IEEE Computational Intelligence Magazine* 7.4 (2012), pp. 66–76. DOI: 10.1109/MCI.2012.2215152 (cit. on p. 65).

[75] S. D. J. McArthur, E. M. Davidson, V. M. Catterson, A. L. Dimeas, N. D. Hatziargyriou, F. Ponci, and T. Funabashi. "Multi-Agent Systems for Power Engineering Applications - Part I: Concepts, Approaches, and Technical Challenges". In: *IEEE Transactions on Power Systems* 22.4 (2007), pp. 1743–1752. DOI: 10.1109/TPWRS.2007.908471 (cit. on pp. 65–66).

[76] R. van Lon and T. Holvoet. "When do agents outperform centralized algorithms?" In: *Autonomous Agents and Multi-Agent Systems* 31.6 (2017), pp. 1578–1609. ISSN: 1387-2532. DOI: 10.1007/s10458-017-9371-y (cit. on p. 65).

[77] C. Rehtanz. *Autonomous Systems and Intelligent Agents in Power System Control and Operation*. Springer, 2003. ISBN: 9783540402022 (cit. on p. 67).

[78] U. Häger, S. Lehnhoff, C. Rehtanz, and H. F. Wedde. "Multi-Agent System for Coordinated Control of Facts Devices". In: *2009 15th International Conference on Intelligent System Applications to Power Systems*. 2009, pp. 1–6. DOI: 10.1109/ISAP.2009.5352945 (cit. on p. 67).

[79] U. Häger, A. Seack, C. Rehtanz, S. Lehnhoff, T. Zimmermann, and H. F. Wedde. "Applicability of coordinated power flow control based on multi-agent systems". In: *2010 IREP Symposium Bulk Power System Dynamics and Control - VIII (IREP)*. 2010, pp. 1–8. DOI: 10.1109/IREP.2010.5563276 (cit. on p. 67).

[80] U. Häger. "Agent-based Real-time Coordination of Power Flow Controllers". PhD thesis. Technical University of Dortmund, 2013. 149 pp. ISBN: 9783868445077 (cit. on p. 67).

[81] S. C. Müller, U. Häger, and C. Rehtanz. "A Multiagent System for Adaptive Power Flow Control in Electrical Transmission Systems". In: *IEEE Transactions on Industrial Informatics* 10.4 (2014), pp. 2290–2299. DOI: 10.1109/TII.2014.2315499 (cit. on p. 67).

[82] *FIPA Contract Net Interaction Protocol Specification*. standard. Geneva, CH: Foundation for Intelligent Physical Agents (FIPA), Mar. 2002 (cit. on pp. 68, 96).

[83] L. Robitzky, S. Dalhues, M. Albrecht, S. C. Müller, U. Häger, and C. Rehtanz. "Agent-based prevention of voltage collapse in electrical transmission systems". In: *2016 Power Systems Computation Conference (PSCC)*. 2016, pp. 1–7. DOI: 10.1109/PSCC.2016.7540915 (cit. on p. 68).

[84] N. Dorsch, F. Kurtz, S. Dalhues, L. Robitzky, U. Häger, and C. Wietfeld. "Intertwined: Software-defined communication networks for multi-agent system-based Smart Grid control". In: *2016 IEEE International Conference on Smart Grid Communications (SmartGridComm)*. 2016, pp. 254–259. DOI: 10.1109/SmartGridComm.2016.7778770 (cit. on p. 68).

[85] S. Dalhues, L. Robitzky, U. Häger, N. Dorsch, F. Kurtz, and C. Wietfeld. "Analysis of real-time coordination of distributed power flow controllers using software-defined networking communication". In: *2018 IEEE Power Energy Society Innovative Smart Grid Technologies Conference (ISGT)*. 2018, pp. 1–5. DOI: 10.1109/ISGT.2018.8403388 (cit. on pp. 68, 134).

[86] Y. Han, K. Zhang, H. Li, E. A. A. Coelho, and J. M. Guerrero. "MAS-Based Distributed Coordinated Control and Optimization in Microgrid and Microgrid Clusters: A Comprehensive Overview". In: *IEEE Transactions on Power Electronics* 33.8 (2018), pp. 6488–6508. DOI: 10.1109/TPEL.2017.2761438 (cit. on p. 68).

[87] P. Trojan. "Agent-based provision of system services". PhD thesis. Otto-von-Guericke-Universität Magdeburg, 2018. 165 pp. (cit. on p. 68).

[88] A. A. Babalola, R. Belkacemi, and S. Zarrabian. "Real-Time Cascading Failures Prevention for Multiple Contingencies in Smart Grids Through a Multi-Agent System". In: *IEEE Transactions on Smart Grid* 9.1 (2018), pp. 373–385. ISSN: 1949-3053. DOI: 10.1109/TSG.2016.2553146 (cit. on p. 68).

[89] J. Mohammadi, S. Kar, and G. Hug. "Fully distributed corrective security constrained optimal power flow". In: *2017 IEEE Manchester PowerTech*. 2017, pp. 1–6. DOI: 10.1109/PTC.2017.7981066 (cit. on pp. 68–69).

[90] Gesamtverbund InnoSys 2030. *InnoSys 2030 - Innovationen in der Systemführung bis 2030: Der InnoSys-Systemführungsprozess*. July 2022 (cit. on p. 70).

[91] J. C. Mankins. *Technology Readiness Levels – A White Paper*. Ed. by N. Aeronautics and S. A. (NASA). 2004 (cit. on p. 70).

[92] European Network of Transmission System Operators for Electricity (ENTSO-E). *ENTSO-E Technopedia - TRLs*. URL: https://www.entsoe.eu/Technopedia/trls/ (visited on 05/31/2024) (cit. on p. 70).

[93] European Commission. *adopting the 2014-2015 work programme in the framework of the Specific Programme Implementing Horizon 2020 – The Framework Programme for Research and Innovation (2014-2020)*. implementing decision. July 2014 (cit. on p. 70).

[94] J. Niemela and M. Fisher. "The Use of Technology Readiness Levels for Software Development". In: *Army Acquisition Logistics & Technology*. Vol. May-June. Department of the Army (USA), 2004, pp. 10–14 (cit. on p. 70).

[95] *FIPA ACL Message Structure Specification*. standard. Geneva, CH: Foundation for Intelligent Physical Agents (FIPA), Mar. 2002 (cit. on pp. 74, 96).

[96] F. Bellifemine, G. Caire, and D. Greenwood. *Developing Multi-Agent Systems with JADE*. John Wiley & Sons, 2004. ISBN: 978-0-470-05747-6 (cit. on p. 84).

[97] A. Spina and C. Rehtanz. "Power hardware-in-the-loop testbeds for advances laboratory testing of smart grid applications". In: *at - Automatisierungstechnik* 70.12 (2022), pp. 1034–1046. DOI: 10.1515/auto-2022-0084 (cit. on p. 91).

[98] A. Spina. "Advanced laboratory testing of smart grid applications with power hardware-in-the-loop approach". PhD thesis. Technische Universität Dortmund, 2021. DOI: 10.17877/DE290R-22399 (cit. on p. 91).

[99] *Transmission Protocols - Network access for IEC 60870-5-101 using standard transport profiles*. Standard. International Electrotechnical Commission (IEC), July 2018 (cit. on pp. 92, 94).

[100] R. Olsen. *QTester104*. 2019. URL: https://github.com/riclolsen/qtester104 (cit. on p. 94).

[101] PSI GridConnect GmbH. *Datasheet Smart Telecontrol Unit: Gateway for Secure Smart Grids*. Ed. by PSI GridConnect GmbH (cit. on p. 95).

[102] PSI GridConnect GmbH. *IEC 104 Security Proxy: Secure process interfacing & cyber protection*. Ed. by PSI Software AG. 2019. URL: https://www.psigridconnect.com/fileadmin/files/downloads/PSI_GridConnect/marketing/Flyer_IEC104_SecProxy_V4_20190201_en.pdf (visited on 05/31/2024) (cit. on p. 95).

[103] *FIPA Agent Management Specification*. standard. Geneva, CH: Foundation for Intelligent Physical Agents (FIPA), Mar. 2004 (cit. on p. 96).

[104] *Leitungsseile: Aluminium-Stahl-Seile*. Standard. Deutsches Institut für Normung e. V. (DIN), Apr. 1984 (cit. on p. 97).

[105] *Leiter für Freileitungen: Leiter aus konzentrisch verseilten runden Drähten*. Standard. Deutsches Institut für Normung e. V. (DIN), 2001 (cit. on p. 97).

[106] EGSTON System Electronics Eggenburg GmbH. *COMPISO System Unit 100-2 GAMP 4*. Ed. by EGSTON System Electronics Eggenburg GmbH. URL: https://www.egstonpower.com/portfolio/csu100/ (visited on 05/31/2024) (cit. on pp. 98, 100).

[107] Berufsgenossenschaft Energie Textil Elektro Medienerzeugnisse. *DGUV Vorschrift 15 / Unfallverhütungsvorschrift Elektromagnetische Felder: BGV B11* (cit. on p. 98).

[108] W. Ren, M. Steurer, and T. L. Baldwin. "Improve the Stability and the Accuracy of Power Hardware-in-the-Loop Simulation by Selecting Appropriate Interface Algorithms". In: *IEEE Transactions on Industry Applications* 44.4 (2008), pp. 1286–1294. DOI: 10.1109/TIA.2008.926240 (cit. on pp. 106–107).

[109] R. Kentchim. *Spezifikation: Aufbau und Anbindung des PSI-Leitsystems an den Labor-Demonstrator, Forschungsprojekt IDEAL*. Ed. by PSI Software AG. 2019 (cit. on p. 112).

[110] M. Anello and A. Del Rosso. "Optimal placement, sizing and control of distributed series reactor to improve system reliability". In: *2017 IEEE PES Innovative Smart Grid Technologies Conference - Latin America (ISGT Latin America)*. 2017. DOI: 10.1109/ISGT-LA.2017.8126721.

Scientific publications

[OP1] O. Pohl, F. Rewald, S. Dalhues, P. Jörke, C. Rehtanz, C. Wietfeld, A. Kubis, R. K. Tamgue, and D. Kirsten. "Advancements in Distributed Power Flow Control". In: *2018 53rd International Universities Power Engineering Conference (UPEC)*. 2018, pp. 1–6. DOI: 10.1109/UPEC.2018.8542100 (cit. on pp. 3, 71).

[OP2] M. Lindner, J. Peper, N. Offermann, C. Biele, M. Teodosic, O. Pohl, J. Menne, and U. Häger. "Operation strategies of battery energy storage systems for preventive and curative congestion management in transmission grids". In: *IET Generation, Transmission & Distribution* 17.3 (2023), pp. 589–603. DOI: 10.1049/gtd2.12739 (cit. on p. 17).

[OP3] S. Dalhues, O. Pohl, B. Lüttecken, T. Schwierz, U. Häger, and S. C. Müller. "Optimal Positioning and Sizing of Power Flow Controllers Using a Scenario Based SCOPF Approach". In: *2021 IEEE Madrid PowerTech*. 2021, pp. 1–6. DOI: 10.1109/PowerTech46648.2021.9494817 (cit. on pp. 19, 39, 57).

[OP4] O. Pohl, S. Dalhues, and C. Rehtanz. "DC-sensitivities for impedance controllers in an agent-based power flow control system". In: *2018 IEEE Power Energy Society Innovative Smart Grid Technologies Conference (ISGT)*. 2018, pp. 1–5. DOI: 10.1109/ISGT.2018.8403390 (cit. on pp. 30, 53).

[OP5] H. Ibrahim, O. Pohl, and U. Häger. "Comparison of Different Heuristic Algorithms in a Centralized Implementation of a Distributed Power Flow Control System". In: *8th International Youth Conference on Energy*. 2022, pp. 1–6 (cit. on p. 57).

[OP6] J. Hinker, O. Pohl, and J. Myrzik. "Impact assessment of inhabitants on the economic potential of energy efficient refurbishment by means of a novel socio-technical multi-agent simulation". In: 7th International Conference on Energy and Environment of Residential Buildings, November 20-24 2016, Brisbane, Australia, 2016. DOI: 10.4225/50/5810785526981 (cit. on p. 67).

[OP7] F. Rewald, O. Pohl, U. Häger, and C. Rehtanz. "State Estimation and Determination of Flexibility Potential in Medium Voltage Networks*". In: *EPJ Web Conf.* 217 (2019), p. 01013. DOI: 10.1051/epjconf/201921701013 (cit. on p. 71).

[OP8] A. Spina, O. Pohl, U. Häger, and C. Rehtanz. "A Power Hardware-in-the-Loop Setup for Testing Distributed Series Reactors". In: *2020 AEIT International Annual Conference (AEIT)*. IEEE, 2020, pp. 1–6. ISBN: 978-8-8872-3747-4. DOI: 10.23919/AEIT50178.2020.9241165 (cit. on pp. 97, 100–101).

[OP9] O. Pohl, R. Kentchim, L. Hito, H. Ibrahim, O. Al Samman, U. Häger, A. Kubis, and M. Heine. "Integrating an autonomous agent-based power flow control system into control center software". In: *VDE ETG-Congress 2021*. Ed. by VDE ETG. IEEE, 2021 (cit. on pp. 112, 134).

[OP10] J. Hinker, O. Pohl, and J. M. A. Myrzik. "How thermal comfort affects the energy-efficiency gap in residential buildings". In: *2015 50th International Universities Power Engineering Conference (UPEC)*. 2015, pp. 1–6. DOI: 10.1109/UPEC.2015.7339790.

[OP11] O. Pohl, A. Spina, and U. Häger. "Demonstration of automated curative power flow control with a multi-agent system using distributed series reactors in a PHIL simulation". In: *Electric Power Systems Research* 211 (2022), p. 108422. ISSN: 0378-7796. DOI: 10.1016/j.epsr.2022.108422.

[OP12] S. Dalhues, Y. Zhou, O. Pohl, F. Rewald, F. Erlemeyer, D. Schmid, J. Zwartscholten, Z. Hagemann, C. Wagner, D. M. Gonzalez, H. Liu, M. Zhang, J. Liu, C. Rehtanz, Y. Li, and Y. Cao. "Research and practice of flexibility in distribution systems: A review". In: *CSEE Journal of Power and Energy Systems* 5.3 (2019), pp. 285–294. DOI: 10.17775/CSEEJPES.2019.00170.

[OP13] O. Kraft, O. Pohl, U. Häger, K. Heussen, N. Müller, Z. Afzal, M. Ekstedt, H. Farahmand, D. Ivanko, A. Singh, S. Leksawat, and A. Kubis. "Development and Implementation of a Holistic Flexibility Market Architecture". In: *2022 IEEE Power Energy Society Innovative Smart Grid Technologies Conference (ISGT)*. 2022, pp. 1–5. DOI: 10.1109/ISGT50606.2022.9817470.

Supervised project groups

[PG1] P. Frasheri. "Implementation of agent-based communication between remote terminal units". Project Group. TU Dortmund University, Aug. 2019 (cit. on p. 96).

[PG2] L. Spies, G. M. Djifack, and V. Thomas. "Alternativen zur klassischen (n-1) Sicherheit im internationalen Vergleich". Project Group. TU Dortmund University, Sept. 2020.

Supervised bachelor theses

[BA1] H. Ibrahim. “Zentralisierte Nachbildung eines Multi-Agenten Systems zur Leistungsflussregelung in Hochspannungsnetzen”. Bachelor Thesis. TU Dortmund University, Nov. 2021 (cit. on p. 57).

[BA2] H. H. Satouf. “Entwicklung einer Methodik zur Bewertung des Einsatzes flexibler Leistung zur Auflösung von Engpässen in elektrischen Verteilnetzen”. Bachelor Thesis. TU Dortmund University, Oct. 2020.

[BA3] O. Al Samman. “Bestimmung des Betriebsbereichs einer Power Hardware-in-the-Loop Testumgebung”. Bachelor Thesis. TU Dortmund University, July 2021.

[BA4] A. Bröckling. “Erweiterung der Sensitivitätsberechnung für Impedanzregler mit Hilfe zusätzlicher Informationen über den Netzbetriebszustand”. Bachelor Thesis. TU Dortmund University, Aug. 2021.

Supervised master theses

[MA1] B. Lüttecken. “Entwicklung eines Verfahrens zur optimalen Positionierung von Impedanzreglern in Hochspannungsnetzen”. Master Thesis. TU Dortmund University, June 2019.

[MA2] B. Schmitz. “Koordinierung des Einsatzes mehrerer leistungsflussregelnder Betriebsmittel im Hochspannungsnetzbetrieb”. Master Thesis. TU Dortmund University, Dec. 2019.

[MA3] A. Soennecken. “Entwicklung von Fallback-Strategien für ein autonomes, agentenbasiertes Leistungsflussregelungssystem”. Master Thesis. TU Dortmund University, Dec. 2020.

Acronyms

List of symbols and indices

Throughout this dissertation, the following writing conventions are applied.

1. Variables (as well as indices and exponents that can be numbers) are italic: var
2. Descriptive indices or exponents are non-italic: p_{N} (N describes the *nodal* character of p)
3. A scalar value is a small, non-bold letter: s
4. A vector is a small, bold letter: $\boldsymbol{v}$
5. A matrix is a capital, bold letter: $\boldsymbol{M}$
6. A set is a capital, non-bold letter in calligraphic font: $\mathcal{S}$

Symbol	Meaning
$\boldsymbol{A}$	Incidence matrix
b	Susceptance
c	Line loading threshold OR element in inverted susceptance matrix
d	Direction of flexible power change OR a specific grid device
D	Diagonal matrix indicator (index)
g	Electrical conductance
G	Transfer function
H	Magnetic field strength
i	Current OR start node of a power line l
j	End node of a power line l
k	Scaling factor OR counting variable
l	Power line
m	(Remedial) measure
n	Node
n_{T}	Transformer turns ratio
p	Active power
q	Reactive power
r	Resistance OR radius
r	Rated (index)
s	Apparent power
t	Time
v	Voltage OR start node of power line λ with impedance change
w	End node of power line λ with impedance change
x	Reactance
y	Admittance
z	Impedance

Symbol	Meaning
γ	Sensitivity
$\gamma^{\Delta \mathrm{P}}$	Power Transfer Distribution Factor
$\gamma^{\Delta \mathrm{X}}$	Reactance Change Distribution Factor
δ	Voltage angle
ε	Linearization error
Δ	Change of following variable
η	Efficiency indicator
θ	Voltage angle difference
κ	Cost
λ	Power line with impedance change applied to it
τ	Setpoint (of a remedial measure)
χ	Severity indicator
ψ	Accuracy indicator
▲	Measure at top of list sorted by sensitivity (index)
▼	Measure at bottom of list sorted by sensitivity (index)
⧫	Combined measure (index)

List of Figures

List of Tables

Appendix

A.1 Grid model for HIL simulations

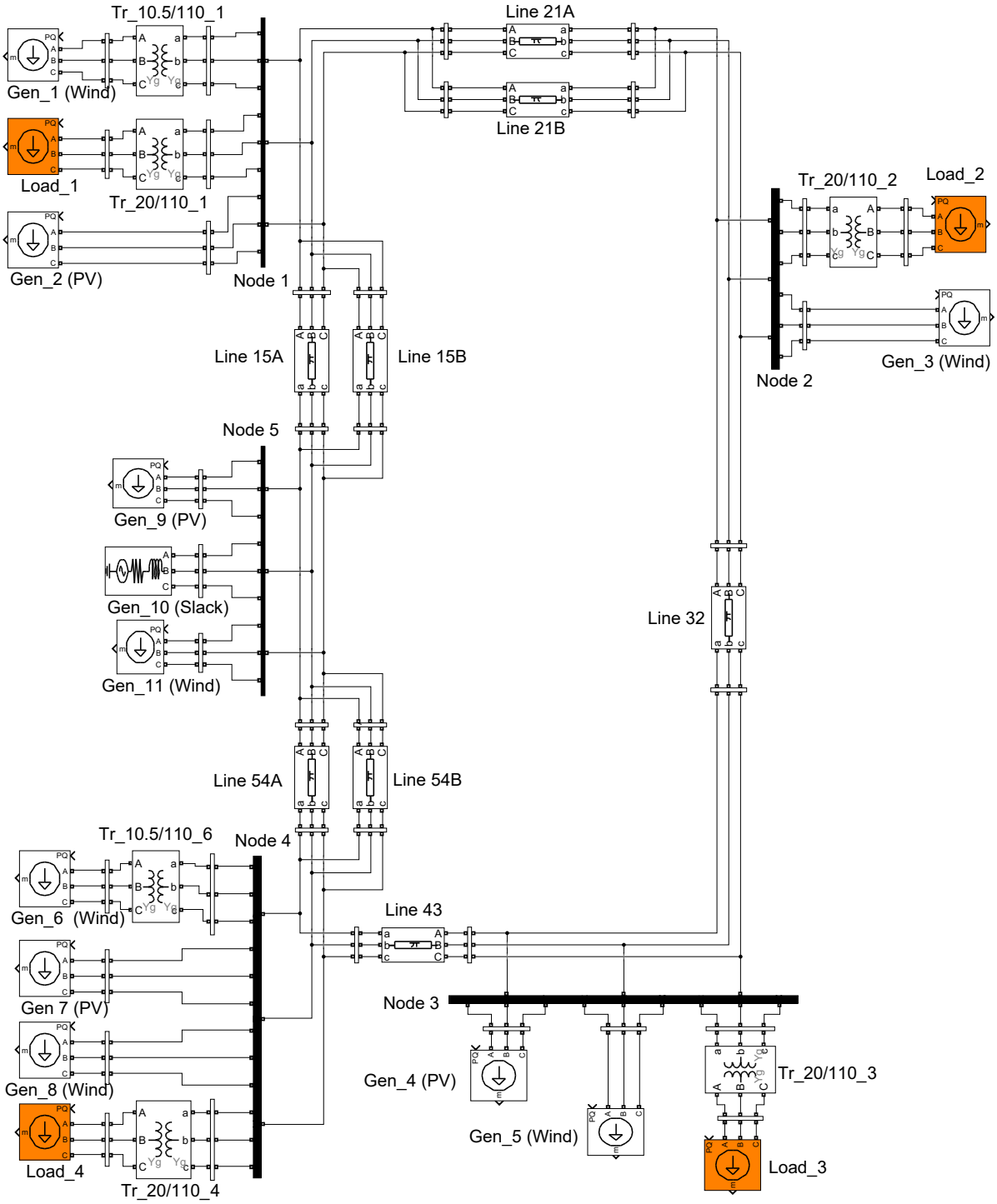

Figure 8.1: grid model used in the laboratory tests

Table 8.1: Nodes in laboratory grid model

Node ID	Name	v_{nom} (kV)	Type	Monitored by
1	n1	110	PQ	Agent 1
2	n2	110	PQ	Agent 2
3	n3	110	PQ	Agent 3
4	n4	110	PQ	Agent 4
5	n5	110	Slack	Agent 5
6	n1_10	10	PQ	Agent 1
7	n1_20	20	PQ	Agent 1
8	n1_20	20	PQ	Agent 1
9	n3_20	20	PQ	Agent 3
10	n4_20	20	PQ	Agent 4
11	n4_10	10	PQ	Agent 4

Table 8.2: Generators in laboratory grid model

Gen ID	Name	Node	Type	p_{nom} (MW)	q_{nom} (Mvar)
1	G1	n1_10	PQ	50	45
2	G2	n1	PQ	43	5
3	G3	n2	PQ	100	5
4	G4	n3	PQ	30	0
5	G5	n3	PQ	12	5
6	G6	n4_10	PQ	75	40
7	G7	n4	PQ	35	5
8	G8	n4	PQ	20	5
9	G9	n5	PQ	13	0
10	G11	n5	PQ	10	0
11	G10	n5	Slack	999	999

Table 8.3: DSRs in laboratory grid model

DSR ID	Line	$n_{\text{tap,max}}$	Δx_{tap} (mΩ)
1	21A	3	0.02

Table 8.4: Loads in laboratory grid model

Load ID	Name	Node	p_{nom} (MW)	q_{nom} (Mvar)
1	D1	n1_20	15	15
2	D2	n1_20	7.5	3
3	D3	n3_20	10	2
4	D4	n4_20	2	0.5

Table 8.5: Lines in laboratory grid model

Line ID	Name	Node 1	Node 2	r_{L} (Ω)	x_{L} (Ω)	i_{max} (kA)
1	15A	n1	n5	0.5778138	1.61032003	1070
2	15B	n1	n5	0.862203	3.05143995	680
3	21A	n2	n1	3.797579	9.43717998	420
4	21B	n2	n1	5.757716	14.3082	535
5	54A	n5	n4	3.476625	12.304	680
6	54B	n5	n4	3.476625	12.304	680
7	32	n3	n2	4.551057	12.8802	610
8	43	n4	n3	7.745162	15.707	470

Table 8.6: Transformers in laboratory grid model

Trafo ID	Name	Node 1	Node 2	r_T (Ω)	x_T (Ω)	i_{max} (kA)
1	T-n1-n1_10	n1	n1_10	0.202675	9.980443	839.78221
2	T-n1-n1_20	n1	n1_20	0.4782525	16.570103	524.863881
3	T-n2-n1_20	n2	n1_20	0.4782525	16.570103	524.863881
4	T-n3-n3_20	n3	n3_20	0.4782525	16.570103	524.863881
5	T-n4-n4_20	n4	n4_20	0.4782525	16.570103	524.863881
6	T-n4-n4_10	n4	n4_10	0.69066231	17.638291	446.134299

A.2 Agent database

Table 8.7: Agent database

Type	Unit	Bus	Line	Transformer	FPU	DSR
Constant data						
ID	-	✓	✓	✓	✓	✓
Type	-	✓	✓	✓	✓	✓
Agent	-	✓	✓	✓	✓	✓
v_{nom}	kV	✓				
Bus type	-	✓				
Bus 1 ID	-		✓	✓	✓	
Bus 2 ID	-		✓	✓		
Line ID	-					✓
i_{max}	A		✓	✓		
$c^{\text{thresholds}}$	%		✓	✓		
$\Delta\tau^{\text{step}}$	Ω or MW				✓	✓
$\tau^{\text{max/min}}$	Ω or MW				✓	✓
Measurements						
v_{meas}	kV	✓				
i_{meas}	A		✓	✓		✓
p_{meas}	MW		✓	✓	✓	
q_{meas}	Mvar		✓	✓	✓	
$p_{\text{flx,max/min}}$	MW				✓	
τ	Ω or MW				✓	✓

A.3 Laboratory scaffold

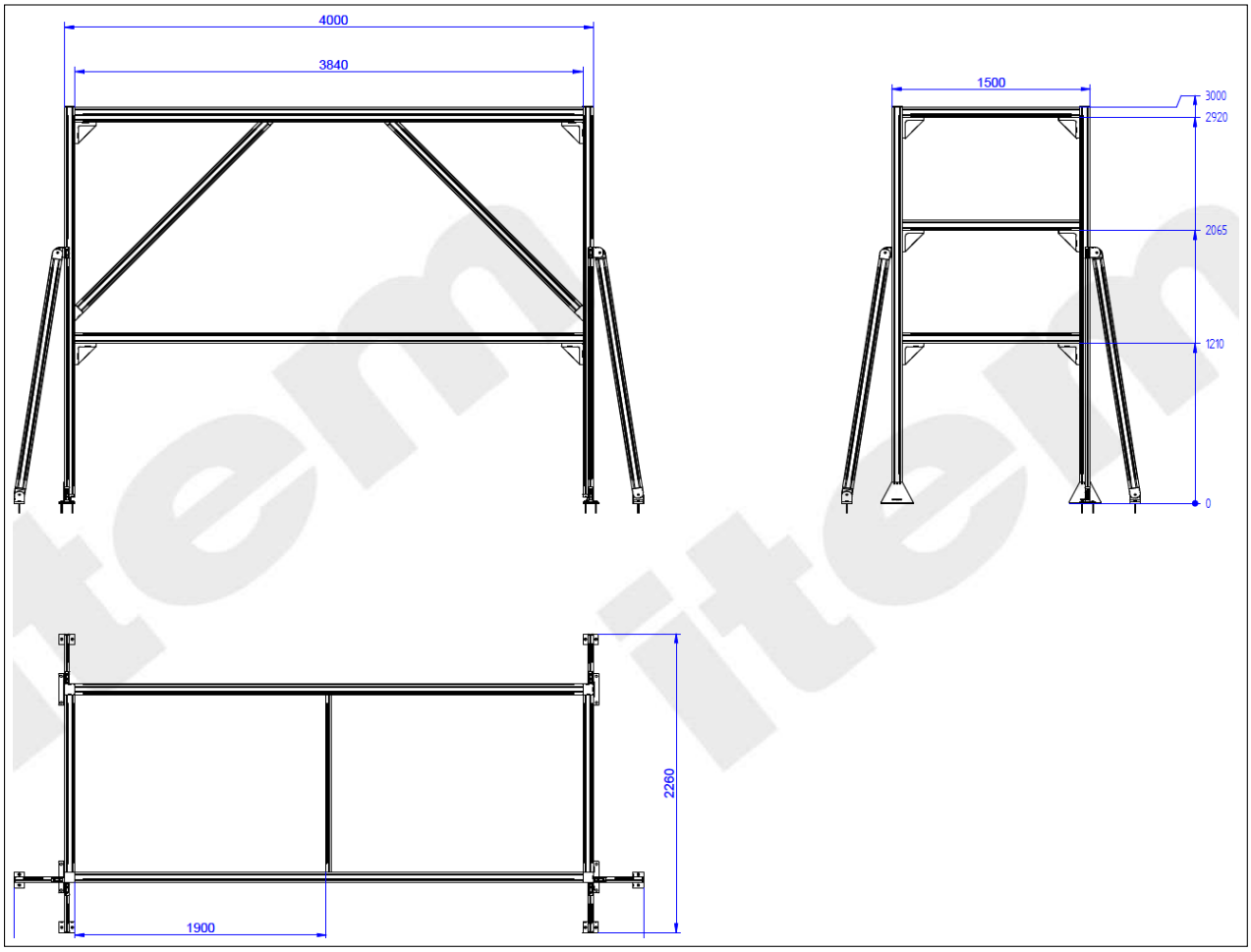

Figure 8.2: Scaffold concept for installation of DSRs

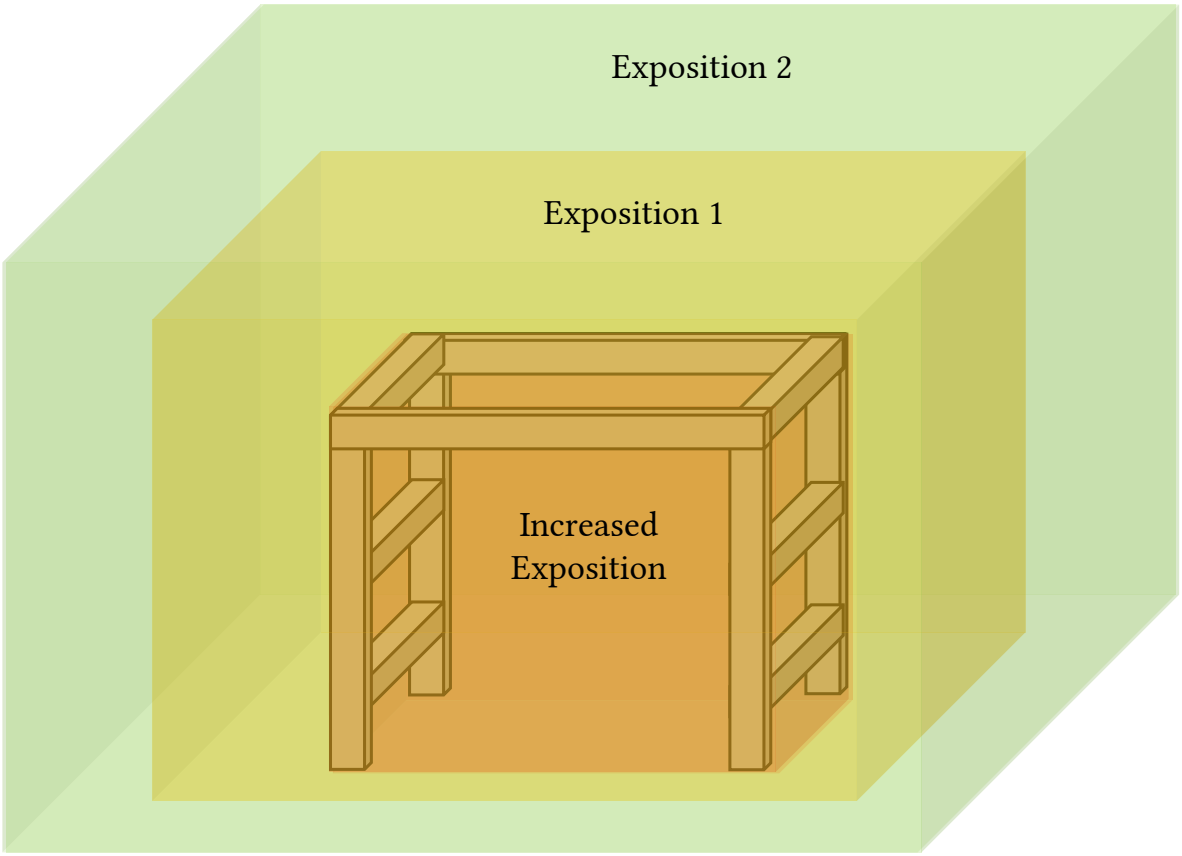

Figure 8.3: Areas of varying exposition to electromagnetic fields around the scaffold

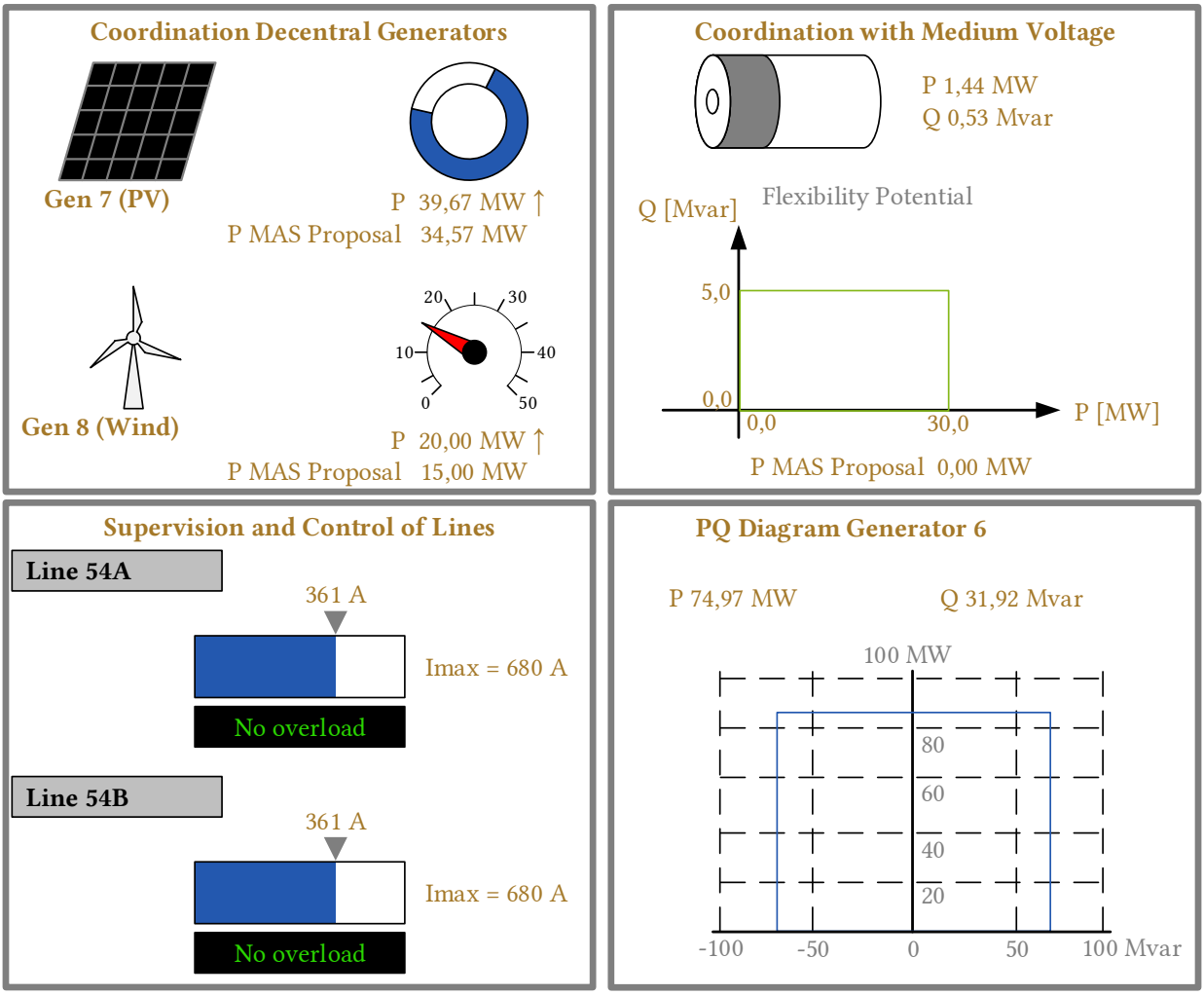

Figure 8.4: Dashboard overview of the agent at bus 4

A.4 Laboratory control center

A.4 Additional visualizations of laboratory results

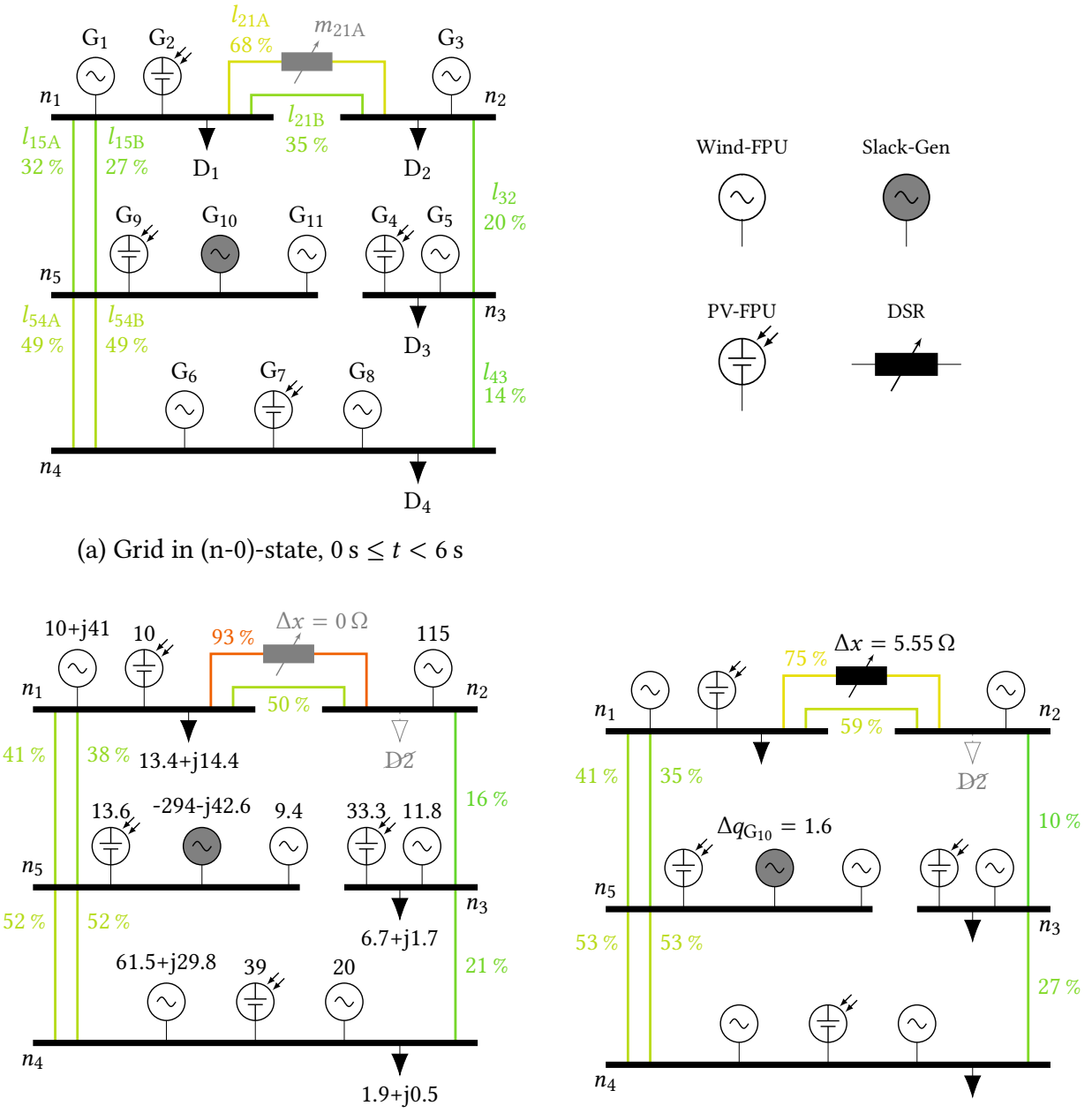

(a) Grid in (n-0)-state, $0\,\text{s} \leq t < 6\,\text{s}$

(b) Grid in (n-1)-state before DSR-activation, $6\,\text{s} \leq t < 33.6\,\text{s}$, re-/active power in pu

(c) Grid in (n-1)-state after DSR-activation, $33.6\,\text{s} \leq t < 64\,\text{s}$, re-/active power in pu

Figure 8.5: Static grid states during the DSR-only test case

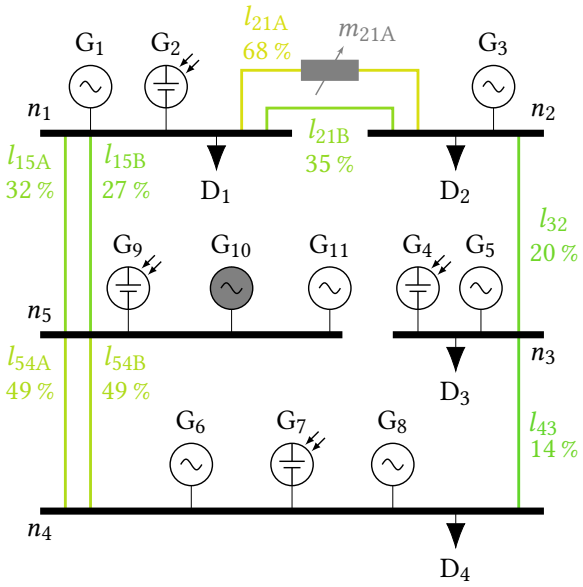

(a) Grid in (n-0)-state

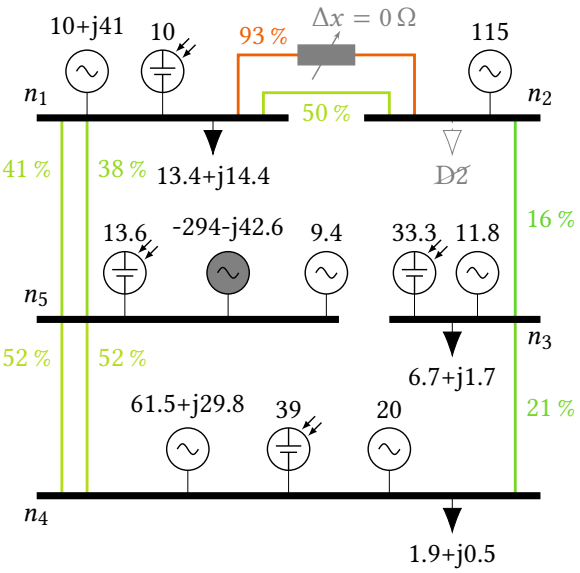

(b) Grid in (n-1)-state before RM-activation

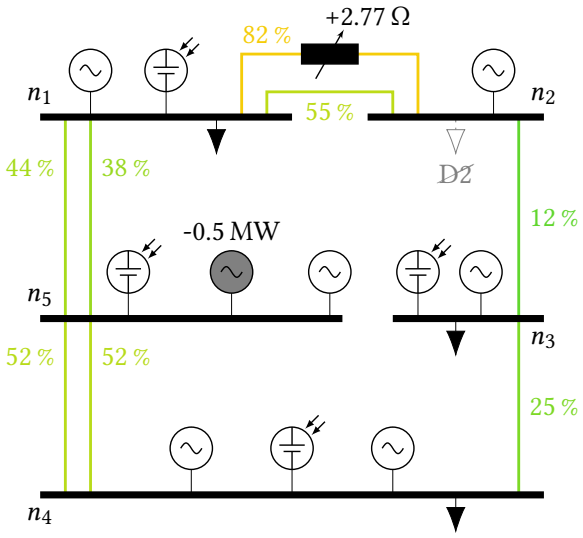

(c) Grid in (n-1)-state after DSR-activation

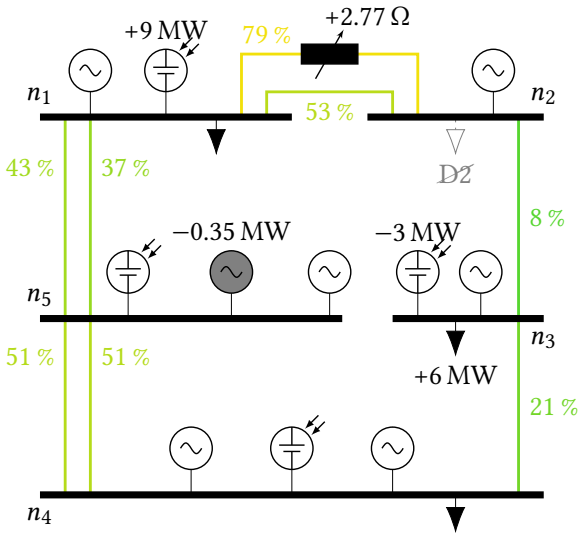

(d) Grid in (n-1)-state after RM-activation

Figure 8.6: Static grid states during the FPU + DSR grid use case

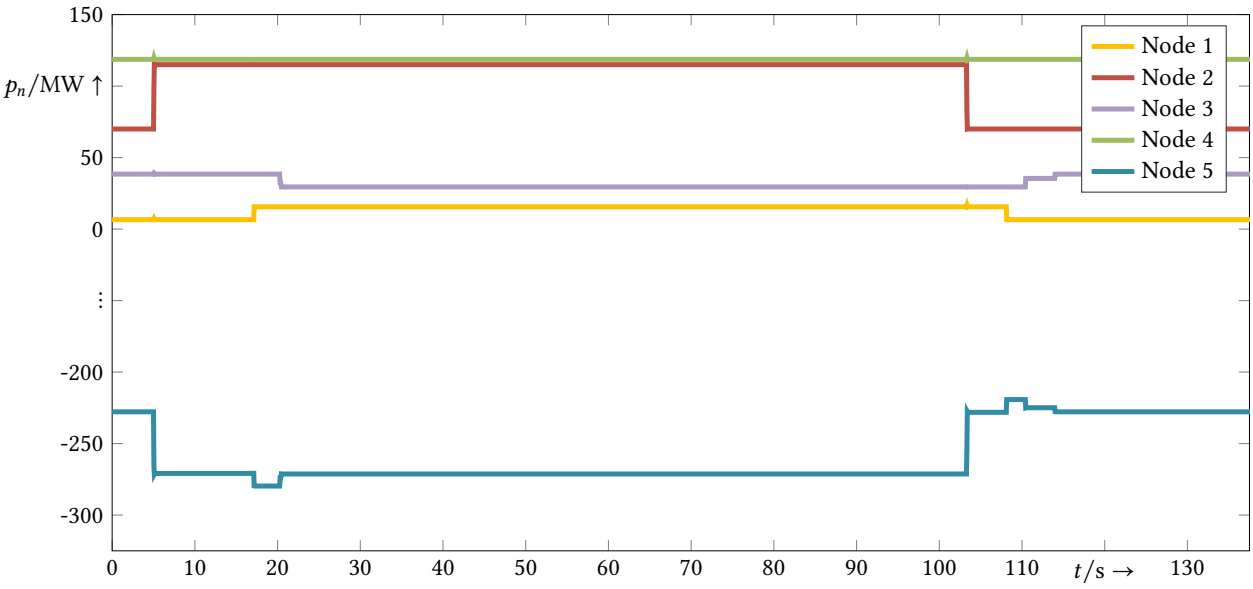

Figure 8.7: Nodal active power balances during test case with DSRs and FPUs

Name	n-0	n-1 before MAS	n-1 after MAS
Current limit violations:	**I/I_limit [%]**	**I/I_limit [%]**	**I/I_limit [%]**
21B			
21A	64.00	96.51	85.81

Figure 8.8: Resulting contingency list from control center's analysis